Forschungsbericht 2023-09

# Experimental Investigation of Supersonic Fluid–Structure Interaction for Future Space Transportation Systems

Dennis Daub

Deutsches Zentrum für Luft- und Raumfahrt
Institut für Aerodynamik und Strömungstechnik
Abteilung Über- und Hyperschalltechnologien
Köln

Deutsches Zentrum
DLR für Luft- und Raumfahrt

Forschungsbericht 2023-09

# Experimental Investigation of Supersonic Fluid–Structure Interaction for Future Space Transportation Systems

Dennis Daub

Deutsches Zentrum für Luft- und Raumfahrt
Institut für Aerodynamik und Strömungstechnik
Abteilung Über- und Hyperschalltechnologien
Köln

164 Seiten
96 Bilder
21 Tabellen
185 Literaturstellen

Deutsches Zentrum
DLR für Luft- und Raumfahrt

*Herausgeber:*

Deutsches Zentrum
für Luft- und Raumfahrt e. V.
Wissenschaftliche Information
Linder Höhe
D-51147 Köln

ISSN 1434-8454
ISRN DLR-FB-2023-09
Erscheinungsjahr 2023

DOI: 10.57676/cbaa-ce26

**License**

*fluid–structure interaction (FSI), shock-wave/boundary-layer interaction (SWBLI), supersonic flow, hypersonic flow, turbulence, wind tunnel, flutter, aeroelasticity, thermal buckling, reusable launch vehicles*

Dennis DAUB
German Aerospace Center (DLR), Institute of Aerodynamics and Flow Technology,
Supersonic and Hypersonic Technology Department, Cologne

***Experimental Investigation of Supersonic Fluid–Structure Interaction for Future Space Transportation Systems***
Doctoral Thesis RWTH Aachen University

Efficient orbital launch vehicles require a weight-optimized structure that can reliably withstand severe aerothermodynamic loads. The relevant loads, which are crucial for the design of such light-weight structures, can depend on the interaction of the thermal and deformation state of the structure with the surrounding flow field. This is referred to as Fluid–structure interaction (FSI). The reliable prediction of these loads is difficult, both for simplified engineering models and high-fidelity models, because such FSI problems are typically non-linear and, in many cases, dependent on turbulence. To improve fundamental understanding of such problems and to provide validation and reference data for modelling, a set of wind tunnel experiments was conducted where thin elastic panels were subjected to super- and hypersonic flow conditions ranging from cold conditions at high Reynolds numbers to high-enthalpy conditions. The experiments were conducted in the wind tunnels TMK, H2K, and L3K at DLR, Cologne. The observed behaviors of the panels include structural dynamics driven by the intrinsic dynamics of Shock-wave/boundary-layer interaction (SWBLI) and also by prescribed incident shock movements, panel flutter with and without SWBLI, and thermal buckling, in some cases with plastic effects. Cases combining both temperature- and pressure-driven effects were used to study the influence of the thermal and buckling state of the structure on structural dynamics. The experiments were accompanied by reference measurements on rigid wall structures to characterize thermal and pressure loads. The results of this study enabled a detailed analysis of the behavior of structures in super- and hypersonic flow environments, and also their influence on the flow field. Several data sets from these experiments have already successfully been used for comparison to numerical simulations.

*Strömung-Struktur-Wechselwirkung (FSI), Stoß-Grenzschicht-Wechselwirkung (SWBLI), Überschall, Hyperschall, Turbulenz, Windkanal, Flattern, Aeroelastizität, thermisches Beulen, Wiederverwendbare Raumtransportsysteme*

*(Veröffentlicht auf Englisch)*

Dennis DAUB
Deutsches Zentrum für Luft- und Raumfahrt, Institut für Aerodynamik und Strömungstechnik, Abteilung Über- und Hyperschalltechnologien, Köln

***Experimentelle Untersuchung von Strömung-Struktur-Wechselwirkung in Überschallströmungen für zukünftige Raumtransportsysteme***
Dissertation RWTH Aachen

Für den Bau effizienter Trägerraketen werden gewichtsoptimierte Strukturen benötigt, die zuverlässig extremen aerothermodynamischen Lasten standhalten. Diese Lasten, die für die Auslegung solcher Leichtbaustrukturen ausschlaggebend sind, können von Wechselwirkungen zwischen Deformation und Temperatur der Struktur und der umgebenden Strömung abhängen. Dies wird als Strömung-Struktur-Wechselwirkung (FSI) bezeichnet. Die zuverlässige Vorhersage der resultierenden Lasten ist sowohl bei vereinfachter als auch bei detaillierter Modellierung schwierig, weil FSI typischerweise nichtlinear und in vielen Fällen turbulenzabhängig ist. Um das grundlegende Verständnis solcher Probleme zu verbessern, und um Validierungs- und Referenzdaten für die Modellierung bereit zu stellen, wurden Experimente an dünnen elastischen Platten in Über- und Hyperschallströmungen durchgeführt. Die Strömungsbedingungen reichten von kalter Strömung bei hoher Reynoldszahl bis hin zu Hochenthalpieströmung. Diese Experimente wurden in den Windkanälen TMK, H2K und L3K des DLR in Köln durchgeführt. Das beobachtete Verhalten der Platten beinhaltet Strukturdynamik, die von der intrinsischen Dynamik von Stoß-Grenzschicht-Wechselwirkung (SWBLI) oder von vorgegebenen Bewegungen eines einfallenden Stoßes verursacht wird, aber auch Flattern mit und ohne SWBLI sowie thermisches Beulen, in einigen Fällen mit plastischer Deformation. Fälle, in denen gleichzeitig temperatur- und druckabhängige Effekte auftreten, wurden genutzt, um den Einfluss thermischen Beulens auf die Strukturdynamik zu untersuchen. Diese Versuche wurden ergänzt durch Referenzversuche zur Bestimmung von Temperatur- und Drucklasten an starren Referenzstrukturen. Die Ergebnisse ermöglichten eine detaillierte Analyse des Verhaltens von Strukturen in Über- und Hyperschallströmungen und derer Effekte auf das Strömungsfeld. Datensätze aus mehreren Experimenten wurden bereits erfolgreich zum Vergleich mit numerischen Simulationen verwendet.

# Experimental Investigation of Supersonic Fluid–Structure Interaction for Future Space Transportation Systems

## Experimentelle Untersuchung von Strömung-Struktur-Wechselwirkung in Überschallströmungen für zukünftige Raumtransportsysteme

Von der Fakultät für Maschinenwesen
der Rheinisch-Westfälischen Technischen Hochschule Aachen
zur Erlangung des akademischen Grades eines Doktors der Ingenieurwissenschaften
genehmigte Dissertation

vorgelegt von

Dennis Michael Daub

Berichter: Universitätsprofessor Dr.-Ing. Wolfgang Schröder
Universitätsprofessor Dr.-Ing. Nikolaus A. Adams

Tag der mündlichen Prüfung: 5.4.2023

# Vorwort

An dieser Stelle möchte ich allen danken, die mich beim Erstellen dieser Arbeit unterstützt haben.

Ich bedanke mich bei Prof. Dr. Wolfgang Schröder für die wissenschaftliche Betreuung dieser Arbeit und bei Prof. Dr. Nikolaus Adams für die Übernahme der Aufgabe des zweiten Berichters. Bei beiden bedanke ich mich auch für die Begleitung dieser Arbeit im Rahmen des Sonderforschungsbereichs Transregio 40.

Mein besonderer Dank gilt Prof. Dr. Ali Gülhan, der mir die Möglichkeit zu dieser Arbeit eröffnet und mich in der Durchführung immer unterstützt hat.

Mein besonderer Dank gilt auch Dr. Sebastian Willems für die vorhergehende Arbeit, die Einführung in die Thematik und eine Vielzahl hilfreicher und kritischer Diskussionen zum Thema. Ebenso gilt mein Dank Dr. Burkard Esser für die Mitbetreuung der Arbeit im Sonderforschungsbereich Transregio 40 und die Betreuung der Versuche im lichtbogenbeheizten Windkanal.

Für die kritische Durchsicht des Manuskripts danke ich Daniel Kirchheck, Dr. Andreas Flock, Prof. Dr. Karlheinz Blank, Sigrid Blank und meiner Schwester.

Ich danke Daniel Habegger, Eddy Habegger, Martin Achner, Alexander Ruf, Matthias Koslowski, Marcus Schröder, Marco Schmors und Michael Kosbow für die verlässliche und gewissenhafte Durchführung der Versuche. Ebenso bedanke ich mich bei Markus Miketta und Silvia Alker für die Unterstützung bei der Konstruktion der Windkanalmodelle und der H2K Schlierenoptik.

Bei den Beteiligten des Sonderforschungsbereichs Transregio 40, insbesondere Dr. Vito Pasquariello und Katharina Martin, bedanke ich mich für die gute Zusammenarbeit.

Bei meinen Kollegen bedanke ich mich für viele hilfreiche Diskussionen und das hervorragende Arbeitsklima.

Ich bedanke mich bei meinen Eltern, meiner Familie und meinen Freunden für ihre fortwährende Unterstützung.

Köln, April 2023 Dennis Daub

# Contents

# List of Figures

# List of Tables

# Nomenclature

## Abbreviations

| | |
|---|---|
| ANSYS | Commercial FEM software |
| C/C-SiC | Carbon fibre reinforced ceramics |
| CARS | Coherent anti-Stokes Raman spectroscopy |
| DFG | Deutsche Forschungsgemeinschaft |
| DIC | Digital image correlation |
| DLR | Deutsches Zentrum für Luft- und Raumfahrt e.V. |
| DNS | Direct numerical simulation |
| FEM | Finite element method |
| FSI | Fluid–structure interaction |
| H2K | Hypersonic Wind Tunnel H2K (see Section 4.1.1) |
| IR | Infrared |
| L3K | Arc-heated Wind Tunnel L3K (see Section 3.1.1) |
| LES | Large eddy simulation |
| NASA | National Aeronautics and Space Administration |
| PDF | Probability density function |
| PEEK | Polyether ether ketone |
| PIV | Particle image velocimetry |
| PSD | Power spectral density |
| PSI | Pressure Systems, Inc. |
| RANS | Reynolds-averaged Navier–Stokes equations |
| ROBOT | Render Object Based Orientation Tracking |
| SFB TRR 40 | Collaborative Research Center "Technological Foundations for the Design of Thermally and Mechanically Highly Loaded Components of Future Space Transportation Systems" (financially supported by DFG) |
| SHM | Structural health monitoring |
| SLS | Space Launch System |
| SWBLI | Shock-wave/boundary-layer interaction |
| TAU | DLR numerical flow solver |
| TBC | Thermal barrier coating |
| TBL | Turbulent boundary layer |
| TMK | Trisonic Wind Tunnel TMK (see Section 2.1.1) |
| TPS | Thermal protection system |

## Latin Symbols

| | |
|---|---|
| $c$ | Constant for 0-1 Test for Chaos |
| $f$ | Frequency |
| $I$ | Grey scale value |
| $i$ | Index |
| $j$ | Index |
| $K$ | Growth rate for the 0-1 Test for Chaos |
| $M$ | Mean square displacement for the 0-1 Test for Chaos |
| $Ma$ | Mach number |
| $N$ | Sample size |
| $n$ | Sample index |
| $P$ | Translation variable for 0-1 Test for Chaos |
| $p$ | Pressure |
| $Q$ | Translation variable for 0-1 Test for Chaos |
| $Re$ | Reynolds number |
| $T$ | Temperature |
| $t$ | Time |
| $u$ | Flow velocity in $x$-direction |
| $x$ | $x$-coordinate |
| $y$ | $y$-coordinate |
| $z$ | $z$-coordinate |

## Greek Symbols

| | |
|---|---|
| $\alpha$ | Angle relative to undisturbed flow field |
| $\kappa$ | Heat capacity ratio |
| $\Phi$ | Sample |

## Subscripts

| | |
|---|---|
| 0 | Total, settling chamber |
| $\infty$ | Free stream condition |
| $max$ | Maximum |
| $w$ | Wall |

# 1 Introduction

Improving reliability and affordability of access to space is crucial for increasing humanity's space capabilities, ranging from earth-centered services such as navigation, communication, climate monitoring, and manufacturing to science and exploration within and beyond the solar system. Progress towards this goal can be made by improved design of expendable vehicles like Ariane 6, partial reuse as in the case of Falcon 9 and Electron, or full reuse including recovery of the upper stage. The most promising effort to achieve the latter is the SpaceX Starship currently under development (Fig. 1.1, [120]). One of the most notable previous attempts, the X-33 (Fig. 1.2), proceeded to an advanced stage of development [181] before the program was cancelled. The iconic Space Shuttle achieved many years of service but fell short of practical reusability due to immense requirements for overhaul between flights [18, 105].

These types of vehicles require a minimum-weight exterior shell, including control surfaces and propulsion components, which has to reliably withstand a broad range of aerothermodynamic loads. For reusable vehicles, it additionally has to withstand repeated load cycles from ascent through atmospheric entry to landing. The design of such structures depends on detailed knowledge of these loads.

For the prediction of these aerothermodynamic loads and resulting requirements for vehicle structures, it is crucial to understand the interdependency of the thermal and deformation state and dynamics of the structure with the surrounding flow field. This interdependent behavior is called Fluid–structure interaction (FSI). Failure to appropriately address these issues can render design solutions impossible or lead to structural failures on flight vehicles (e. g. [44, 86, 97, 166]).

The behavior of such structures depends on a number of partially interdependent factors:

- The mechanical behavior of a structure depends on its mass, stiffness, and damping, which has to be considered in conjunction with mounting and support structure.
- For high-speed vehicles, typically the thermal state of the structure is of central importance. The thermal state of the structure results from its thermal properties, and from heat transfer to and from the flow field as well as the internal substructure [8]. This in turn affects the properties of the structure, which can result in changed stiffness and deformation altering the dynamic behavior [95] and heat transfer [93].
- Certain combinations of dynamic pressure, panel mass, and stiffness can lead to self-excited oscillations of surface panels called flutter [41]. Panel flutter is strongly dependent on in-plane loading, which can be connected to the thermal state of the structure or mechanical loads from the vehicle (e. g. [123]). Both factors can facilitate or inhibit panel dynamics. Flutter also occurs in cases with

**Figure 1.1:** SpaceX Starships (Photo by SpaceX CC BY-NC 2.0 [148])

an aerodynamic shock impinging on a panel, which has been shown to lower the required dynamic pressure for the onset of flutter in some cases [161]. Furthermore, flutter is influenced by the state of the boundary layer or Shock-wave/boundary-layer interaction (SWBLI) [40, 162].

- A buckled structure can have more than one equilibrium position. In such cases, external loading can lead to a dynamic change between these states referred to as snap-through [90, 150], which can alter the flow field, heat transfer, and dynamic properties of the structure.

- Turbulence and SWBLI impose dynamic loads on the structure [16, 38, 107]. Furthermore, the state of the boundary layer or SWBLI has a large impact on heat transfer (e. g. [67, 139, 170]) and thus again the thermal state of the structure. In turn, the thermal state of the structure as well as static and dynamic deformation both influence the behavior of the flow field [128, 146, 164].

Given these interdependencies, it becomes obvious that the behavior of FSI can be strongly path-dependent or non-linear. This is especially complicated in cases that include turbulence-driven flow features that can drastically alter heat transfer as well as pressure loads.

Thus, FSI poses a complex challenge for the design of vehicle structures. Potentially opposing requirements arise if a broad range of flight conditions needs to be covered, e. g. large dynamic pressures and large heat loads occurring during different parts of the trajectory. Also, it is not necessarily apparent which combinations of loads and conditions of the structure can be considered worst cases, e. g. the combination of maximum heating


**(a)** TPS panels mounted on F-15B for in-flight Fluid–structure interaction (FSI) testing

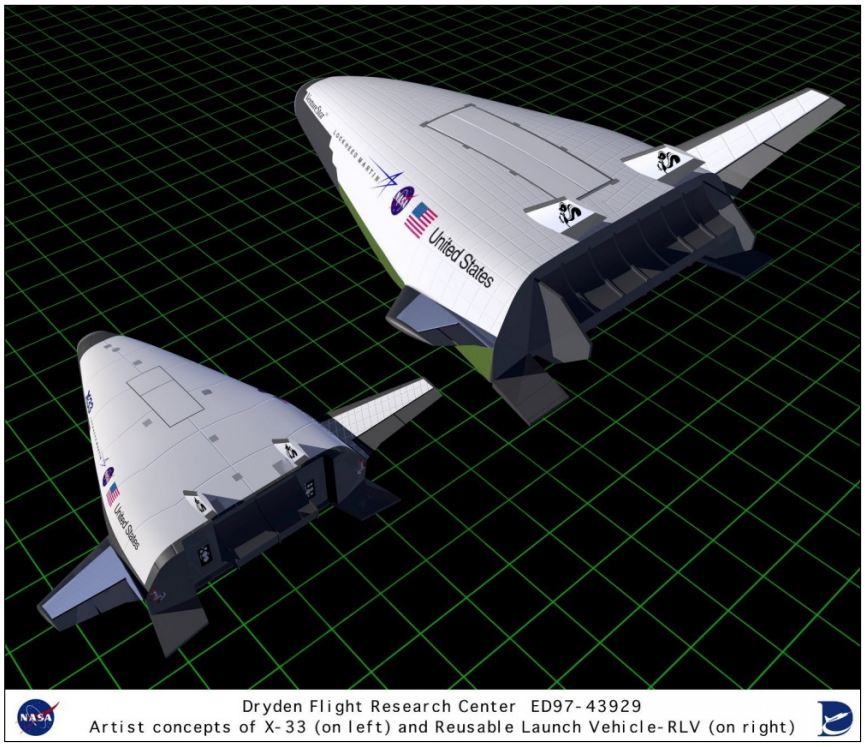


**(b)** Reusable orbtial launch vehicle concepts

**Figure 1.2:** X-33 (Photos courtesy of NASA)

and maximum dynamic pressure may well not be the worst case in terms of structural dynamics as heating may both inhibit or enable dynamic behavior of the structure.

Suitable modelling is needed that is both reliable and feasible in terms of computational resources. However, currently neither simplified modelling nor models using Large eddy simulation (LES) or Direct numerical simulation (DNS) can fully and reliably predict all relevant FSI cases. The former omits physical phenomena that can influence the resulting behavior. The latter, while in principle capturing the underlying physics at the required level, is usually too computationally expensive for use beyond a very limited range of generic cases. Therefore, experiments are crucial to further advance fundamental understanding and validation of modelling in this area. Only very few studies are currently available.

The present effort, based within the Collaborative Research Center "Technological Foundations for the Design of Thermally and Mechanically Highly Loaded Components of Future Space Transportation Systems" (SFB TRR 40) [68, 69] of the Deutsche Forschungsgemeinschaft (DFG), aims at making a contribution in this area by conducting experimental studies of fluid–structure coupled problems to help understand the fundamental processes and gain experience with structures under such conditions as well as to provide reference or validation data for numerical simulations.

## 1.1 Previous Work

### 1.1.1 Documented Examples of FSI on Flight Vehicles

Examples of structural damage on flight vehicles were documented for the X-15, a hypersonic rocket-powered research aircraft. Melting damage due to enhanced heating near incident shocks was reported in [166], thermal buckling occurred near the wing leading edges [154]. Fatigue cracks were found on surface panels due to flutter occurring in flight, which was also reproduced in wind tunnel tests [86].

An Ariane 5 was lost due to insufficient load definition in the nozzle area. This resulted in the rapid destruction of the main engine nozzle including buckling of cooling channels that define the shape of the nozzle contour [44, 97].

It is also interesting to look at the development of the SR-71, the fastest piloted air-breathing aircraft ever made, cruising in excess of $Ma = 3$, for which, to the author's knowledge, no FSI-related failures were reported. In the development phase, extensive thermomechanical testing was conducted, some of it even using full size vehicles [85, 117]. The lower fuselage of the retired vehicles shows large panel deformation (Fig. 1.3, [150]).

Structural dynamics measurements of interstage adapters from three flights of Atlas-Centaur were reported in [104]. It was concluded that probably no panel flutter occurred and that the "high degree of skin oscillation" observed during these flights resulted from aerodynamic excitation. Interestingly, in a related study presented in [121], even

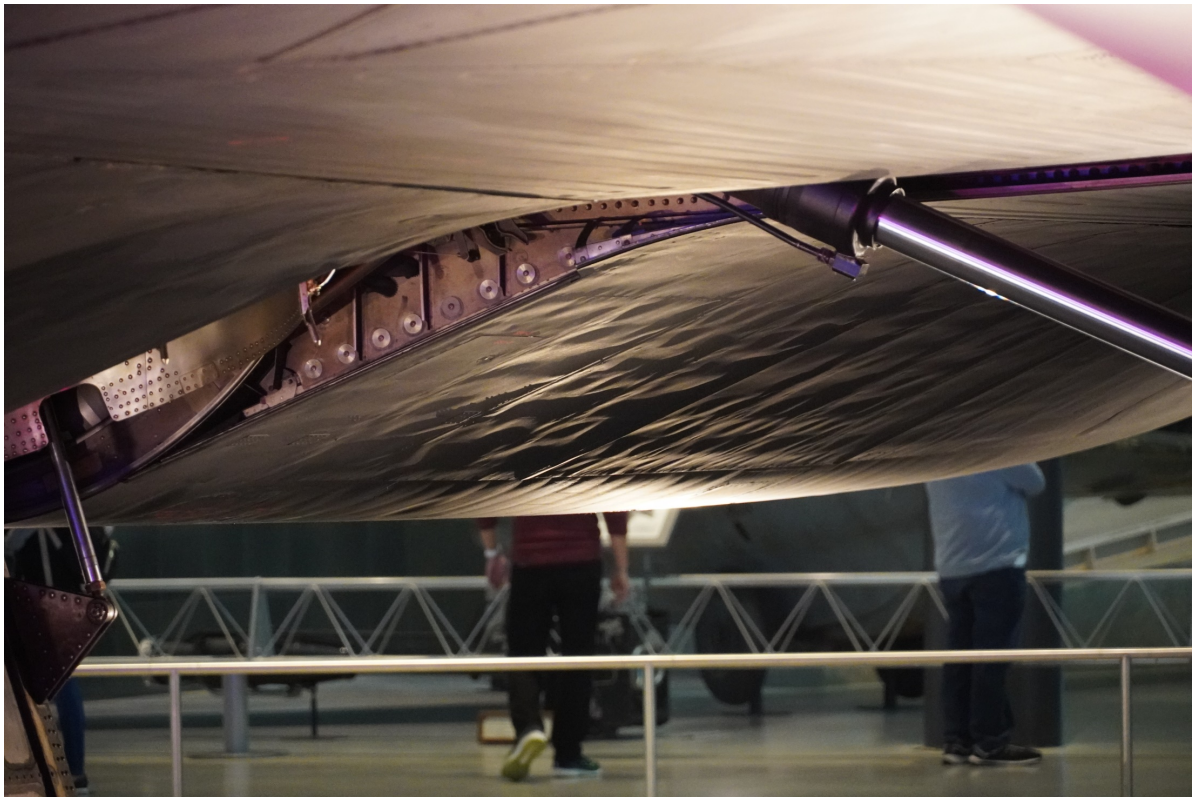

**Figure 1.3:** SR-71 surface panels (Photo by the author)

a cryogenic tank was included in a wind tunnel flutter investigation to assure suitable boundary conditions.

Similarly, significant surface pressure fluctuations at lift-off through the transonic well into the supersonic part of the trajectory of the first flights of the Saturn V were reported in [99]. Surface panels had been subjected to full scale wind tunnel tests where flutter was obtained for some conditions inside the flight envelope. Compressive loading as it would be imposed from the full vehicle was also taken into account [123, 132].

While no complete X-33 vehicle was ever flown, it is interesting to note that orbital reentry Thermal protection system (TPS) panels were tested in a low-altitude supersonic flow environment by mounting them on a F-15B supersonic jet (Fig. 1.2a). These investigations even included incident shock loads [181]. Unfortunately, no test data was published.

### 1.1.2 Thermal Effects

Heat transfer in boundary layers has been thoroughly investigated for decades [139]. The possibly most challenging aspect troubling high-speed vehicles is the large difference in heat transfer between laminar and turbulent boundary layers, because the transition from a laminar to a turbulent state is still not reliably predictable. Additionally, this process can locally enhance heat transfer beyond the level of a turbulent boundary layer [170].

A further complication occurs in cases with SWBLI, which can drastically enhance local heat transfer (e. g. [67, 74, 101, 140]). The behavior of a SWBLI depends on the state of the incoming boundary layer (e. g. [178]) amplifying the uncertainty caused by unreliable predictions of the state of the boundary layer. Furthermore, SWBLI heat transfer in cases involving turbulence is only well predicted by computationally very expensive high-fidelity methods such as LES and DNS but not by simpler Reynolds-averaged Navier–Stokes equations (RANS)-based simulations [38, 52]. Additionally, several studies have shown effects of the wall temperature on the size of SWBLI-induced flow separation [84, 163, 164], which can change the resulting heat transfer and pressure loads.

At sufficiently high temperatures, effects such as chemical non-equilibrium and catalytic effects on the wall might need to be considered [79]. Thermally coupled hypersonic FSI cases with laminar boundary layer were investigated in [174, 176]. Heating of rigid Carbon fibre reinforced ceramics (C/C-SiC) structures in a high-temperature hypersonic flow environment was measured in an arc-heated hypersonic wind tunnel and compared to thermally coupled simulations. Despite generally good agreement, experimentally observed transient changes in heat transfer could not fully be reproduced. These differences were attributed to insufficient modelling of catalytic effects on the model surface.

The effect of similar flow conditions on a thin metallic panel was experimentally and numerically investigated in [73, 124], showing significant thermal buckling. This included plastic effects and led to local increases in heat transfer due to the deformation of the structure. The heat flux augmentation for a similar configuration had previously been demonstrated in [57]. Rigid structures with dome-shaped protuberances were used as a model for a deforming TPS panel. This resulted in heat flux augmentations of up to 30 %. Notably, maximum heat transfer augmentation was obtained for a transitional boundary layer. These studies, along with numerical investigations in [72, 93, 94, 157], demonstrate the strong interdependence of heat transfer and structural deformation that makes coupled treatment of these problems inevitable for reliable predictions of temperature and deformation of the structure. An interesting complement to these studies, but without flow field, is found in [46], where the thermal buckling behavior of similar structures was investigated experimentally. The study shows the effects of localized heating on deformation patterns.

### 1.1.3 Flutter

Flutter of panel configurations in supersonic flow is well understood with regard to its onset for simple panel cases without incident shock [41, 116]. The situation becomes more complicated when the effects of boundary layers are taken into account. In [40], damping effects stemming from the boundary layer were observed, whereas later studies found both stabilizing and destabilizing effects [1, 71]. The influence of in-plane loads obtained from aerodynamic heating of panels was studied experimentally in [145] and theoretically in [160]. In these experiments, panels were heated by the airflow, leading to buckling. In most cases, flutter occurred before buckling of the structure and subsided eventually because of the stiffening of the structure due to buckling. However, no full

time-resolved data set was included. Similar results were also reported in [95]. In most other studies, the observations were limited to obtaining the conditions for flutter onset. A rare exception is the study in [89], which was specifically aimed at measuring flutter dynamics. It was found that in-plane compressive loads could reduce the dynamic pressure required for flutter onset in some cases by 75 %, whereas even a small rise in pressure differential significantly stiffened the panel. Thermal effects were not considered and compressive loads were applied by the experimental setup. However, heating would induce in-plane stresses in a similar way.

The influence of an incident shock on panel flutter was numerically investigated in [161, 162], showing that the dynamic pressure required for flutter onset could be strongly reduced for configurations with a strong shock, while a weaker shock could suppress panel flutter by stiffening the structure through added deformation. In some cases, the presence of a laminar boundary layer was shown to drastically increase flutter amplitudes for an incident shock configuration compared to an inviscid configuration [9].

The first published case known to the author with full data not only on the onset but also on the panel dynamics during flutter with and without shock generator, including thermal effects was reported in [150]. The results highlight the strong dependency of the observed panel dynamics on the thermal state of the structure. One case from that study without shock generator was numerically modelled in [55], using a low-fidelity simulation, which yielded good agreement given the limitations of the approach.

### 1.1.4 Snap-Through

A buckled panel may have several equilibrium positions. Aerodynamic loads can cause a dynamic change between these, which is referred to as snap-through. Reference experiments without flow field were conducted in [46, 90, 171]. In configurations with airflow, this behavior was observed in [10, 150, 151]. It can both manifest in a singular change of panel deformation or sustained oscillations. Interestingly, the latter case as observed in [10] showed chaotic flutter of the structure that could be reproduced in a simulation without consideration of turbulent effects [12]. However, the authors of that study suggest that some instances observed in [150] may be driven by turbulent aerodynamic loads. Generally, such behavior strongly depends on thermal or vehicle-induced in-plane loads as well as pressure dynamics or excitation from the vehicle [118]. The existence of FSI cases with chaotic structural dynamics for inviscid flow has been predicted in [41, 43].

### 1.1.5 Turbulent Effects and SWBLI Dynamics

A notable example of the actual loads in a relevant environment was provided in [107] where boundary-layer noise on a X-15 was measured at various locations on the vehicle and during various parts of the trajectory. Pressure dynamics of up to 150 db were found. Early ground experiments were reported in [16, 110, 111] where the response of wall panels to attached or separated boundary layers was studied, showing that the presence of

SWBLI can significantly increase panel dynamics compared to cases with an undisturbed boundary layer. Besides thermal aspects, the most striking feature of SWBLI is that it can produce low-frequency pressure oscillations in the order of about 100 Hz–1000 Hz [14], which is also a typical range for eigenfrequencies of vehicle structures. While this is a well-known occurrence, the underlying dynamics are still not fully understood. In various studies, the properties of the SWBLI dynamics were attributed to upstream disturbances or the properties of the separation itself (see [131] for a detailed discussion). A numerical study of the interaction of these effects with an elastic structure inevitably requires LES or DNS approaches that can reliably predict such dynamics whereas RANS-based approaches do not resolve the dynamics of the SWBLI flow field [78].

The effect of a turbulent SWBLI with large separation on FSI was studied experimentally in [174, 177], showing excitation of the structure linked to the dynamics of the flow separation and also a feedback of panel oscillations into the flow field most notably detectable in downstream pressure measurements. A similar configuration was also used in [150]. For this case, differences between experiment and simulation were observed that were assumed to be caused by the SWBLI dynamics not included in the modelling [58, 59]. Similar discrepancies were also reported for a later modelling effort in [11]. It was shown in [159] that excitation of some modes of an elastic panel was stronger in presence of the SWBLI. A ramp configuration was used in [169] to induce SWBLI on an elastic panel. For this configuration, it was found that the size of the separation changes the frequencies occurring in the observed panel dynamics. Furthermore, a feedback of the panel dynamics into the flow field was found, similar to results for incident shock configurations in [150, 174].

A number of works aim to use the apparent interdependency between panel deformation and SWBLI dynamics to favorably influence dynamic pressure loads. An interesting example was provided in [133], where a compliant rubber insert was used to reduce SWBLI dynamics. In [64], a deformable wall was set to various static deformation shapes to reduce observed shock dynamics.

A FSI-coupled numerical study using DNS in [146] showed another intricate way in which structural dynamics can feed back into the flow field. For a configuration with transitional SWBLI, FSI was shown to promote laminar–turbulent transition of the boundary layer. The influence of wall vibrations on boundary-layer transition was also discussed in [50, 51]. Furthermore, it was shown in [13] that intermittent turbulent spots can be used to excite a structure, leading to structural responses which greatly exceeded those with a laminar boundary layer.

Studies directly related to or based on the present results [81, 130, 131, 185] will be discussed in Chapter 2.

### 1.1.6 Scaling and Application

Typically, wind tunnel tests cannot fully match flow conditions and geometrical dimensions of vehicle structures. However, there are exceptions, perhaps most notably, in the development of the Saturn V where full-size segments were FSI-tested [123]. For more

humble endeavours, this leads to the question how smaller wind tunnel models relate to flight-size vehicles and respective flow conditions.

Engineering approximations are available to estimate surface pressure dynamics for various flow configurations appearing on launch vehicles that can be scaled with free stream dynamic pressure [45]. Similarly, wind tunnel dynamic wall pressure measurements can be scaled with wind tunnel and flight dynamic pressure, for example as done in [76, 153] during development of the Space Launch System (SLS). However, these approaches do not include any influence of the structure on the flow field.

Simplified modelling allows to obtain flutter boundaries depending on dynamic pressure, Mach number, and structural properties [40]. This enables some degree of scaling, including estimates of flutter amplitudes. But these approaches are limited to cases where the static and dynamic structural behavior do not depend on detailed knowledge of aerodynamics. Shock waves, flow separation, localized heat transfer, and turbulence-related dynamics, all commonly occurring during the flight of supersonic vehicles, complicate matters considerably.

For all cases where these simplified methods may fail, more detailed modelling that reproduces the relevant features of the respective FSI configuration is essential. The main purpose of the present study is to improve understanding of the underlying processes, provide reference and validation data for modelling, and to clarify what level of fidelity is required to capture various FSI effects as well as to understand related uncertainties.

Increased life time of reusable vehicles and related life-time prediction will place stricter requirements on reliability of such modelling than previously necessary for expendable vehicles. Additionally, such vehicles require suitable Structural health monitoring (SHM) systems [56, 112, 142] that reliably work in an exceptionally broad range of ambient conditions where temperature changes and unsteady pressure loads pose particular challenges [34, 37, 119, 180]. Furthermore, only little flight or ground test data is available for development and testing of such systems [87].

It should also be noted that the structures considered in the present work are quite similar in size to actual flight vehicle structures regarding the free panel area between mounting or support structure (e. g. in case of the SR-71 in Fig. 1.3 or X-33 [127]). This means that some observations made in the present study may in fact be quite similar to effects observed on flight vehicles.

## 1.2 Scope of the Present Work

Given the complex interdependencies between fluid and structure, and the limitations of present modelling approaches, two crucial areas were identified: Thermal effects on static and dynamic deformation, and the effects of the SWBLI. The scope of the present work is to explore configurations where simplified scaling or modelling fails by conducting extensive experimental studies to improve fundamental understanding of such problems, and to provide reference and validation data for modelling.

Points of particular interest are:

- Structural dynamics of panel flutter in hypersonic flow, including in particular the effect of an incident shock that was predicted to facilitate flutter in cases where it would not occur without incident shock based on numerical simulations of simplified cases at lower Mach number in [161, 162]
- FSI effects of intrinsic low-frequency SWBLI dynamics, complementing previous observations of such effects at lower Mach number with incident shock configurations [58, 59, 174] or in hypersonic flow, using a ramp configuration [169], where an influence of intrinsic SWBLI dynamics on structural dynamics was found
- Effects of a moving incident SWBLI on an elastic panel
- Thermal effects that influence the dynamic behavior of the structure, leading to changes in the occurring frequencies as well as influencing the onset and stop of flutter, complementing results that were either obtained at lower Mach number [150] or for ramp configurations [169]
- Large amplitude buckling in a high-enthalpy environment with plastic deformation adding to previous experimental studies in [57, 124] to obtain time-resolved full-field data both on surface deformation and temperature

This work is structured into three main chapters on the results of the three considered experimental setups. Chapter 2 describes experiments on the effects of intrinsic and prescibed SWBLI dynamics on FSI in supersonic flow focusing on the resulting structural dynamics, whereas Chapter 3 presents FSI cases in hypersonic high-enthalpy flow primarily driven by aerothermal heating, leading to buckling of the structure. Chapter 4 combines aspects of both with experiments in hypersonic flow at moderate temperature where thermal effects, SWBLI-dynamics, and flutter can be observed. These chapters can be read independently. However, all chapters contain cross-references in the respective discussion of the setup and the results.

Some of the outcomes have already been used for comparison to simulations [81, 82, 113, 114, 128, 130, 131, 182, 183, 185]. Comments on the various approaches and results are included in the relevant chapters.

## 1.3 Previous Publications of the Present Work

Parts of the work presented here have previously been published.

Peer-reviewed journals:

- Daub, D., S. Willems, and A. Gülhan, "Experiments on the Interaction of a Fast-Moving Shock with an Elastic Panel", *AIAA Journal*, vol. 54, no. 2, pp. 670–678, 2016. DOI: 10.2514/1.J054233

- Daub, D., S. Willems, and A. Gülhan, "Experimental results on unsteady shock-wave/boundary-layer interaction induced by an impinging shock", *CEAS Space Journal*, vol. 8, no. 1, pp. 3–12, 2016. DOI: 10.1007/s12567-015-0102-4
- Daub, D., B. Esser, and A. Gülhan, "Experiments on High-Temperature Hypersonic Fluid-Structure Interaction with Plastic Deformation", *AIAA Journal*, vol. 58, no. 4, pp. 1423–1431, 2020. DOI: 10.2514/1.j059150
- Daub, D., S. Willems, and A. Gülhan, "Experiments on aerothermoelastic fluid-structure interaction in hypersonic flow", *Journal of Sound and Vibration*, 2022. DOI: 10.1016/j.jsv.2021.116714
- Martin, K., D. Daub, B. Esser, A. Gülhan, and S. Reese, "Coupled Simulation of Hypersonic Fluid–Structure Interaction with Plastic Deformation", *AIAA Journal*, vol. 60, no. 6, pp. 3424–3437, 2022. DOI: 10.2514/1.j060561

Book chapters:

- Daub, D., S. Willems, B. Esser, and A. Gülhan, "Experiments on Aerothermal Supersonic Fluid-Structure Interaction", in *Future Space-Transport-System Components under High Thermal and Mechanical Loads*, Adams, N., W. Schröder, R. Radespiel, O. Haidn, T. Sattelmayer, C. Stemmer, and B. Weigand, Eds., Notes on Numerical Fluid Mechanics and Multidisciplinary Design, vol. 146, Springer, 2021, pp. 323–339. DOI: 10.1007/978-3-030-53847-7_21
- Martin, K., D. Daub, B. Esser, A. Gülhan, and S. Reese, "Numerical Modelling of Fluid-Structure Interaction for Thermal Buckling in Hypersonic Flow", in *Future Space-Transport-System Components under High Thermal and Mechanical Loads*, Adams, N., W. Schröder, R. Radespiel, O. Haidn, T. Sattelmayer, C. Stemmer, and B. Weigand, Eds., Notes on Numerical Fluid Mechanics and Multidisciplinary Design, vol. 146, Springer, 2021, pp. 341–355. DOI: 10.1007/978-3-030-53847-7_22
- Fiedler, T., J. Rösler, M. Bäker, F. Hötte, C. v. Sethe, D. Daub, M. Haupt, O. Haidn, B. Esser, and A. Gülhan, "Mechanical Integrity of Thermal Barrier Coatings - Coating Development and Micromechanics", in *Future Space-Transport-System Components under High Thermal and Mechanical Loads*, Adams, N., W. Schröder, R. Radespiel, O. Haidn, T. Sattelmayer, C. Stemmer, and B. Weigand, Eds., Notes on Numerical Fluid Mechanics and Multidisciplinary Design, vol. 146, Springer, 2021, pp. 295–307. DOI: 10.1007/978-3-030-53847-7_19

Conferences:

- Daub, D., S. Willems, and A. Gülhan, "Experimental Results on Shock-Wave/ Boundary-Layer Interaction induced by a Movable Wedge", in *8th European Symposium on Aerothermodynamics*, Lisbon, 2015
- Pasquariello, V., S. Hickel, N. Adams, G. Hammerl, W. A. Wall, D. Daub, S. Willems, and A. Gülhan, "Coupled simulation of shock-wave/turbulent boundary-layer interaction over a flexible panel", in *6th European Conference for Aerospace Sciences*, Krakow, Poland: EUCASS, 2015

- Martin, K., S. Reese, D. Daub, B. Esser, A. Gülhan, F. Hötte, and M. Haupt, "Simulationsmethoden und experimentelle Validierung für thermisches Beulen dünnwandiger Strukturen unter aerothermodynamischen Lasten", in *66. Deutscher Luft- und Raumfahrtkongress*, München, 2017
- Daub, D., S. Willems, and A. Gülhan, "Experiments on Shock Induced Instationary Fluid-Structure Interaction", in *1st International Aerospace Symposium on Acoustic Fatigue*, Glasgow, UK, 2017
- Daub, D., S. Willems, B. Esser, and A. Gülhan, "Experimental Studies on Supersonic Aerothermal Fluid-Structure Interaction.", in *68th International Astronautical Congress*, Adelaide, Australia, 2017
- Daub, D., B. Esser, S. Willems, and A. Gülhan, "Experimental Studies on Aerothermal Fluid-Structure Interaction with Plastic Deformation", in *69th International Astronautical Congress*, Bremen, 2018

Annual reports of the SFB TRR 40:

- Daub, D., S. Willems, A. Gülhan, and B. Esser, "Experimental Setup for Excitation of Fluid-Structure Interaction", in *SFB/TRR40 Annual Report*, Stemmer, C., N. A. Adams, O. J. Haidn, R. Radespiel, T. Sattelmayer, W. Schröder, and B. Weigand, Eds., Garching bei München: Lehrstuhl für Aerodynamik und Strömungsmechanik, Technische Universität München, 2014, pp. 305–314
- Daub, D., S. Willems, A. Gülhan, and B. Esser, "Experimental Results on Fluid-Structure Interaction excited by an Incident Shockwave on an Elastic Panel", in *SFB/TRR40 Annual Report*, Stemmer, C., N. A. Adams, O. J. Haidn, R. Radespiel, T. Sattelmayer, W. Schröder, and B. Weigand, Eds., Garching bei München: Lehrstuhl für Aerodynamik und Strömungsmechanik, Technische Universität München, 2015, pp. 281–292
- Pasquariello, V., G. Hammerl, D. Daub, S. Willems, S. Hickel, W. A. Wall, A. Gülhan, and N. Adams, "Coupled simulation of shock-wave/turbulent boundary-layer interaction over a flexible panel", in *SFB/TRR40 Annual Report*, Stemmer, C., N. A. Adams, O. J. Haidn, R. Radespiel, T. Sattelmayer, W. Schröder, and B. Weigand, Eds., Garching bei München: Lehrstuhl für Aerodynamik und Strömungsmechanik, Technische Universität München, 2015, pp. 261–280
- Hammerl, G., A. Seitz, F. Verdugo, W. Wall, D. Daub, S. Willems, and Gülhan, "FSI of rocket nozzles - On the influence of simplified modeling of structural boundary conditions for an FSI experiment & scalable solvers for strongly coupled problems", in *SFB/TRR40 Annual Report*, Stemmer, C., N. A. Adams, O. J. Haidn, R. Radespiel, T. Sattelmayer, W. Schröder, and B. Weigand, Eds., Garching bei München: Lehrstuhl für Aerodynamik und Strömungsmechanik, Technische Universität München, 2016, pp. 253–262
- Daub, D., B. Esser, S. Willems, and A. Gülhan, "Experiments on Thermomechanical Fluid-Structure Interaction in Supersonic Flows", in *SFB/TRR40 Annual Report*, Stemmer, C., N. A. Adams, O. J. Haidn, R. Radespiel, T. Sattelmayer, W. Schröder,

and B. Weigand, Eds., Garching bei München: Lehrstuhl für Aerodynamik und Strömungsmechanik, Technische Universität München, 2017, pp. 243–254

- Daub, D., B. Esser, S. Willems, and A. Gülhan, "Experimental Studies on Aerothermal Fluid-Structure Interaction with Plastic Deformation", in *SFB/TRR40 Annual Report*, Stemmer, C., N. A. Adams, O. J. Haidn, R. Radespiel, T. Sattelmayer, W. Schröder, and B. Weigand, Eds., Garching bei München: Lehrstuhl für Aerodynamik und Strömungsmechanik, Technische Universität München, 2018, pp. 269–279
- Daub, D., S. Willems, B. Esser, and A. Gülhan, "Experiments on Elastic Aerothermal Fluid/Structure Interaction in Supersonic Flows", in *SFB/TRR40 Annual Report*, Stemmer, C., N. A. Adams, O. J. Haidn, R. Radespiel, T. Sattelmayer, W. Schröder, and B. Weigand, Eds., Garching bei München: Lehrstuhl für Aerodynamik und Strömungsmechanik, Technische Universität München, 2019, pp. 277–290

# 2 Supersonic Incident SWBLI and FSI

This chapter contains an experimental study on the interaction of a supersonic flow field including incident SWBLI with an elastic panel structure. Furthermore, a rigid reference case was investigated to provide measurements of static and dynamic wall pressures. The setup was developed in parallel to the LES by Pasquariello [128][1] and has already been used as reference for several other numerical studies [81, 82, 182, 183, 185]. For the FSI experiments, the setup was designed to enable configurations with initially undeformed panel and subsequent high-speed loading, and configurations with steady incident shock position. The former was intended to obtain large amplitude oscillations from known initial conditions in a time frame accessible by LES calculation, the latter to yield results on a case where FSI dynamics are mainly driven by the intrinsic dynamics of the SWBLI at constant position of the incident shock.

The experiments were based on previous work by Willems et al. [177]. The experimental setup was substantially improved with regard to instrumentation and properties of the flow field. This made it possible to obtain detailed high-speed wall pressure measurements for incident SWBLI, and measurements of structural dynamics of a FSI configuration in a predominantly two-dimensional flow field with and without high-speed movement of the shock generator.

This chapter is based on previous publications by the author in [23, 24, 29–31]. Section 2.3 contains comments on the various related works on numerical simulation of this problem [81, 82, 128, 130, 131, 182, 183, 185].

## 2.1 Experimental Setup

### 2.1.1 Trisonic Wind Tunnel TMK

To obtain supersonic flow conditions at high Reynolds numbers, the experiments were conducted in the Trisonic Wind Tunnel TMK of the Supersonic and Hypersonic Technology Department at Deutsches Zentrum für Luft- und Raumfahrt e.V. (DLR), Cologne (Fig. 2.1, see [49] for a detailed facility description). TMK is a blow-down facility with a Mach number range of 0.5 to 5.7. The Reynolds number can be varied by using a heater or adjusting total pressure. The pressure range can be extended by using an ejector system. The heater is also required to prevent condensation at high Mach numbers. The test section has a rectangular cross section of $0.6\,\mathrm{m} \times 0.6\,\mathrm{m}$. The nozzle contour is

[1] This reference includes a detailed discussion on the relevance of this configuration for FSI in rocket nozzles.

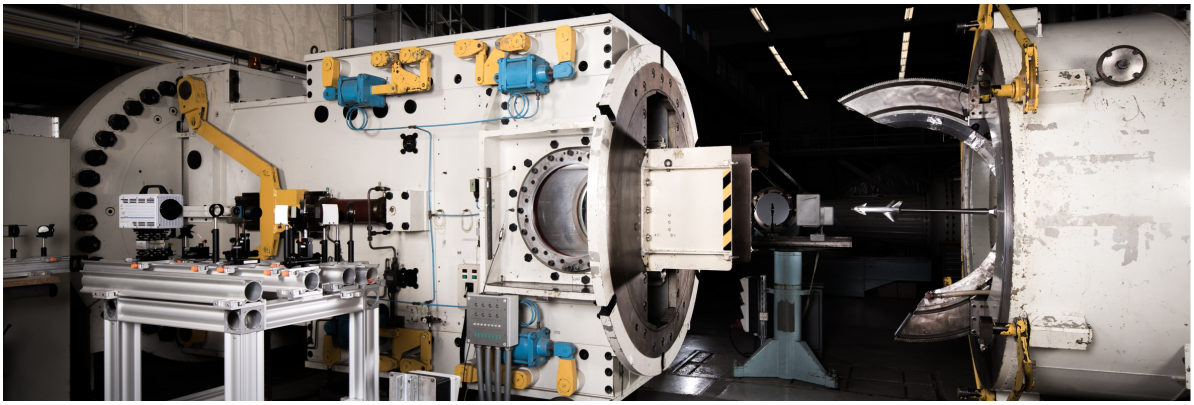

**(a)** Nozzle and test section

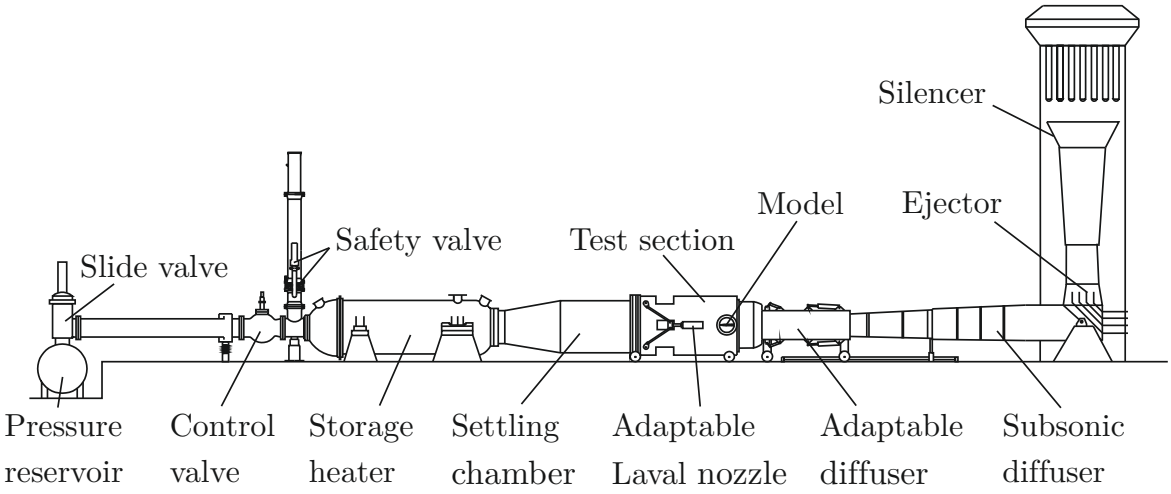


**(b)** Schematic

**Figure 2.1:** Trisonic Wind Tunnel TMK at DLR, Cologne

variable and can be altered during the wind tunnel run. For transonic flow, a special test section with perforated walls has to be used.

The flow conditions used are given in Tab. 2.1. Free stream conditions were calculated based on the measured total conditions using isentropic equations [47]. Viscosity was calculated using a power-law approximation for low temperatures [79]. The molar gas constant was used according to [15] and the mean molecular weight of dry air was used as stated in [79]. The turbulent intensity is 1.9 % in the direction of the flow, and 2.3 % in the orthogonal direction based on Laser-2-Focus velocimetry measurements [174].

### 2.1.2 Wind Tunnel Model

The previous studies by Willems [174] and Willems et al. [177] yielded significant three-dimensional effects in the flow field, stemming from the three-dimensional nature of the impinging shock which was strongly curved even in the center of the test section. For comparison to LES simulations, a two-dimensional case was required because of the large

**Table 2.1:** Flow conditions

| $Ma$ | $p_0$ | $T_0$ | $p_\infty$ | $T_\infty$ | $u_\infty$ | $Re_\infty$ |
|---|---|---|---|---|---|---|
| 3.0 | 582 kPa | 274 K | 15.6 kPa | 97.2 K | 595 m/s | $48.6 \cdot 10^6$ /m |
| 4.0 | 1374 kPa | 274 K | 8.7 kPa | 64.5 K | 649 m/s | $67.3 \cdot 10^6$ /m |

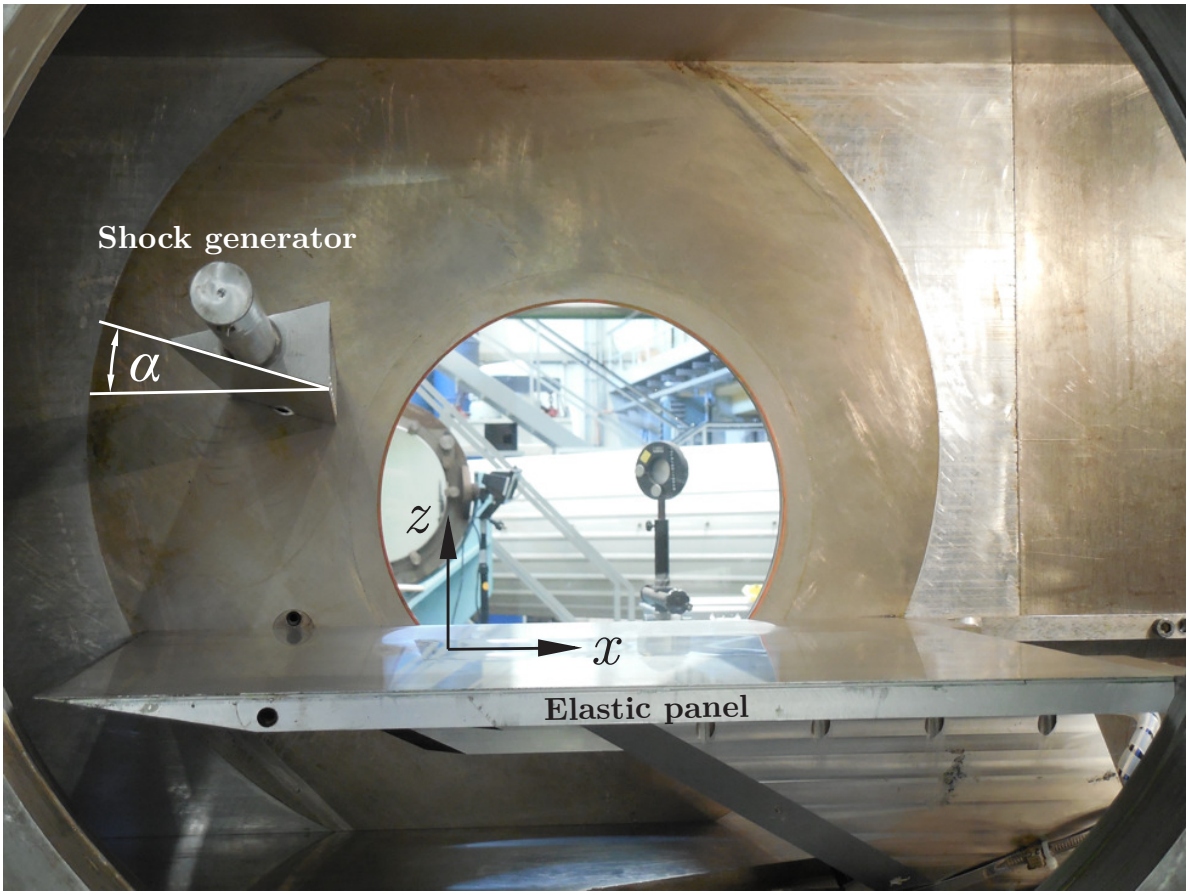


**Figure 2.2:** Wind tunnel model in the TMK test section

computational cost of such calculations that allow only a quasi two-dimensional slice of the experiment to be taken into account. As wind tunnels have finite dimensions, it is not possible to fully eliminate three-dimensional effects. However, three-dimensional effects for such a configuration can be reduced by maximizing the width of the shock generator (e. g. [165]). The outcome was evaluated by the comparison of wall pressure measurements on and off the centerline of the wind tunnel model (Section 2.2.1).

Similarly to many previous SWBLI studies (e. g. [135, 141, 178]), the elastic insert was chosen to be mounted in a flat plate dividing the wind tunnel flow field. For the present experiments, a comparison to LES was planned from the outset and thus a well defined geometry that facilitates the simulation of the boundary layer from its origin was chosen. The other common approach of mounting the panel in the wind tunnel wall has considerable advantages concerning the elastic structure, because it makes the

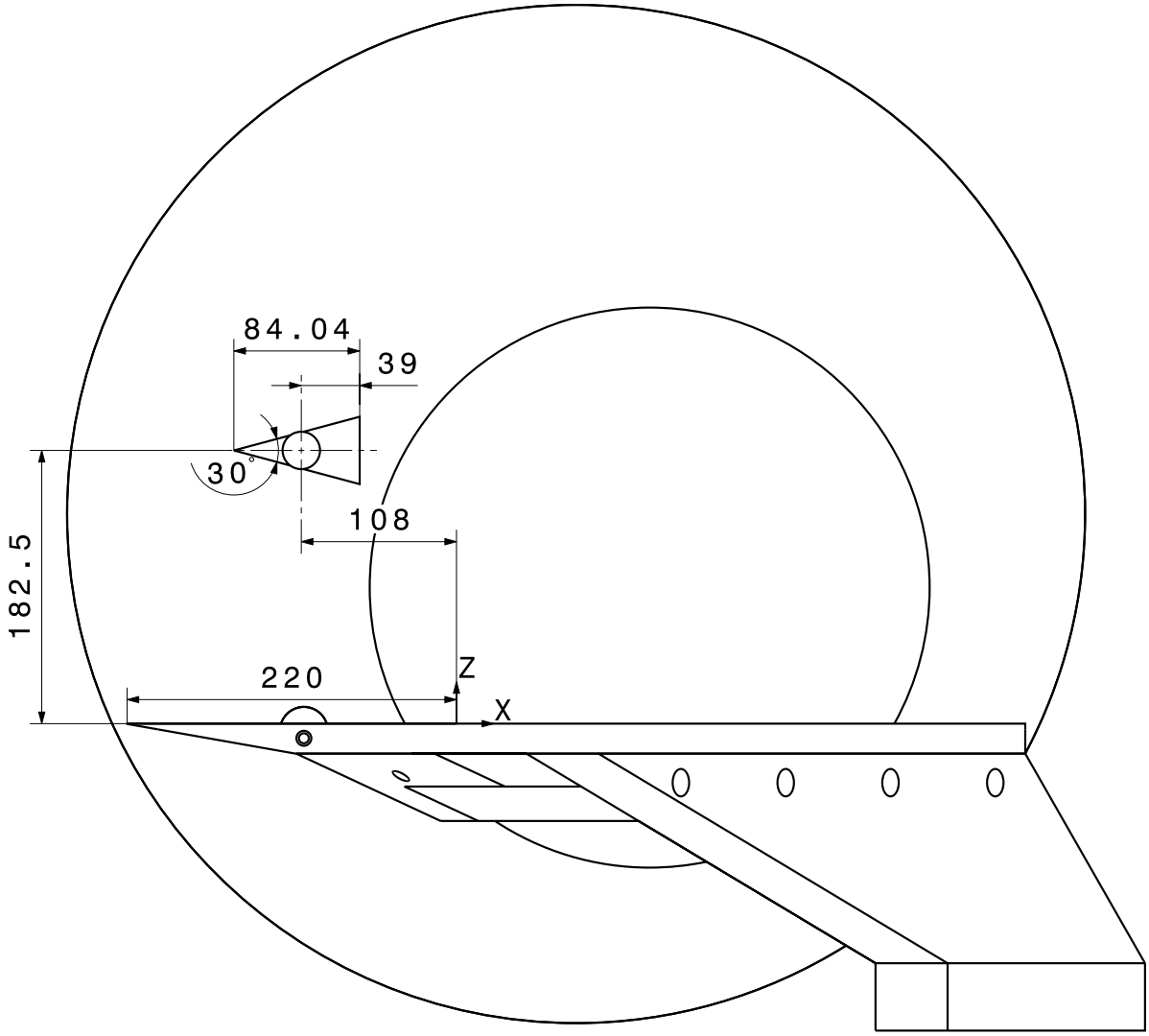


**Figure 2.3:** Drawing of the wind tunnel model in the TMK test section (all measures in mm)

panel easily accessible for instrumentation (e. g. [149, 152]), and eliminates effects of a small cavity underneath the panel [42]. Choosing the wind tunnel wall means that the panel interacts with the wind tunnel wall boundary layer, which in some cases might be considered beneficial if a boundary layer of maximum thickness is desirable. However, the reproduction of the boundary-layer properties may be more complicated. To allow comparison of the FSI case to LES, the elastic panel was mounted on two sides to keep its behavior as two-dimensional as possible.

Based on the above considerations, the splitter plate and insert by Willems et al. [177] was used. A new shock generator assembly, including a full-span rotatable shock generator with a high-performance drive, was developed. Figure 2.2 shows the model in the TMK test section. Figure 2.3 provides the relevant dimensions. The coordinate system used throughout this chapter is located at the leading edge of the free part of the elastic panel or the equivalent location on the rigid insert (see Figs. 2.4 and 2.5). Both shock generator

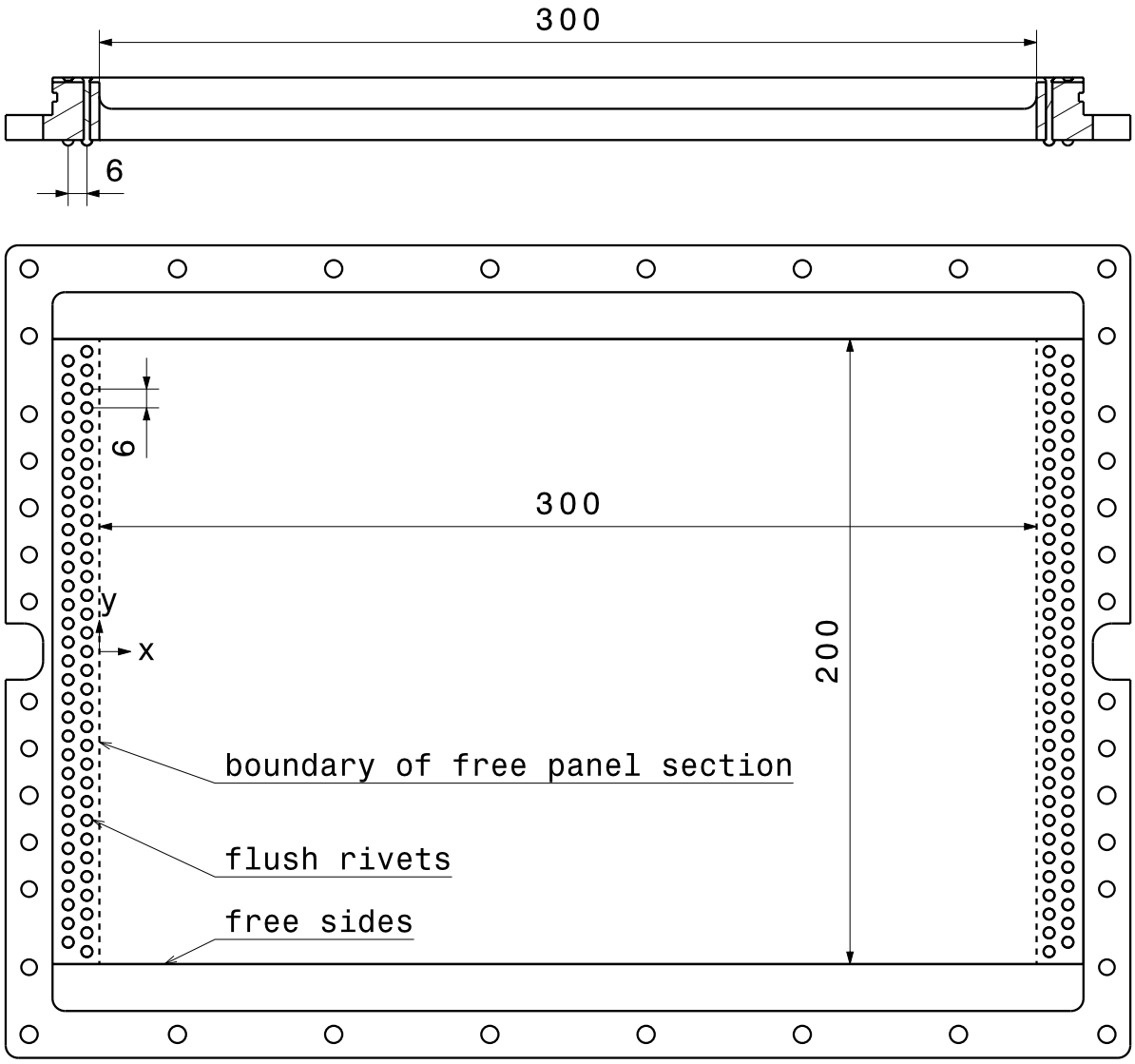


**Figure 2.4:** Drawing of the elastic panel insert (all measures in mm)

and splitter plate span the full test section width of 600 mm. The 300 mm × 200 mm elastic panel (Fig. 2.4) was made of 1.47 mm thick spring steel (CK 75). Leading and trailing edge were clamped by flush rivets (DIN 661; diameter 2 mm). The sides were sealed by soft rubber foam placed underneath the panel to prevent leakage.

### 2.1.3 Actuator

To allow fast changes in shock generator angle, a high-performance drive was used. The setup is shown in Fig. 2.6. This actuator was chosen to allow high-speed rotation of 20° in about 10 ms requiring a torque of about 100 Nm. It can also hold position at any desired angle and perform continuous rotation at a maximum rotation speed of 6000 $\frac{1}{\text{min}}$.

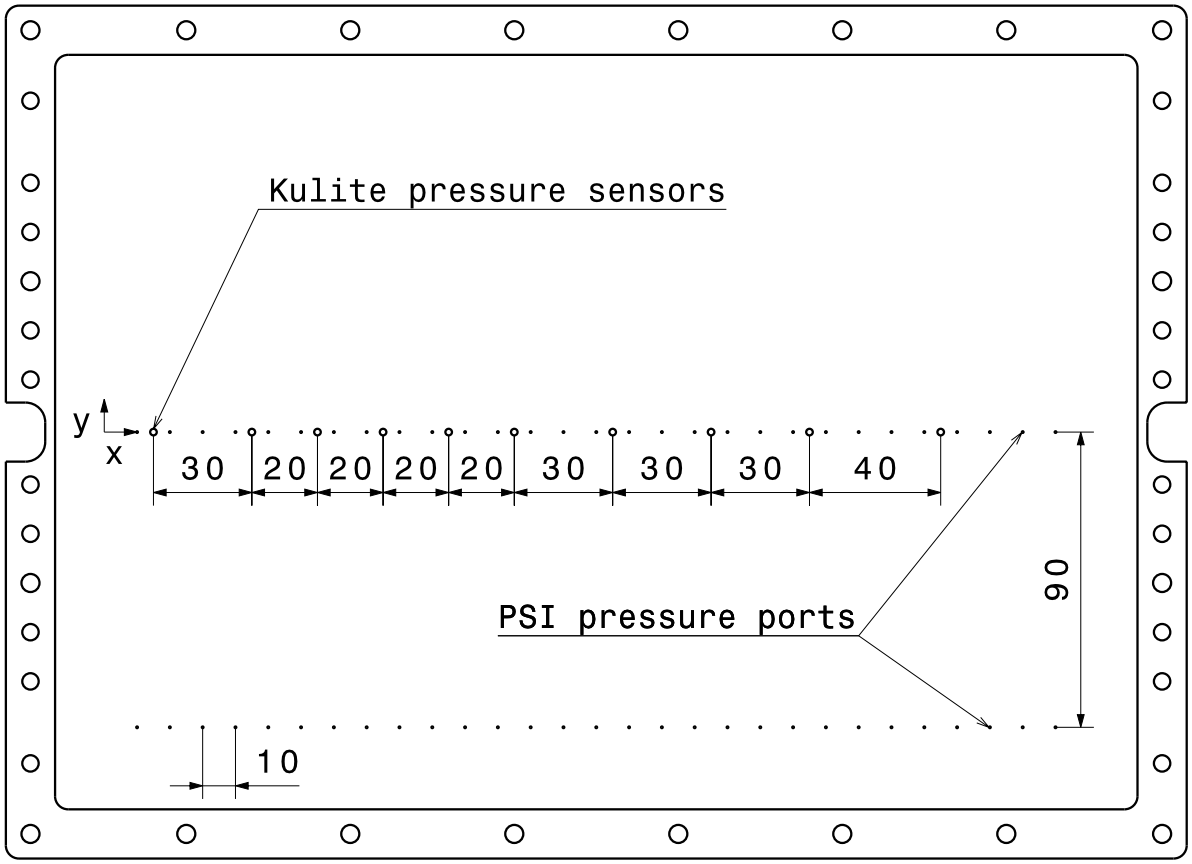


**Figure 2.5:** Drawing of the rigid reference panel insert with pressure sensor positions (all measures in mm)

## 2.1.4 Instrumentation, Uncertainty and Data Processing

### Flow Conditions

Total pressure ($p_0$) and total temperature ($T_0$) were measured in the settling chamber (Fig. 2.1b). The total pressure was measured by GE PMP 4015 pressure sensors with a range of 1 MPa or 3 MPa with an uncertainty of 0.04 % of their range. The uncertainty of the Mach number ($Ma$) is 0.5 % [49]. The total temperature was measured using a Type K thermocouple with an uncertainty of 0.4 % of the measured temperature. For unknown quantities, the uncertainty was obtained from an estimated range as suggested in DIN 1319 [35, 36]. The range of $\kappa$ was estimated based on tabulated values in [3, 106]. The range for wind tunnel model misalignment was based on values typically achieved during the mounting process. The uncertainty of the flow conditions given in Tabs. 2.2 to 2.5 was evaluated following [134, 174]. For each input quantity, the absolute value ($i$), the absolute uncertainty ($\Delta i$), and relative uncertainty ($\Delta i/i$) were evaluated regarding their respective contribution to the wall pressure ($p_w$) and free stream temperature ($T_\infty$) or temperature downstream of an incident shock ($T_2$). These respective contributions were evaluated numerically and added using the variance

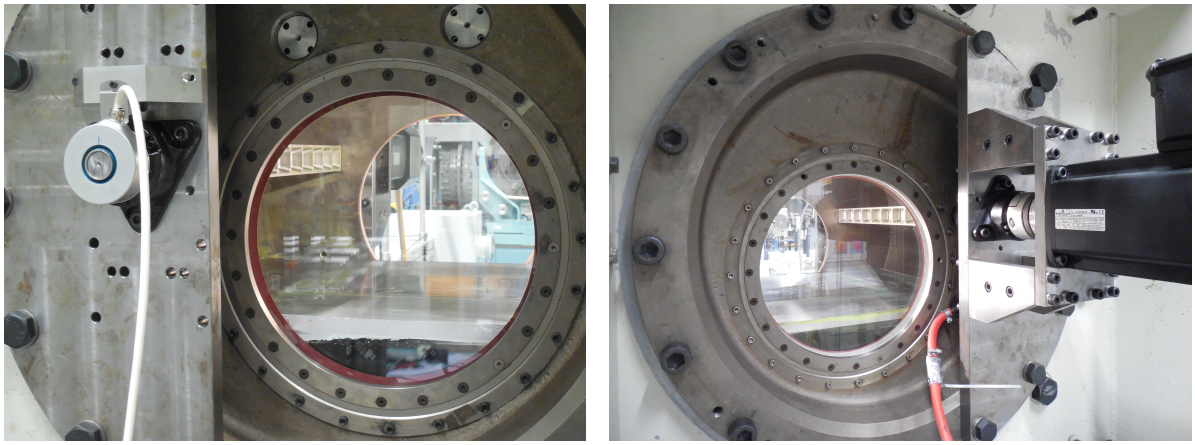

**(a)** Position sensor **(b)** Drive

**Figure 2.6:** Drive assembly and rotatable shock generator

formula[2]. As there is no analytical solution for the wall pressure distribution in the SWBLI, the uncertainty is estimated based on the conditions after an oblique shock with a turn angle of $\alpha = 20°$ for $Ma = 3$ (Tab. 2.3) and with $\alpha = 22.5°$ for $Ma = 4$ (Tab. 2.5).

### Shock Generator Angle

The angular position of the shaft connected to the shock generator was measured by a Hengstler RI 76TD incremental encoder. It can resolve 40000 increments per revolution up to a maximum rotation speed of 6000 $\frac{1}{\text{min}}$, resulting in a resolution better than 0.01°, which is an order of magnitude better than the estimated mounting uncertainty, and can thus be considered negligible.

### Rigid Reference Panel

The rigid panel was outfitted with two rows of pressure ports on and off the center line (Fig. 2.5) to measure the static pressure distribution in the SWBLI. The resulting data was used to evaluate to what extent the flow field can be treated as two-dimensional. To obtain high-precision static measurements, the pressure ports were connected to Pressure Systems, Inc. (PSI) 1615B-TL pressure scanners placed inside the model. For dynamic pressure measurements, the panel was equipped with Kulite XCQ-62 pressure sensors that were mounted flush with the surface of the insert. Their positions, which were chosen to allow a higher resolution in the vicinity of the expected separation shock location, are also shown in Fig. 2.5. The natural frequency of their sensing diaphragm is 240 kHz. However, this diaphragm is located a short distance from the sensor surface that is covered with a "B screen", a protective screen with small holes which limits the frequency

[2]in German referred to as Gauß-Verfahren

**Table 2.2:** Uncertainty estimate of flow conditions upstream of the SWBLI at $Ma_\infty = 3.0$

| | $p_0$ | $T_0$ | $Ma_\infty$ | $\kappa$ | $\alpha$ | $p_w$ | $T_\infty$ |
|---|---|---|---|---|---|---|---|
| $i$ | 582.1 kPa | 273.7 K | 3.01 | 1.400 | 0.00° | 15.55 kPa | 97.2 K |
| $\Delta i$ | 0.4 kPa | 1.5 K | 0.015 | 0.001 | 0.07° | — | — |
| $\Delta i/i$ | 0.07 % | 0.5 % | 0.5 % | 0.1 % | — | — | — |
| $\Delta p_i$ | 0.011 kPa | — | 0.354 kPa | 0.019 kPa | 0.088 kPa | 0.365 kPa | — |
| $\Delta p_i/p_w$ | 0.07 % | — | 2.27 % | 0.12 % | 0.56 % | 2.35 % | — |
| $\Delta T_i$ | — | 0.53 K | 0.63 K | 0.23 K | 0.16 K | — | 0.87 K |
| $\Delta T_i/T_\infty$ | — | 0.55 % | 0.64 % | 0.23 % | 0.16 % | — | 0.89 % |

**Table 2.3:** Uncertainty estimate of flow conditions in the SWBLI at $Ma_\infty = 3.0$

| | $p_0$ | $T_0$ | $Ma_\infty$ | $\kappa$ | $\alpha$ | $p_w$ | $T_2$ |
|---|---|---|---|---|---|---|---|
| $i$ | 582.1 kPa | 273.7 K | 3.01 | 1.400 | 20.00° | 58.90 kPa | 151.9 K |
| $\Delta i$ | 0.4 kPa | 1.5 K | 0.015 | 0.001 | 0.09° | — | — |
| $\Delta i/i$ | 0.07 % | 0.5 % | 0.5 % | 0.1 % | 0.43 % | — | — |
| $\Delta p_i$ | 0.04 kPa | — | 1.04 kPa | 0.14 kPa | 0.28 kPa | 1.09 kPa | — |
| $\Delta p_i/p_w$ | 0.07 % | — | 1.77 % | 0.23 % | 0.48 % | 1.85 % | — |
| $\Delta T_i$ | — | 0.83 K | 0.66 K | 0.58 K | 0.31 K | — | 1.25 K |
| $\Delta T_i/T_2$ | — | 0.55 % | 0.43 % | 0.38 % | 0.21 % | — | 0.82 % |

response of the sensor. The study by Hurst et al. [83] with similar sensors indicates that a flat frequency response can be expected up to about 16 kHz, which makes the sensors well suited for the intended purpose of studying the low-frequency unsteadiness in the SWBLI. However, the characteristic frequency of the Turbulent boundary layer (TBL) (as seen in Pasquariello et al. [131]) cannot be resolved.

For the XCQ-62 sensor, Kulite states a typical combined non-linearity, hysteresis, and repeatability of 0.1 % of its range, a zero shift of 1.8 %/100 K of its range, and a sensitivity shift of 1.8 %/100 K of the measured value. For the PSI pressure scanner 1615B-TL, the manufacturer states an uncertainty of 0.05 % of its range. Uncertainties were added using the variance formula. For relative measurements, the zero shift was not taken into account. Thermal effects were calculated based on a temperature change of 25 K. The resulting values are given in Tab. 2.6. Due to the much lower uncertainty, only the PSI sensors were taken into consideration for static wall pressure measurements, whereas the Kulite sensors were used to analyse the dynamics of the SWBLI.

The Power spectral density (PSD) of the measured pressure signals was calculated following Welch's method [168], using Hann windows, a block length of 5000 samples, and an overlap of 0.5. This results in a frequency resolution of 20 Hz.

**Table 2.4:** Uncertainty estimate of flow conditions upstream of the SWBLI at $Ma_\infty = 4.0$

| | $p_0$ | $T_0$ | $Ma_\infty$ | $\kappa$ | $\alpha$ | $p_w$ | $T_\infty$ |
|---|---|---|---|---|---|---|---|
| $i$ | 1374.3 kPa | 273.9 K | 4.03 | 1.400 | 0.00° | 8.69 kPa | 64.45 K |
| $\Delta i$ | 1.2 kPa | 1.5 K | 0.02 | 0.001 | 0.07° | — | — |
| $\Delta i/i$ | 0.09 % | 0.5 % | 0.5 % | 0.1 % | — | — | — |
| $\Delta p_i$ | 0.008 kPa | — | 0.236 kPa | 0.029 kPa | 0.064 kPa | 0.246 kPa | — |
| $\Delta p_i/p_w$ | 0.09 % | — | 2.72 % | 0.39 % | 0.74 % | 2.84 % | — |
| $\Delta T_i$ | — | 0.35 K | 0.50 K | 0.18 K | 0.14 K | — | 0.65 K |
| $\Delta T_i/T_\infty$ | — | 0.55 % | 0.77 % | 0.28 % | 0.21 % | — | 1.01 % |

**Table 2.5:** Uncertainty estimate of flow conditions in the SWBLI at $Ma_\infty = 4.0$

| | $p_0$ | $T_0$ | $Ma_\infty$ | $\kappa$ | $\alpha$ | $p_w$ | $T_2$ |
|---|---|---|---|---|---|---|---|
| $i$ | 1374.3 kPa | 273.9 K | 4.03 | 1.400 | 22.50° | 53.46 kPa | 127.12 K |
| $\Delta i$ | 1.2 kPa | 1.5 K | 0.02 | 0.001 | 0.09° | — | — |
| $\Delta i/i$ | 0.09 % | 0.5 % | 0.5 % | 0.1 % | 0.38 % | — | — |
| $\Delta p_i$ | 0.05 kPa | — | 1.09 kPa | 0.25 kPa | 0.28 kPa | 1.15 kPa | — |
| $\Delta p_i/p_w$ | 0.09 % | — | 2.03 % | 0.47 % | 0.53 % | 2.15 % | — |
| $\Delta T_i$ | — | 0.70 K | 0.52 K | 0.62 K | 0.35 K | — | 1.13 K |
| $\Delta T_i/T_2$ | — | 0.55 % | 0.41 % | 0.49 % | 0.28 % | — | 0.89 % |

For the present experiments, the measured $p_w$ at the center of the rigid insert is typically within 200 Pa of $p_\infty$, calculated from $p_0$ given in Tab. 2.1. This indicates that the estimates given regarding the inflow conditions (Tabs. 2.2 and 2.4) and measurement uncertainty (Tab. 2.6) are conservative (see also Section 2.2.1).

### Elastic Panel

The elastic panel (Fig. 2.4) was instrumented with several non-intrusive distance sensors placed underneath the panel (Fig. 2.7). Three capacitive distance sensors CS5 and two CSH2FL by Micro-Epsilon were used with Micro-Epsilon capaNCDT 6350 amplifiers, enabling measurements at 50 kHz. The maximum operating temperature of the sensors is 200 °C with a temperature sensitivity of −160 nm/K. Thus, no relevant effect of the sensor temperature on the distance measurements is expected. The non-linearity of the sensors is smaller than 12 $\mu$m for the CSH2FL used with 4 mm range, and smaller than 15 $\mu$m for the CS5 used with 5 mm range. For the runs where measurements exceeded 5 mm, the range of the center CS5 was doubled. This also doubles the non-linearity estimate. The uncertainty caused by non-parallel orientation of sensor and target surface

**Table 2.6:** Uncertainty estimate of wall pressure measurements in TMK for minimum and maximum surface pressures at Mach 3.0

| | | XCQ-062 | PSI | XCQ-062 | PSI |
|---|---|---|---|---|---|
| $p_w$ | kPa | 15.6 | 15.6 | 70.0 | 70.0 |
| $p_{\text{range}}$ | kPa | 170.0 | 100.0 | 170.0 | 100.0 |
| $\Delta p_{\text{general}}$ | Pa | 170.0 | 50.0 | 170.0 | 50.0 |
| $\Delta p_{\text{sensitivity}}$ | Pa | 70.2 | – | 315.0 | – |
| $\Delta p_{\text{zero}}$ | Pa | 765.0 | – | 765.0 | – |
| $\Delta p_{\text{abs}}$ | Pa | 786.8 | 50.0 | 844.6 | 50.0 |
| $\Delta p_{\text{rel}}$ | Pa | 250.2 | 70.7 | 396.3 | 70.7 |
| $\Delta p_{\text{abs}}/p_w$ | % | 5.04 | 0.32 | 1.21 | 0.07 |
| $\Delta p_{\text{rel}}/p_w$ | % | 1.61 | 0.45 | 0.57 | 0.10 |

**Table 2.7:** Displacement sensor positions

| Sensor Type | Position | $x$ /mm | $y$ /mm |
|---|---|---|---|
| CS5 | front | 75 | 0 |
| CS5 | center | 155 | 0 |
| CS5 | rear | 225 | 0 |
| CSH2FL | left | 155 | 62 |
| CSH2FL | right | 155 | −62 |

were provided by Micro-Epsilon [179]. Based on this, an uncertainty of 9 $\mu$m has to be added at the front and rear position for cases with significant panel deflection. The sensor positions are listed in Tab. 2.7.

The PSD of the measured deformation was calculated following Welch's method [168], using Hann windows, a block length of 20000 samples, and an overlap of 0.5. This results in a frequency resolution of 5 Hz.

XTL-DC-123C-190 Kulite sensors were used to measure the pressure underneath the elastic panel. For this sensor, Kulite states an uncertainty of 0.15 % of the measured value.

### Flow Field

A Z-type Schlieren setup with mirrors of 600 mm diameter and 6000 mm focal length was used to obtain images from the flow field [49] (see also [144] for a general discussion). Images were recorded using a high-speed camera Photron FASTCAM SA-X with 1024 pixels × 200 pixels resolution at 20 kHz. The maximum recording duration for this configuration was about 11 s.

The images can only be used for qualitative analysis because the incident shock moves upstream close to the windows, and thus obstructs the view of the flow structure in the

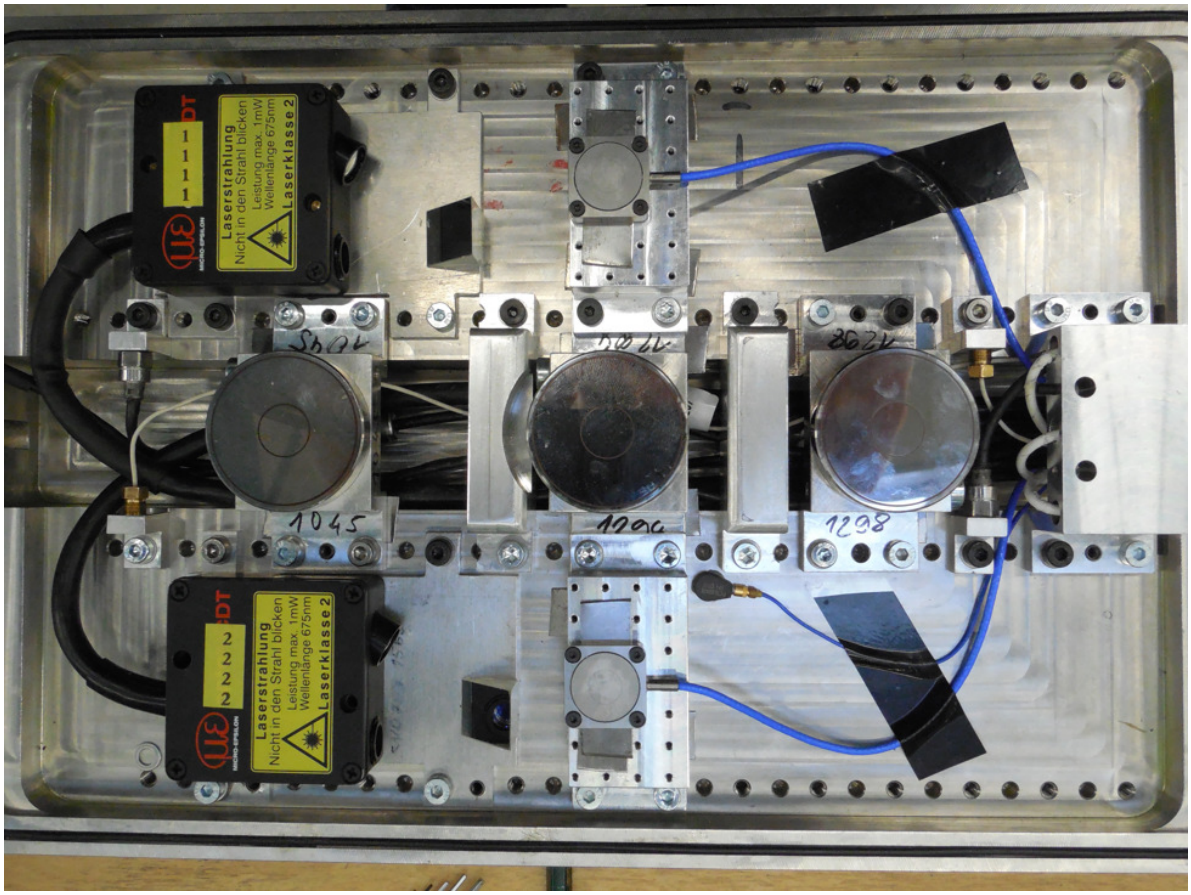


**Figure 2.7:** Elastic panel displacement sensors

center of the test section. However, they are useful for reference regarding sensor positions, and to obtain a general idea of the flow structure. For the previous configuration by Willems [174], a detailed analysis of the high-speed Schlieren recordings was conducted. For that configuration, the flow structure in the center of the test section was well visible due to the three-dimensional nature of the flow field. Using the same analysis, it was shown for the present configuration that a difference in observable flow-field dynamics between the elastic and rigid wall configuration is detectable [31].

### Data acquisition

National Instruments 24 bit high-speed bridge modules PXIe-4331 were used for data acquisition for the Kulite pressure transducers, and 16 bit multifunction data acquisition cards PXIe-6363/6361 for all other sensors. A sampling rate of 100 kHz was used. The PXIe-6363 card was also used to trigger the camera for high-speed Schlieren photography and the actuator. The incremental encoder was connected to the internal high-speed counter of a PXIe-6363.

**Table 2.8:** Computed panel modes (number of neutral lines in x;y-direction) [174]

| | Panel modes | | | | | | | | | | | | |
|---|---|---|---|---|---|---|---|---|---|---|---|---|---|
| Mode (x;y) | 0;0 | 0;1 | 1;0 | 0;2 | 1;1 | 1;2 | 2;0 | 2;1 | 0;3 | 2;2 | 3;0 | 1;3 | 3;1 |
| $f$ /Hz | 88 | 123 | 242 | 284 | 294 | 471 | 475 | 534 | 626 | 730 | 785 | 807 | 850 |

## 2.1.5 Properties of the Elastic Panel

### Dynamic Properties

The panel used has already been subject to a detailed characterization for previous experiments [174, 177], which showed that the observed modes are in good agreement with results from simulations using an ANSYS Finite element method (FEM) model. In addition to these previous considerations, the present configuration allows an in-situ characterization of the frequencies occurring during an actual wind tunnel run without a pressure difference between the flow-exposed side of the panel and cavity underneath. This is particularly valuable as the dynamic properties of the structure can be very sensitive to small changes in boundary conditions. In the experiments, a fast movement of the incident shock to a position on the panel was used to excite structural dynamics. The opposite, the rapid removal of the incident shock load, was facilitated by a fast rotation of the shock generator in the opposite direction. The resulting panel dynamics were used for additional panel characterization shown in Fig. 2.8. The occurring peaks agree well with the ANSYS solution. However, several additional peaks were found near 180 Hz and at what appears to be further multiples of the frequency of the lowest panel eigenmode. Panel modes should typically occur at various frequencies that do not need to be multiples of one another [184]. The appearance of so called harmonics at integer multiples points to a deviation of the displacement signal from a perfect sine function [122]. These harmonics could also be found revisiting previously recorded spectra of the panel dynamics at lower excitation amplitude given in [174]. Thus, there does not appear to be any deterioration of the panel, and previously made assumptions are confirmed. Additionally, the observation of peaks due to the appearance of harmonics of the first panel mode could be explained. Interestingly, harmonics do not prominently appear in characterization of the fully clamped panels used in Chapter 4 (see Section 4.1.4).

### Back Pressure and Cavity Effect

In addition to the wall pressure on the side of the panel that is exposed to the flow, the pressure underneath the panel is an important boundary condition. A pressure difference across the panel leads to deformation and induces stresses that influence mean deformation and structural dynamics (e. g. [10, 174]). The cavity underneath the panel is connected to a static pressure port in the wind tunnel wall to equalize pressure with static $p_\infty$ of the incoming flow. Using $p_\infty$ as cavity pressure for simulations leads to good agreement for static deflections as shown by Willems [174]. Furthermore, it was shown

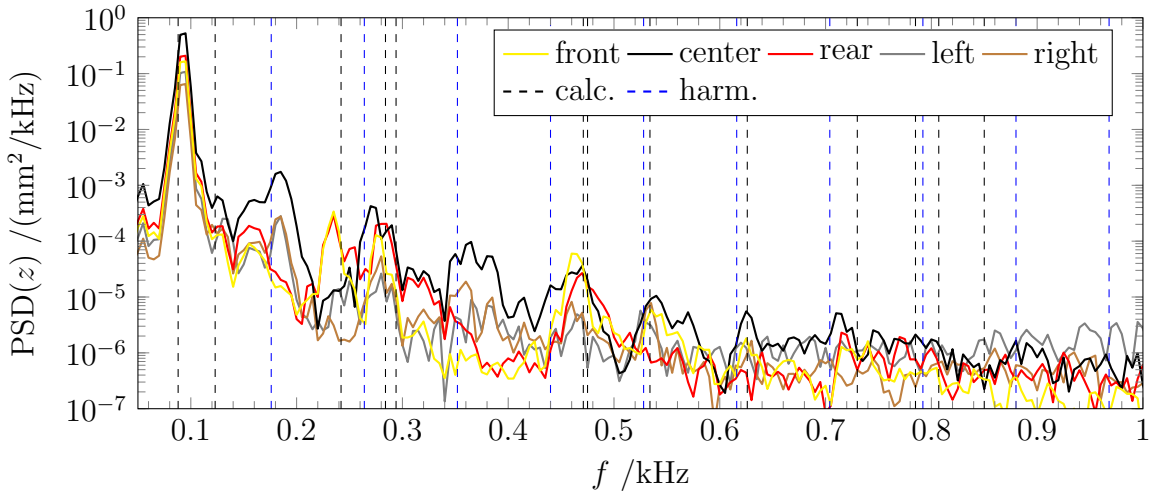


**(a)** No. 1

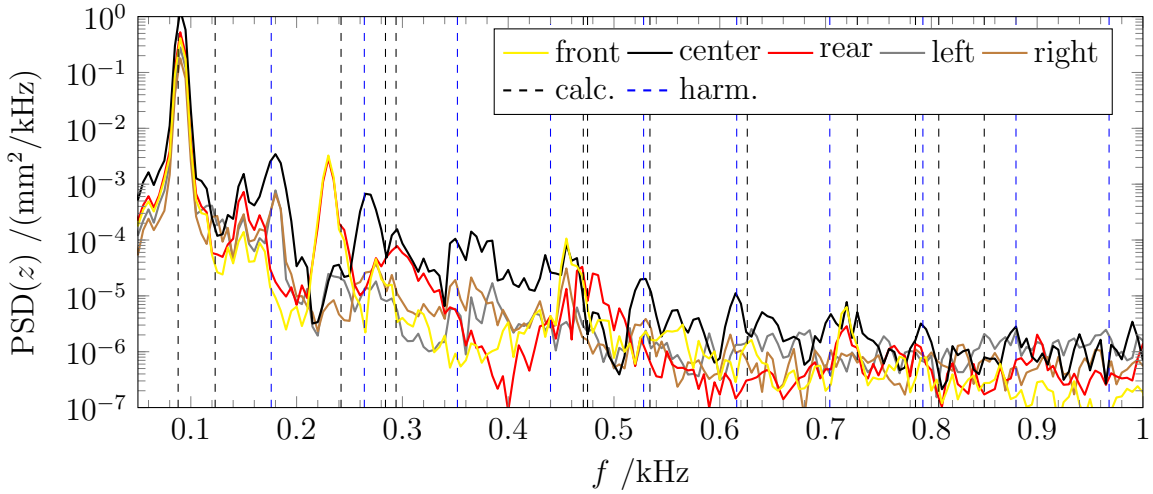


**(b)** No. 2

**Figure 2.8:** PSD($z$) of panel dynamics after fast removal of the incident shock load during a wind tunnel run with calculated modes from Tab. 2.8 and harmonics of the lowest panel mode

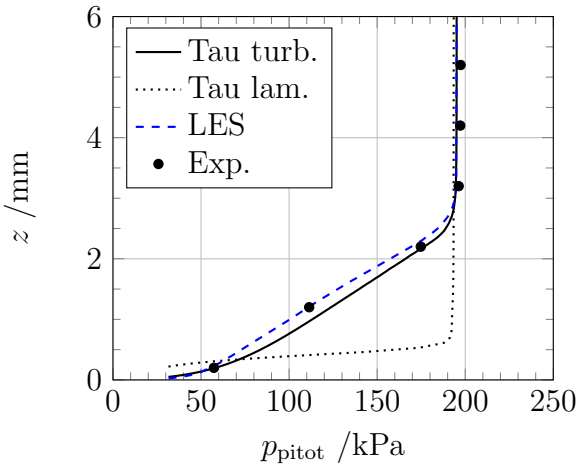


**Figure 2.9:** Incoming boundary-layer profile (TAU results by Willems [174], LES results by Pasquariello [128])

that the change in panel eigenfrequencies in the relevant back-pressure range is small for small panel deflections. However, for larger panel deflections the cavity may have to be taken into account for simulations [70, 130]. The volume of the cavity is $0.0021\,\text{m}^3$. For a general discussion, see [41].

### 2.1.6 Incoming Flow Field

The boundary layer develops starting at the leading edge of the wind tunnel model where tripping was applied. A boundary-layer measurement shown in Fig. 2.9 was conducted on a reference model at $x = -70\,\text{mm}$. It shows good agreement with TAU calculations by Willems [174] and LES calculations by Pasquariello [128]. This supports the assumption that the boundary layer is turbulent upstream of the insert.

## 2.2 Results

First, experiments using the rigid insert were conducted to measure the mean and dynamic properties of the SWBLI, that contribute strongly to the behavior of the coupled configuration. These reference experiments were followed by investigations on the behavior of the coupled system with the elastic panel, which included configurations without incident shock, with prescribed incident shock movement, and with fixed incident shock angle, leading to a broad range of different responses of the elastic panel.

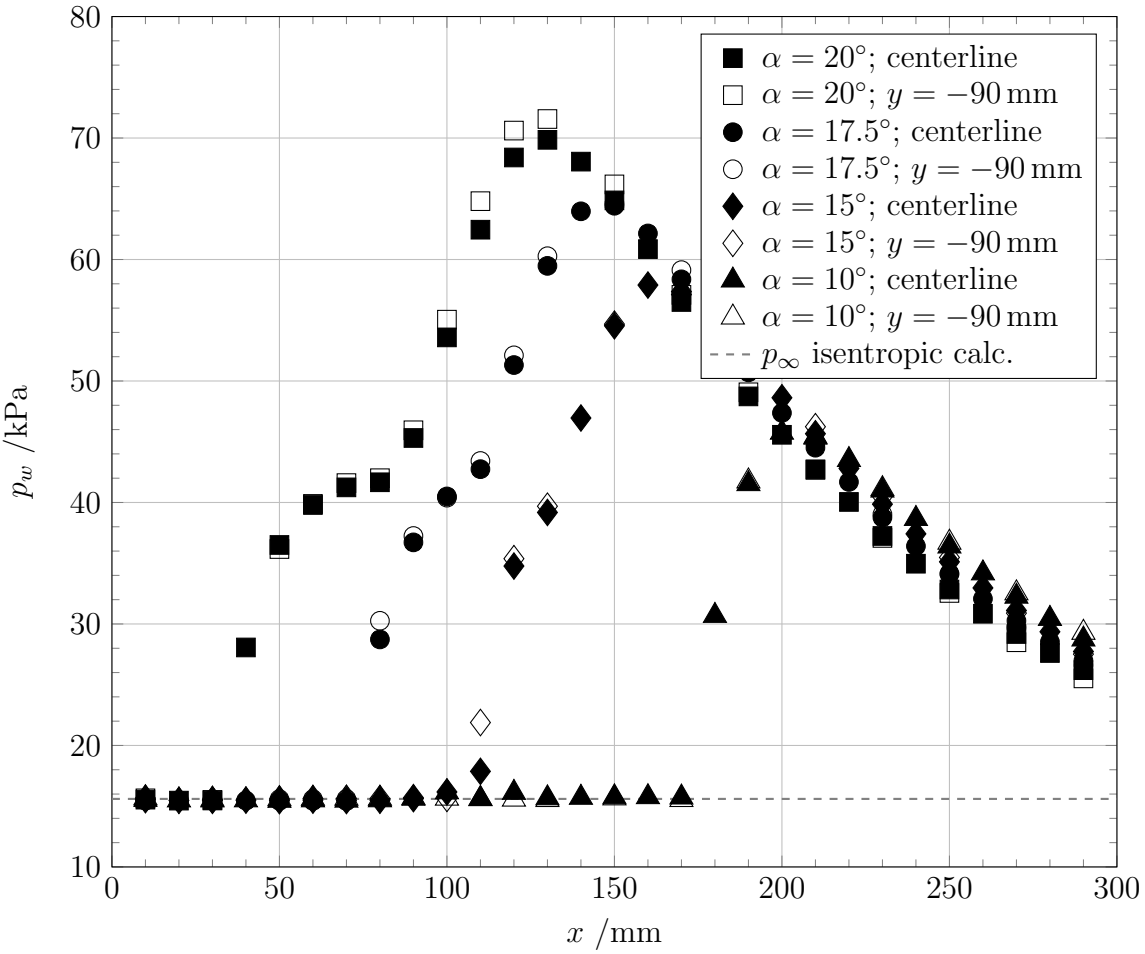


**Figure 2.10:** Average wall pressure ($p_w$) on the rigid panel at $Ma = 3$

## 2.2.1 Reference Measurements on the Rigid Insert

### Mean Wall Pressure

Figures 2.10 and 2.11 show the time-averaged wall pressure distributions along the rigid reference insert for various shock generator angles ($\alpha$). The pressure rise across the SWBLI increases with increasing $\alpha$. Pressure measurements were conducted on the centerline and at $y = -90$ mm to assess any deviations in lateral direction. Generally, agreement is very good, with some small increases of wall pressure at $y = -90$ mm for $\alpha = 20°$ at $Ma = 3$. The flow field is thus considered nearly two-dimensional in $y$-direction, distinctly different from Willems [174] where a highly three-dimensional behavior was obtained. For all cases with $\alpha > 15°$, two locations with a strong rise in wall pressure can be distinguished due to the occurring flow separation. The first one, considerably upstream of the incident shock, results from the initial separation shock (e. g. at $x = 40$ mm for $\alpha = 20°$ and $Ma = 3$). The second one is caused by the reattachment shock downstream of the separated area (e. g. at about $x = 100$ mm for

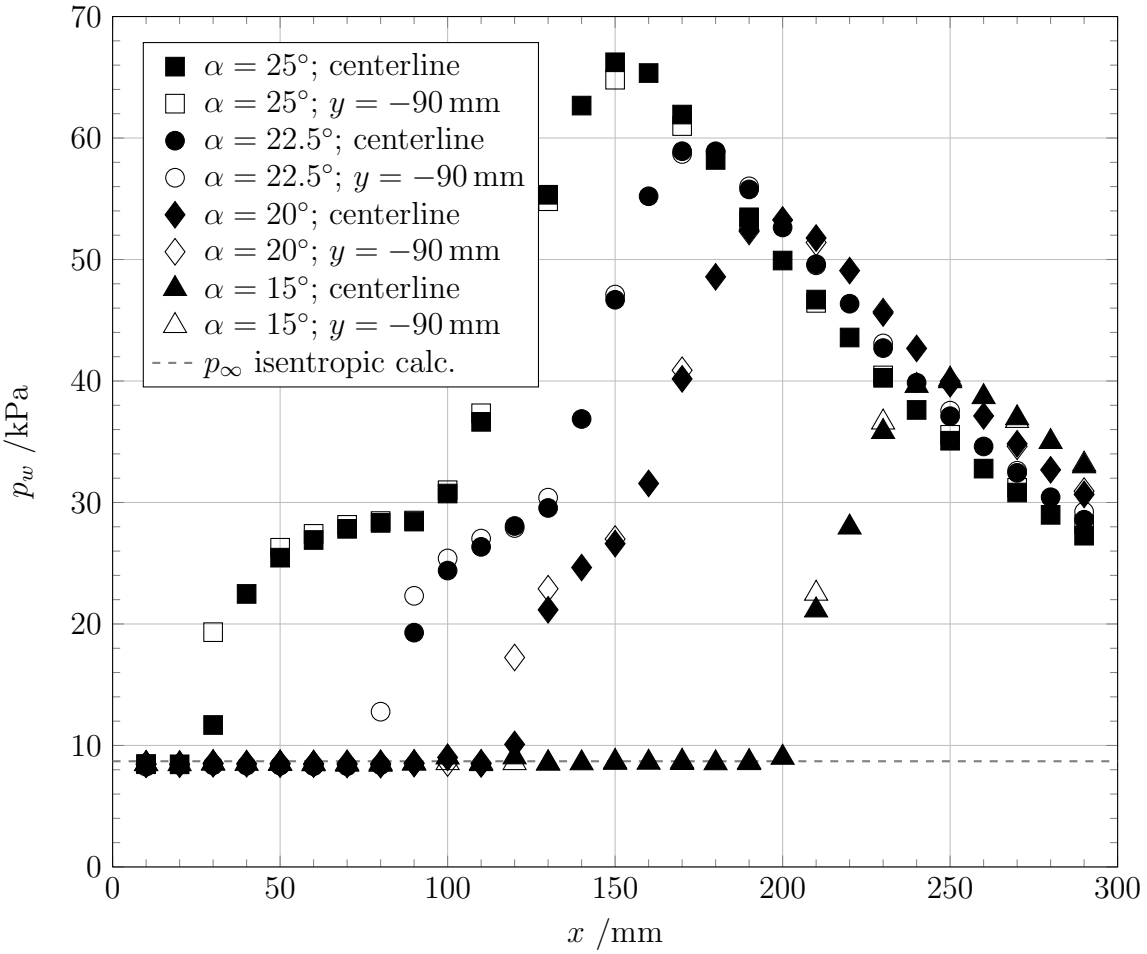


**Figure 2.11:** Average wall pressure ($p_w$) on the rigid panel at $Ma = 4$

$\alpha = 20°$ and $Ma = 3$). The size of the separated area also significantly increases with increasing $\alpha$ and the resulting greater pressure increase across the incident shock.

### Wall Pressure Dynamics

The intrinsic dynamics of the SWBLI that extend to frequencies well below 1 kHz are of central importance to the present study. Figure 2.12 shows an overview of the frequency-multiplied PSD of the wall pressure dynamics for $Ma = 3$ and a steady incident shock angle of $\alpha = 19.6°$, highlighting the drastic local increase in low-frequency dynamics near the separation shock ($x = 45\,\mathrm{mm}$). Furthermore, the comparably lower level of dynamics in the separated area as well as a strong rise in high-frequency dynamics in the vicinity of $x = 85\,\mathrm{mm}$ and $x = 125\,\mathrm{mm}$ are clearly visible. Figure 2.13c shows a shadowgraph image as reference regarding the sensor positions. The shock generator angle was chosen such that the pressure sensor at $x = 45\,\mathrm{mm}$ observes maximum dynamics [30].[3] The observed frequency range is limited by the recording frequency of 100 kHz. Figure 2.13a shows the

[3]This case was used for comparison to the LES with rigid wall in [128, 131].

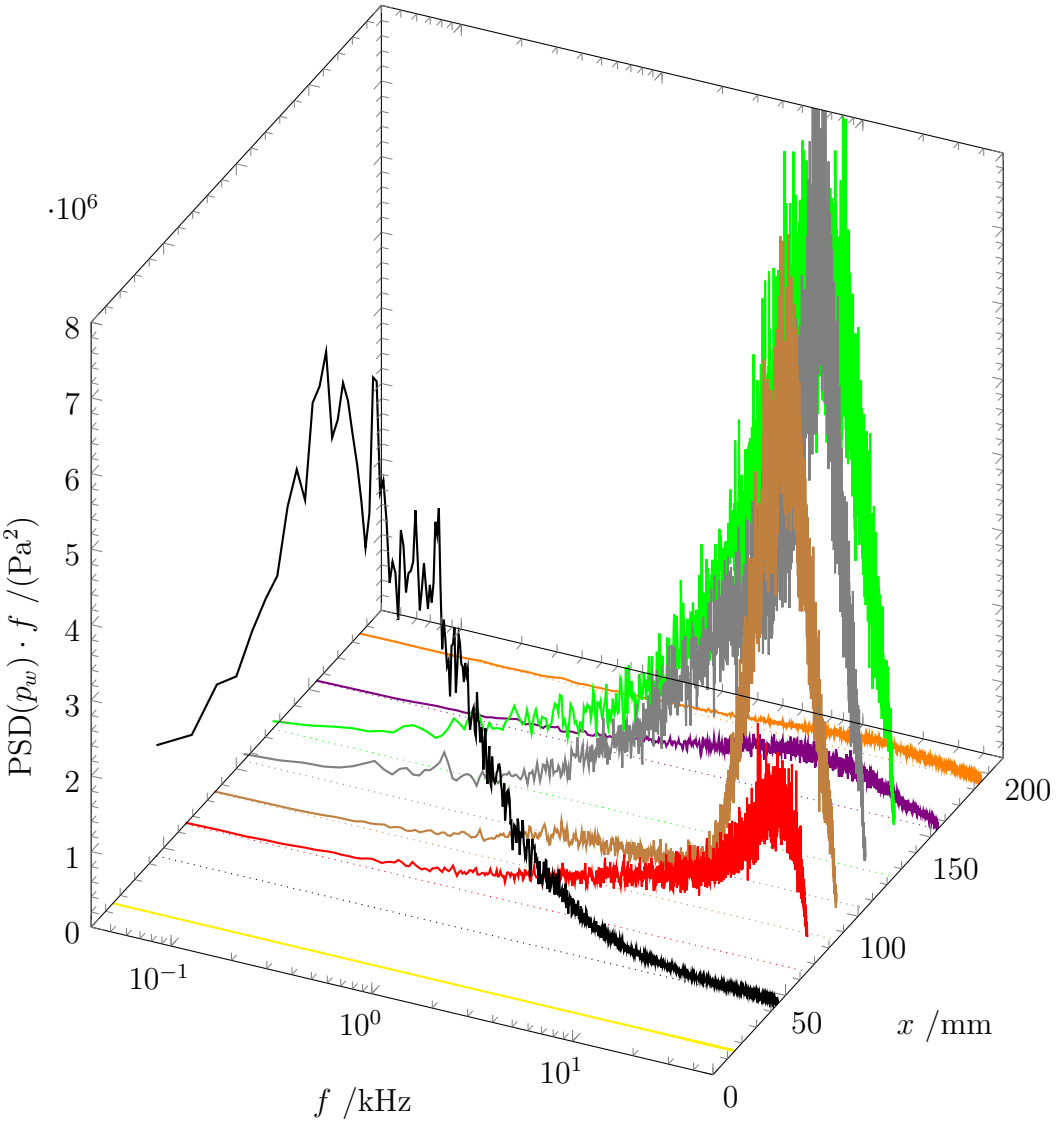


**Figure 2.12:** Wall pressure ($p_w$) dynamics at $Ma = 3$ and $\alpha = 19.6°$

same spectra, but not multiplied by the frequency. Generally, pressure dynamics increase by at least two orders of magnitude throughout the interaction area compared to the measurement at the upstream location at $x = 15\,\text{mm}$. Local maxima for dynamics below 2 kHz are reached at $x = 45\,\text{mm}$ as well as near $x = 105\,\text{mm}$, and $x = 125\,\text{mm}$, with the dynamics at the upstream location about an order of magnitude stronger than at the downstream location. This explains why the low-frequency dynamics in the reattachment area are not distinctly visible in Fig. 2.12. The positions of maximum pressure dynamics agree with the positions of the maximum pressure rise observed in Fig. 2.10. The dynamics at $x = 45\,\text{mm}$ are directly related to movements of the separation shock, thus inducing considerable dynamic loads in the same frequency range as the eigenmodes of the elastic panel. Figure 2.13b, included for reference, is a two-dimensional version of Fig. 2.12. For the case at $Ma = 4$ shown in Fig. 2.14, the results are similar. The

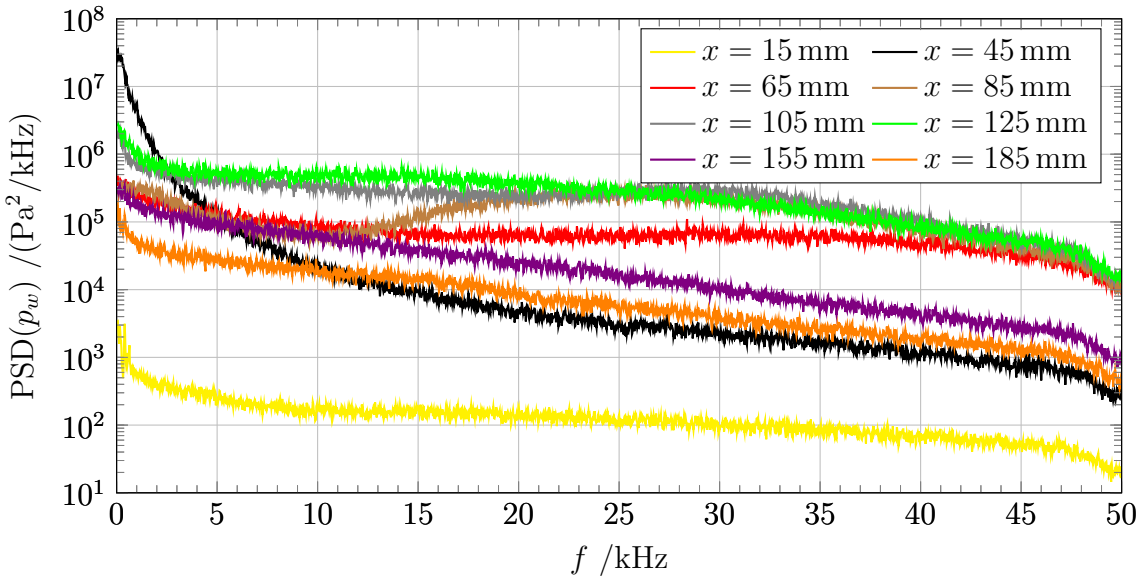


**(a)** Spectra

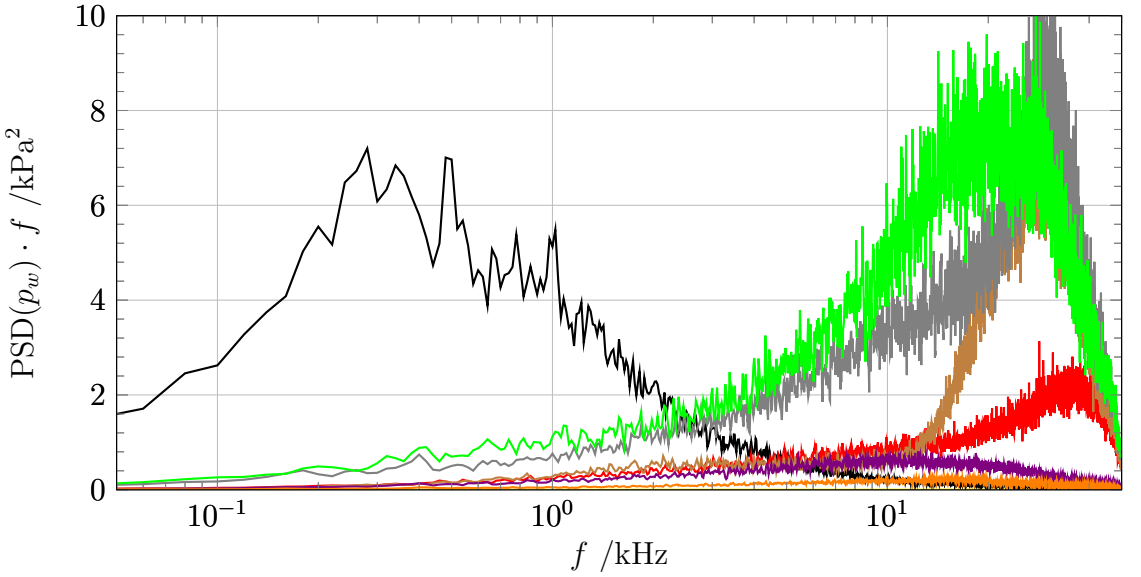


**(b)** Frequency-multiplied spectra

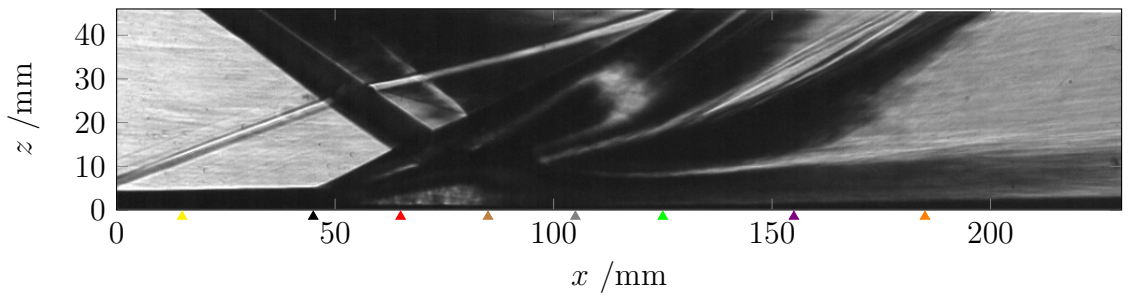


**(c)** Shadowgraph image

**Figure 2.13:** Wall pressure ($p_w$) dynamics at $Ma = 3$ and $\alpha = 19.6°$

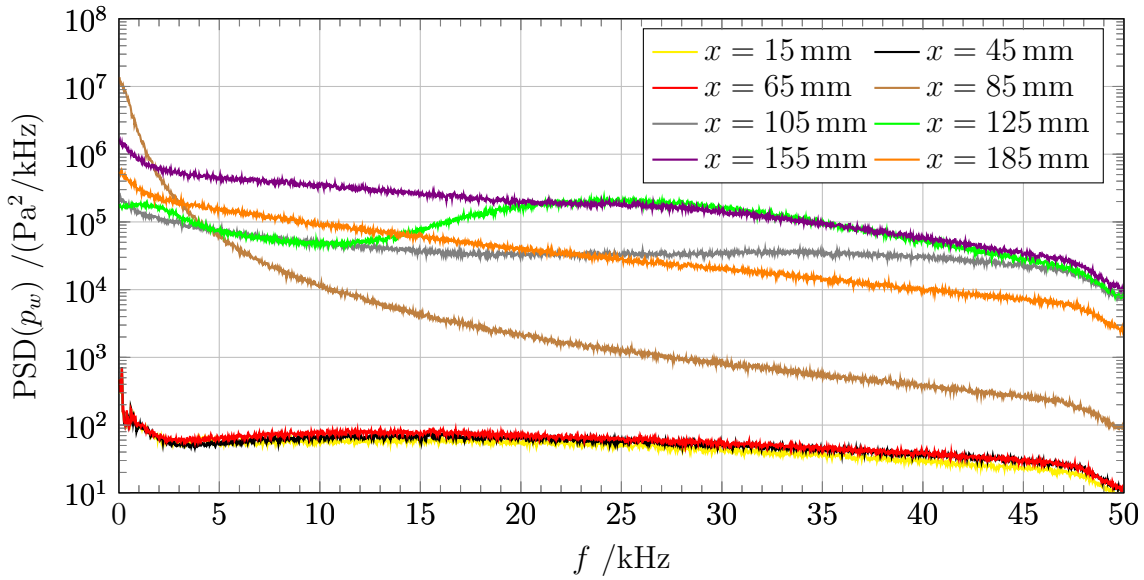


**(a)** Spectra

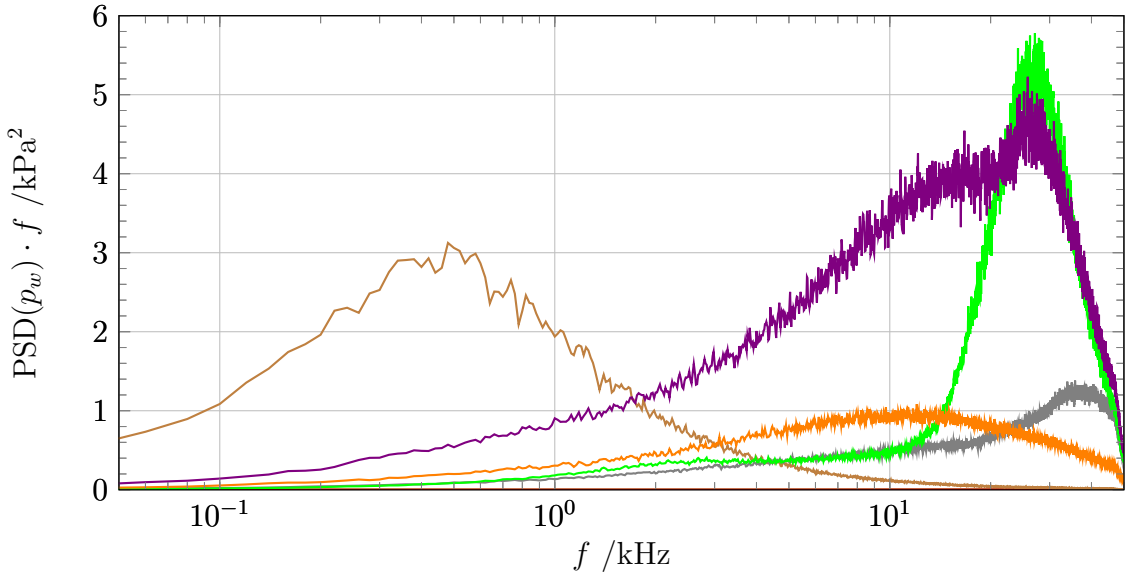


**(b)** Frequency-multiplied spectra

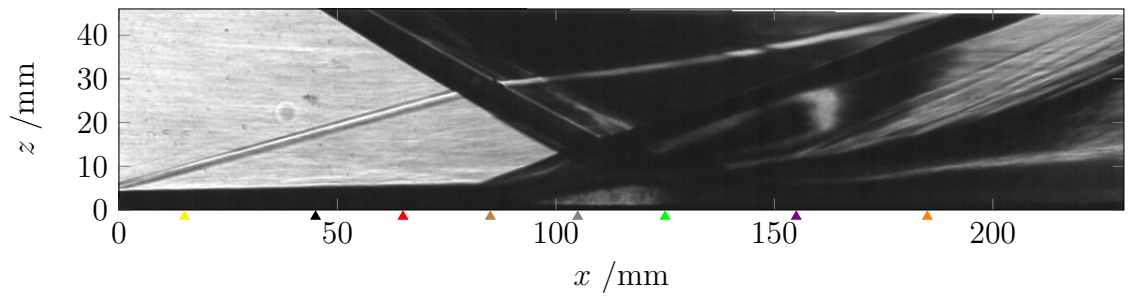


**(c)** Shadowgraph image

**Figure 2.14:** Wall pressure ($p_w$) dynamics at $Ma = 4$ and $\alpha = 22.5°$

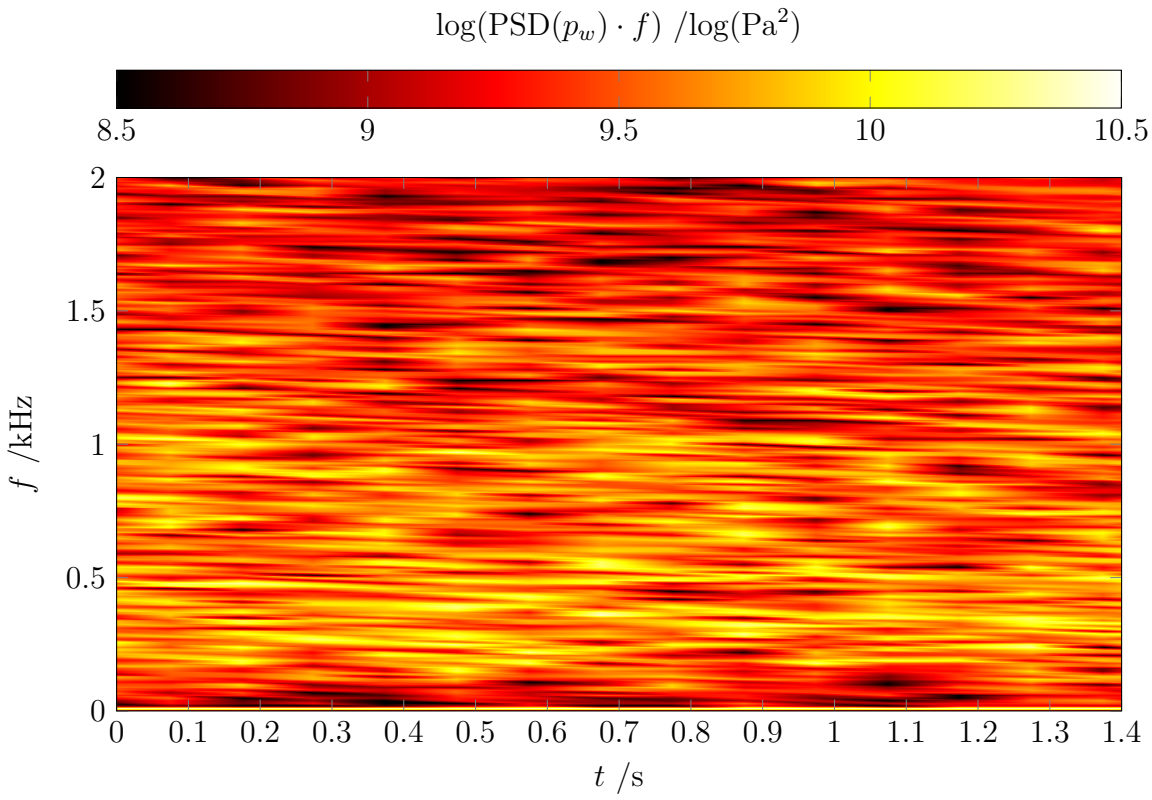


**Figure 2.15:** Spectrogram of the wall pressure ($p_w$) at $Ma = 3$; $\alpha = 19.6°$; $x = 45\,\text{mm}$

difference in PSD of the pressure signals between the undisturbed boundary layer and the interaction area is even larger.

To further illustrate the nature of the ongoing dynamics, Fig. 2.15 shows a spectrogram of the pressure signal at $x = 45\,\text{mm}$ for $Ma = 3$ and $\alpha = 19.6°$ also included in Fig. 2.13. The occurring spectra vary strongly over time. This is particularly interesting in the context of the comparison of experiment and numerical results for low-frequency dynamics in cases where only relatively short time records are available. Additional spectrograms for various other positions were provided in [30] and show qualitatively similar behavior.

Figure 2.16a shows PDFs of the pressure signals at $Ma = 3$ and $\alpha = 19.6°$. At all positions in the interaction, there is a broad range of occurring pressure levels whereas the range is quite narrow at the position upstream of the interaction at $x = 15\,\text{mm}$. The range also declines at the positions farthest downstream at $x = 155\,\text{mm}$ and $x = 185\,\text{mm}$. Notably, the distribution at $x = 45\,\text{mm}$ deviates from the symmetrical behavior found at all other locations. This is due to movement of the separation shock on and off the sensor surface. When the shock moves off the sensor surface, $p_w$ is equal to $p_\infty$ which explains the narrow peak at this pressure. When the shock moves onto the sensor surface, a much wider range of higher pressures is detected. This confirms that the maximum in pressure dynamics found at this location is in fact caused by the movements of the separation shock.

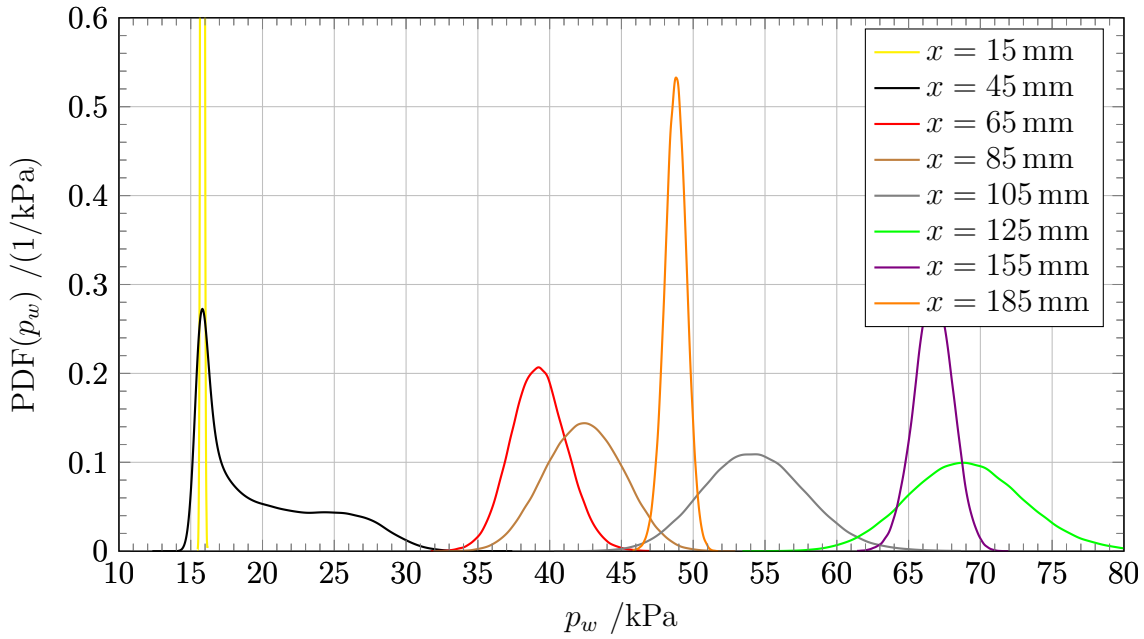


**(a)** Probability density function (PDF) of the wall pressure ($p_w$) at $Ma = 3$ and $\alpha = 19.6°$

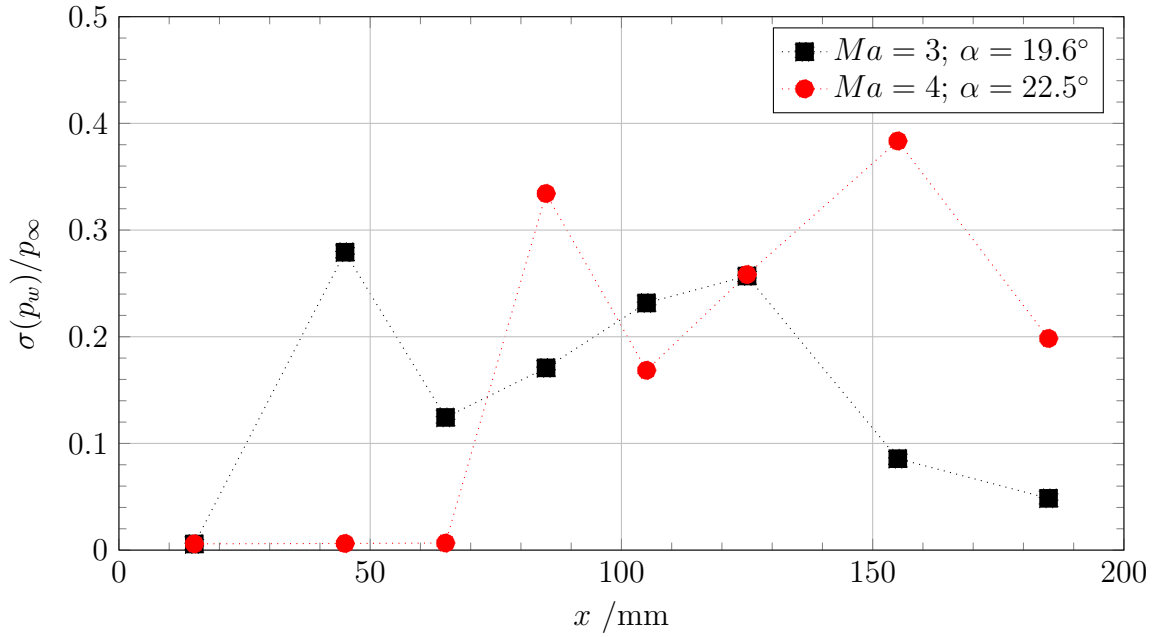


**(b)** Standard deviation of the wall pressure ($p_w$) at $Ma = 3$ and $\alpha = 19.6°$; $Ma = 4$ and $\alpha = 22.5°$

**Figure 2.16:** Properties of the wall pressure dynamics

As a measure of the spatial distribution of the pressure dynamics in the measurement range, Fig. 2.16b shows the standard deviation of the pressure signals at $Ma = 3$ and $\alpha = 19.6°$ as well as at $Ma = 4$ and $\alpha = 22.5°$. In both cases, two local maxima exist, which correspond to the separation and reattachment shock locations (Figs. 2.10 and 2.11).

In addition to experiments with a steady incident shock, the present setup allows fast movements of the incident shock by rotating the shock generator. Figure 2.17 shows a time-series plot of the wall pressure dynamics during such prescribed incident shock movement in upstream (Fig. 2.17a) and downstream (Fig. 2.17b) direction. In the first case, the pressure rise first occurs on the sensor at $x = 85\,\text{mm}$ and then moves farther upstream. The opposite takes place in the second case. Interestingly, there appears to be a certain delay in reaching the new pressure level. To clarify this, Fig. 2.18 shows plots of $p_w$ versus $\alpha$. At all positions, the pressure rise or fall during the shock generator rotation is distinctly different depending on the direction of rotation. These differences occur at a time scale of a similar order of magnitude as the propagation of information from the shock generator given a speed of sound of about $200\,\text{m/s}$ at $Ma = 3$ and $160\,\text{m/s}$ at $Ma = 4$, but could also plausibly be connected to internal processes in the SWBLI during changes in size of the separation area.

### 2.2.2 FSI without Incident Shock

As baseline for the following results, Fig. 2.19 shows the PSD of the deformation of the elastic panel at $Ma = 3$ and $Ma = 4$ without incident shock. The spectra show a relatively broad excitation at frequencies below $600\,\text{Hz}$. However, there are no peaks as distinct as in the reference runs in Fig. 2.8, where a quick removal of the incident shock was used to excite the panel, or in the cases in Chapter 4, where panel flutter at large amplitudes could be observed. The good agreement between the runs at both Mach numbers and the reference runs in Fig. 2.8 in terms of the frequencies of the occurring peaks shows that these are predominantly dependent on the properties of the structure.

### 2.2.3 FSI with Prescribed Incident Shock Movement

Next, cases with a quick movement of the incident shock from a position downstream of the elastic surface onto the panel will be discussed (Figs. 2.20 to 2.25). The panels were initially in an unprestressed condition without SWBLI, as shown in Figs. 2.19a and 2.19b. Then, the shock was moved onto the panel from the rear and comes to a complete stop at a certain position on the elastic surface depending on the preset target angle ($\alpha_{max}$). The shock generator angle ($\alpha$) is shown as a dashed line in Figs. 2.20, 2.22 and 2.24. As has been shown in the rigid wall reference experiments discussed in Section 2.2.1, a large flow separation occurs, which is caused by the pressure gradient imposed by the incident shock for the cases with larger $\alpha_{max}$ (Figs. 2.21 and 2.25), whereas no significant separation is visible in the case with $\alpha_{max} = 15°$ at $Ma = 4$ (Fig. 2.23). In all three cases, the center and rear positions of the panel react first by starting to move into the

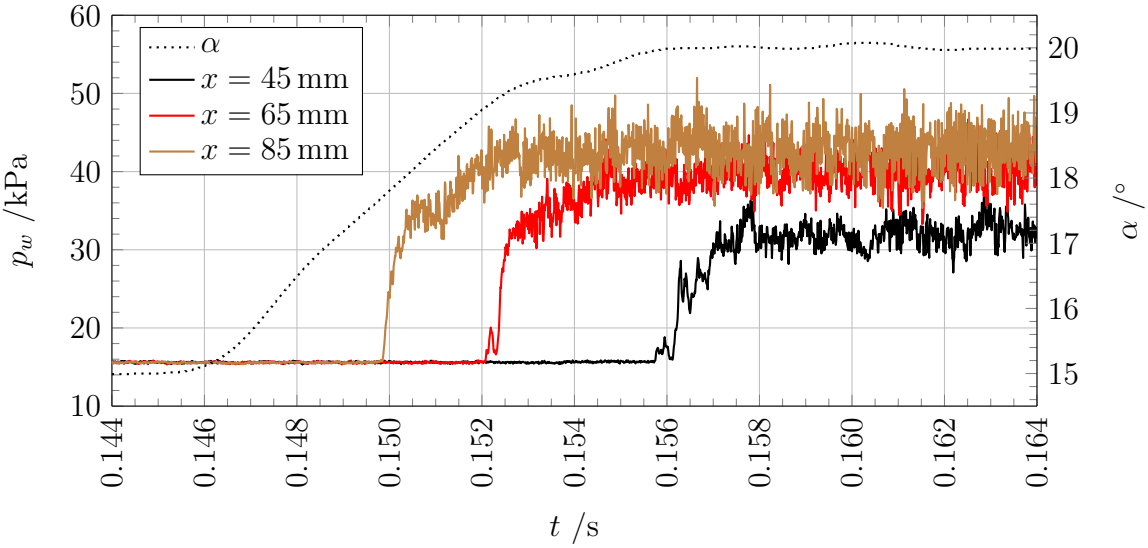


**(a)** Increasing $\alpha$

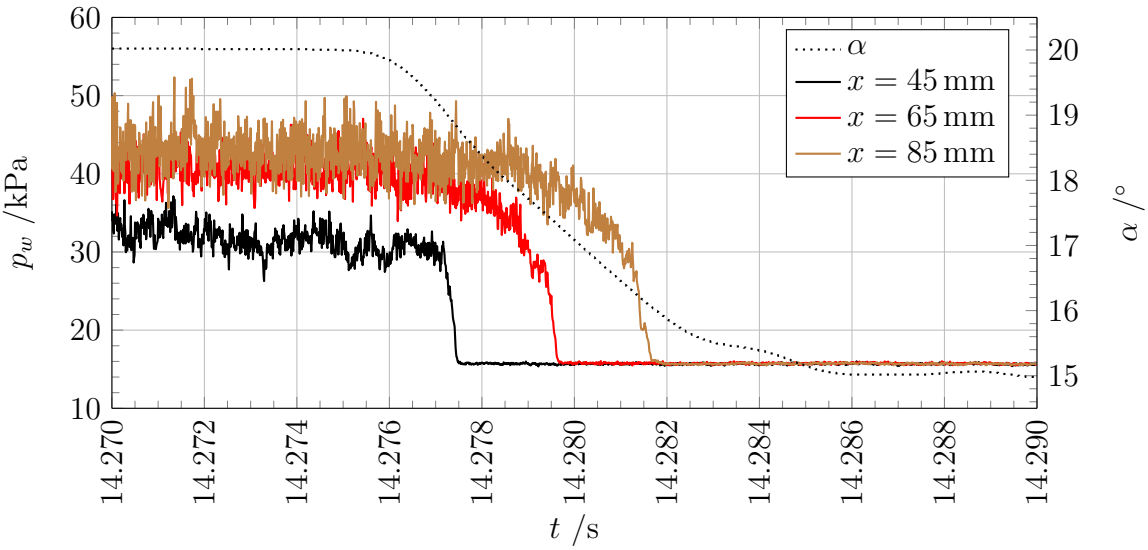


**(b)** Decreasing $\alpha$

**Figure 2.17:** Wall pressure ($p_w$) during shock generator movement at $Ma = 3$ and $\alpha_{max} = 20°$

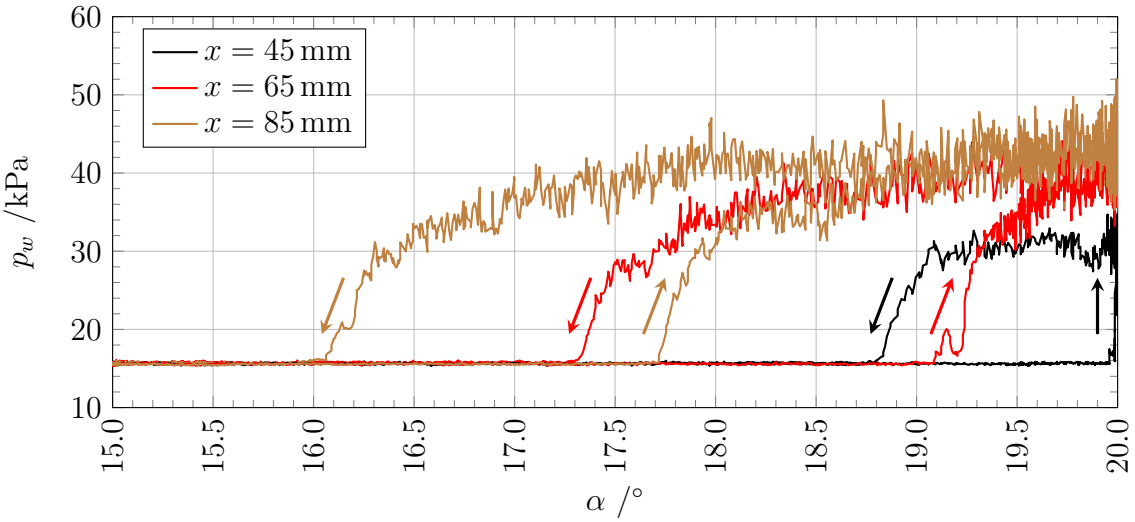


**(a)** $Ma = 3$ and $\alpha_{max} = 20°$

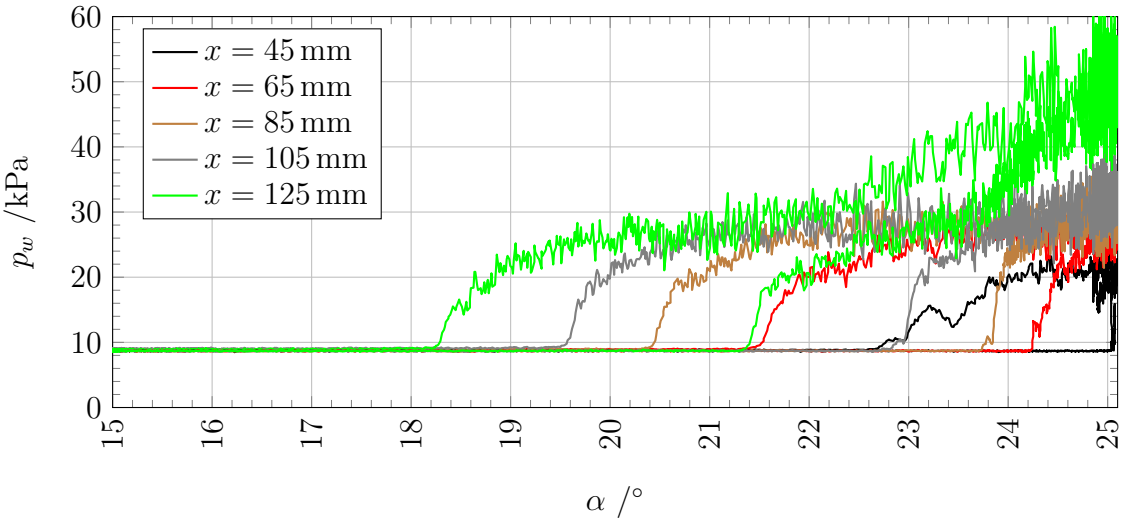


**(b)** $Ma = 4$ and $\alpha_{max} = 25°$

**Figure 2.18:** Wall pressure ($p_w$) dynamics during shock generator movement

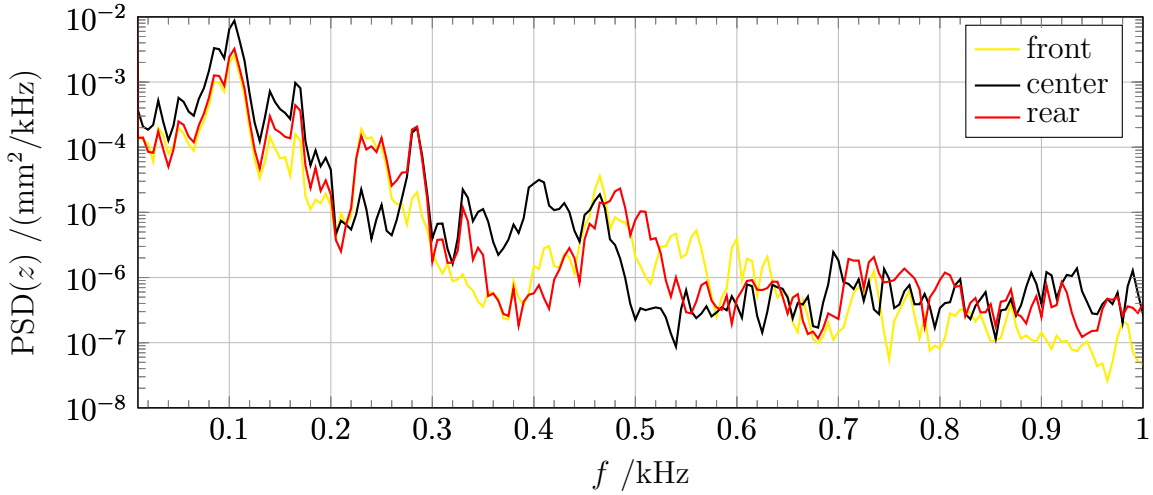


**(a)** $Ma = 3$

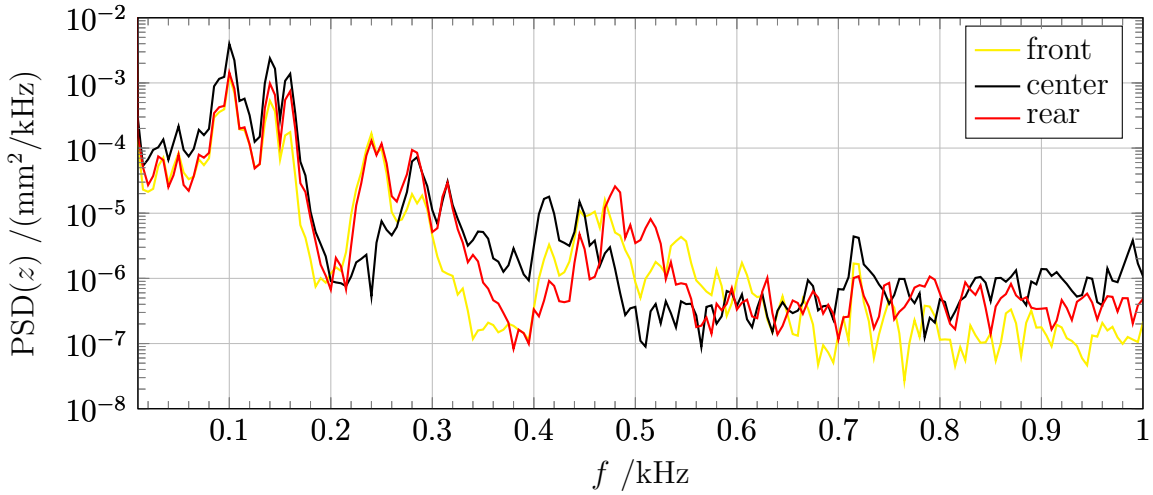


**(b)** $Ma = 4$

**Figure 2.19:** PSD($z$) for the centerline capacitive distance sensors without incident shock

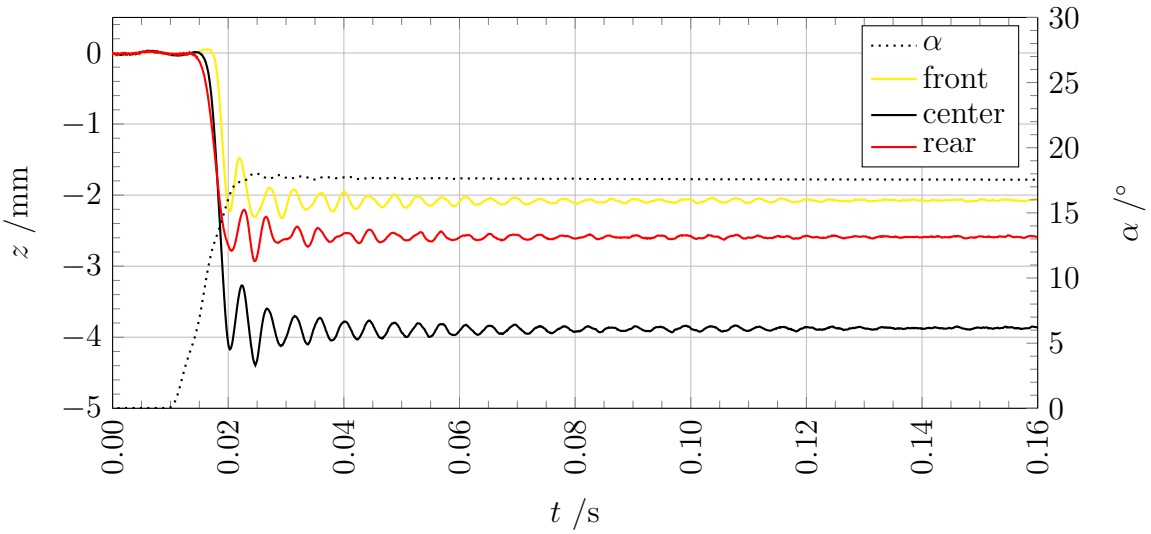


**Figure 2.20:** Prescribed incident shock motion at $Ma = 3$ and $\alpha_{max} = 17.5°$

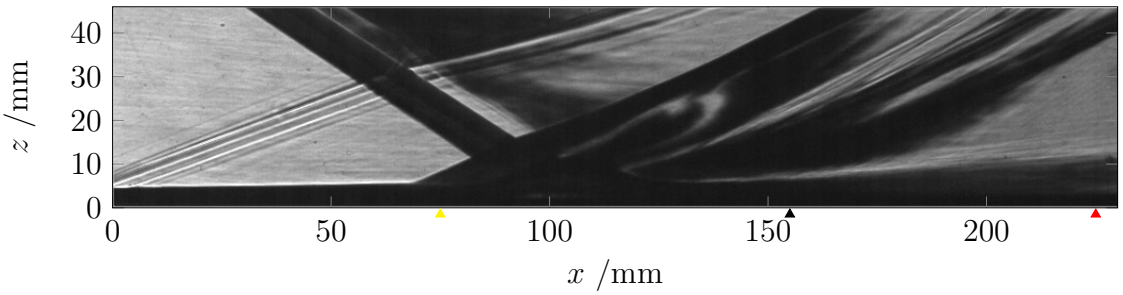


**Figure 2.21:** Shadowgraph image at $Ma = 3$ and $\alpha = 17.5°$ and sensor positions

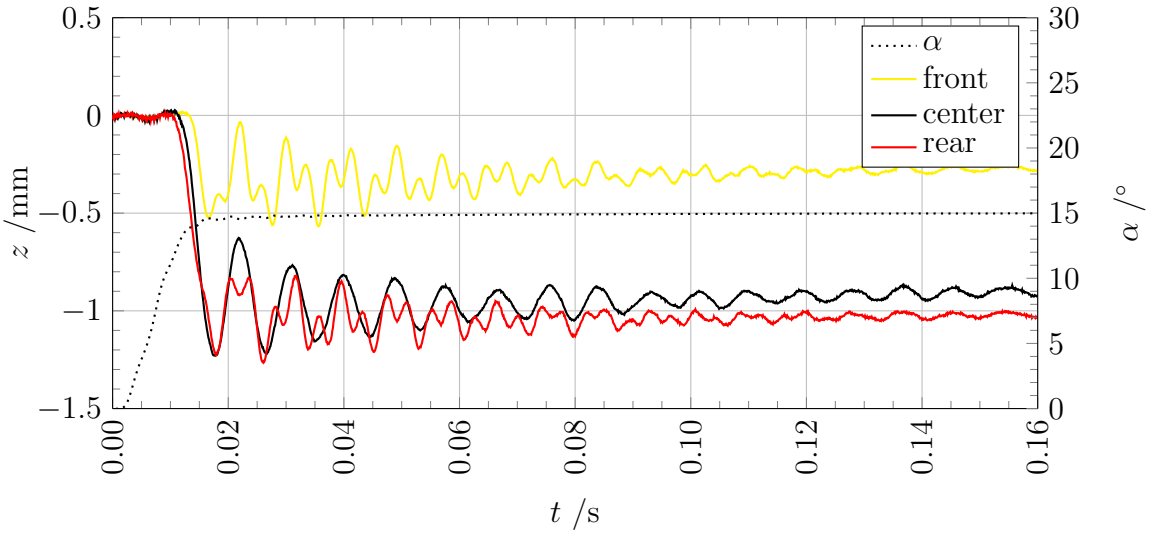


**Figure 2.22:** Prescribed incident shock motion at $Ma = 4$ and $\alpha_{max} = 15°$

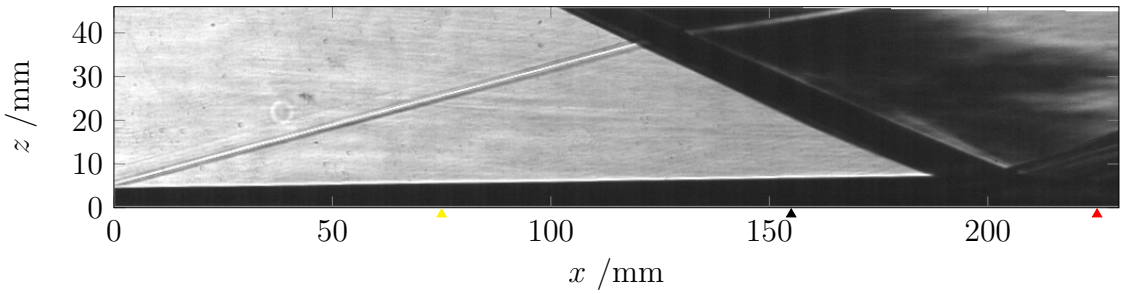


**Figure 2.23:** Shadowgraph image at $Ma = 4$ and $\alpha = 15°$ and sensor positions

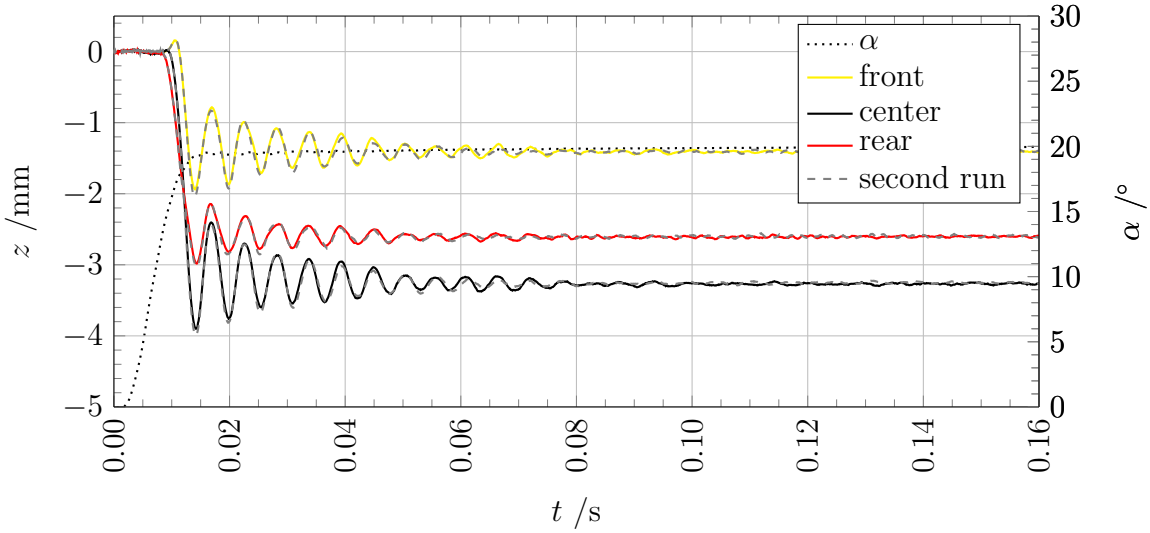


**Figure 2.24:** Prescribed incident shock motion at $Ma = 4$ and $\alpha_{max} = 20°$

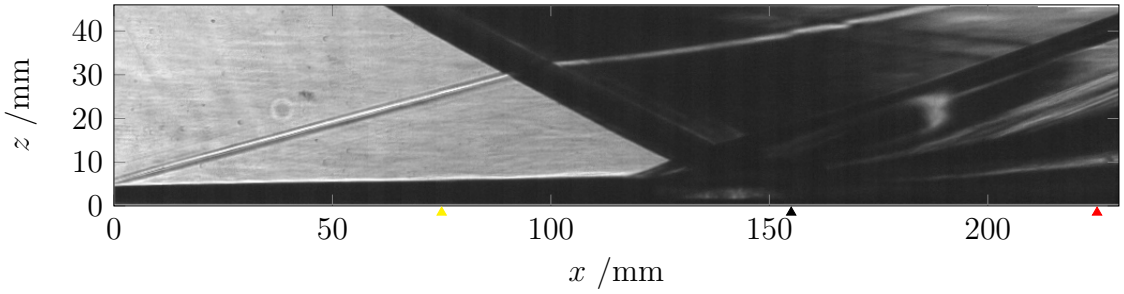


**Figure 2.25:** Shadowgraph image at $Ma = 4$ and $\alpha = 20°$ and sensor positions

cavity. At the front position, the panel first shows a small movement into the flow field, but changes direction away from the flow field immediately afterwards. Once the panel deflection approaches its mean value for the respective configuration, large oscillations begin, initially exceeding amplitudes of 1 mm at the center position in the cases with larger $\alpha_{max}$. In these cases where the incident shock movement ends at the panel center or upstream of the panel center, panel motion at the measured positions is predominantly in phase. In the case with $\alpha_{max} = 15°$ at $Ma = 4$ where the incident shock movement stops in the rear part of the panel, it is excited at a second frequency at which the front and rear part of the panel oscillate opposite in phase in addition to the predominant in-phase oscillation. This is not visible at the center position, pointing to a neutral line in the panel center indicative of the 0;1 mode. This demonstrates that the resulting structural dynamics of the panel depend strongly on the location of excitation. This may also be relevant in more intricate ways regarding the effect of the spatial distribution of pressure dynamics in the SWBLI on the structure in cases that are predominantly driven by intrinsic SWBLI dynamics.

To give an example of the good repeatability obtained with this experimental setup, Fig. 2.24 shows data from two wind tunnel runs of which the second run was conducted after complete removal and reinstallation of the experimental setup in the wind tunnel.

### 2.2.4 FSI with Steady Incident Shock Angle

In addition to FSI cases predominantly driven by the forced movement of the incident shock, cases excited by the intrinsic dynamics of the SWBLI at a fixed incident shock position as shown in Section 2.2.1 were investigated. Figures 2.26 and 2.27 show spectra of the panel displacment at $Ma = 3$ and $Ma = 4$ at various shock generator angles. With increasing shock generator angle, the mean pressure load on the panel rises (as shown in Figs. 2.10 and 2.11) and the panel is more strongly deformed and thus less susceptible to excitation by the flow field. Despite this, the dynamics imposed on the structure by the SWBLI (see e. g. Figs. 2.13 and 2.14) lead to an increase in broadband dynamics with an increase in incident shock angle at both considered Mach numbers. This clearly demonstrates that the observed structural dynamics are caused by the SWBLI dynamics. As expected, the occurring peaks increase in frequency with rising $\alpha$ and the respective rise in panel deformation. They have been shown to be close to the natural frequencies of the structure under a comparable uniform pressure load [31, 174]. This is of course a simplification, but it seems sufficient to plausibly explain the observed behavior despite the real pressure distribution being far from uniform.

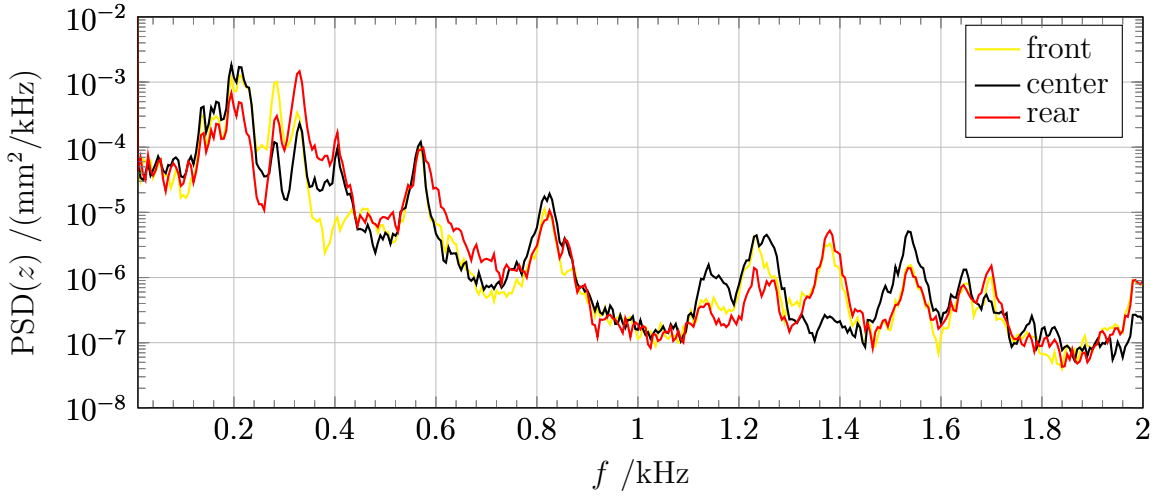


**(a)** $\alpha = 15°$

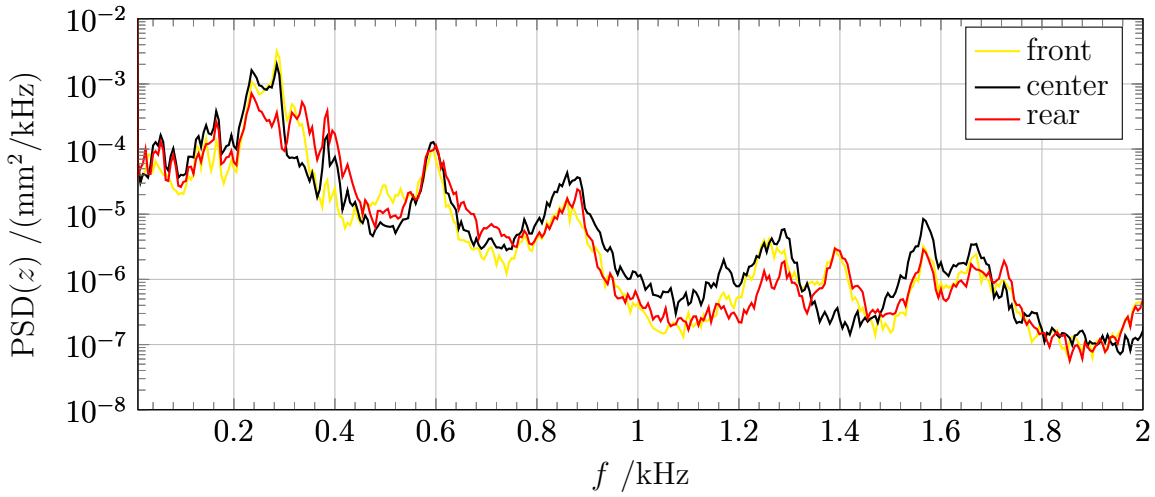


**(b)** $\alpha = 17.5°$

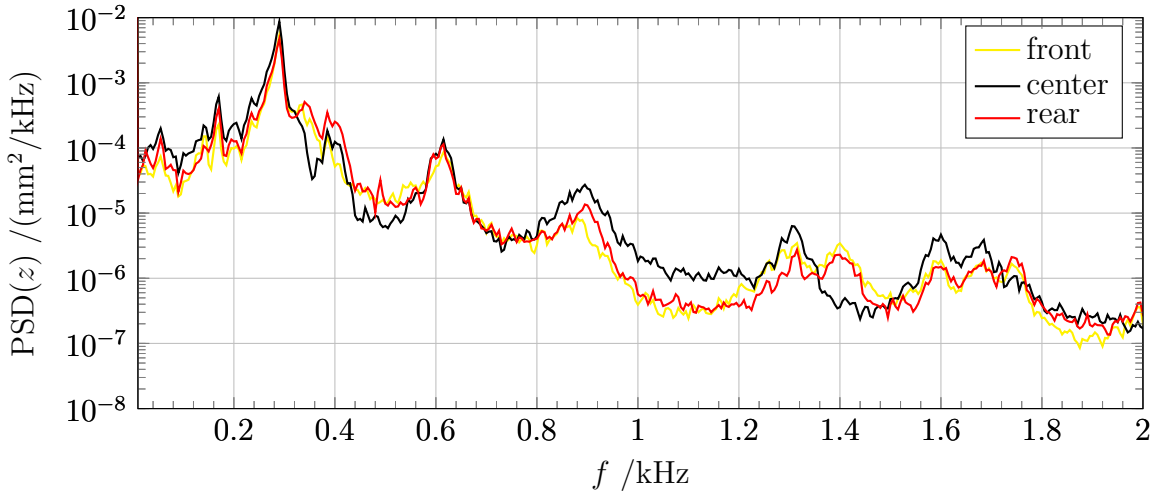


**(c)** $\alpha = 20°$

**Figure 2.26:** PSD($z$) for the centerline capacitive distance sensors $Ma = 3$

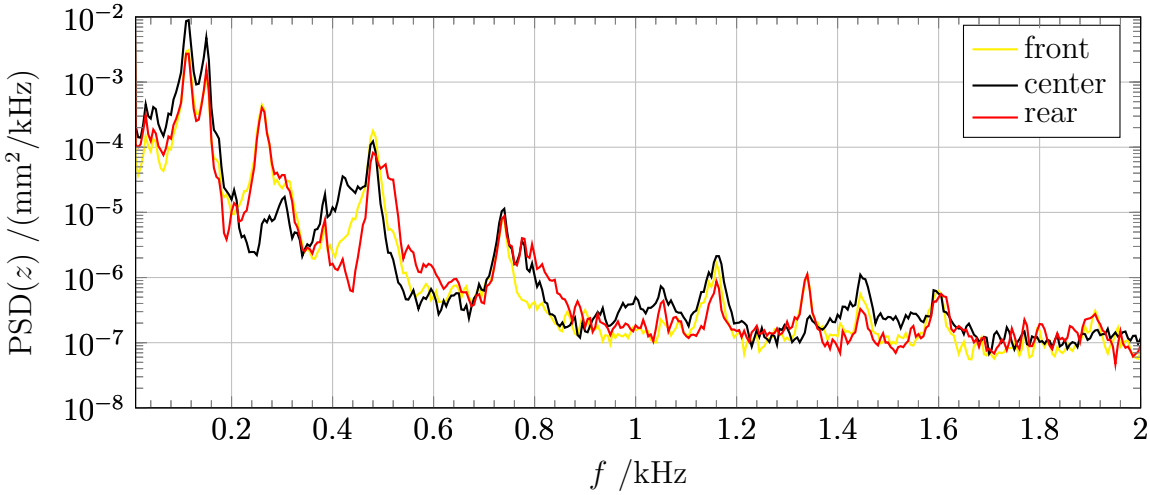


**(a)** $\alpha = 15°$

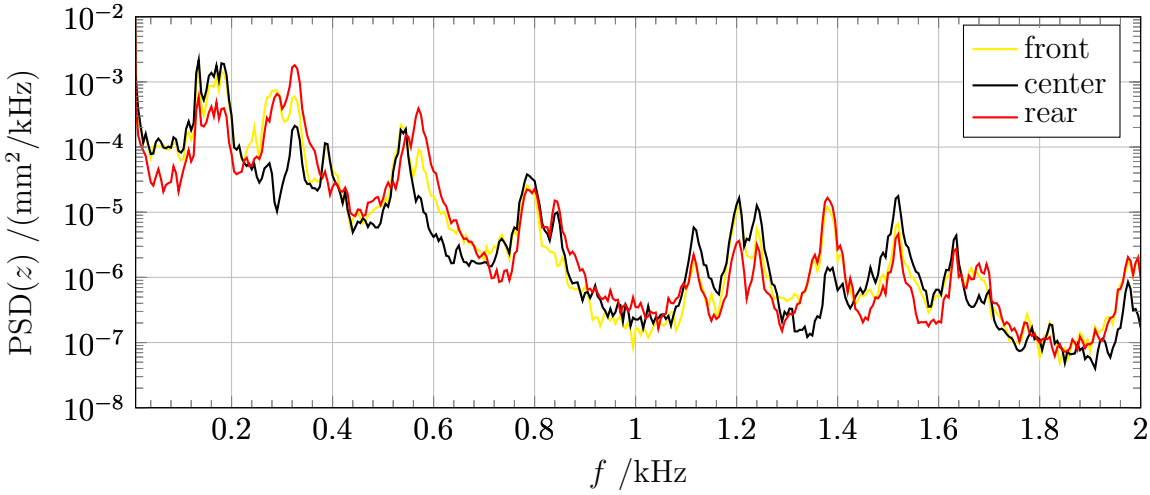


**(b)** $\alpha = 20°$

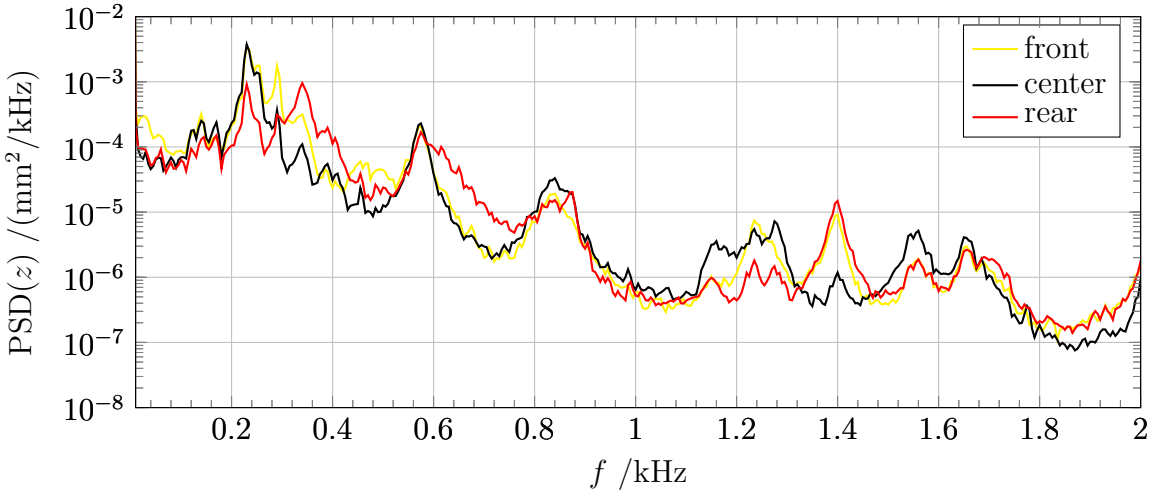


**(c)** $\alpha = 22.5°$

**Figure 2.27:** PSD($z$) for the centerline capacitive distance sensors $Ma = 4$

## 2.3 Discussion

In the precursor configuration by Willems [174, 177], intrinsic SWBLI dynamics in an incident shock configuration were shown to excite an elastic panel. The flow field in this setup was strongly three-dimensional because of the design of the shock generator. The elastic panel showed clearly detectable SWBLI-induced dynamics of low amplitude despite being prestressed by the mean pressure rise along the wall caused by the SWBLI. These dynamics were also visible downstream of the elastic insert in high-speed wall pressure measurements, demonstrating the effect of the elastic panel dynamics on the flow field. Based on this previous work, the setup was improved to obtain a nearly two-dimensional flow field and to add the unprecedented capability to excite the fluid–structure coupled configuration by fast movements of the incident shock generator. These changes allowed a direct comparison to the LES by Pasquariello [128].

In cases with high-speed moving incident shock, the SWBLI was quickly moved onto the unprestressed panel from the downstream side and stopped at a preset position on the panel. Before the shock moved onto the panel, the panel was undeformed and displayed very little dynamics. When the shock moved onto the panel, mean deformation into the cavity developed and large panel oscillations of several millimetres in amplitude set in. It was shown that various modes could be excited depending on the stopping position of the shock on the panel. On a rigid reference panel, it could be shown that the instantaneous wall pressure depends on the movement of the shock generator. This is similar to recent results in [17], where the shock generator rotated continuously, or also [158], where linear movements of a shock generator were used. This observation may also be helpful in understanding incident SWBLI FSI cases where large amplitude structural dynamics like panel flutter occur. In such cases, it is not the incident shock but the panel that moves, and the influence of the dynamic behavior of the SWBLI on the resulting structural dynamics and vice versa is still not well understood (see also Chapter 4).

Reference measurements on the mean pressure and pressure dynamics in the SWBLI were also conducted for steady incident shock angles. For these, the rotatable shock generator made it possible to change the incident shock angle in small steps so that the maximum wall pressure dynamics of the SWBLI for a steady incident shock position could be detected despite limited spatial resolution of the high-speed wall pressure sensors. As typical for such configurations [14], the pressure measurements showed significant low-frequency dynamics below 1 kHz predominantly in the vicinity of the separation shock. This is in the same range as all lower panel modes that start from around 100 Hz. Thus, the intrinsic SWBLI dynamics are well suited to excite structural dynamics in cases without forcing by incident shock movement. Consequently, the adjustable incident shock angle was used to investigate the effect of the intrinsic SWBLI dynamics on the elastic panel for various steady incident shock angles and respective changes in SWBLI dynamics. An increased incident shock angle was shown to cause increased excitation of the structure. This happened despite the increased effective panel stiffness caused by the rising mean wall pressure load that also increased with a rising shock generator angle. With cavity pressure adjusted to reduce the pressure difference across the panel, the excitation would even be stronger. This complements recent results in [169] where

similar observations were made for a configuration with an elastic panel on a ramp. In this context, it should be noted that it was shown by Willems [174] for the precursor configuration that it is possible to track and analyse the separation shock position in high-speed shadowgraph recordings. For the present configuration, it was shown that the rigid and elastic case can be distinguished by using this approach (see [31]). But this was not used for further detailed analysis, since the middle of the test section is not well visible in the shadowgraph images. A focusing Schlieren setup [54, 167] to circumvent this problem would be a very useful addition for future studies. This would require additional preparatory work for integration at the TMK.

The results of the conducted experiments were compared to the results by Pasquariello [128]. First, the mean and time-resolved wall pressure results in the rigid reference case were considered [131]. Generally, very good agreement was found both in the static pressure distribution and wall pressure dynamics. As the LES only considered a thin slice of the flow field, this confirms the nearly two-dimensional behavior of the flow field in the experiment. Because of the nature of the employed methods, a difference between the experiment and the LES is that the experiment can easily obtain run times of several seconds while the LES is quite limited in physical time duration due to limited computational resources. However, the upper end of the frequency range obtained by the LES is greater than what is attainable in wind tunnel measurements limited by the maximum available recording frequency. This means that the wall pressure spectra of both methods overlap in a certain frequency range whereas lower frequencies can be obtained from the experimental data and higher ones from the LES. The resulting spectra provided in [131] show very good agreement overall, including a distinct maximum in frequency-premultiplied form as predicted in the literature. Some deviations appear towards the lower end of the frequency range covered by the LES. It appears that a comparison at the lower end of the frequency spectrum extracted from the LES may not be fully conclusive due to its limited run time. This highlights the advantages and drawbacks of both methods as well as the value of such collaborative efforts.

In a next step, the first LES-structure coupled simulation of such a configuration was conducted by Pasquariello et al. [130]. Due to the limited physical time, this was only possible for cases with forced excitation but not for the cases with excitation by the intrinsic SWBLI dynamics at constant incident shock angle that would have required significantly longer physical time scales for meaningful analysis. The coupled simulation showed good agreement in the resulting mean deformation after moving the shock on the panel, and also reproduced the large scale oscillations with a slight shift in the occurring frequency and a significant difference in damping, that was not included in the structural model (Fig. 2.28).

A recent coupled wall-modelled LES study by Hoy and Bermejo-Moreno [81], where damping was considered, yielded significantly improved agreement regarding the resulting deformation dynamics of the panel both in observed frequency and damping behavior. They also showed the influence of the coupled configuration on wall pressure dynamics downstream of the interaction. Furthermore, they observed a significant increase in low-frequency wall pressure dynamics in the SWBLI for the elastic wall case. Quite interestingly, Fig. 2.28 shows good agreement regarding the onset of the panel movements

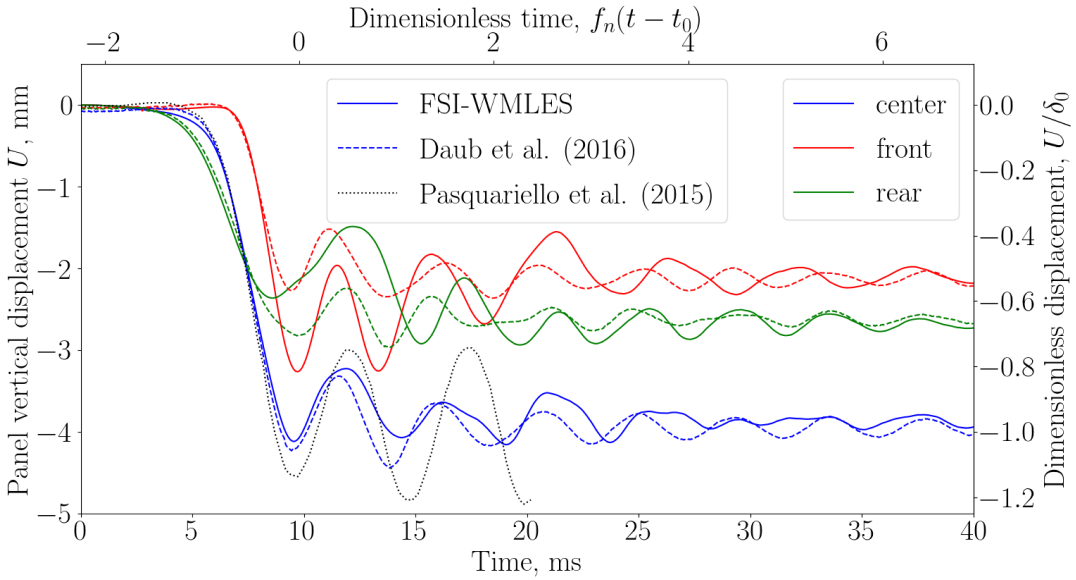


**Figure 2.28:** Comparison of FSI-coupled wall-modelled LES results by Hoy and Bermejo-Moreno [81] to present experimental results, and LES results by Pasquariello et al. [130] (Figure reprinted from [81] by permission of the American Institute of Aeronautics and Astronautics, Inc.)

at about $t = 5\,\text{ms}$, the resulting predominant frequency of panel oscillations, damping, and mean deformation. However, a peculiar difference in panel dynamics regarding oscillation amplitude and mean deformation can be observed at the front and rear positions between about $t = 10\,\text{ms}$ and $t = 25\,\text{ms}$. This behavior might be caused by differences in the wall pressure distribution in the SWBLI during the fast movement of the incident shock that has been shown to depend both on shock angle and velocity. An interesting subject for further investigation might be whether this is connected to the performance of the wall-modelled LES in this transient phase.

Another interesting effort based on this configuration has been started by Zope et al. [185]. They have begun a comparison of methods of different levels of fidelity ranging from RANS to hybrid LES to determine the required level of fidelity to model central features of the coupled system. The work appears to be ongoing and not yet fully concluded.

Data from the rigid wall reference case was also used in other studies with different levels of fidelity. A simplified engineering model for SWBLI wall pressure dynamics was proposed in [82], whereas predictions of mean flow field properties were considered in [182, 183].

# 3 Hypersonic High-Temperature FSI Including Plastic Deformation

This chapter presents experimental results on hypersonic FSI with focus on high thermal loads that result in the buckling of thin panel structures, including plastic deformation. To obtain suitable high-enthalpy flow conditions, experiments were conducted in the Arc-heated Wind Tunnel L3K. During the experiments, time-resolved surface deformation and temperature fields were measured. The challenging Digital image correlation (DIC) measurements through the flow field were validated by comparison to internal laser triangulation measurements. The resulting data set facilitates a detailed analysis of the coupling between thermal loads and structural deformation. Severe localized heating and resulting deformations of more than 12 times the panel thickness were observed. In addition to single exposure measurements, the effects of repeated load cycles were investigated. The mechanical setup was based on previous experiments by Haupt et al. [73] and Niesner [124]. This chapter is based on [25, 28], preliminary results were published in [20, 21]. The obtained measurements of surface deformation and temperature were used to validate coupled simulations by Martin et al. [113, 114]. Furthermore, experiments with Thermal barrier coating (TBC) were conducted in cooperation with Fiedler et al. [53] to investigate the behavior of newly developed TBC in a high-temperature environment and with large structural deformations.

## 3.1 Experimental Setup

### 3.1.1 Arc-Heated Wind Tunnel L3K

To obtain the aerothermal loads required for large deformation of the structure, the experiments were performed in the Arc-heated Wind Tunnel L3K at DLR, Cologne (Fig. 3.1, see [48, 65] for a full description of the facility). In this facility, air is heated to total temperatures between 4000 and 7000 K by a segmented arc-heater and expanded in a conical nozzle to hypersonic velocities. A free jet is formed at the nozzle exit. Models are mounted on a swiveling mount to keep the model out of the jet during startup and shutdown of the facility. The test chamber walls are located at a large distance from the free jet and remain close to ambient temperature. The model was moved into the free jet after steady flow conditions were established. Before shutdown, the model was moved out of the jet for the duration of the shutdown. During this time, no optical measurements on the model surface were possible. Afterwards, it was moved back into the test position to continue Infrared (IR) and DIC measurements of the cool-down process. For the later runs, the model was kept in measuring position for jet shutdown.

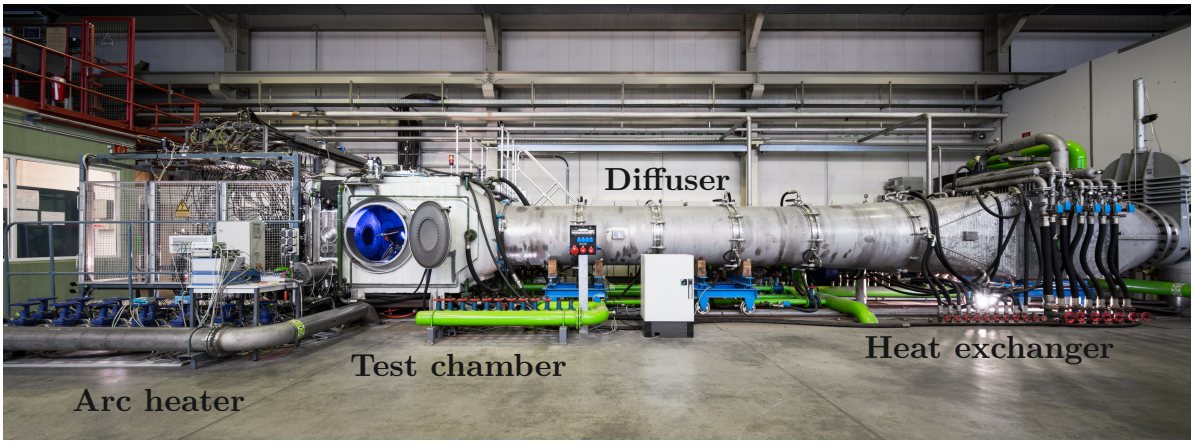


**Figure 3.1:** Arc-heated Wind Tunnel L3K at DLR, Cologne

**Table 3.1:** Flow conditions

| Flow Parameters | | Flow Composition | |
|---|---|---|---|
| Variable | Value | Species | Mass Fraction |
| $Ma_\infty$ | 7.7 | $N_2$ | 0.755 |
| $p_\infty$ | 50.3 Pa | $O_2$ | 0.021 |
| $T_\infty$ | 477 K | NO | 0.022 |
| $v_\infty$ | 3756 m/s | N | $< 0.0001$ |
| | | O | 0.202 |

The experiments were conducted at 20° angle of attack at the flow conditions shown in Tab. 3.1. These flow conditions were computed based on measured values of reservoir pressure and mass flow rate using the DLR numerical flow solver (TAU) [109], taking into account thermal and chemical non-equilibrium. The flow is considered to be in equilibrium in the reservoir, and frozen at nearly constant conditions in the test section. This was confirmed by Coherent anti-Stokes Raman spectroscopy (CARS) measurements [66]. Figure 3.2 shows examples of the operating conditions to illustrate the excellent repeatability of the flow conditions, allowing direct comparison between results from multiple wind tunnel runs. Furthermore, the conditions are constant throughout the duration of each run.

### 3.1.2 Wind Tunnel Model

The experimental setup (Fig. 3.3) is based on previous experiments by Niesner [124]. The main goal was to obtain reliable deformation and temperature measurements of a structure with large plastic deformation induced by a high-enthalpy flow field. The 200 mm × 200 mm panels of 1 mm or 2 mm thickness made of Incoloy 800 H were mounted in a solid Incoloy 800 H frame that mechanically constrained the thermal expansion of the test panel. The manufacturing tolerance of the length of the panel in $x$- and $y$-direction was specified to be between 0 and −0.2 mm to get as close to the nominal

**Table 3.2:** Thermal properties of the insulation

| Schupp UltraBoard 1850/500 | |
|---|---|
| Density | $500\,\mathrm{kg/m^3}$ |
| Heat capacity | $1130\,\mathrm{J/(kgK)}$ |
| Thermal conductivity at | |
| 800 °C | $0.21\,\mathrm{W/(mK)}$ |
| 1000 °C | $0.26\,\mathrm{W/(mK)}$ |
| 1200 °C | $0.33\,\mathrm{W/(mK)}$ |
| 1400 °C | $0.38\,\mathrm{W/(mK)}$ |
| Emissivity | 0.3 |

**Table 3.3:** Temperature-dependent material parameters for Incoloy 800 H as given in [114, 124]; * linearly interpolated values; + linear hardening parameter, the hardening parameter $\beta$ does not exist for these values

| | Incoloy 800 H | | | | | |
|---|---|---|---|---|---|---|
| temperature /°C | Young's modulus /GPa | yield stress /MPa | hardening parameter H /MPa | hardening parameter $\beta$ – | Poisson's ratio – | thermal expansion $/(10^{-5}/\mathrm{K})$ |
| 20 | 197 | 231 | 350.3 | 5.0 | 0.288 | 1.54 |
| 100 | 185 | 226 | 388.5 | 6.6 | 0.289 | 1.54 |
| 200 | 180 | 189 | 400.8 | 7.0 | 0.292* | 1.60* |
| 300 | 169 | 187 | 370.8 | 6.65 | 0.294 | 1.65 |
| 400 | 165 | 173 | 400.0 | 6.15 | 0.297* | 1.69* |
| 500 | 159 | 150 | 410.7 | 6.1 | 0.299 | 1.72 |
| 600 | 151 | 144 | 380.3 | 6.1 | 0.303* | 1.76* |
| 700 | 144 | 137 | 250.5 | 12.6 | 0.306 | 1.79 |
| 800 | 140 | 130 | 75.8 | 53 | 0.310 | 1.83 |
| 900 | 133 | 107 | 49.8+ | – | 0.314 | 1.86 |
| 1000 | 127 | 59 | 22.0+ | – | 0.319 | 1.90 |

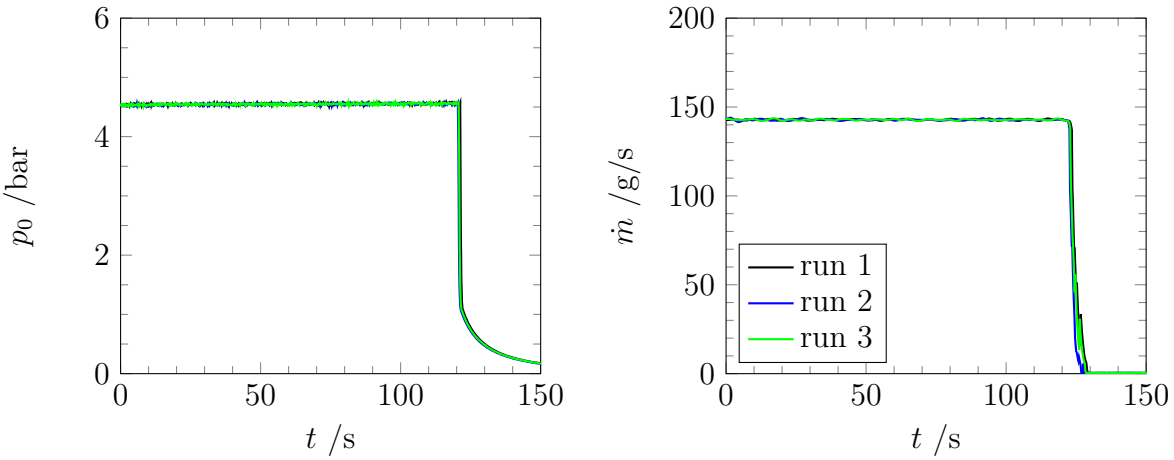


**(a)** Reservoir pressure

**(b)** Mass flow rate

**Figure 3.2:** Comparison of Arc-heated Wind Tunnel L3K (L3K) operating conditions for several runs

value as possible and assure that they can be mounted to the frame without significant initial stresses. The 1 mm panels were at about −0.1 mm below nominal dimensions and the 2 mm panels around −0.2 mm unless stated otherwise. During the experiment, the frame heated up more slowly than the panel due to its higher thermal capacity, leading to the desired buckling of the panel. Both model nose and base plate were water-cooled. The frame was thermally separated from the holder by insulation made of UltraBoard 1850/500 by Schupp Industriekeramik (Tab. 3.2). Information on the properties of Incoloy 800 H provided in [114, 124] is given in Tab. 3.3. Specifications can also be obtained from Special Metals Corporation. In preparation, the panels were subjected to heat treatment at 950 °C for 30 minutes to prevent a strong change in surface emissivity caused by oxidation during the wind tunnel run. The experiment duration is limited to 120 s to avoid plastic deformation of the frame.

### 3.1.3 Instrumentation, Uncertainty and Data Processing

The instrumentation was selected to allow time-resolved measurements of the temperature and deformation fields on the panel surface. It was required to be non-intrusive to prevent any influence on panel heating and deformation. Furthermore, it had to withstand thermal and vacuum conditions in the model or be suitable for operation through the test section's limited optical access.

#### Digital Image Correlation in Supersonic Flow

DIC systems are well established and commonly used measuring systems. Their application in supersonic wind tunnels for FSI studies, however, poses special problems. Only rarely does the experimenter have the luxury of unobstructed view on the structure from

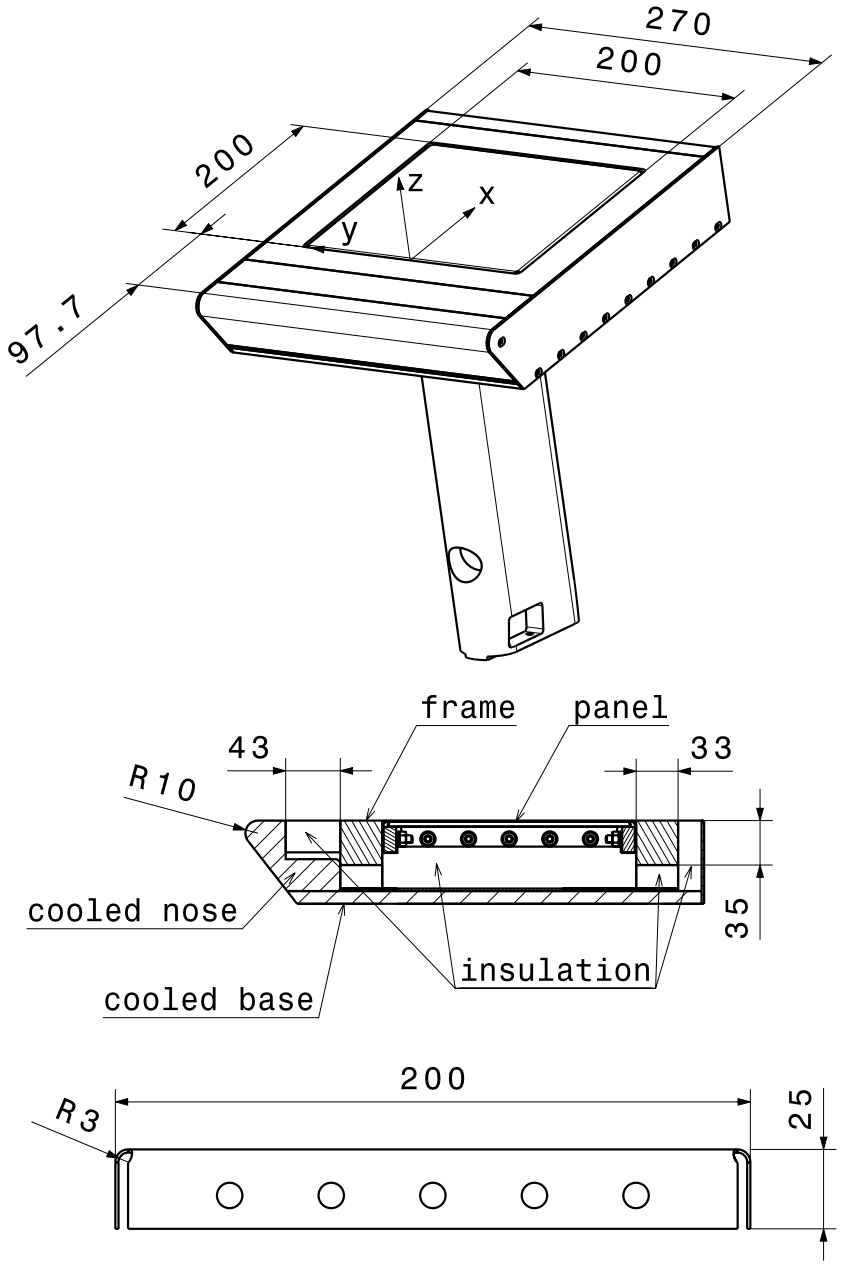


**Figure 3.3:** L3K wind tunnel model (in mm, R 3 refers to the inside radius)

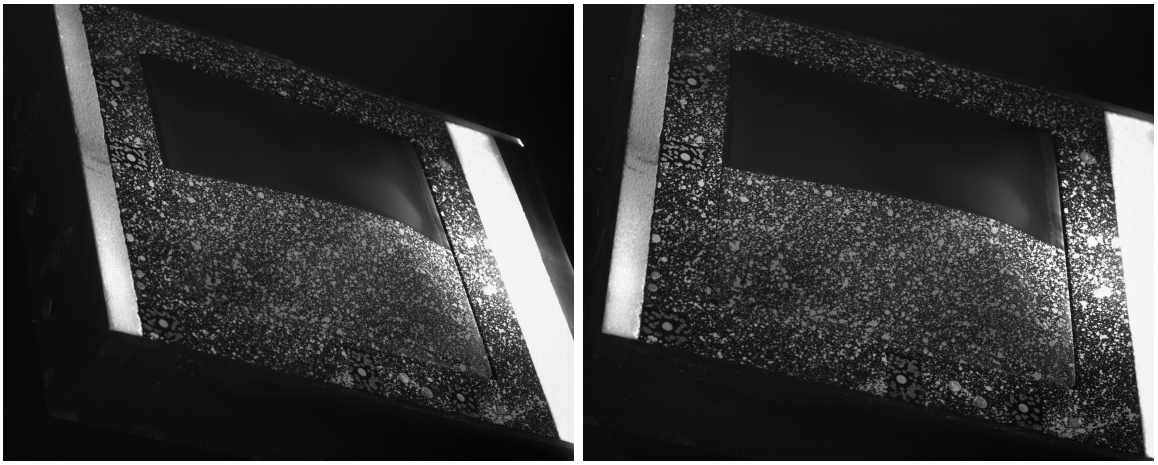

**Figure 3.4:** Example of DIC image pair at maximum deformation (flow from right to left)

the outside of the facility (e. g. [58, 59, 150]). In most cases, measurements through the flow field are necessary (e. g. [64, 102, 108, 124, 137, 143]). For these cases, optical disturbances from windows and density gradients in the flow field have to be considered. The effects of the window can usually be mitigated by calibration, but the effects of the flow field can be hard to quantify for all relevant configurations. To address this issue, Spottswood et al. [150] compared DIC measurements on the back side of a structure, which was freely accessible, to measurements through the flow field, achieving good agreement. Experimenters without direct optical access placed rigid calibration objects (e. g. [64]) or reference marks (e. g. [143]) in the flow field to assess the influence of the flow field. For the present configuration, this approach is not possible because creating a calibration object that remains rigid under the conditions in L3K with flow on is not feasible. Marking the model surface poses additional challenges. The pattern has to withstand flow conditions and deformations of the wind tunnel model due to its heating, and also has to be well visible despite reflections from the heater.

### Digital Image Correlation at L3K

To use DIC in L3K, the following procedure was developed. Image pairs as shown in Fig. 3.4 were recorded using two Basler A504k cameras (1280 pixels × 1024 pixels monochrome) and Titanar 50 mm lenses. The surface pattern was applied using $TiO_2$ on one half of the panel. The other half was not marked in order to retain a clean surface for IR temperature measurements. Discrete markers were applied to position the initial coordinate system. The panel was illuminated by a blue LED (456 nm), for which the cameras were fitted with suitable band pass filters to reduce reflections of the heater on the model. The cameras were positioned at an angle of about 18°, which is limited by the windows of the wind tunnel test section and the model position. This resulted in a measurement volume of 295 mm × 200 mm × 200 mm. A sampling rate of 2 Hz during the wind tunnel run and 1 Hz for the cool-down phase was used. For later runs, the sampling rate was set to 10 Hz for model insertion to better resolve dynamic events.

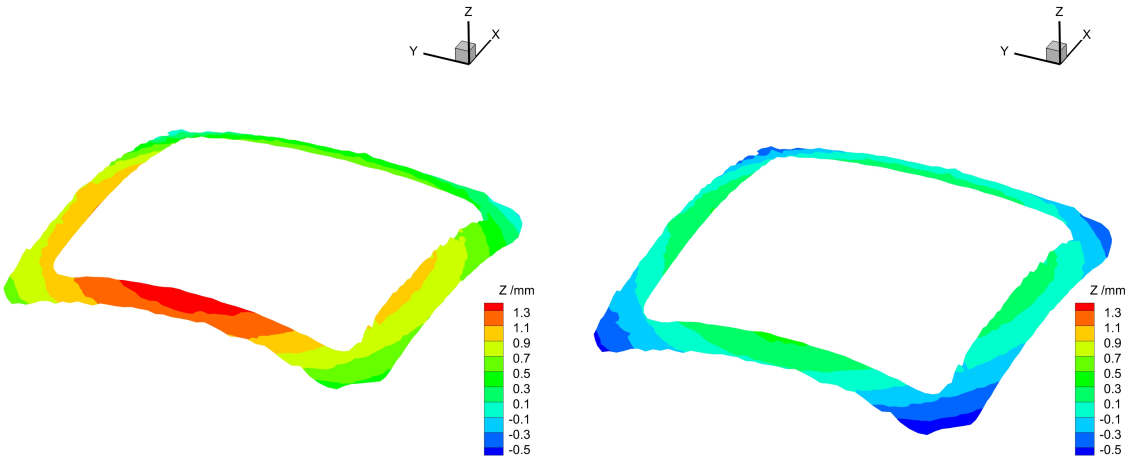


**(a)** Initial coordinate system **(b)** Corrected coordinate system

**Figure 3.5:** DIC measurement of the heated frame after 120 s (flow parallel to $x$-axis, deformation not to scale)

The calibration procedure was conducted using a GOM CP 20 175 mm × 140 mm reference object. It was placed at the position of the wind tunnel model so that the DIC system could be calibrated in a configuration identical to the wind tunnel run including the test section windows. Unlike during the wind tunnel run, calibration was performed under atmospheric conditions because the reference object had to be moved several times for the calibration procedure. Calibration was repeated before every experiment.

### DIC Data Analysis

The DIC software GOM Correlate Professional 2017 was used for image correlation and analysis. For computation of the surface deformation, the surface was divided into facets of 19 pixels × 19 pixels with a distance of 16 pixels so that there was a small overlap between the facets. The choice of facet size was based on a trade-off between spatial resolution, computation time, and reliability of facet recognition. 5.5 mm diameter round markers were used to obtain the position of the reference coordinate system.

The coordinate system was defined based on markers at known positions on the initially undeformed frame. Because of the frame deformation and movement of the wind tunnel model during the experiment, the coordinate system was corrected by the displacement of a plane fitted to the frame surface for each following image pair. In the uncorrected result (Fig. 3.5a), it can be seen that the corners of the frame deform in negative $z$-direction, while the frame generally moves in positive $z$-direction, which is more pronounced on the upstream part. The coordinate system for this plot remains at the initial position from before the wind tunnel run. Figure 3.5b shows the corrected version where the frame displacement is removed by the correction of the coordinate system. The deformation of the frame remains but is now nearly symmetrical. This process also removes any

**Table 3.4:** Measurement positions

| Designation | Position $(x/y)$ | Sensor |
|---|---|---|
| front | 50/0 | (DIC) |
| center | 100/0 | Micro-Epsilon ILD 1420-50 |
| rear | 150/0 | Micro-Epsilon ILD 1420-50 |
| left | 100/50 | Micro-Epsilon ILD 1420-50 |

**Table 3.5:** Laser triangulation measurement uncertainty during wind tunnel run

| Properties of ILD 1420-50 sensor | | Resulting uncertainty | |
|---|---|---|---|
| Range | 50 mm | | |
| Linearity | 0.08 % | $\Delta z_{lin}$ | 40 $\mu$m |
| Temperature stability | 0.015 % /K | $\Delta z_{temp}$ ($\Delta T_{sensor} = 15$ K) | 113 $\mu$m |
| | | $\Delta z_{abs}$ | 153 $\mu$m |
| | | $\Delta z_{rel}$ | 193 $\mu$m |

displacements in camera position, although this does not appear be significant for this setup.

### Deformation Measurement Uncertainty

To validate the results of the stereo-optic deformation tracking, Micro-Epsilon laser triangulation sensors ILD 1420-50 were used to measure the panel displacement from underneath the panel at three positions (Tab. 3.4). These sensors are relatively sensitive to temperature changes with a temperature sensitivity of 0.015 % of their range per Kelvin [7]. They have a maximum operating temperature of 50 °C. Therefore, the sensors were embedded in the insulation material shown in Fig. 3.3, and their temperatures were monitored throughout the experiments. Due to spatial constraints, the sensors were mounted at 90° towards the panel surface, similar to the setup used in [174] with mirrors with high IR transmission to reduce thermal loads, as suggested in [124]. The total uncertainty of the laser triangulation sensors mainly depends on the temperature change of the sensors during the wind tunnel run, which is typically around 15 K, and to a lesser extent on the linearity error of the sensors, which is specified by Micro-Epsilon to be smaller than 40 $\mu$m [7]. For relative measurements, the linearity error is taken into account twice. The temperature error is only considered once as the sensors operate at nominal temperature initially and heat up continuously during the course of the experiment. This amounts to a total uncertainty of approximately 0.2 mm (Tab. 3.5). Agreement between the DIC system and laser triangulation sensors is similar or in many cases better than the uncertainty of the laser sensors. Thus, the uncertainty of the DIC system can be estimated to be in a similar range or better.

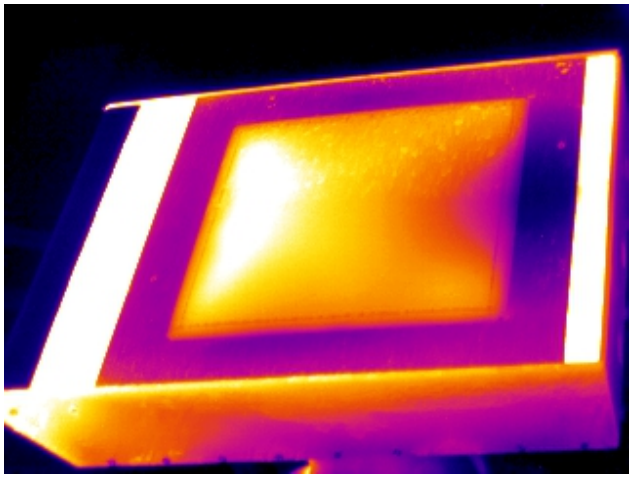

**Figure 3.6:** Example of an unprocessed IR image (flow left to right)

#### Surface Temperature

Surface temperature was measured using an AGEMA THV570 IR camera with a resolution of 320 pixels × 240 pixels and a sensitive wavelength range of 7.5 – 13 $\mu$m. The camera has a measurement uncertainty of 2 % of its range, which was set to 2000 °C. In a preparatory step, the emissivity of an Incoloy 800 H sample after pre-wind tunnel heat treatment was measured at various temperatures. An emissivity coefficient of 0.81 was thus used for the analysis of IR data. The transmission coefficient of the IR camera window was determined using a Landcal R1500T blackbody calibration source. Measurements with and without window were conducted, resulting in a transmission coefficient of 0.87. The temperature distribution measured by the IR camera was mapped to the deformed panel surface obtained from DIC measurements to allow spatially resolved analysis. The results were compared to pyrometer measurements using a Maurer KTRD 1485 at a wavelength of 0.85 – 1.1 $\mu$m and an uncertainty of 0.5 % of the measured value. Fig. 3.6 shows an example image before processing.

## 3.2 Results

The experiments were conducted with several panels with a thickness of 1 mm and 2 mm. After completion of a wind tunnel run and cool-down of the structure, the panels were either replaced or subjected to a second load cycle. The measured results are presented in time-series plots showing the development over time of the measured quantities at fixed locations given in Tab. 3.4, and in full-field contour plots for various time steps.

### 3.2.1 Heating

Figures 3.7a and 3.8a show the surface temperature on the model with a 1 mm panel and a 2 mm panel at designated locations as recorded by the IR camera and mapped

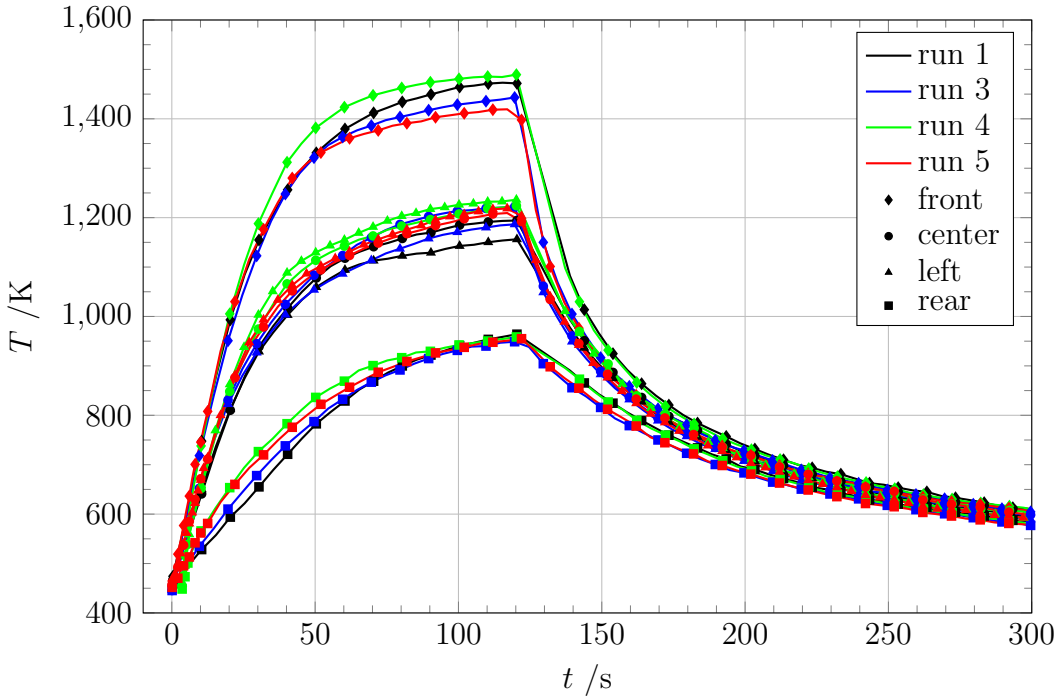


**(a)** IR camera measurements

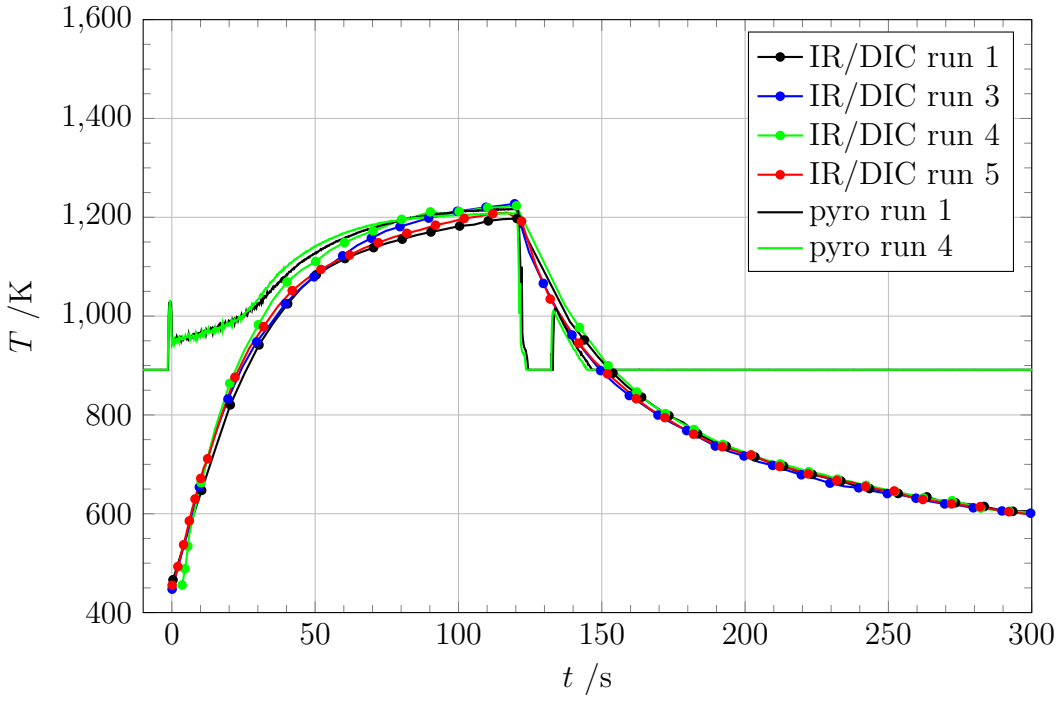


**(b)** Comparison to pyrometer (panel center)

**Figure 3.7:** IR camera measurements and comparison to pyrometer data – 1 mm panels

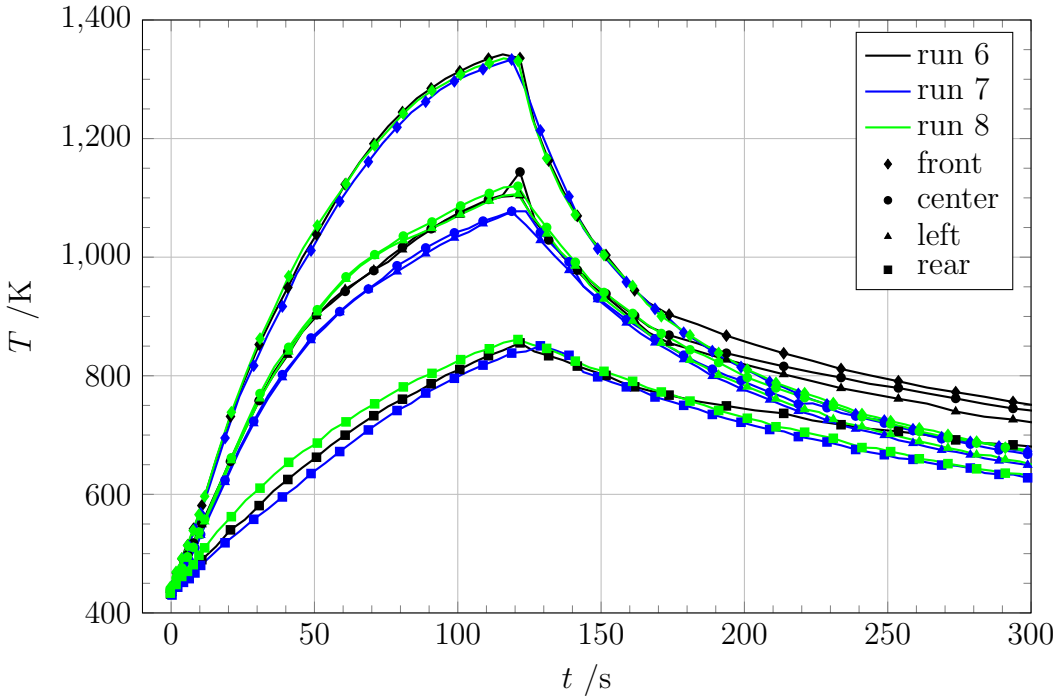


**(a)** IR camera measurements

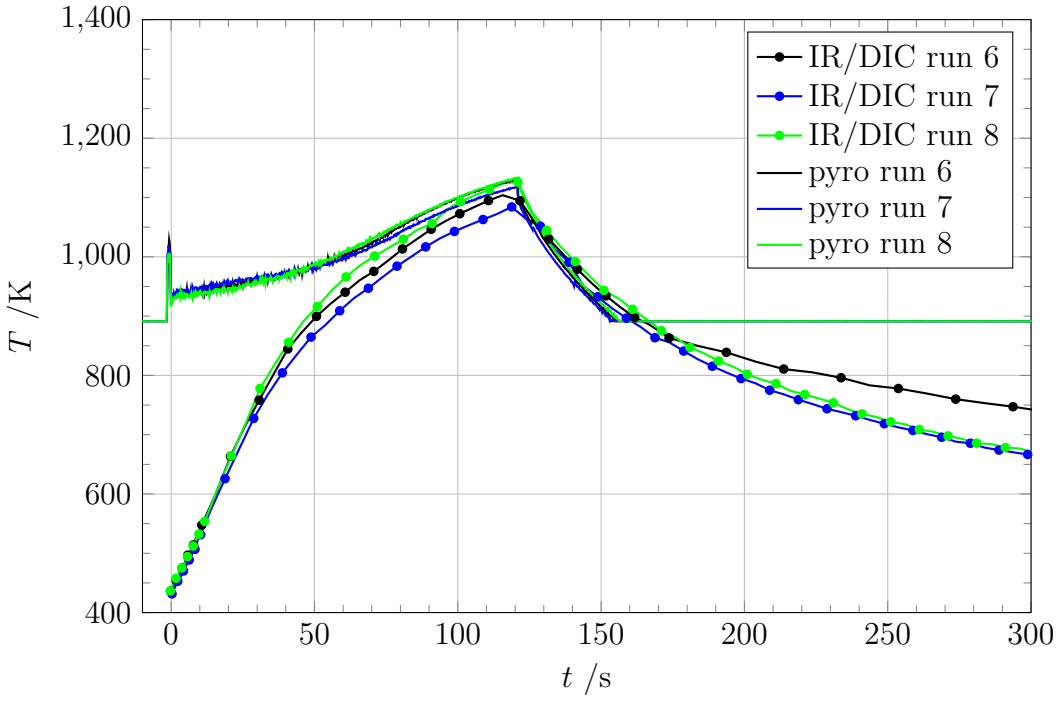


**(b)** Comparison to pyrometer (panel center)

**Figure 3.8:** IR camera measurements and comparison to pyrometer data – 2 mm panels

to the surface of the deformed panel. This procedure is important to look at the same position on the panel throughout the experiment regardless of large panel deformation. The strongest heating took place at the front position. The panels started heating up immediately after entering the jet. The temperature rose continuously but with declining rate of change during jet exposure until, in case of the 1 mm panels, steady-state surface conditions were nearly reached, whereas temperatures were still significantly rising for the 2 mm panels at the time of jet shut down. The fact that the temperature rise of the 1 mm panels does not fully subside towards the end of the run is most likely caused by the slowly increasing temperature of the frame that provides the boundary conditions for the panel. The model cooled down rapidly after the wind tunnel jet was turned off at 120 s. The test section remained evacuated after the heating phase and the model was kept at measuring position to observe cool-down of the structure with defined boundary conditions.

For comparison to the IR camera measurements, a pyrometer was placed aiming at the center location. The measurements of the IR camera and pyrometer at this location (Figs. 3.7b and 3.8b) show very good agreement. The startup behavior of the pyrometer at the beginning of the heating phase is typical for these sensors when measuring close to the lower end of their range and thus not taken into account for the comparison. Before the heating phase, the pyrometer indicates an artificial value of 873 K which refers to the lower end of its range.

### 3.2.2 Deformation

The deformation history is illustrated in Figs. 3.9 and 3.10. Data are plotted relative to the initial position of the panel for comparison between laser triangulation sensors and the DIC system. DIC system and laser triangulation measurements show very good agreement with differences of typically equal to or smaller than 0.2 mm for both 1 mm and 2 mm panels (Figs. 3.9a and 3.10a). The small change in measured distance at 120 s in Fig. 3.9a occurs when the model is quickly rotated out of the flow field for flow shutdown.

After the beginning of the heating phase, 1 mm panels (Figs. 3.9a and 3.9b) buckled into the flow quickly and continued with a declining rate of change until reaching maximum deformation after about 60 s. The subsequent small decline in deformation of the 1 mm panel was caused by the heating and resulting deformation of the frame as shown in Fig. 3.5 while the panel was close to reaching an equilibrium state. This should be taken into account when defining boundary conditions for coupled simulation. The 2 mm panels (Figs. 3.10a and 3.10b) similarly buckled into the flow immediately after the beginning of the heating phase and continued with a declining rate of change until the jet was shut off. The panels generally showed similar maximum deformation with about 1 mm difference between the highest and lowest measuring cases of the 1 mm panels (Fig. 3.9b). For the 2 mm panels, the deviations were even smaller (Fig. 3.10b). While the results for the 1 mm panels show good agreement at the center of the panel, differences of several millimeters on the left position occur that need further examination using the measured full-field data.

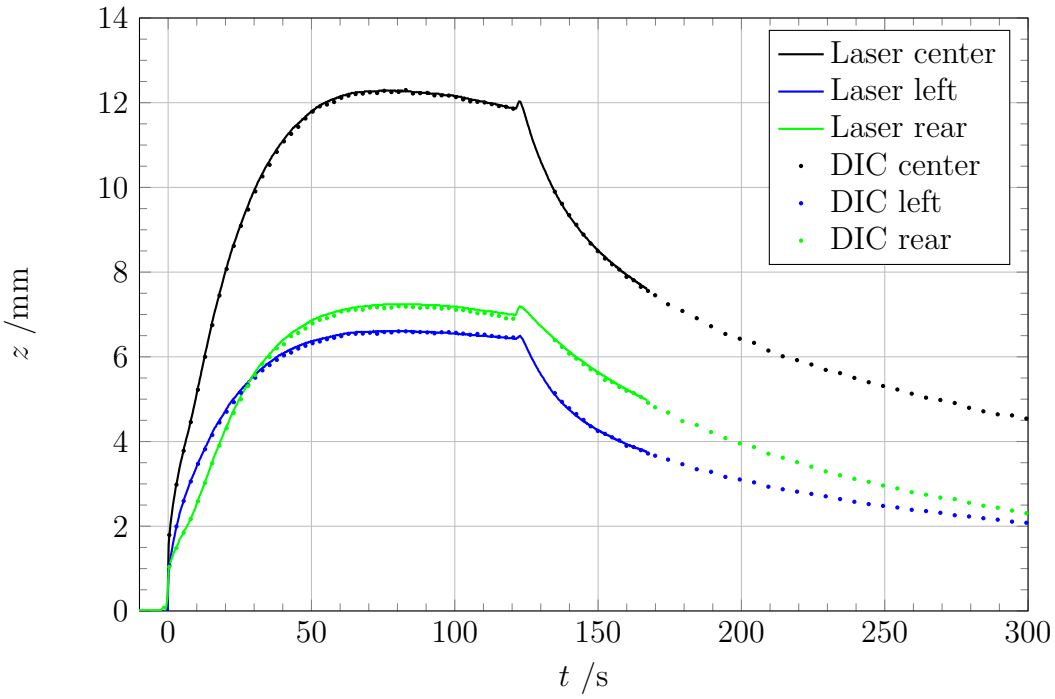


**(a)** Run 1

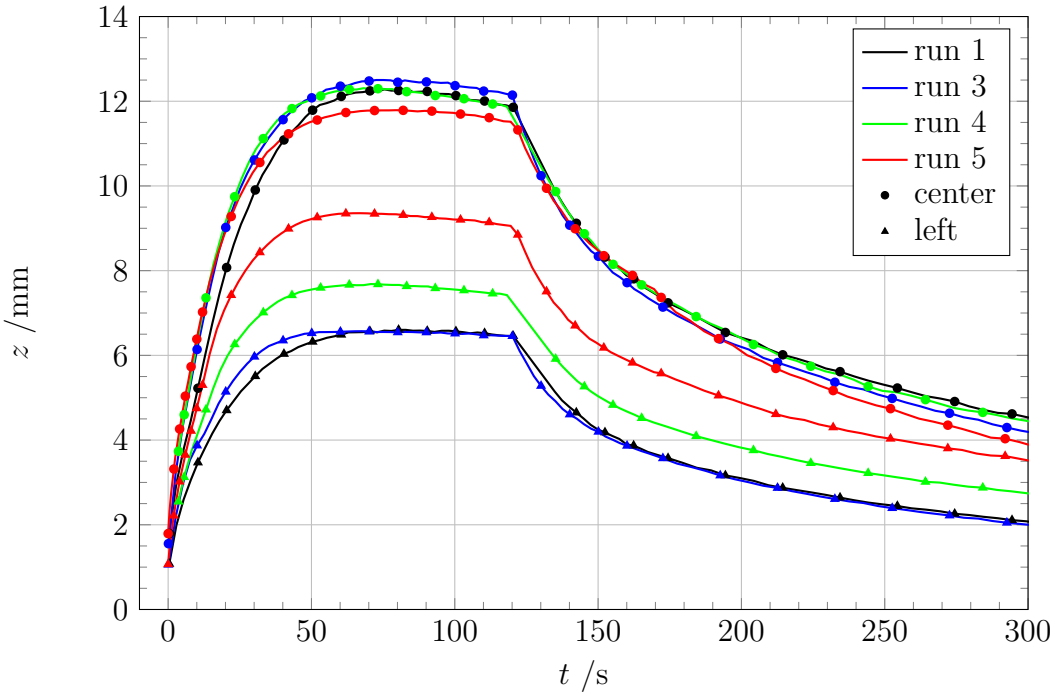


**(b)** Overview (DIC)

**Figure 3.9:** Comparison of DIC and laser triangulation measurements – 1 mm panels

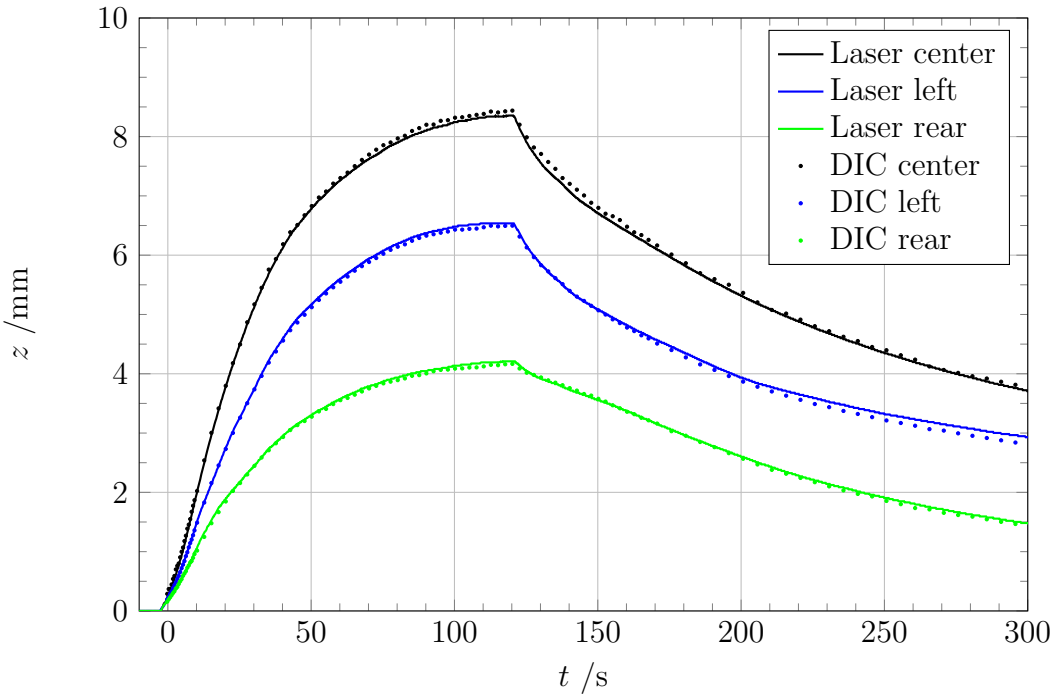


**(a)** Run 6

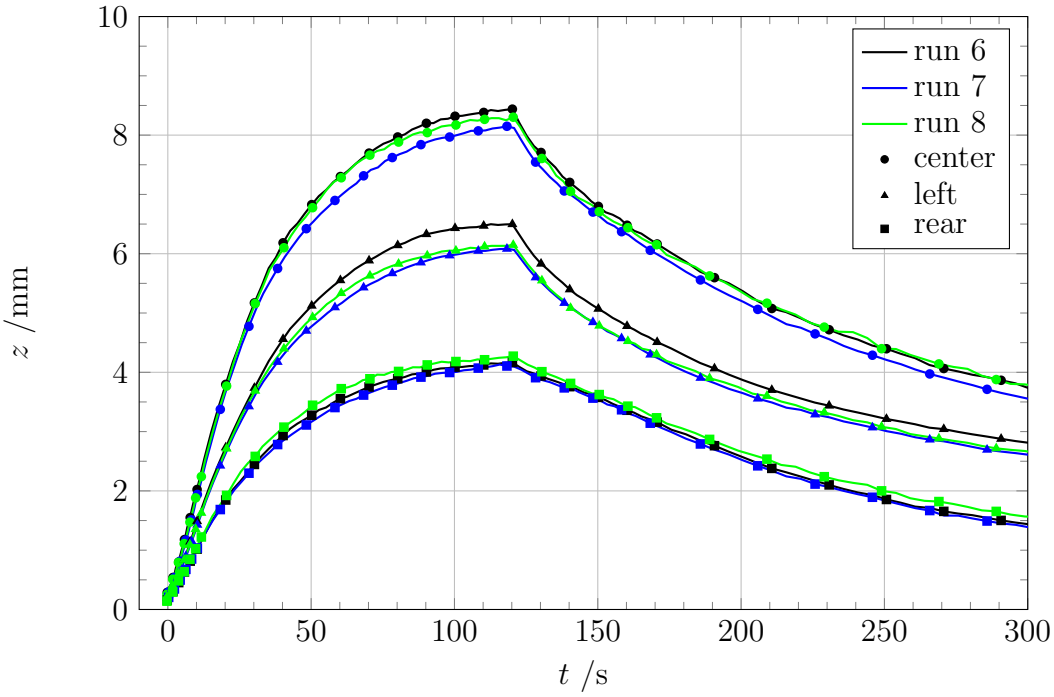


**(b)** Overview (DIC)

**Figure 3.10:** Comparison of DIC and laser triangulation measurements – 2 mm panels

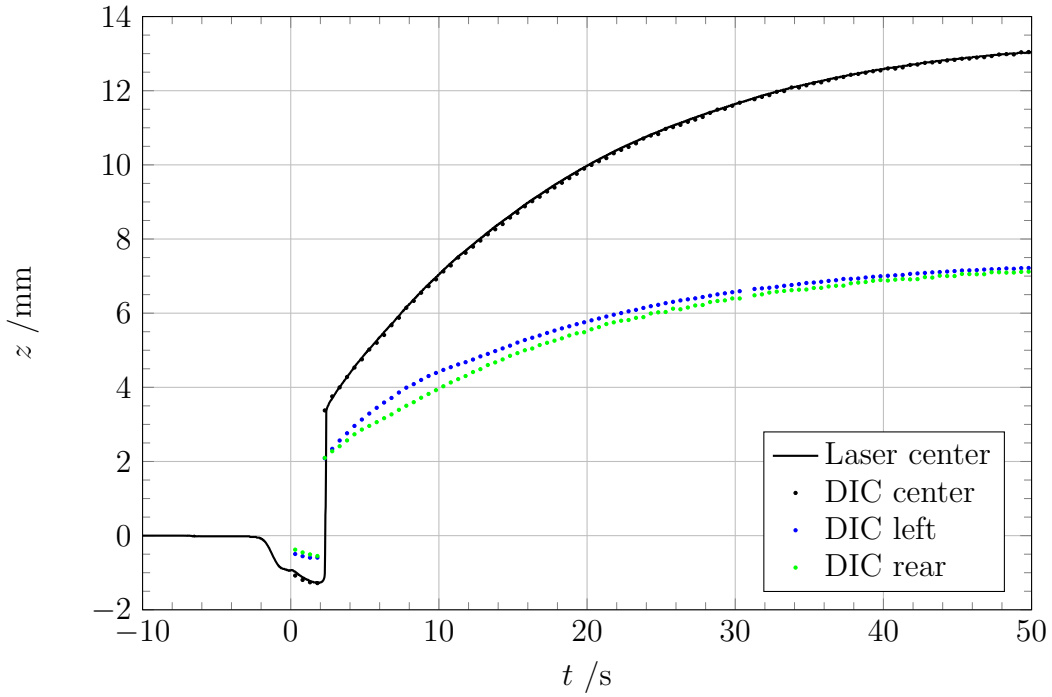


**Figure 3.11:** Anomalous behavior during run 2 – 1 mm panel

A particularly interesting case is shown in Fig. 3.11. After insertion into the wind tunnel flow, panel 2 quickly started to buckle away from the flow. A few seconds later, the panel snapped to a different buckling shape that was deformed into the flow field similar to the other panels, resulting in a very quick change of displacement in the panel center larger than 4 mm. In all other wind tunnel runs as well as in the simulations [113, 114], all panels deformed towards the flow field. This was expected since the heating from the flow field leads to a temperature gradient in the structure, resulting in a slightly larger expansion of the structure on the flow side. Panel 2 was about 0.1 mm smaller than the specified manufacturing tolerances. However, this does not explain the observed behavior. This example is probably not suitable for direct comparison to a coupled simulation, but it is an instructive demonstration of the system's sensitivity to small differences in initial conditions. These can result in highly dynamic events of significant amplitude.

### 3.2.3 Deformation and Temperature Fields

Figures 3.12 to 3.15 show the measured deformation and temperature fields on the surface of the panel. Isolines are included for better illustration of the gradients. Generally, the peak deformation occurred forward (upstream) of the center of the panel, deviating from the symmetrical deformation that would be expected of the same panel under a uniform temperature load. In the 1 mm case (Figs. 3.13a and 3.13b), a relatively complex shape occurred compared to the 2 mm panel (Figs. 3.15a and 3.15b), which might be connected to the lower deformation of the 2 mm panels.

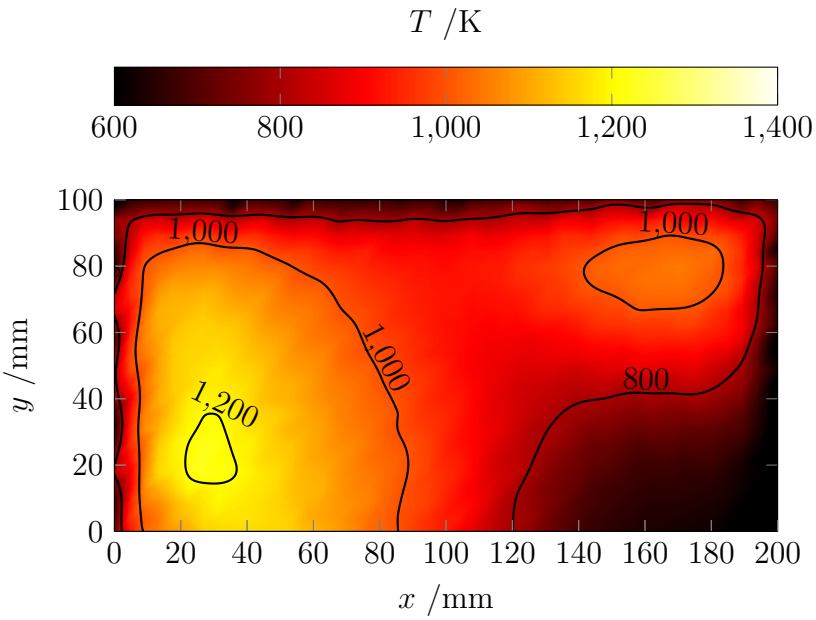


**(a)** Temperature at 30 s (Run 1)

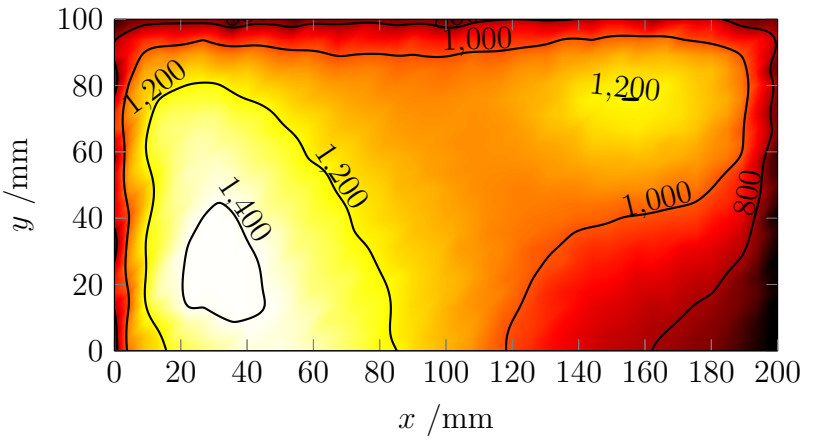


**(b)** Temperature at 60 s (Run 1)

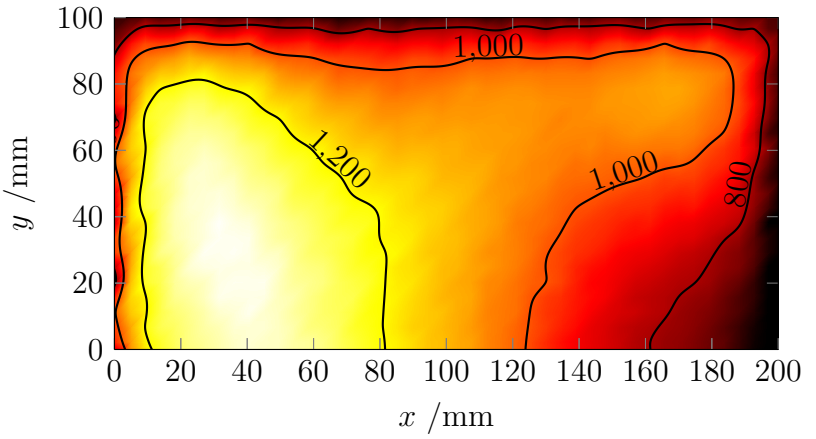


**(c)** Temperature at 60 s (Run 5)

**Figure 3.12:** Surface temperature distribution – 1 mm panels

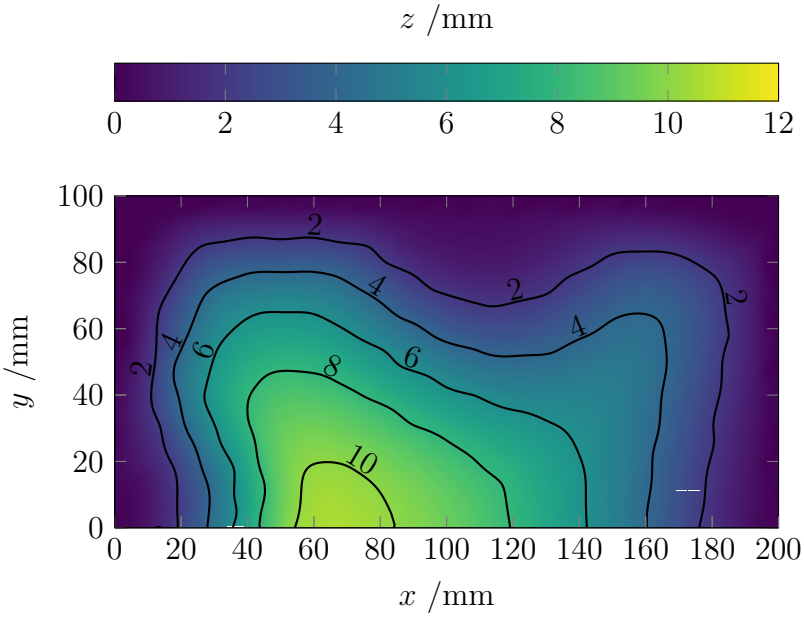


**(a)** Deformation at 30 s (Run 1)

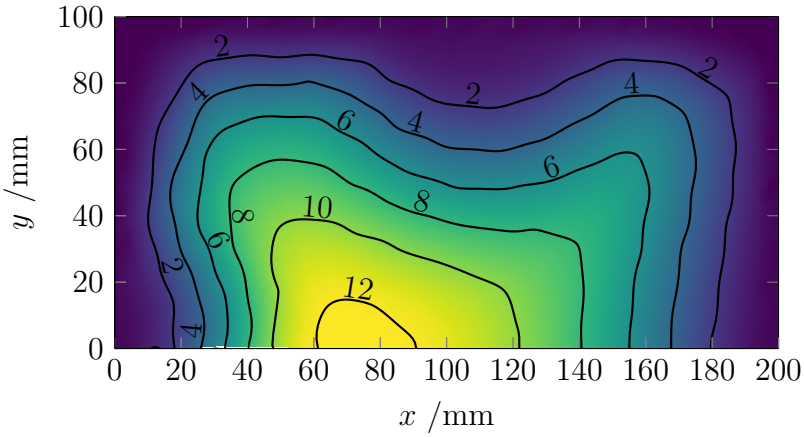


**(b)** Deformation at 60 s (Run 1)

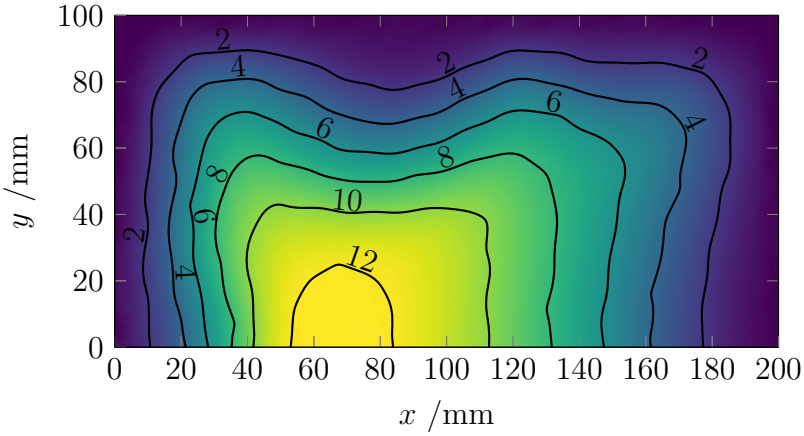


**(c)** Deformation at 60 s (Run 5)

**Figure 3.13:** Surface deformation contour – 1 mm panels

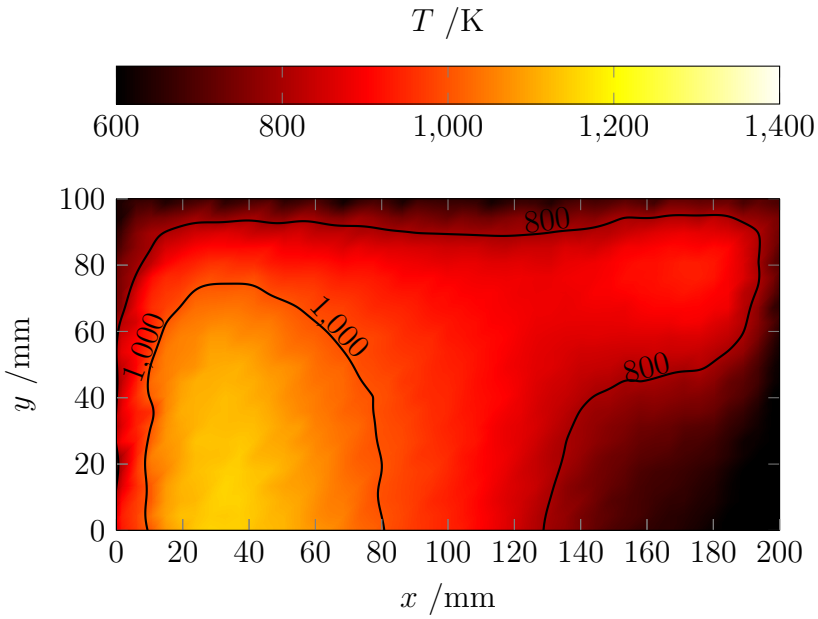


**(a)** Temperature at 60 s

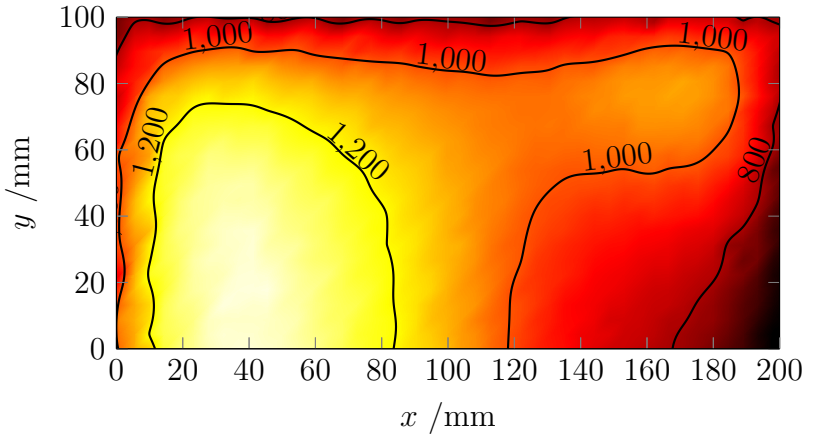


**(b)** Temperature at 120 s

**Figure 3.14:** Surface temperature distribution for run 6 – 2 mm panel

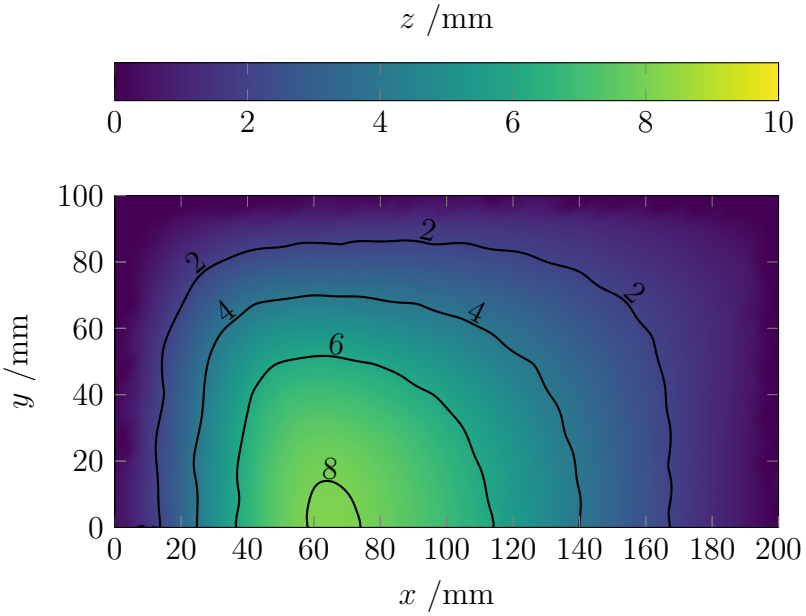


**(a)** Deformation at 60 s

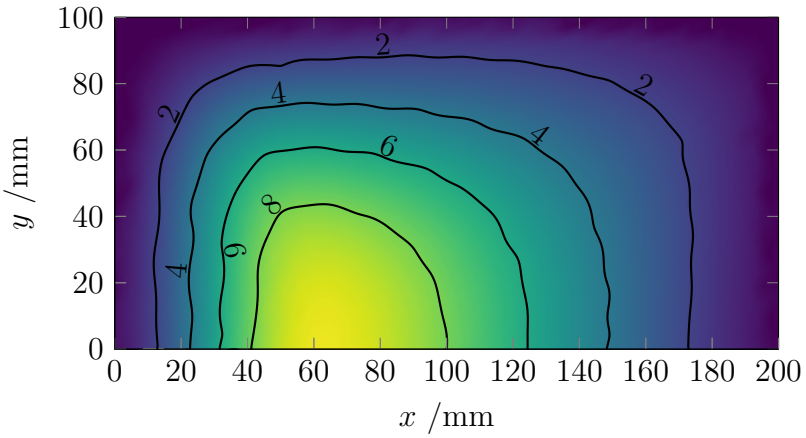


**(b)** Deformation at 120 s

**Figure 3.15:** Surface deformation contour for run 6 – 2 mm panel

The heating of the panels showed a maximum on the upstream side where the surface bends into the flow deviating from the heating expected of a rigid structure, for which heat transfer should continuously decline in the direction of the flow. The increase in local heating is caused by the deflection of the flow. For both panels, increased heating was observed on the downstream half at the side of the panels, while they remained colder on the centerline. Heating was generally stronger on the 1 mm panels where the occurring deformations were larger.

As noted in the previous paragraph, Figs. 3.13b and 3.13c show that some variation occurred in the deformation shape of the 1 mm panels. Agreement on the centerline is good, but the deformation isolines (especially for 10 mm) on the side of the panel run mostly in parallel to the centerline for run 5 (Fig. 3.13c), whereas they show a gradient towards the centerline for run 1 (Fig. 3.13b). This behavior is more distinct in the surface displacement, but small differences that are connected to the differences in deformation are also noticeable in the temperature distribution on the surface (Figs. 3.12b and 3.12c). Measurements of the panel dimensions after manufacturing were very similar for both panels. In both cases deviations from the nominal 200 mm length of the sides were about −0.1 mm and thus do not explain the differences. Furthermore, no influence of the direction of rolling of the sheet metal could be seen in metallographic analysis, which was expected after the heat treatment conducted prior to the experiment.

### 3.2.4 Response to Multiple Load Cycles

In addition to the effects discussed in the previous sections, the response of the panels to repeated load cycles were investigated. The panels remained in the facility until the model was fully cooled down to ambient temperature. Then, the complete run was repeated with the same panel. Interestingly, it was found that the maximum deformation remained almost the same with a slight increase towards the end of the run for the 1 mm panels (Fig. 3.16a). Maximum deformation decreased for all 2 mm panels (Fig. 3.16b) by about 0.7 mm in the center and about 0.5 mm at the rear position with good agreement between the panels. Furthermore, one of the 1 mm panels (run 4.2) showed interesting dynamic behavior during cool-down at the rear position at about 200 s that it had not shown in the initial load cycle. The measured panel displacement very quickly changed by about 1 mm, similarly to what has been observed in Fig. 3.11. However, the panel used for run 5 showed very similar behavior in the first run but not in the second. This further underlines the difficulty of reliably predicting the behavior of real structures under such conditions. Figures 3.17a and 3.17b show the deformation contour during run 5.2 and 6.2 and can be compared to the respective plots in Figs. 3.13b and 3.15b that show data from runs 5 and 6. As indicated in Figs. 3.16a and 3.16b, there was an increase in deformation for the 1 mm panel and a decrease for the 2 mm panel, while the general shape remained very similar.

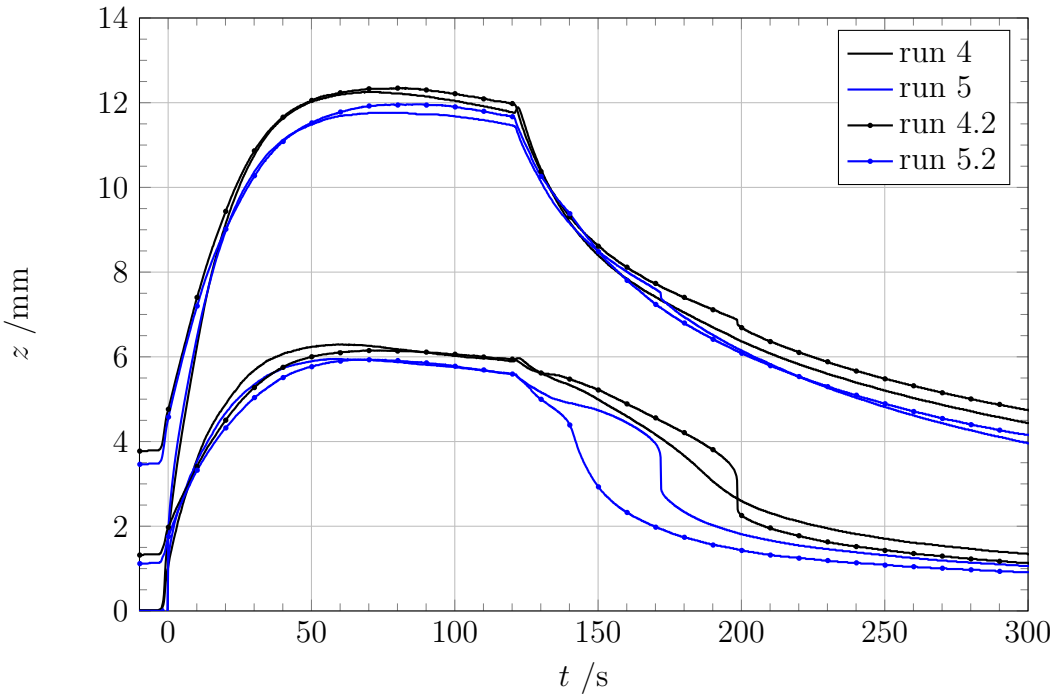


**(a)** 1 mm panels (center and rear position)

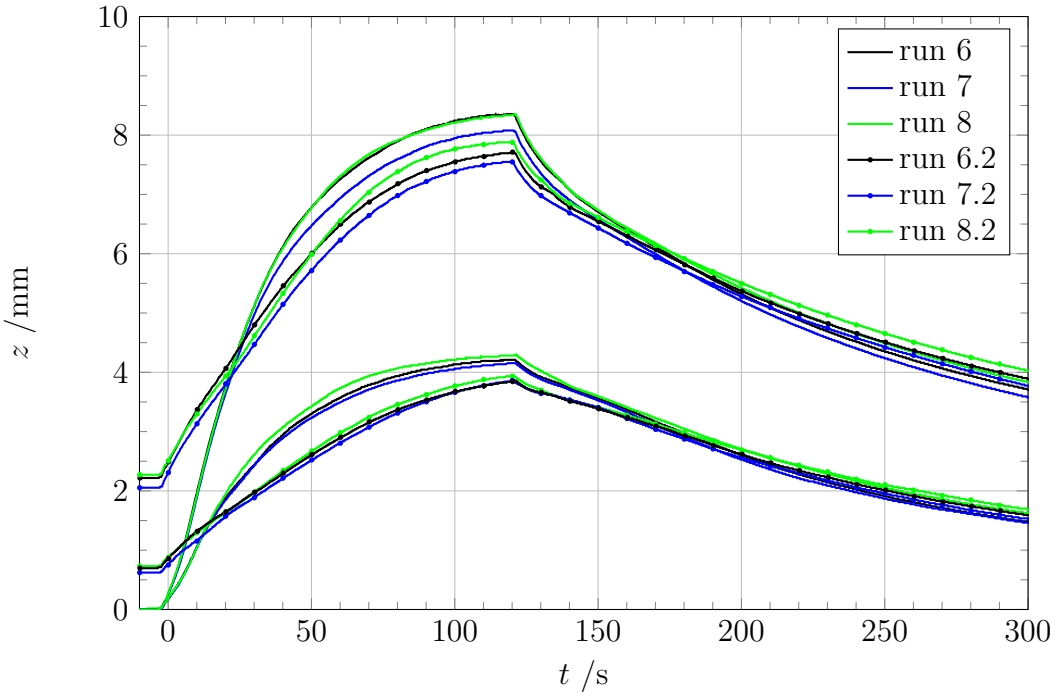


**(b)** 2 mm panels (center and rear position)

**Figure 3.16:** Deformation during second load cycle

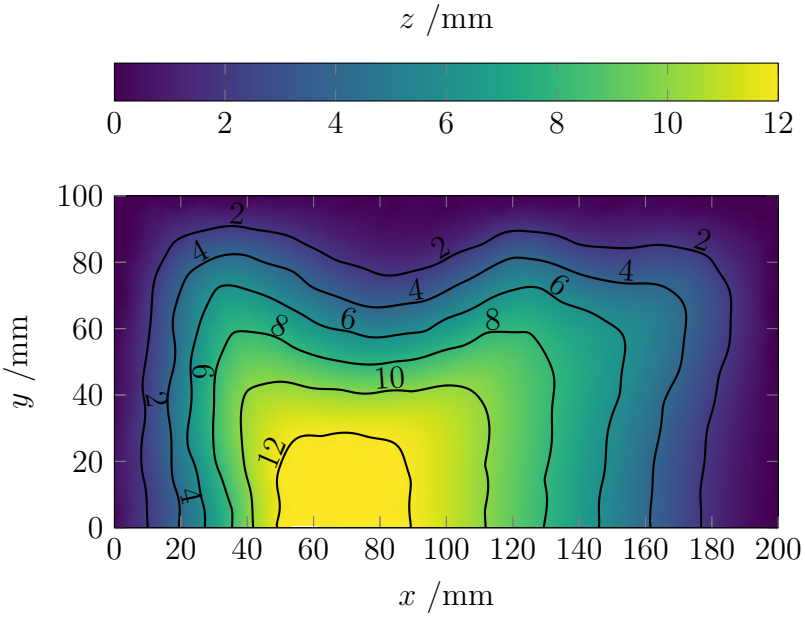


**(a)** Run 5.2 at 60 s

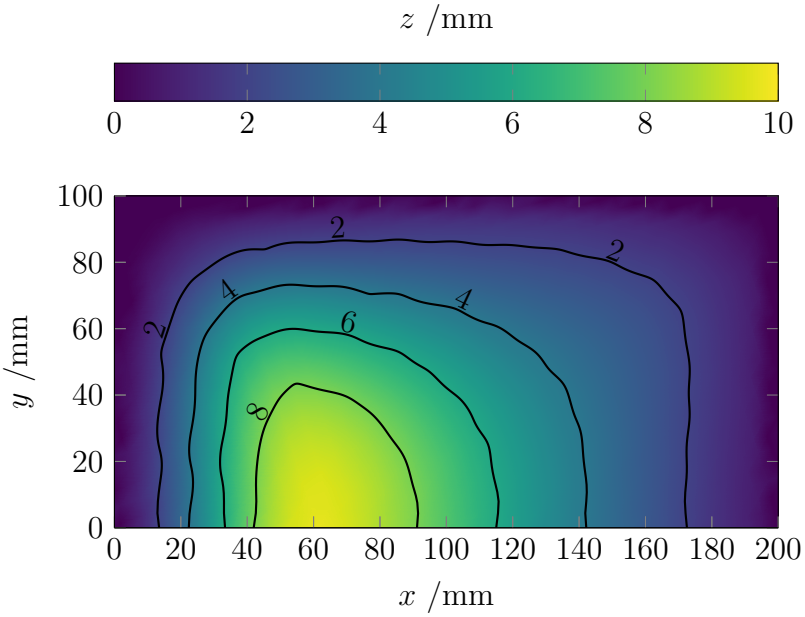


**(b)** Run 6.2 at 120 s

**Figure 3.17:** Deformation contours during second load cycle

## 3.3 Discussion

Adding to previous hypersonic wind tunnel experiments on heat flux augmentation of rigid spherical protuberances [57] and deformable structures in [73, 124], this work presents the first spatially and temporally resolved surface deformation and temperature data of an FSI experiment in an high-enthalpy flow field. In this challenging environment, both temperature and deformation measurements were validated using two independent methods to obtain each quantity. Deformations of up to 12 times the panel thickness were observed. In the experiments, aerothermal heating leads to structural deformation, which, in turn, leads to localized increases in heating and consequent non-uniform deformation. The maximum of both temperature and deformation is shifted upstream, demonstrating the effect of FSI and thus showing that coupled treatment of such problems is necessary. In this context, it is interesting to note that such temperature-dependent deformation of a structure also influences its dynamic properties which can be observed in the cases discussed in Chapter 4 or, for example, at lower $Ma$ in [150].

In one run, a panel started to deform away from the flow field and then snapped through to the deformation path also observed in the other runs. Such snap-through behavior warrants further study as it can very quickly change the properties of both structure and flow field. Similar quick changes in deformation were also observed during cool-down of two other panels. Such behavior can be, as shown here, predominantly dependent on the thermal state and mechanical properties of the structure, but can also occur in cases where unsteady pressure loads play a role in initiating a sudden change in deformation shape (e. g. [150]). Further studies in this area will greatly benefit from detailed thermomechanical characterization of structures as, for example, presented in [46]. Future research could also explore whether small design changes can be used to force deformation in a desired direction, e. g. away from the flow, which may reduce local heating.

Furthermore, the panels' behavior during a second load cycle was investigated. Despite differences of several millimeters in the initial conditions caused by the remaining plastic deformation from the previous run, only a small increase in maximum deformation for the 1 mm panels was found, whereas the maximum deformation for the 2 mm panels decreased under the same conditions. While this effect is modest over one repetition, deformation and potential damage may in some cases accumulate over a larger number of load cycles, as can be observed, for example, in FSI experiments and modelling for rocket combustion chambers [4, 80, 136]. Also, plastic changes of a structure have an influence on its dynamic properties that can have a drastic impact on lifetime estimates in cases with dynamic mechanical loads [103]. For example, imagine a structure that is repeatedly exposed to a full trajectory of a reusable launch vehicle that may also encompass load conditions similar to the experiments in Chapters 2 and 4.

Recent numerical simulations based on the present setup by Martin et al. [113, 114] generally show good agreement with the experimental results (Fig. 3.18). In the simulations, surface temperatures remain somewhat lower, and the maximum of the occurring deformation appears further downstream at similar amplitude. Interestingly, it was shown by a parametric variation of the inflow conditions, that if conditions are chosen

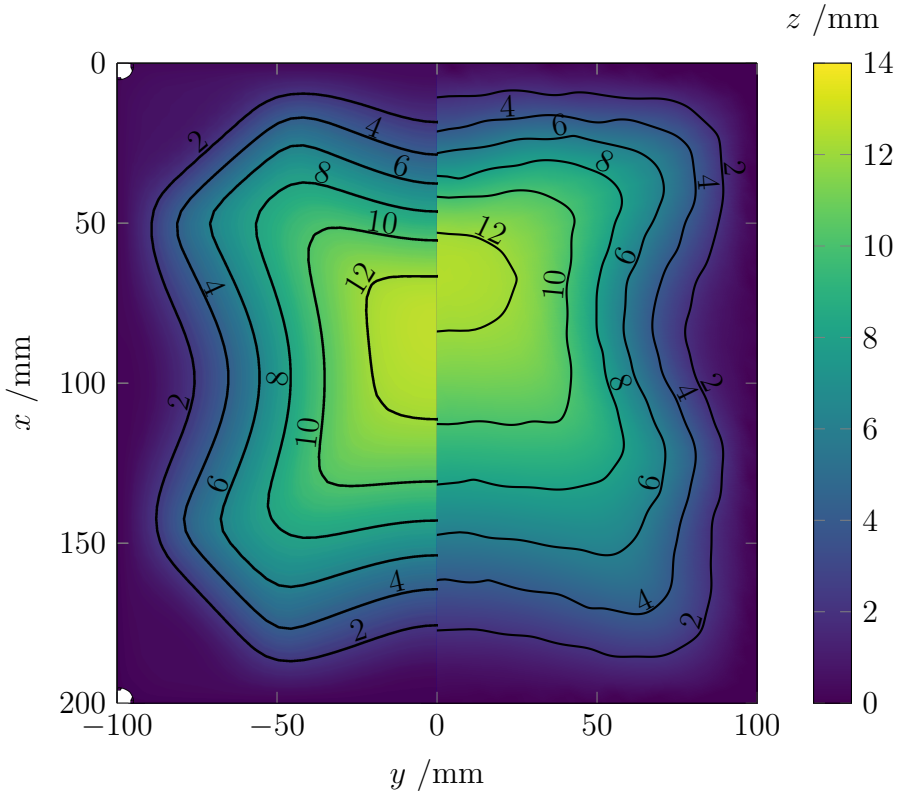


**(a)** Deformation

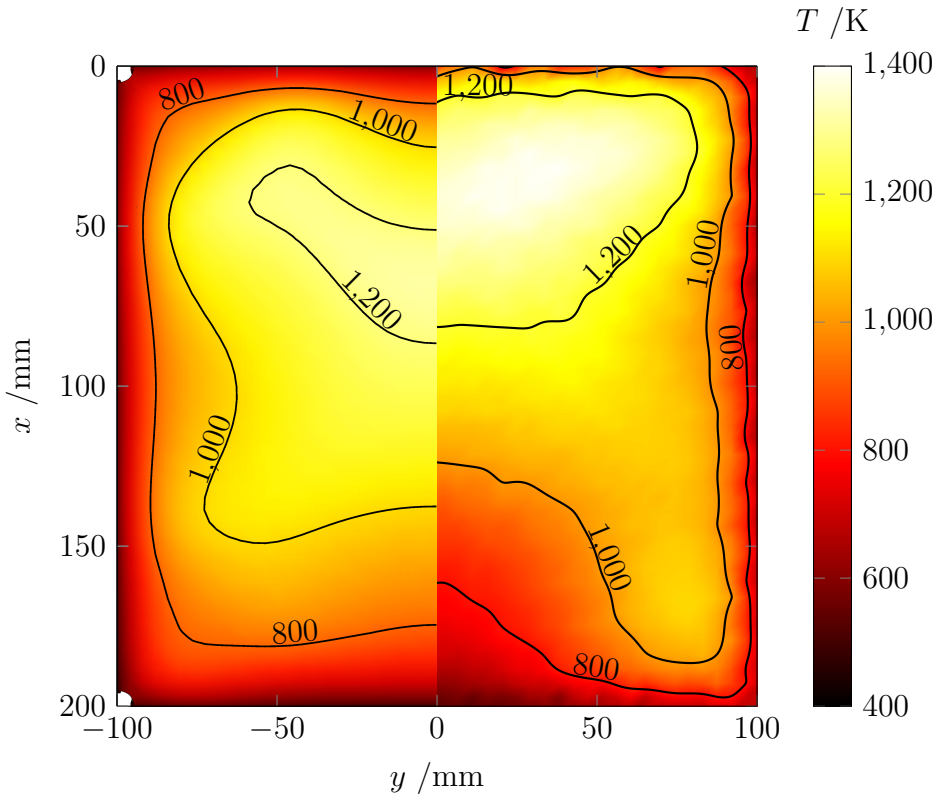


**(b)** Temperature

**Figure 3.18:** Comparison to numerical results by Martin et al. [114] – 1 mm panels (numerical results on the left)

so that the wall temperatures between experiment and simulation agree, this then leads to an upstream shift of the maximum of the deformation more closely resembling the experimental results. Thus, the main question arising from this comparison is why this difference in surface temperature occurs. The thermal and mechanical boundary conditions are potential sources of differences between experiment and model. The simulated model includes the full wind tunnel model, and thus the entire relevant substructure that could have a thermal or mechanical influence as well as internal radiative heat transfer [114]. To reduce potential differences in emissivity during the wind tunnel run, the panels were subjected to heat treatment before the first wind tunnel run of each panel. The emissivity of the panel was measured after this procedure and used for the simulations. However, small changes during the wind tunnel run may still occur. In previous studies in similar conditions for thermally coupled cases, it was shown that catalytic effects on the wall can lead to temperature changes in the same order of magnitude as the differences between the present experiment and simulation [138, 174]. However, catalytic effects were not considered in the present simulations. This could potentially account for the majority of the occurring differences and is subject to further investigation by addition of non-equilibrium chemistry including catalytic effects on the wall to the simulation.

# 4 Hypersonic FSI with Combined Thermal and Pressure-Driven Effects

This chapter contains experiments on combined thermal and pressure-driven FSI effects in hypersonic flow both with and without incident SWBLI. Severe dynamic effects were obtained, which even led to the failure of one panel. The results show a strong dependency of the dynamics of the coupled system on small temperature changes and the related buckling state of the structure. Also, the effect of the incident shock angle on panel dynamics was investigated. It was demonstrated that an incident shock can facilitate flutter in cases where it would not occur without incident shock, but also that it can prevent or reduce structural dynamics in other cases. Furthermore, the intricate interaction of structural dynamics and the dynamics of the SWBLI is of particular interest. Detailed reference experiments regarding aerothermal heating, wall pressure, and dynamic properties of the flow field were conducted using a rigid reference structure. This chapter is partly based on previous publications by the author [22, 28, 33], where the setup and initial results are presented. These results were extended by a further variation in panel thickness, inflow total temperature, and shock generator position, yielding a large extension of the resulting panel and flow dynamics.

## 4.1 Experimental Setup

### 4.1.1 Hypersonic Wind Tunnel H2K

The experiments were performed in the Hypersonic Wind Tunnel H2K at DLR, Cologne (Fig. 4.1, see [77, 125] for a detailed facility description). H2K is a blow-down facility with a free jet test section. The nozzle can be exchanged to vary the Mach number. Its exit diameter is 600 mm. Resistance heaters are used to adjust the total temperature. Maximum test time is about 30 s depending on flow conditions.

Flow conditions (Tab. 4.1) were chosen to obtain the maximum $Re$ available at $Ma = 5.33$. The flow conditions include a correction of $Ma$ depending on $Re$, which accounts for the boundary-layer thickness in the nozzle [125]. Free stream conditions were calculated from

**Table 4.1:** Nominal flow conditions

| $Ma$ | $p_0$ | $T_0$ | $p_\infty$ | $T_\infty$ | $u_\infty$ | $Re_\infty$ |
|---|---|---|---|---|---|---|
| 5.33 | 1250 kPa | 390 K | 1628 Pa | 58 K | 816 m/s | $19.3 \cdot 10^6$ /m |

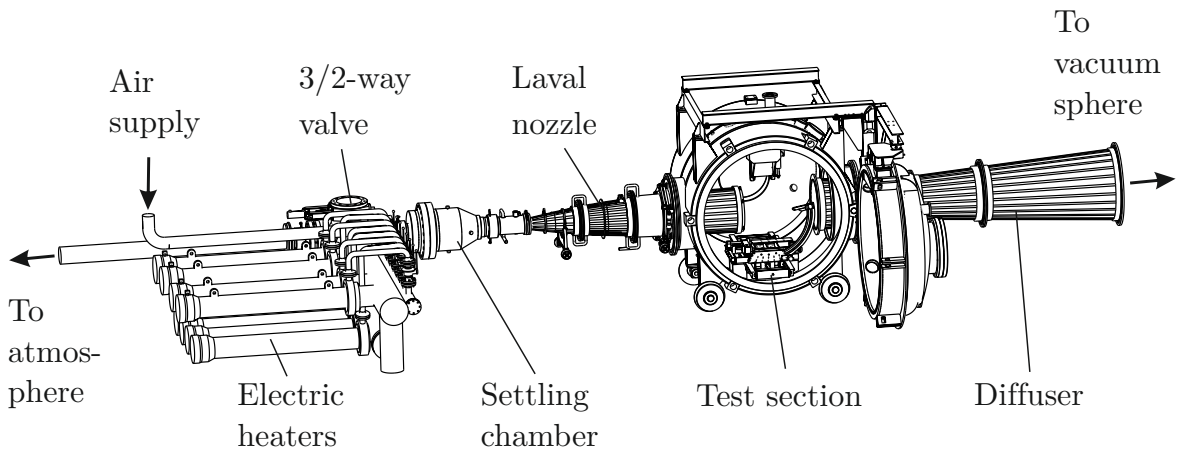


**Figure 4.1:** Hypersonic Wind Tunnel H2K at DLR, Cologne

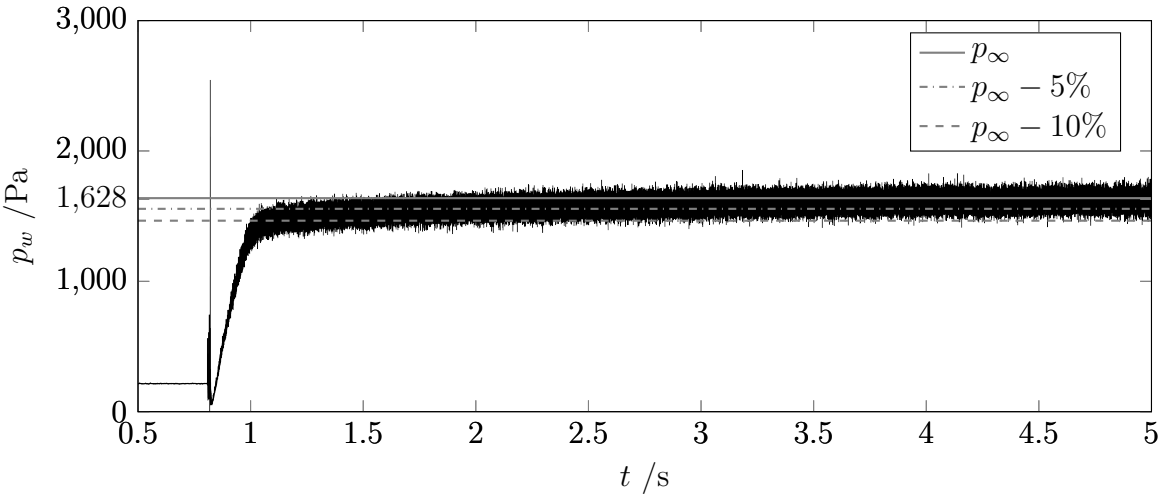


**Figure 4.2:** Wall pressure ($p_w$) during wind tunnel start

the measured total conditions using isentropic equations [47]. Viscosity was calculated using a power-law approximation for low temperatures [79]. The molar gas constant was used according to [15] and the mean molecular weight of dry air was used as stated in [79]. Small variations in total pressure and temperature occur between the wind tunnel runs. A table of the exact conditions for each run is given in Appendix A. The turbulent intensity in the undisturbed inflow was measured using Laser-2-Focus velocimetry and found to be about 1 % [178].

Before the wind tunnel run is started, the airflow is directed through the heaters and into an exhaust pipe. Only once nominal conditions are reached, the flow is redirected into the nozzle using the 3/2-way valve (Fig. 4.1). In this way, the flow in the test section is close to nominal conditions in about 0.2 s (Fig. 4.2).

## 4.1.2 Wind Tunnel Model

### Design of the Elastic Panel

Various options for manufacturing the elastic panels were considered. Machining the panel/frame assembly from a solid piece is beneficial due to the good connection of panel and frame [150], but manufacturing panels of the desired size and thickness was unsuccessful. Using adhesive to fix the panel to a frame is favorable because a high-precision panel can easily be obtained and its properties are not changed by the mounting procedure. The downside of this method is that the behavior of the adhesive, especially while undergoing temperature changes, would be challenging to model even if an adhesive sufficient for the desired temperature range could be found. Flush rivets as used in Chapter 2 and [174] require a certain panel thickness and are thus not suitable for very thin panels either. Considering these aspects, laser welding was chosen to manufacture the present set of panels. The laser was set to minimal power to obtain a good connection while keeping the induced stresses at a minimum. As the weld is warm on all sides during manufacturing and cools down afterwards, this procedure leads to a somewhat prestressed panel. The dynamic properties of the elastic panel are described in Section 4.1.4.

### Configuration

The elastic panel/frame assembly (Fig. 4.3a) was mounted in a flat plate with a sharp leading edge (Fig. 4.3b). The complete model was mounted inside the free jet test section of H2K (Fig. 4.4). Thus, well defined boundary conditions on the flow side are established as a new boundary layer forms, originating from the leading edge of the model. Note that unlike for the experiment in TMK described in Chapter 2, no boundary-layer tripping is applied. Furthermore, there is no influence on the flow field from side walls. Figure 4.4b shows a Schlieren image during a wind tunnel run to clarify the wind tunnel model configuration and basic properties of the flow field. The shock generator on top is removable and adjustable in height and angle towards the flow field ($\alpha$) as well as in axial position in flow direction (see Fig. 4.3b). For the present experiments, it was adjusted so that the nominal impingement point remains at the center of the exchangeable insert in the bottom wall ($x = 150\,\mathrm{mm}$) for the majority of the runs. Deviations are pointed out with the respective results. The wall insert always remains parallel to the direction of the undisturbed flow field. Both the shock generator and the lower wall have 20° leading edges. The elastic part of the exchangeable wall section begins 114.8 mm from the leading edge. The coordinate system is placed at this position with $x$ facing in free stream flow direction (Fig. 4.3b). Figure 4.3a shows the frame for flush mounting the elastic insert with a thickness of 0.3 mm. In this way, panels with a free surface area of 300 mm × 200 mm can be mounted. Panels made of stainless steel (1.4301) were manufactured with 0.3 mm, 0.5 mm, and 0.7 mm nominal thickness. The thickness of the panels was found to be 0.307 mm, 0.484 mm, and 0.687 mm. Total model width is 400 mm.

It should also be noted that the wind tunnel model, except for the elastic insert, is made of thick stainless steel of large thermal capacity. This means that, for the given

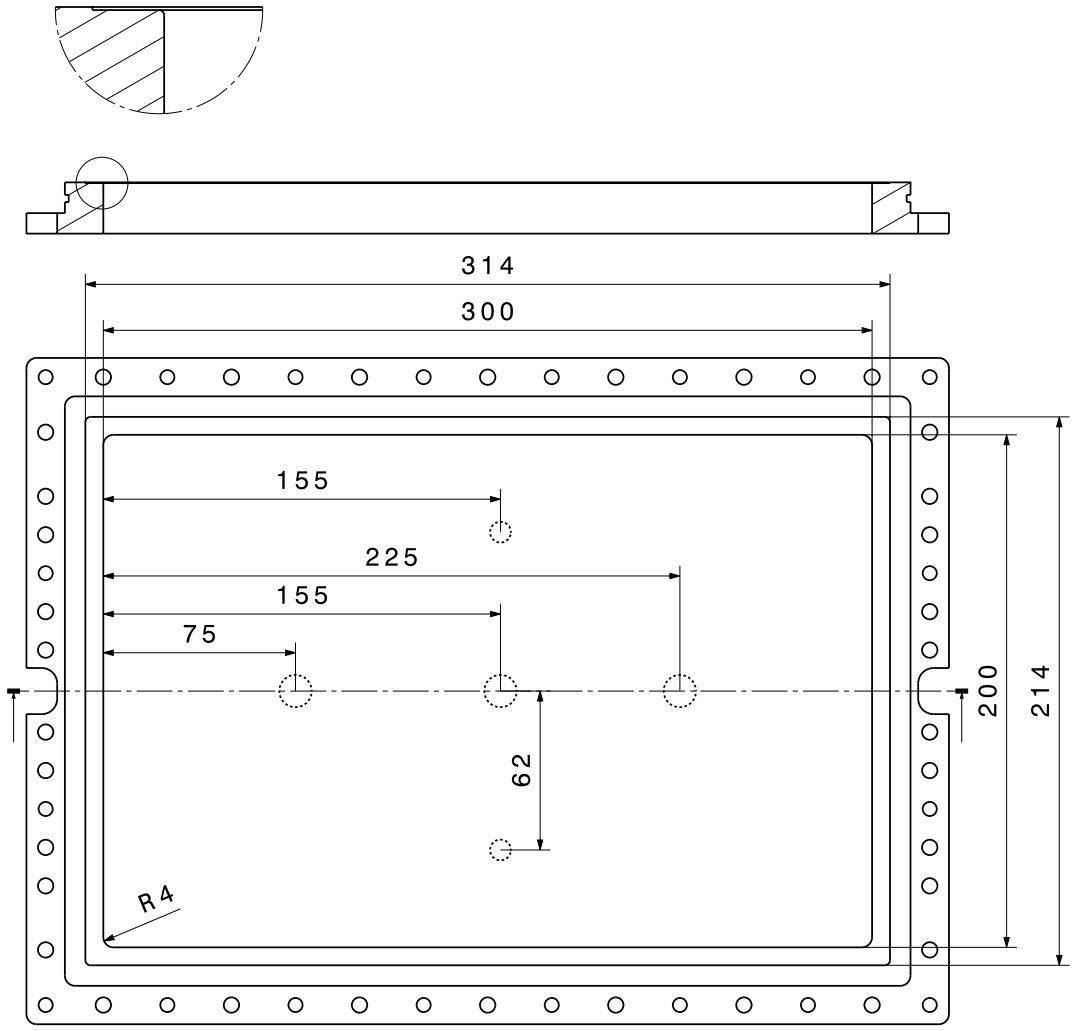


**(a)** Frame with elastic panel (0.3 mm version) and distance sensor positions (see also Tab. 4.5)

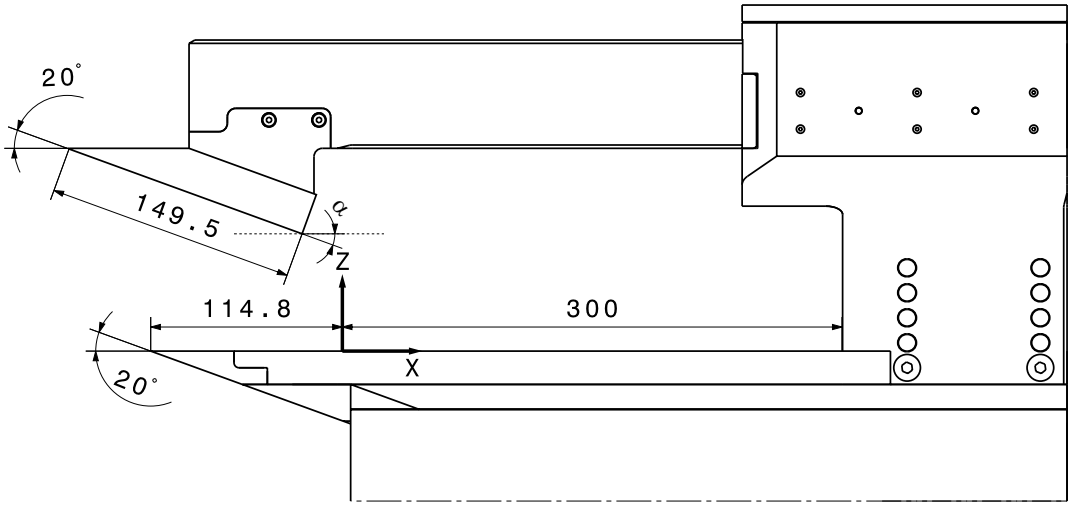


**(b)** Side view

**Figure 4.3:** Wind tunnel model geometry (all measures in mm)

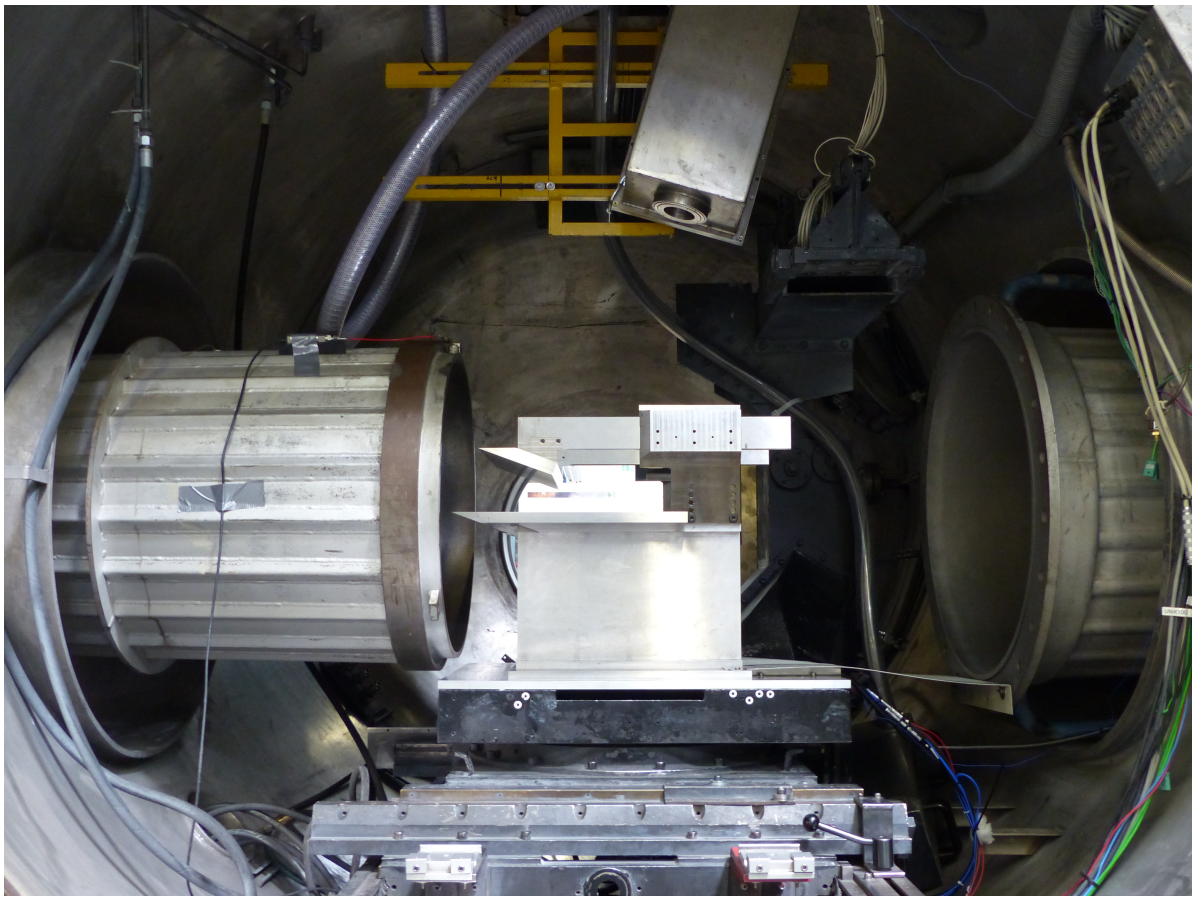

**(a)** Side view of the wind tunnel model in the H2K test section

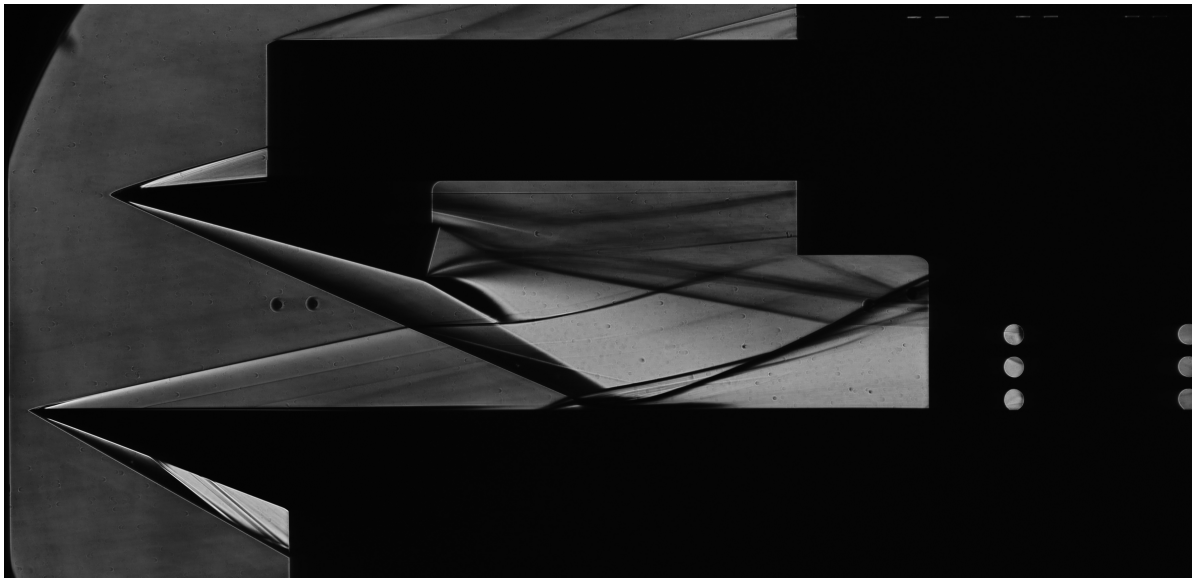

**(b)** Example Schlieren image

**Figure 4.4:** Experimental setup

**Table 4.2:** Uncertainty estimate of flow conditions upstream of the SWBLI at $Ma_\infty = 5.33$

| | $p_0$ | $T_0$ | $Ma_\infty$ | $\kappa$ | $\alpha$ | $p_w$ | $T_\infty$ |
|---|---|---|---|---|---|---|---|
| $i$ | 1250.0 kPa | 390.00 K | 5.33 | 1.400 | 0.00° | 1.628 kPa | 58.4 K |
| $\Delta i$ | 2.0 kPa | 1.56 K | 0.015 | 0.001 | 0.07° | — | — |
| $\Delta i/i$ | 0.16 % | 0.4 % | 0.28 % | 0.1 % | — | — | — |
| $\Delta p_i$ | 0.003 kPa | — | 0.027 kPa | 0.010 kPa | 0.016 kPa | 0.033 kPa | — |
| $\Delta p_i/p$ | 0.16 % | — | 1.7 % | 0.64 % | 0.96 % | 2.05 % | — |
| $\Delta T_i$ | — | 0.23 K | 0.28 K | 0.18 K | 0.16 K | — | 0.44 K |
| $\Delta T_i/T$ | — | 0.40 % | 0.48 % | 0.31 % | 0.27 % | — | 0.75 % |

**Table 4.3:** Uncertainty estimate of flow condition in the SWBLI at $Ma_\infty = 5.33$

| | $p_0$ | $T_0$ | $Ma_\infty$ | $\kappa$ | $\alpha$ | $p_w$ | $T_2$ |
|---|---|---|---|---|---|---|---|
| $i$ | 1250.0 kPa | 390.00 K | 5.33 | 1.400 | 20.00° | 12.56 kPa | 130.8 K |
| $\Delta i$ | 2.0 kPa | 1.56 K | 0.015 | 0.001 | 0.087° | — | — |
| $\Delta i/i$ | 0.16 % | 0.4 % | 0.28 % | 0.1 % | 0.43 % | — | — |
| $\Delta p_i$ | 0.02 kPa | — | 0.159 kPa | 0.097 kPa | 0.080 kPa | 0.204 kPa | — |
| $\Delta p_i/p$ | 0.16 % | — | 1.27 % | 0.78 % | 0.636 % | 1.63 % | — |
| $\Delta T_i$ | — | 0.52 K | 0.31 K | 0.72 K | 0.49 K | — | 1.06 K |
| $\Delta T_i/T$ | — | 0.40 % | 0.24 % | 0.55 % | 0.37 % | — | 0.81 % |

flow conditions, heating of the model itself is negligible. However, the thin elastic panel can heat up sufficiently to buckle against its cold frame, similar to the observations in Chapter 3, but at much lower temperatures.

### 4.1.3 Instrumentation, Uncertainty and Data Processing

#### Flow Conditions

Total pressure ($p_0$) and total temperature ($T_0$) were measured in the settling chamber (Fig. 4.1). The total pressure was measured using a GE UNIK 5000 with an uncertainty of 0.04 % of its range of 5 MPa. The total temperature was measured using a Type K thermocouple with an uncertainty of 0.4 % of the measured temperature. For unknown quantities, the uncertainty was obtained from an estimated range as suggested in DIN 1319 [35, 36]. The range of $\kappa$ was estimated based on tabulated values in [3, 106]. The range for wind tunnel model misalignment was based on values typically achieved during the mounting process. The uncertainty of the flow conditions given in Tabs. 4.2 and 4.3 was evaluated following [134, 174]. For each input quantity, the absolute value ($i$), the

**Table 4.4:** Thermal properties of the PEEK insert [6, 19]

| Ensinger TECAPEEK | |
|---|---|
| Density | $1310\,\mathrm{kg/m^3}$ |
| Heat capacity | $1100\,\mathrm{J/(kgK)}$ |
| Thermal conductivity | $0.27\,\mathrm{W/(mK)}$ |
| Emissivity | 0.95 |

absolute uncertainty ($\Delta i$), and relative uncertainty ($\Delta i/i$) were evaluated regarding their respective contribution to the wall pressure ($p_w$) and free stream temperature ($T_\infty$) or temperature downstream of an incident shock ($T_2$). These respective contributions were evaluated numerically and added using the variance formula[1]. As there is no analytic solution for the wall pressure in the SWBLI, the uncertainty is estimated based on the conditions after an oblique shock with a turn angle of $\alpha = 20°$ (Tab. 4.3).

### Rigid Reference Panel

A rigid Polyether ether ketone (PEEK) panel of 20 mm thickness, which could be inserted in place of the elastic panel, was used for reference measurements. The respective structural properties are given in Tab. 4.4. It was outfitted with PSI 1615B-TL pressure scanners connected to pressure ports to assess the static pressure distribution on the panel. Uncertainty for these sensors is 0.05 % of the 100 kPa range.

The surface temperature was recorded using an IR camera InfraTec ImageIR 8380 (640 pixels × 512 pixels, $2-5.7\,\mu$m) with a maximum frame rate of 100 Hz. The measurement uncertainty given by InfraTec for measurements below 372.15 K is 1 K. The geometrical properties of the system were calibrated using a GOM CP 20 reference object. The image position was thus corrected using the in-house tool Render Object Based Orientation Tracking (ROBOT) [175]. Heat fluxes into the wall were calculated using the in-house tool VisualHeatflow [75], assuming one-dimensional heat flow in wall-normal direction. The lower wall of the rigid panel facing into the cavity was assumed to be adiabatic. For comparison, Stanton numbers for a laminar and turbulent boundary layer were computed using the correlations given in [96]. Prandtl number and recovery factor were chosen according to [79].

### Elastic Panel

The elastic panels were instrumented with several non-intrusive distance sensors placed underneath the panel. Three capacitive distance sensors CS5 and two CSH2FL by Micro-Epsilon were used with Micro-Epsilon capaNCDT 6350 amplifiers, enabling measurements at 50 kHz (−3 db). The maximum operating temperature of the sensors is 200 °C with a temperature sensitivity of −160 nm/K. Thus, no relevant effect of the sensor temperature

[1] in German referred to as Gauß-Verfahren

**Table 4.5:** Displacement sensor positions

| Sensor Type | Position | $x$ /mm | $y$ /mm |
|---|---|---|---|
| CS5 | front | 75 | 0 |
| CS5 | center | 155 | 0 |
| CS5 | rear | 225 | 0 |
| CSH2FL | left | 155 | 62 |
| CSH2FL | right | 155 | −62 |

on the distance measurements is expected. The non-linearity of the sensors is smaller than 12 $\mu$m for the CSH2FL used with 4 mm range, and smaller than 15 $\mu$m for the CS5 with 5 mm range. For the runs where measurements exceeded 5 mm, the range of the CS5 sensors was doubled, also doubling the non-linearity estimate. The uncertainty caused by non-parallel orientation of the sensor and the target surface were provided by Micro-Epsilon [179]. Based on this, an uncertainty of 9 $\mu$m has to be added for cases with significant panel deflection. The sensor positions are listed in Tab. 4.5 and also shown in Fig. 4.3a.

The PSD of the measured deformation was calculated following Welch's method [168], using Hann windows, a block length of 10000 samples, and an overlap of 0.5, resulting in a frequency resolution of 5 Hz. For the spectrograms, the PSD was averaged for 5 blocks with an overlap of 0.6, resulting in a time step of 0.2 s.

Two GE UNIK 5000 pressure sensors with 10 kPa and 20 kPa range were used to measure the pressure inside the cavity underneath the panel with an uncertainty of 0.4 % of their respective range, allowing measurements at up to 5 kHz.

### Flow Field

Special attention was given to the Schlieren optical system. Previously, a coincident Schlieren system was used at H2K. This system was designed for maximum sensitivity but has some drawbacks regarding sharpness of the images and two-dimensional configurations. For example, images obtained with that setup with a preliminary version of the present wind tunnel model are shown in [20]. Thus, the system was replaced by a newly built Z-type setup with 600 mm diameter mirrors with 6 m focal length (Appendix B). To facilitate short duration imaging, the FASTCAM SA-X2 high-speed camera was outfitted with a 290 ns shutter. Due to the free jet test section of H2K, the present setup does not suffer from a distortion of the flow field caused by the wind tunnel walls, which obstructs the view of the test section center in similar setups (e. g. Chapter 2 and [135]), complicating the analysis of the flow field. Images were recorded at 10 kHz to resolve effects of structural dynamics on the flow field as well as low-frequency dynamics of the SWBLI. The analysis was conducted similarly to [5, 91, 92, 155], calculating the PSD of the grey scale value ($I$) for each pixel using Welch's method with Hann windows, a block length of 1000 samples, and an overlap of 0.5, resulting in a frequency resolution of 10 Hz.

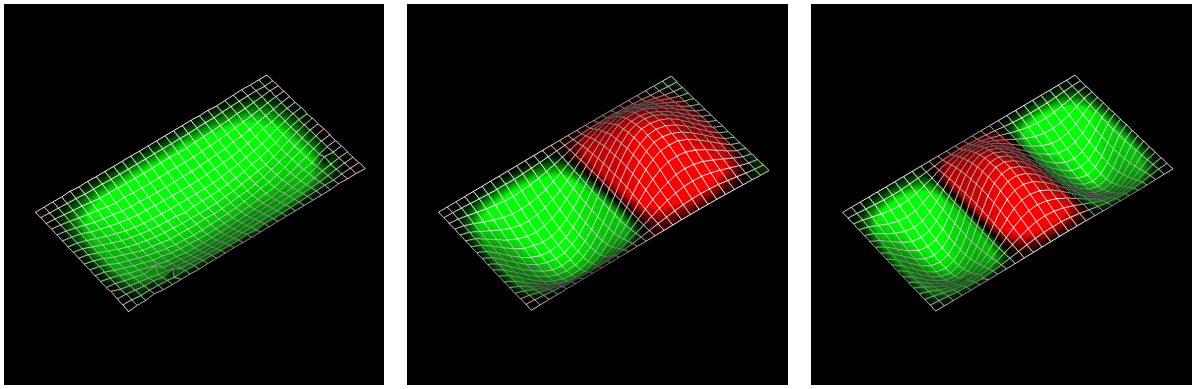

**(a)** 255 Hz **(b)** 341 Hz **(c)** 436 Hz

**Figure 4.5:** Examples of measured modes of the 0.7 mm panel without flow (amplitudes not to scale)

This method has been shown to achieve good agreement in comparison to measurements of structural displacement of an elastic structure regarding the lower panel modes [33]. A different approach has previously been pursued for a similar configuration in [31, 174, 177], tracking various shocks appearing in the flow field and using these measurements for further analysis. This approach works well with Schlieren images (e. g. Fig. 4.4b). For the high-speed recordings with the present setup, high-speed shadowgraph images were recorded without a cut-off, which brings out the shocks less drastically, but allows a better view of most of the SWBLI area. Furthermore, it simplifies setting up the system consistently throughout several measurement campaigns, improving comparability of the images.

### 4.1.4 Properties of the Elastic Panel

#### Dynamic Properties

Prior to the wind tunnel runs, the properties of the elastic panel were investigated using an automatic impact hammer Maul-Theet vlimpact-60 equipped with a force sensor and a Maul-Theet ScanSet. This system is equipped with a laser Doppler velocimeter OptiMet Nova that allows measurements of the surface velocity at multiple locations in order to obtain eigenfrequencies of the panel and respective mode shapes. Exemplary results are shown in Fig. 4.5. Furthermore, in addition to the described prestress of the panels from the welding procedure, we found an influence of the panel mounting on the eigenfrequencies of the panel.

An ANSYS FEM model was set up to support this assumption and analysis of the measured panel dynamics. The edges of the panel were considered clamped and the prestress was adjusted using the measured eigenfrequencies of the panel after the final mounting in the wind tunnel. A density of 7900 $\mathrm{kg/m^3}$ and an elastic modulus of 200 GPa were used. The result was compared to the measured eigenfrequencies of the

panel after the final mounting in the wind tunnel. Results and discussion are included in Sections 4.2.2 and 4.2.3. Calibrating a structural model with measured results is often necessary for similar setups [55, 150].

#### Effects of the Cavity

In addition to the wall pressure on the side of the panel that is exposed to the flow, the pressure underneath the panel is an important boundary condition. A pressure difference across the panel leads to deformation and induces stresses that influence mean deformation and structural dynamics (e. g. [10, 174]). For the present experiments, the pressure in the cavity is always set to the average static wall pressure obtained from measurements on the rigid reference panel (see Section 4.2.1). This avoids large prestress and deformation of the panel, that limited panel dynamics in previous experiments in TMK (see Chapter 2 and [174]). The pressure was set before wind tunnel startup and the cavity underneath the panel remained sealed throughout the run. During some initial runs, small leakage occurred most likely along the cabling of the instrumentation in the cavity. However, the leakage did not appear to have a detectable influence which was discussed at length in [33]. This concerns only runs 24 – 26 (Section 4.2.2). Furthermore, the cavity itself can have an influence on the panel dynamics [42]. A calculation for a cavity of the same size for various pressure levels and reference experiments are provided in [174], showing that no significant effects are expected for the present configuration for small deflections because of the low cavity pressure. For large panel deflections, the cavity may have to be included in simulations. The volume of the cavity is $0.0022\,\mathrm{m}^3$.

## 4.2 Results

First, experiments with the rigid reference insert were conducted to obtain data on wall pressure, flow field dynamics, and structural heating for various shock generator angles and without shock generator. Following these experiments, elastic panels were installed to study FSI with and without shock generator. The effects of variations of the inflow temperature, shock generator angle and position as well as panel thickness were investigated. A broad range of structural responses was obtained including thermal buckling, flutter, and SWBLI-dependent dynamics.

### 4.2.1 Reference Measurements on the Rigid Insert

#### Wall Pressure

Figures 4.6 and 4.7 show time-averaged wall pressure measurements on the rigid wall for various shock generator angles on and off the centerline. As expected, the maximum pressure rises with increasing shock generator angle. In lateral direction, the pressure measurements at $y = 90\,\mathrm{mm}$ show good agreement with the measurements on the centerline, confirming that the flow field is nearly two-dimensional in the area of the insert. For

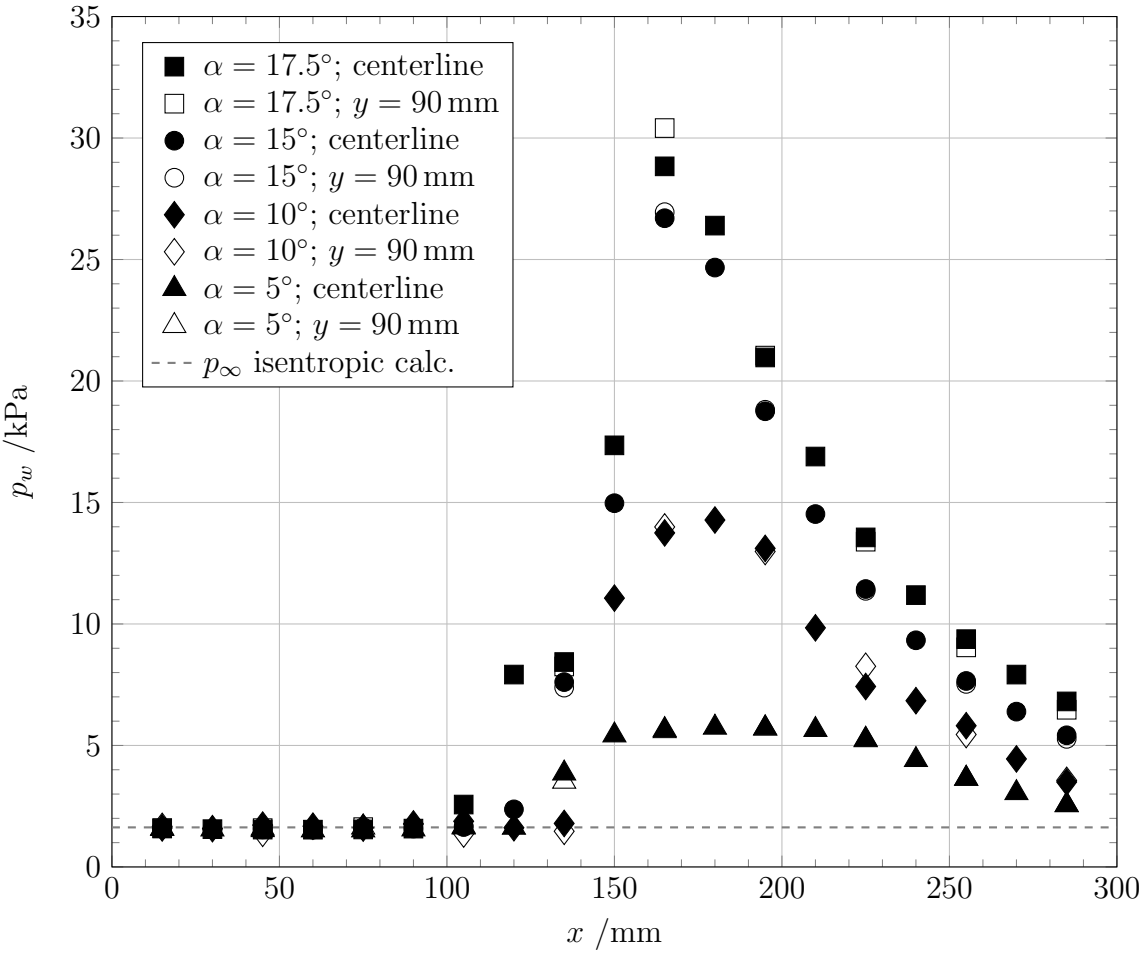


**Figure 4.6:** Average wall pressure ($p_w$) on the rigid insert at various shock generator angles

large shock generator angles, the initial pressure rise takes place considerably upstream of the nominal impingement position in the center of the panel ($x = 150\,\text{mm}$) due to the occurring flow separation. The second distinct pressure rise in flow direction in these cases is caused by the reattachment shock on the downstream side of the separated area.

At $\alpha = 20°$, the separated area drastically increases in size (Fig. 4.7), apparently so much that the separation takes place where the boundary layer is still laminar. To confirm this assumption, the shock generator was moved downstream in several stages. The resulting measurements were shifted upstream in the plot (Fig. 4.7) by the respective $\Delta x$ for easier comparison. It can be seen that no change occurs for a change in shock generator position of $\Delta x = 10\,\text{mm}$. However, starting from $\Delta x = 25\,\text{mm}$ the size of the separation drastically decreases and looks more similar to a separation in a turbulent boundary layer. A further downstream shift of $\Delta x = 50\,\text{mm}$ does not change the resulting pressure distribution detectably.

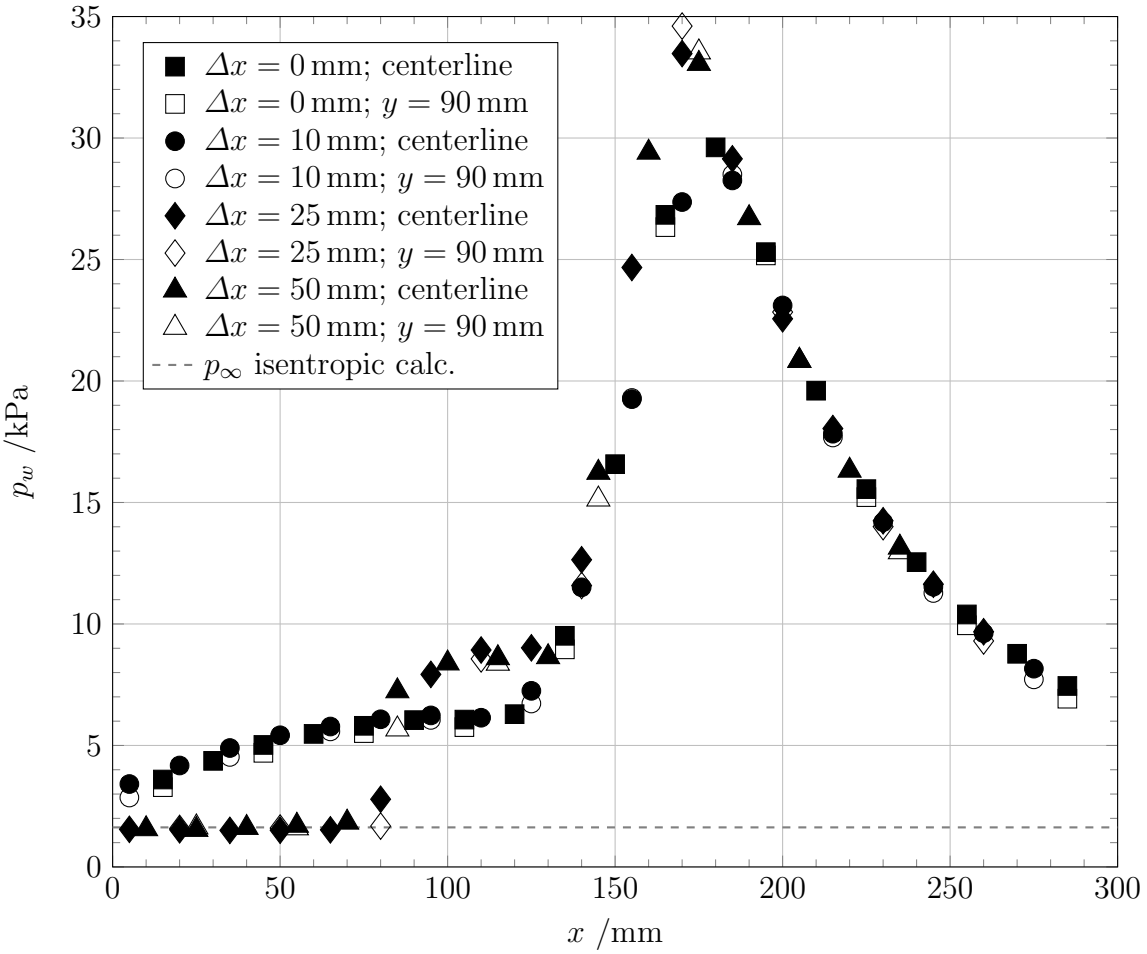


**Figure 4.7:** Average wall pressure ($p_w$) on the rigid insert at $\alpha = 20°$; $\Delta x$ indicates a downstream shift in nominal shock impingement position for the wind tunnel run, but the respective plot is shifted upstream by the same value for easier comparison

### Wall Temperature

The effect of this flow structure on the the heating of the rigid insert is shown in Figs. 4.8 to 4.12. Figure 4.8 shows the heating of the wall without shock generator. The wall temperature distribution shows a local maximum starting from about $x = 50$ mm which is relatively constant in lateral direction (Fig. 4.8a). This is consistent with the suspected boundary-layer transition near the beginning of the insert. To support this assumption, Stanton numbers were computed from the measured temperature data and correlations for a laminar and turbulent boundary layer. The correlation by Korkegi [96] was used because it has shown good agreement in similar flow conditions in previous studies [178]. The values computed from the experimental data show a distinct rise beginning at the upstream end of the panel and a local maximum at about $x = 60$ mm indicative of a laminar-turbulent transition of the boundary layer (Fig. 4.8b). This confirms the assumption made based on the wall pressure measurements that the boundary-layer transition takes place on the upstream part of the insert. The slightly different trend on

the downstream end of the insert might be caused by heat transfer to the colder wind tunnel model in $x$-direction that the computation of the experimental data does not take into account. It is also interesting to note that, as expected, heat transfer from about $x = 50\,\mathrm{mm}$ locally exceeds what would be expected from a fully turbulent boundary layer.

Next, cases with shock generator were investigated (Fig. 4.9 to 4.12). Changes in the upstream boundary of the visible area are caused by the shock generator blocking the view of the IR camera. Generally, the resulting wall temperature increases with rising shock generator angle with a local maximum near the nominal impingement position ($x = 150\,\mathrm{mm}$). The initial temperature rise shifts slightly upstream for low incident shock angles as can be seen in comparison between Figs. 4.9a and 4.9b (see also Fig. 4.12a). This is caused by the shock at lower incident angle impinging onto the boundary layer upstream of the nominal location in the panel center. Starting from $\alpha = 15°$ (Fig. 4.10a), a second peak in maximum temperature upstream of the nominal impingement position can be observed. These peaks are also visible at about $x = 110\,\mathrm{mm}$ in Fig. 4.10b for $\alpha = 17.5°$, and at about $x = 120\,\mathrm{mm}$ in Fig. 4.11b for $\alpha = 20°$ at a downstream shift of the shock generator by $\Delta x = 50\,\mathrm{mm}$. These locations correspond to the pressure rise caused by the shock upstream of the separated area of the SWBLI (Figs. 4.6 and 4.7).

However, for the case at $\alpha = 20°$ at nominal shock generator position, a different behavior occurs as already indicated by the pressure measurements. The upstream temperature peak disappears from the field of view (Fig. 4.11a). It presumably still exists, but is located so far upstream that the view is blocked by the shock generator. The pressure measurements suggest (Fig. 4.7) that the location of the flow separation may even be upstream of the rigid insert. In Fig. 4.12b, this case is compared to the case with the shock generator moved downstream by $\Delta x = 50\,\mathrm{mm}$ (again, the plot for this case is shifted upstream for easier comparison). For the latter case, two distinct peaks are visible similar to the cases with lower shock generator angle (Fig. 4.12a). Figures 4.9 to 4.11 all show nearly two-dimensional spatial distribution of $T_w$ in lateral direction on the rigid insert. However, it appears that the separation shock slightly curves, increasing with rising incident shock angle. This is presumably caused by three-dimensional effects in the separated area as, for example, discussed in [74, 100, 101] for a similar configuration. Such effects are nearly unavoidable in wind tunnel configurations but considered small for the present setup based on the presented temperature and pressure measurements.

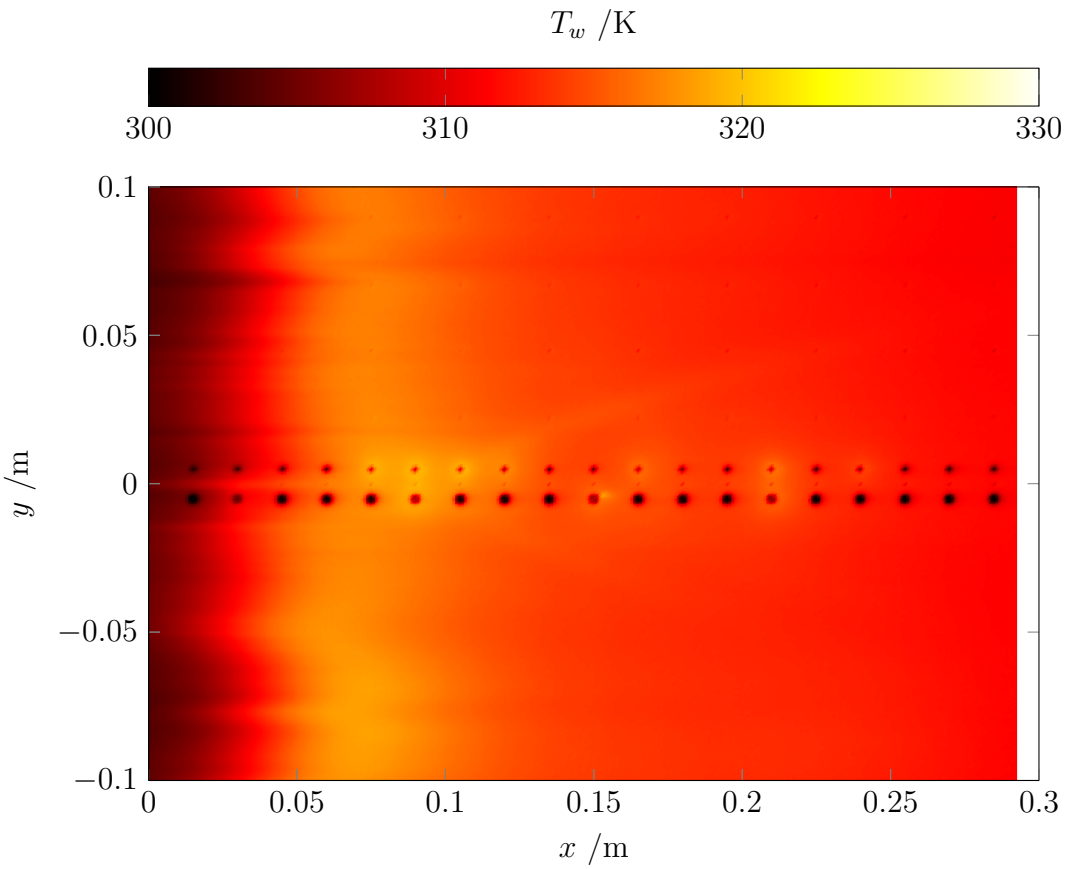


**(a)** Wall temperature

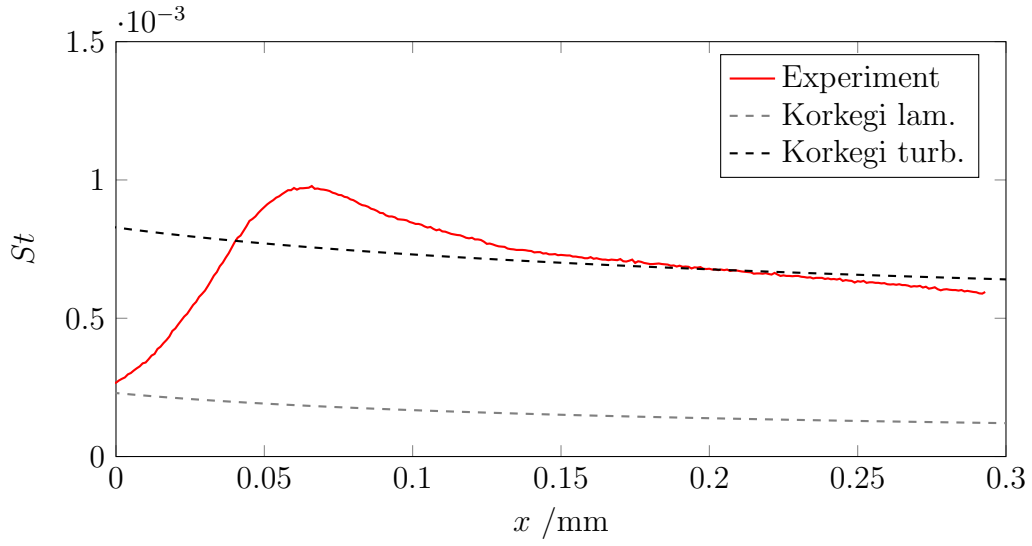


**(b)** Stanton number distribution

**Figure 4.8:** IR temperature measurements on the rigid insert after $t = 10\,\mathrm{s}$ without shock generator

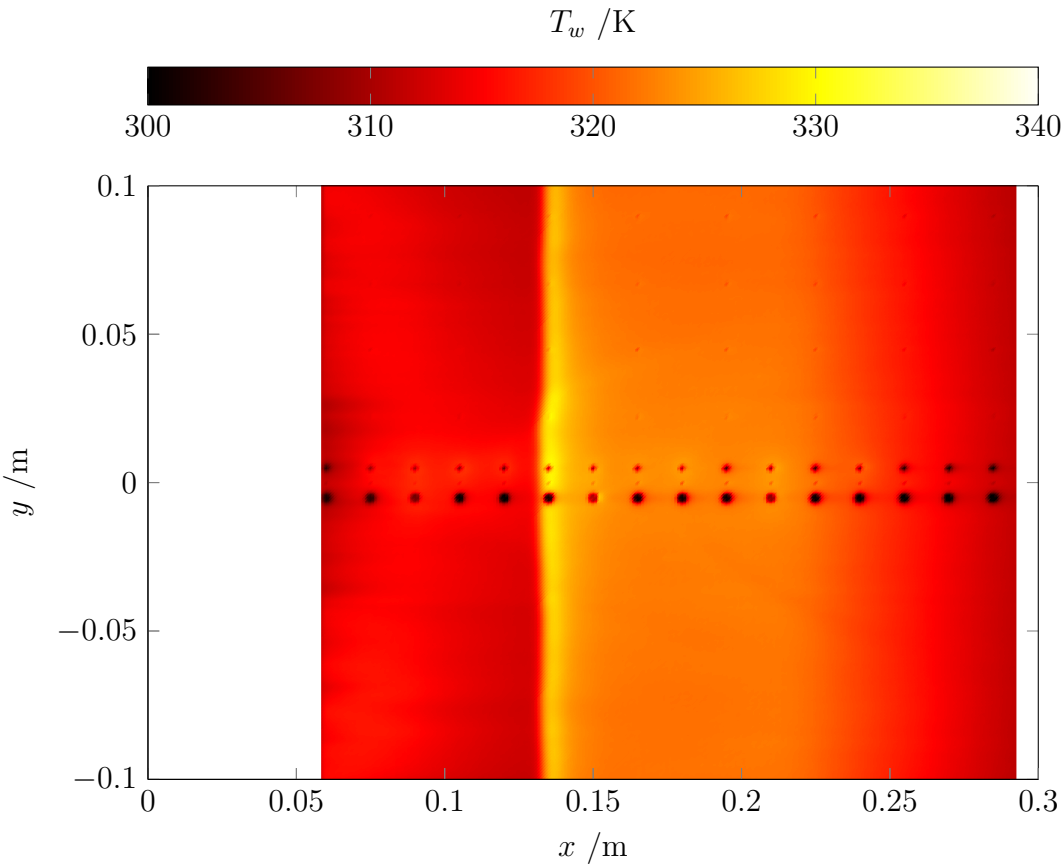


**(a)** $\alpha = 5°$

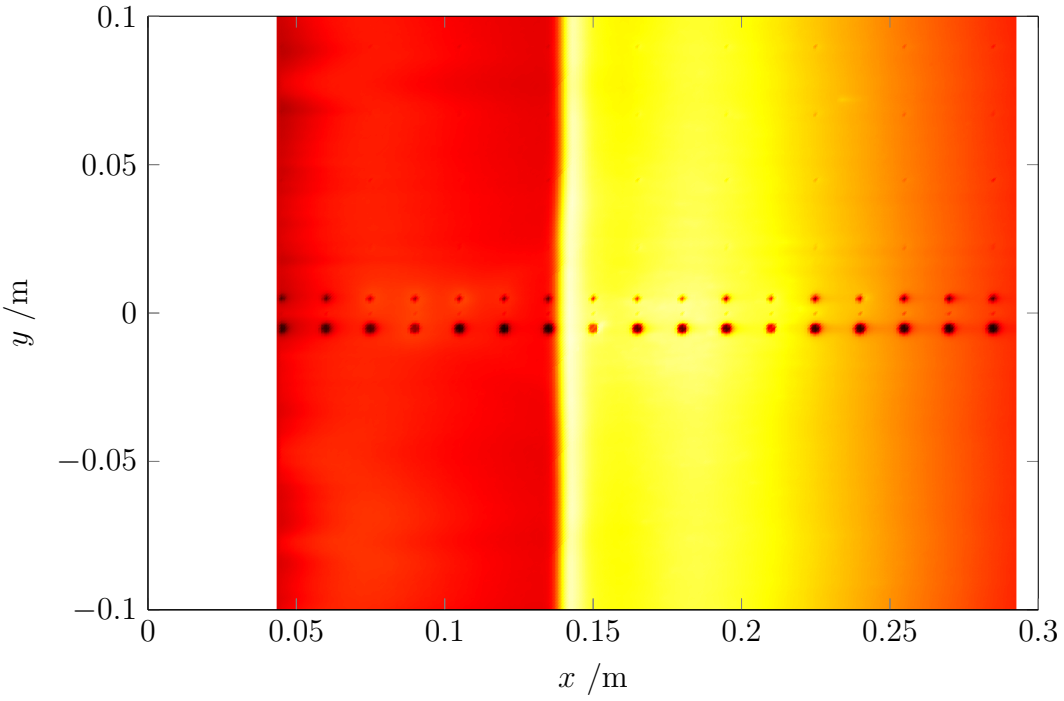


**(b)** $\alpha = 10°$

**Figure 4.9:** IR measurements of $T_w$ on the rigid insert after $t = 10\,\mathrm{s}$ with shock generator

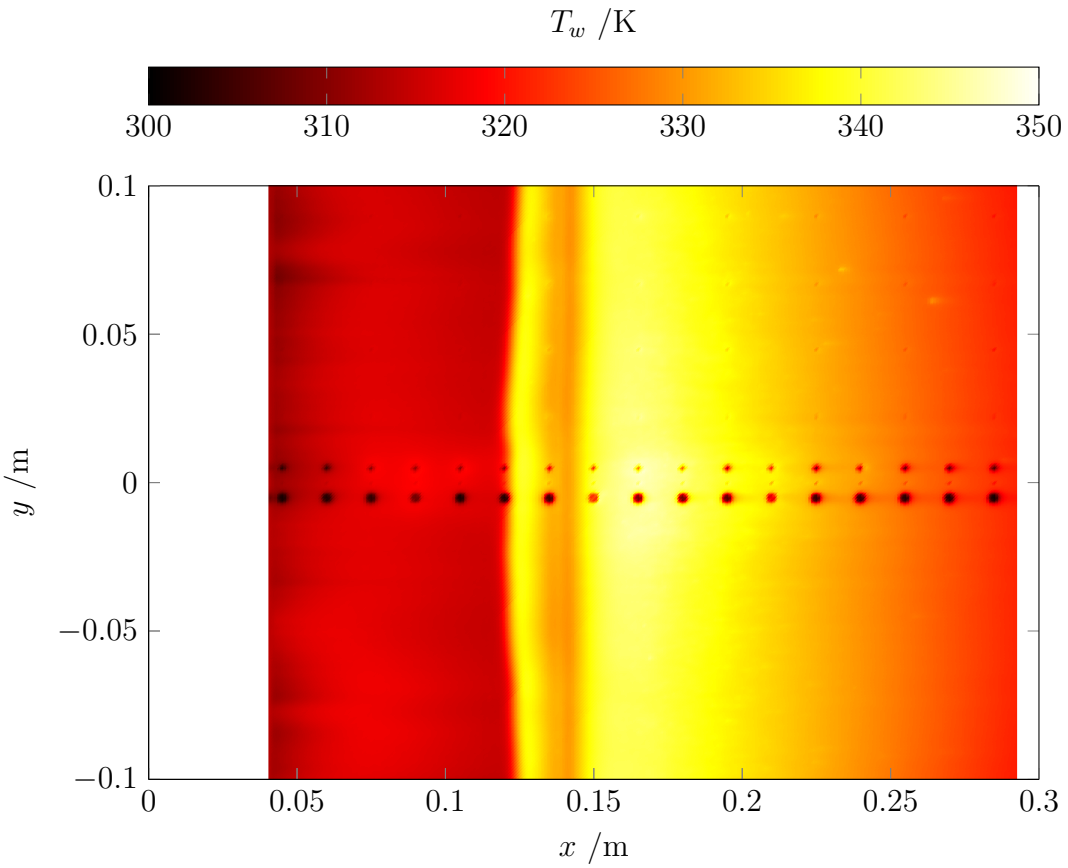


**(a)** $\alpha = 15°$

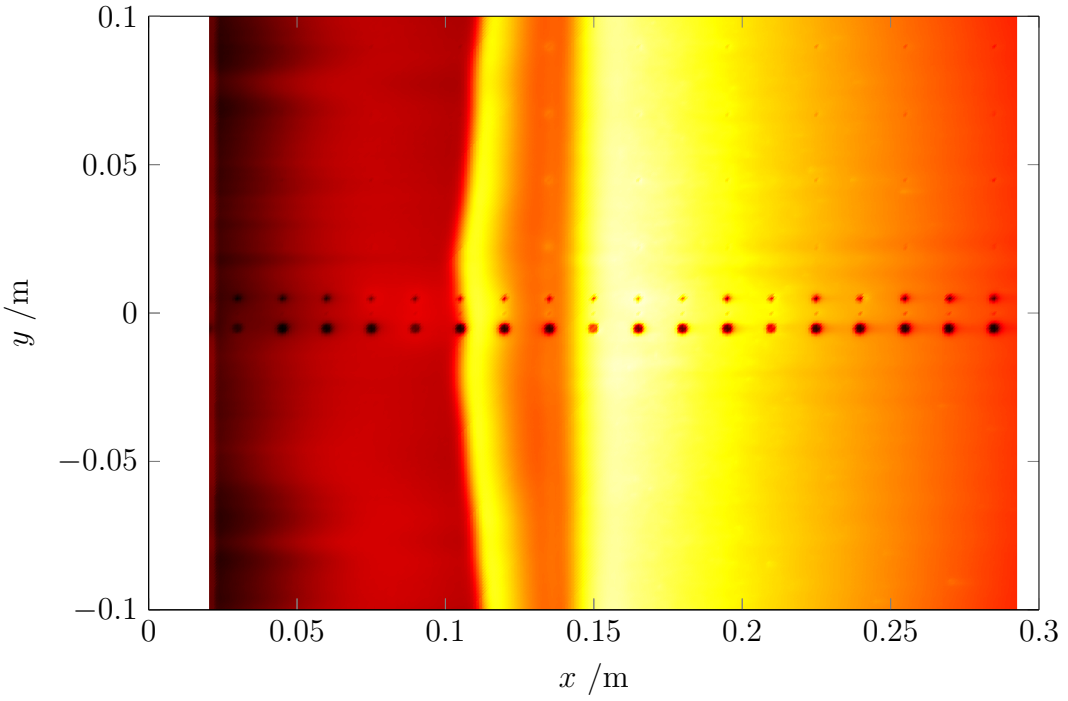


**(b)** $\alpha = 17.5°$

**Figure 4.10:** IR measurements of $T_w$ on the rigid insert after $t = 10\,\mathrm{s}$ with shock generator

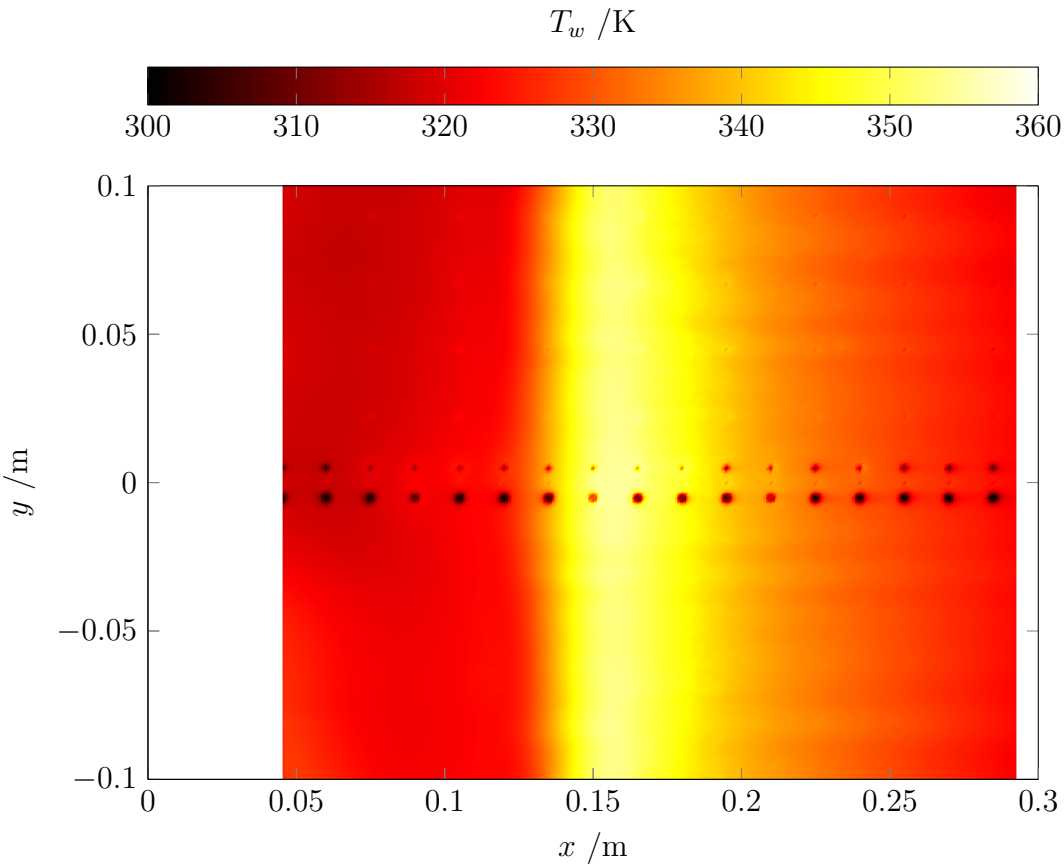


**(a)** $\alpha = 20°$

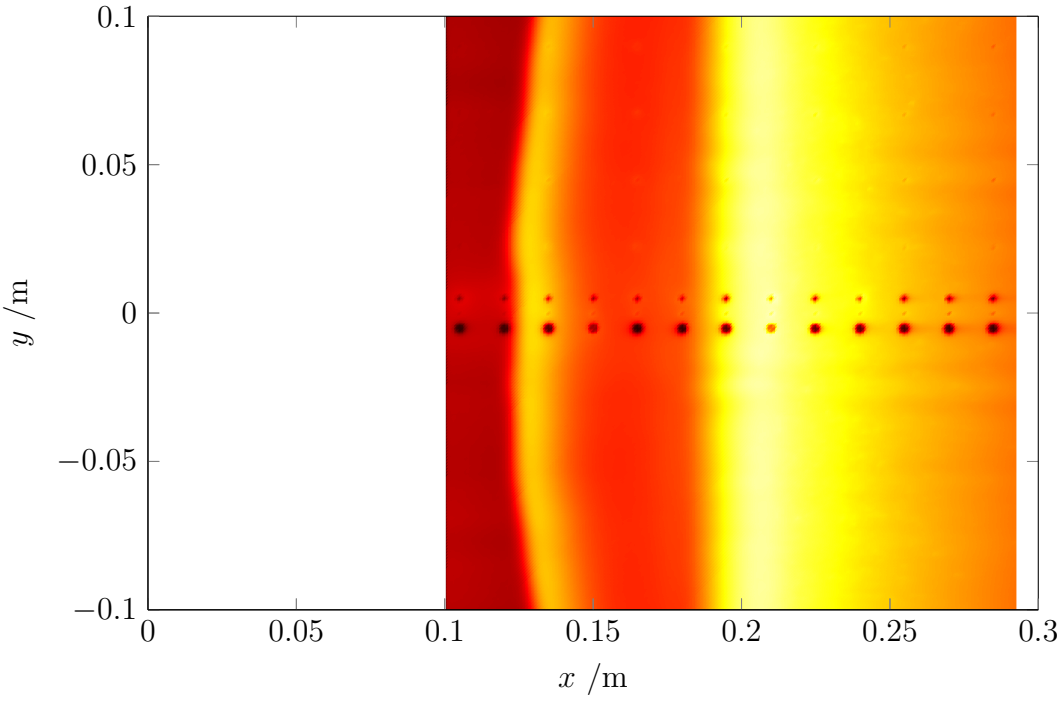


**(b)** $\alpha = 20°$ and $\Delta x = 50\,\text{mm}$

**Figure 4.11:** IR measurements of $T_w$ on the rigid insert after $t = 10\,\text{s}$ with shock generator

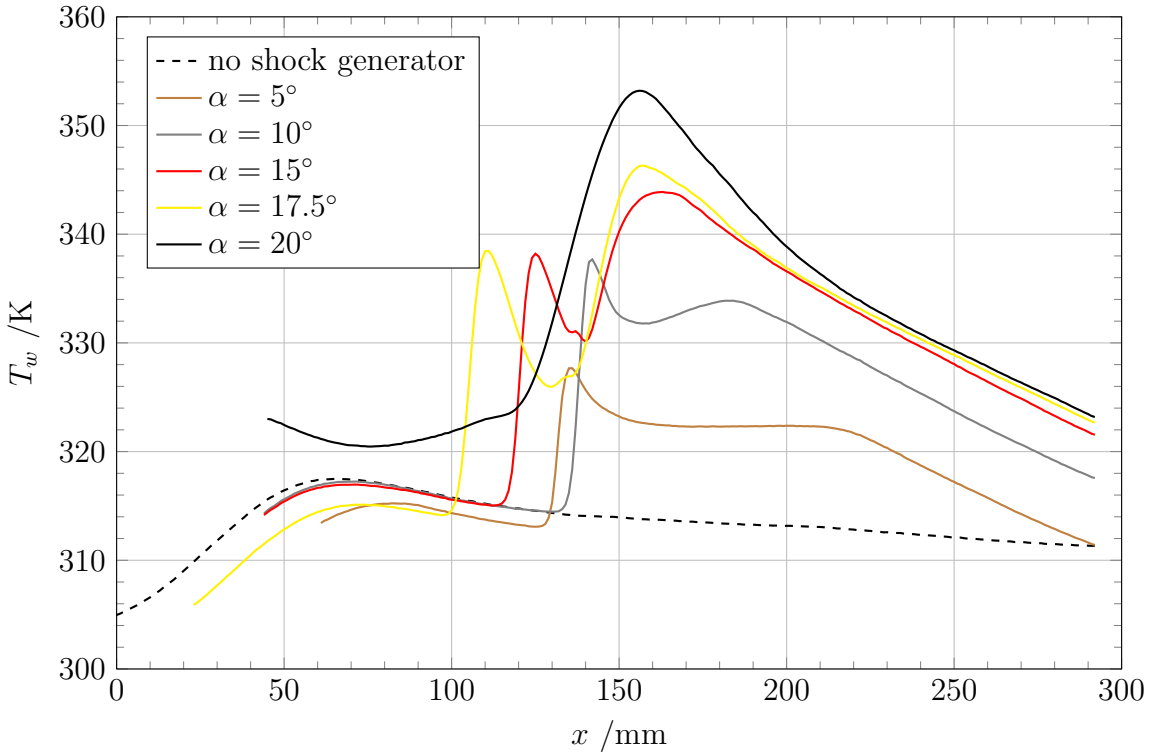


**(a)** Overview

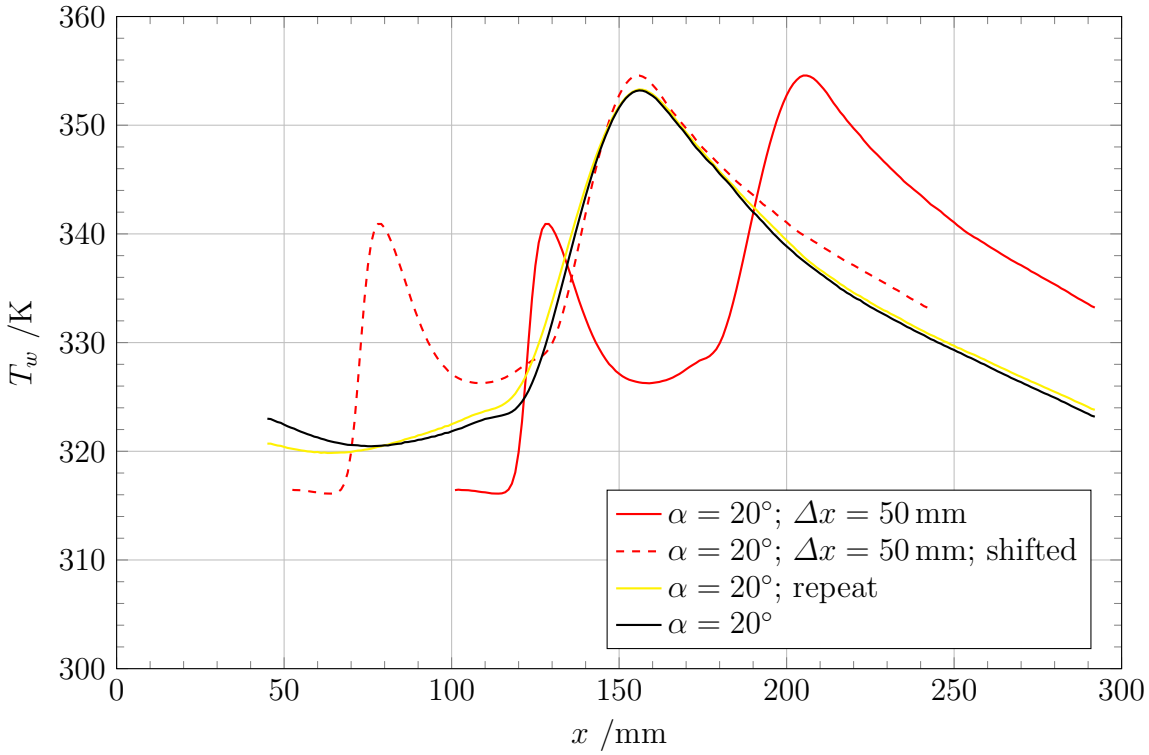


**(b)** Comparison of cases with $\alpha = 20°$

**Figure 4.12:** Spatial average of $T_w$ on the rigid insert after $t = 10\,\mathrm{s}$

### Shadowgraph Images

The high-speed shadowgraph recordings (Figs. 4.13 to 4.15) provide further insight into the flow structure and dynamics of the flow field. Figure 4.13a shows an image for $\alpha = 17.5°$. The location of the initial separation can clearly be seen at about $x = 110\,\text{mm}$, again corresponding to the initial pressure rise shown in Fig. 4.6 and the temperature peak in Fig. 4.12a. Furthermore, there is a change in the boundary layer visible at about $x = 50\,\text{mm}$ that is most likely linked to the transition of the boundary layer. At the lower left corner of the plot, a weak shock is emanating from the upstream end of the insert at $x = -15\,\text{mm}$. Also, the shock stemming for the leading edge of the wind tunnel model is clearly visible traversing the $y$-axis at about $y = 23\,\text{mm}$. For the case at $\alpha = 20°$ and $\Delta x = 50\,\text{mm}$ (Fig. 4.13c), the behavior is similar. The size of the separation is increased and shows good agreement to the measured pressure and temperature distributions. Again, a drastically different behavior can be observed for $\alpha = 20°$ at nominal shock generator position (Fig. 4.13b). The most striking feature is the very large size of the separation. Here it becomes evident that, as already suspected based on the pressure and temperature distributions, the separation shock starts considerably upstream of the rigid insert. Based on the wall temperature measurements (Fig. 4.8), the flow separation appears upstream of the boundary-layer transition, which is consistent with the large observed size of the separation.

The high-speed videos provide insight into the dynamics of the flow field. Figures 4.14 and 4.15 show results based on the PSD of the grey scale values of each pixel from the recorded videos. It should be kept in mind that this approach is limited to flow features that are visible in the shadowgraph images. Furthermore, the shadowgraph images integrate along the line of sight. Figure 4.14 shows the mean PSD of the grey scale values below 1 kHz. The low-frequency unsteadiness is of particular interest as it occurs in the same frequency range as eigenfrequencies of the structure. Figure 4.14 shows that such dynamics occur throughout the area where the SWBLI is visible in Fig. 4.13. Figures 4.14a and 4.14c show that a maximum in visible dynamics occurs at the separation shock. This is in line with previous experimental and simulation results that generally show a maximum in low-frequency dynamics connected to the movements of the separation shock (e. g. [131]). In the case with $\alpha = 20°$ shock generator angle at nominal position, dynamics are also visible throughout the interaction area. However, no distinct maximum was detected at the separation shock. A second maximum in low-frequency dynamics occurs near the reattachment at the end of the separated area in all three cases.

Additionally, it is interesting to look at frequency spectra at various locations in the interaction region. In Fig. 4.15, spectra along a line parallel to the inflow at $z = 10\,\text{mm}$ are shown. This distance to the wall is chosen for comparison to the elastic cases to avoid looking directly at the flexible structure or the boundary layer. The distribution of the maximum dynamics in flow direction is consistent with the above description. In all cases, broadband dynamics without any distinct peaks occur, which corresponds to previous measurements based on Schlieren images and pressure measurements for similar configurations (e. g. at lower $Ma$ [174, 177]).

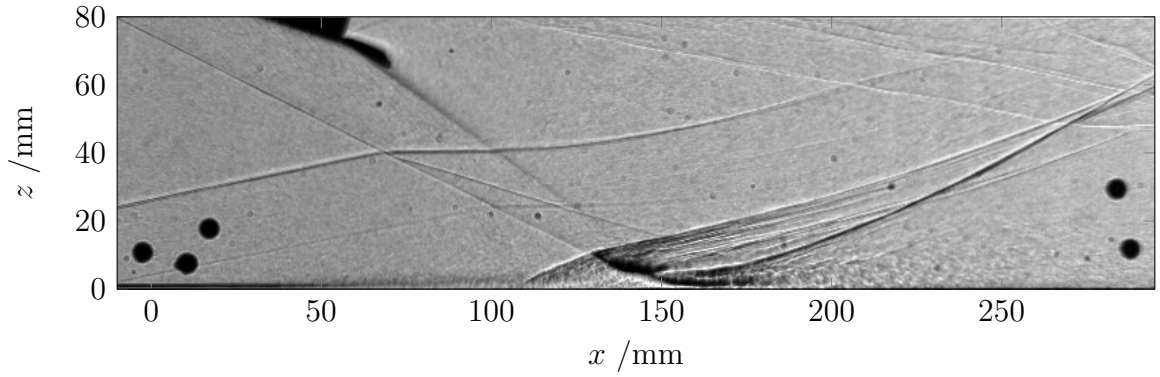


**(a)** $\alpha = 17.5°$

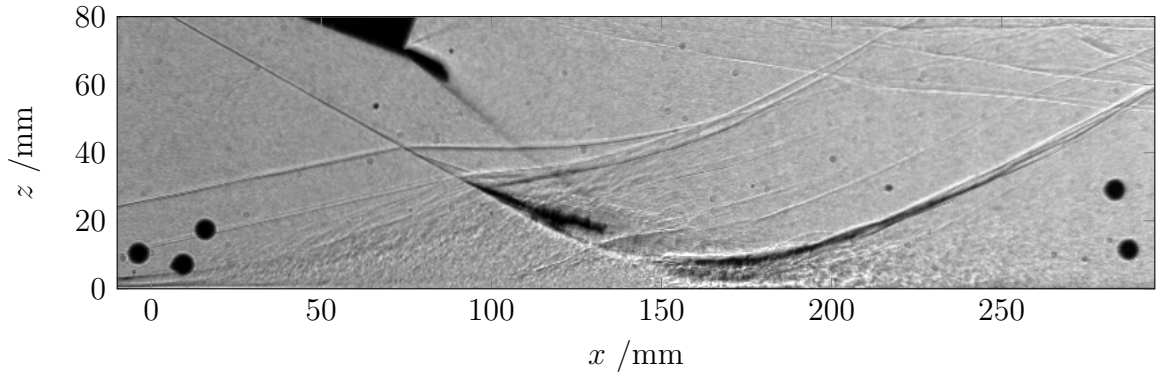


**(b)** $\alpha = 20°$

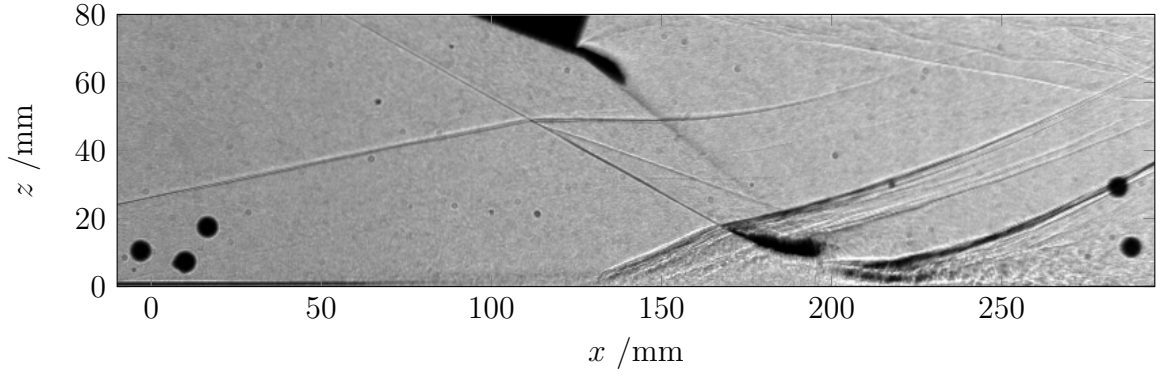


**(c)** $\alpha = 20°$, $\Delta x = 50\,\mathrm{mm}$

**Figure 4.13:** Frames from high-speed shadowgraph videos for the rigid wall configuration

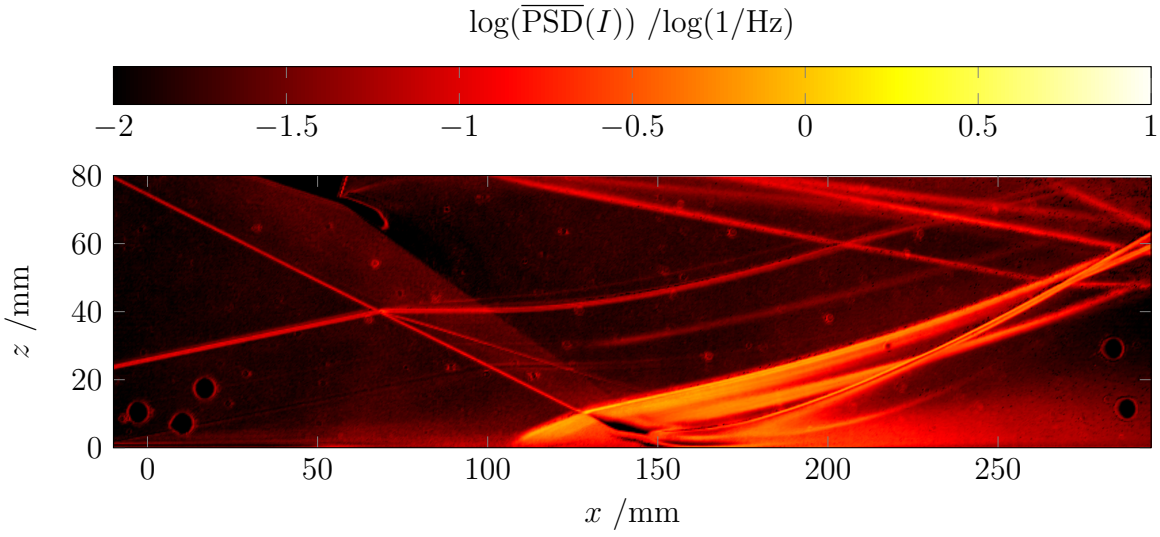


**(a)** $\alpha = 17.5°$

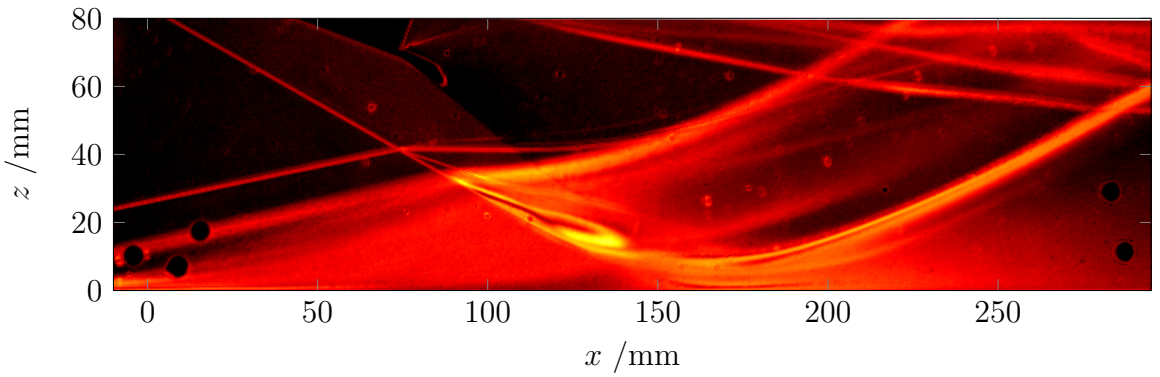


**(b)** $\alpha = 20°$

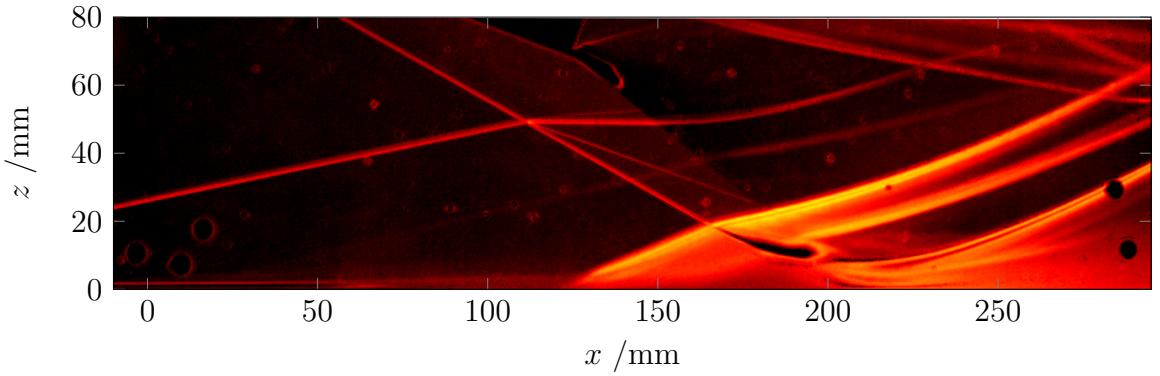


**(c)** $\alpha = 20°$, $\Delta x = 50\,\mathrm{mm}$

**Figure 4.14:** Mean PSD of grey scale values ($I$) from high-speed shadowgraph videos for the rigid wall configuration below 1 kHz

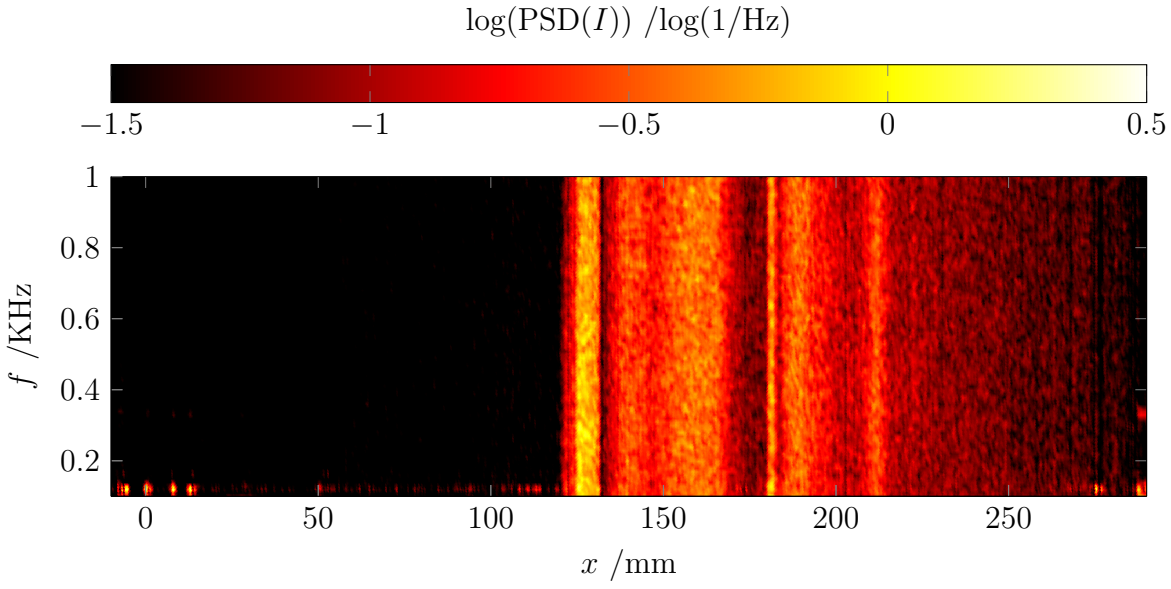


**(a)** $\alpha = 17.5°$

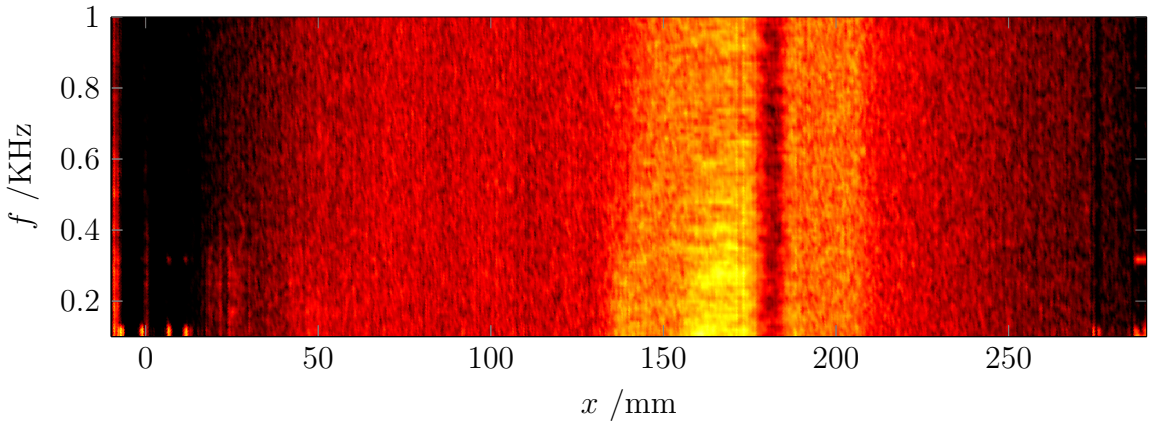


**(b)** $\alpha = 20°$

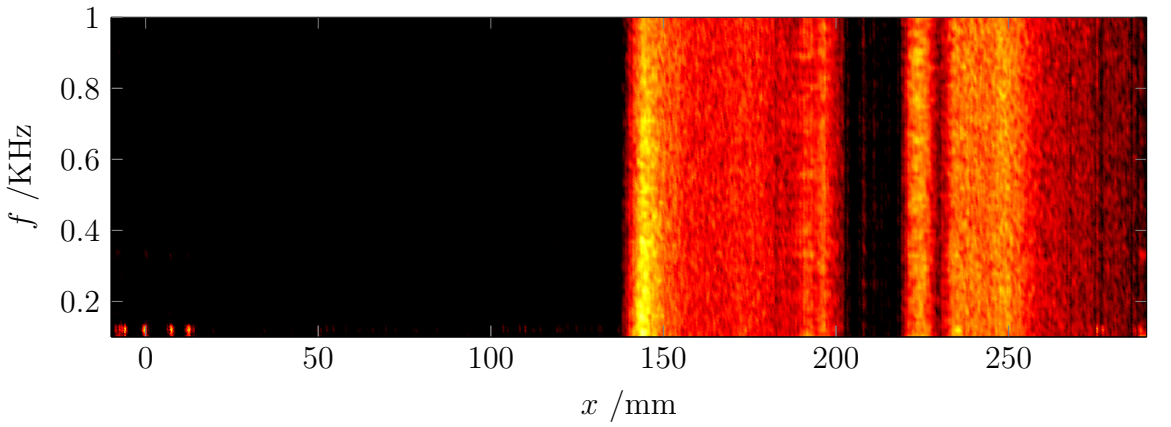


**(c)** $\alpha = 20°$, $\Delta x = 50\,\mathrm{mm}$

**Figure 4.15:** PSD spectra of grey scale values ($I$) from high-speed shadowgraph videos for the rigid wall configuration along $z = 10\,\mathrm{mm}$ below $1\,\mathrm{kHz}$

### 4.2.2 FSI without Incident Shock

#### 0.3 mm Panel and Damage

Figures 4.16 to 4.18 show results of wind tunnel runs with a 0.3 mm panel without incident shock.[2] Before the flow was started, the wind tunnel model including the panel was at ambient temperature. The pressure in the cavity underneath the panel was set to the expected $p_\infty$ while the test chamber was evacuated. Because the test section remains evacuated before the run, the panel is slightly deformed towards the test chamber for $t < 0$ s, which can be seen in the time series plot of the displacement measurements in Fig. 4.16a. When the flow is started, the panel quickly assumes an undeformed neutral position. After a few seconds, large amplitude panel oscillations in excess of 2 mm set in while the average displacement remains near $z = 0$ mm (Fig. 4.16b). The oscillations appear at a frequency slightly above 200 Hz and slowly decrease throughout the wind tunnel run (Fig. 4.16c). This trend also includes oscillations of lower amplitude during tunnel startup around $t = 0$ s. It appears that the panel, as discussed previously, is slightly prestressed from the manufacturing process. It then slowly heats up throughout the wind tunnel run reducing prestress in the panel and passes through a threshold that allows flutter dynamics to start. Another interesting event occurs at about $t = 18.5$ s: After the average deformation of the panel remains at nearly 0 mm throughout the wind tunnel run, suddenly a small change sets in that consists of a reduced flutter amplitude (Fig. 4.16a), a small change in average deformation (Fig. 4.16b), and a reduction in the resulting frequency (Fig. 4.16c). As all other conditions remain constant throughout the wind tunnel run, this behavior is most likely caused by the heating of the panel throughout the run leading to an expansion and buckling of the structure and consequently changing its dynamic properties. A nominal repeat run is given in [33], showing good agreement with the present run.

A total of four runs were conducted with this 0.3 mm panel. Figure 4.17 shows the results of the last run during which a crack occurred on one side between panel and frame. After the wind tunnel run and cool-down of the model, the panel receded to the undeformed position. The damage was not visible but could be confirmed by significant leakage when pressurizing the cavity before an intended next wind tunnel run. During the wind tunnel run, the damage becomes apparent in a change in the temporal gradient of the dominant frequency seen in Fig. 4.17c at about $t = 13$ s. A small change is also visible in the cavity pressure at the same time [33]. Interestingly, panel flutter continues at slightly reduced frequency until about $t = 21$ s, when suddenly the panel assumes a buckled position (Fig. 4.17b) that instantly stops panel oscillations while the wind tunnel continues to run at unchanged conditions. The buckling amplitude reached by the damaged panel is significantly larger than what was observed in the previous run (Fig. 4.16b).

For the run shown in Fig. 4.18, the protective nose cover on the leading edge of the wind tunnel model was left on, adding a small radius of about 3 mm and a corresponding small backward facing step. This geometry is not well defined, but led to remarkably large

[2] Run numbers 24 – 26 are consistent with [33].

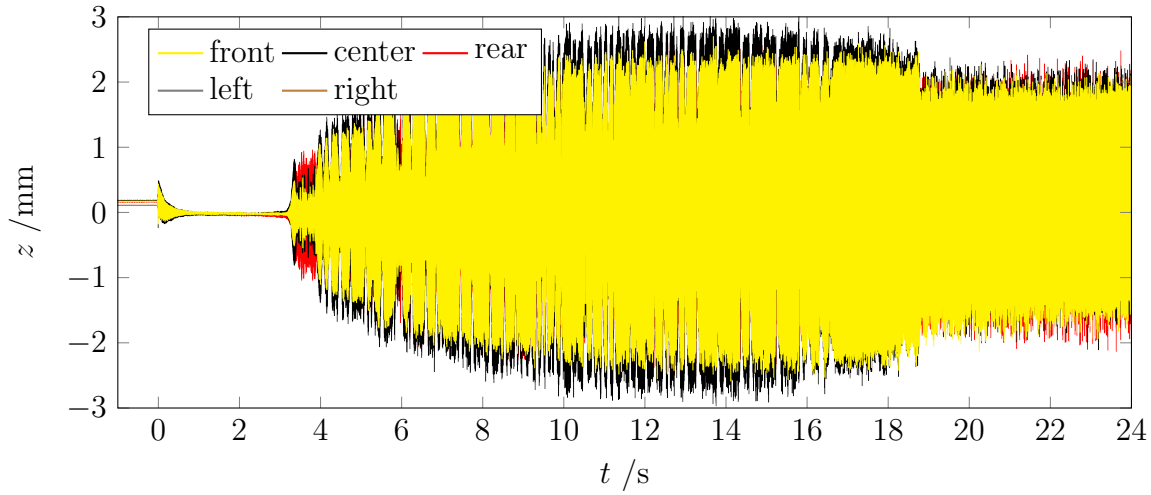


**(a)** Time series plot of the panel displacement

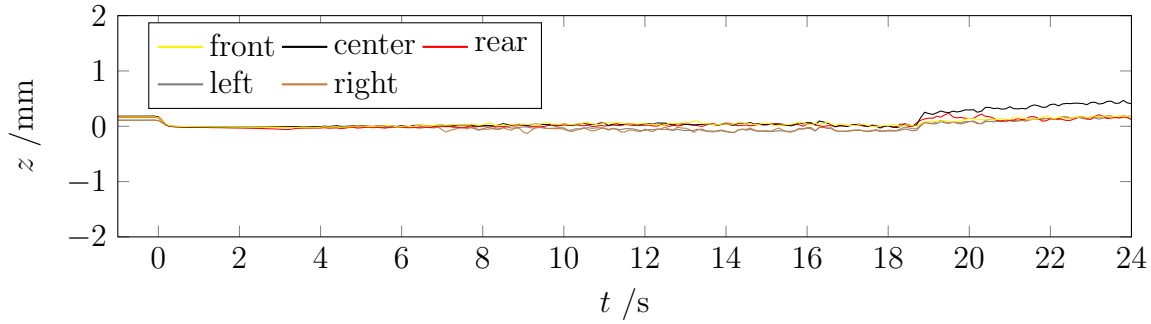


**(b)** Moving average of the panel displacement

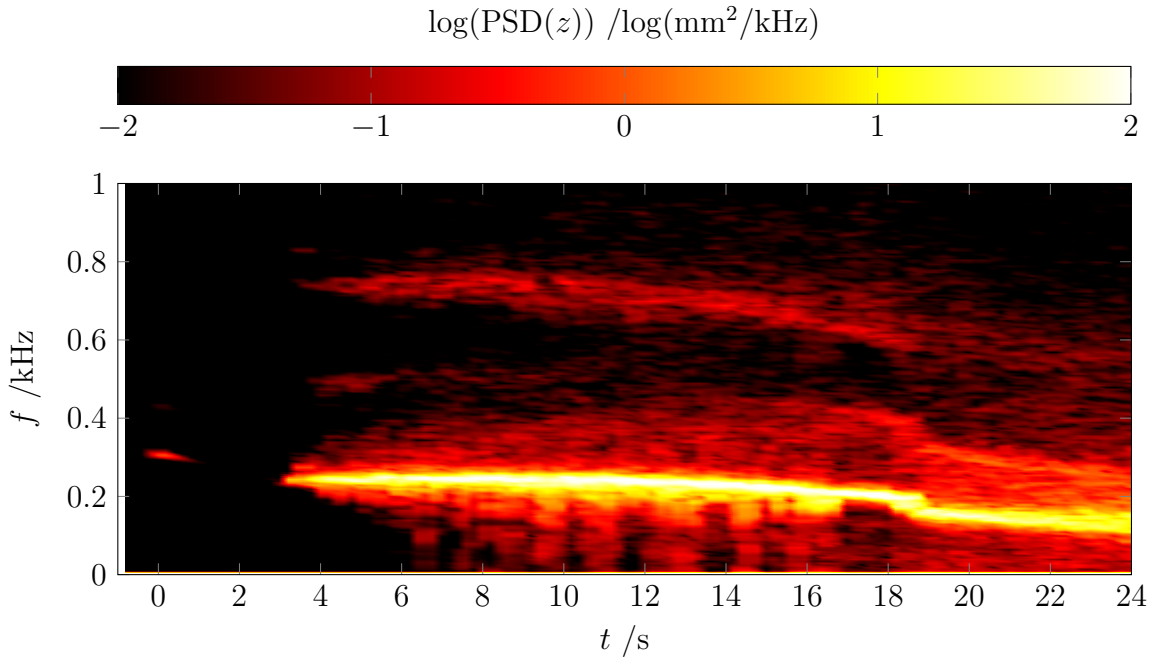


**(c)** PSD of the center displacement

**Figure 4.16:** Panel displacement for 0.3 mm panel no. 1 without shock generator (run 25)

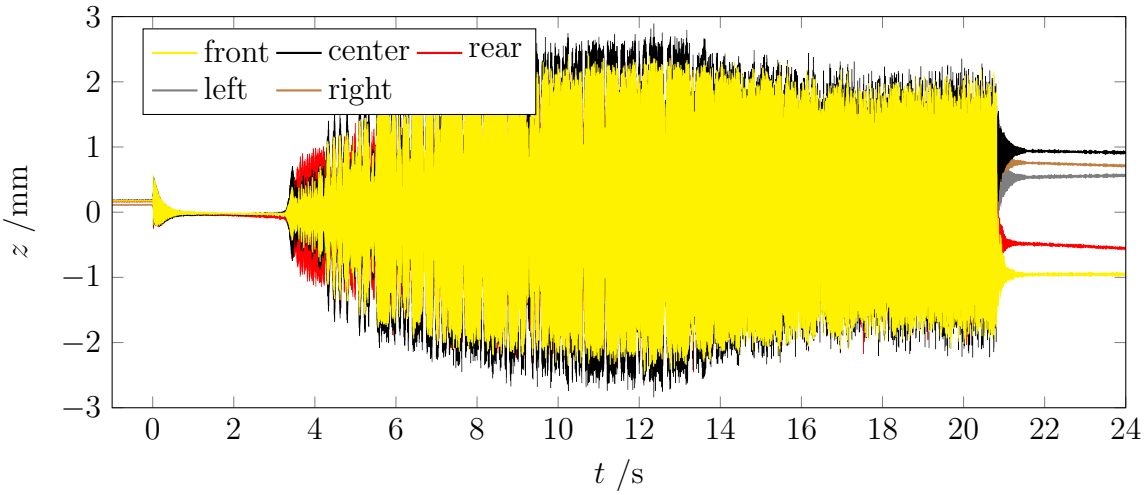


**(a)** Time series plot of the panel displacement

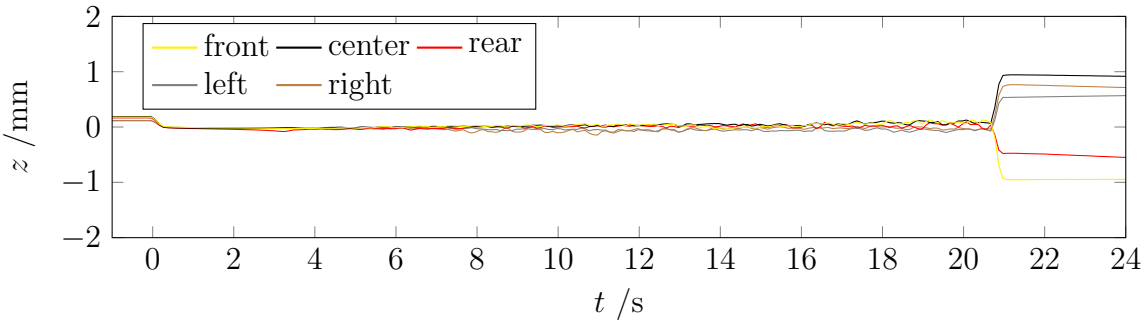


**(b)** Moving average of the panel displacement

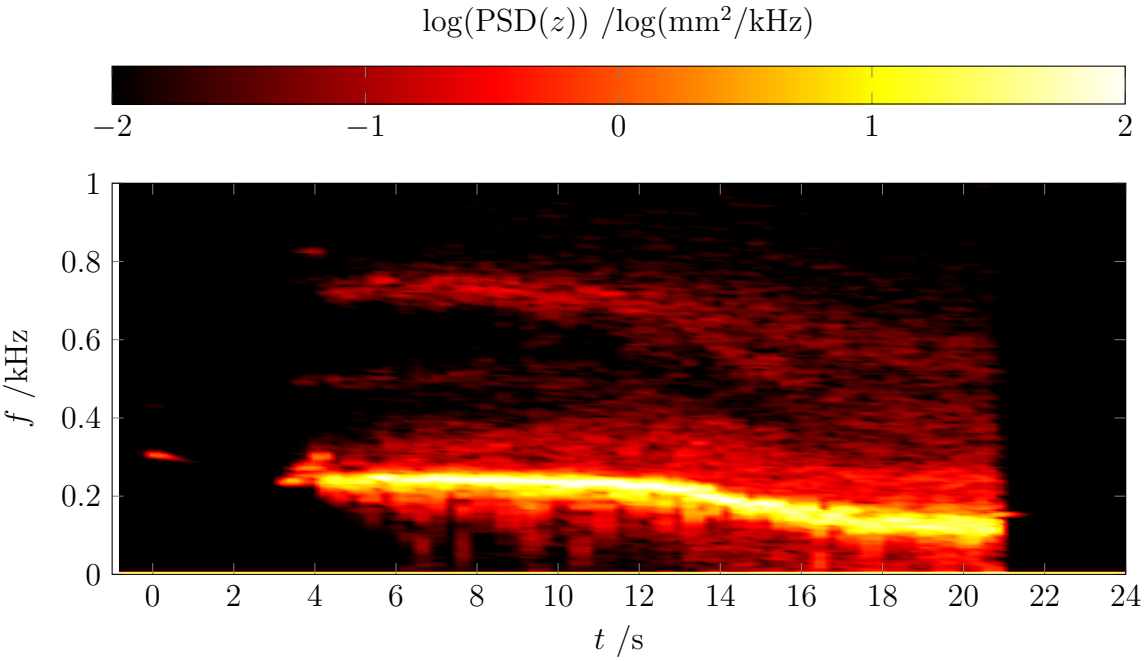


**(c)** PSD of the center displacement

**Figure 4.17:** Panel displacement for 0.3 mm panel no. 1 without shock generator including panel damage (run 26)

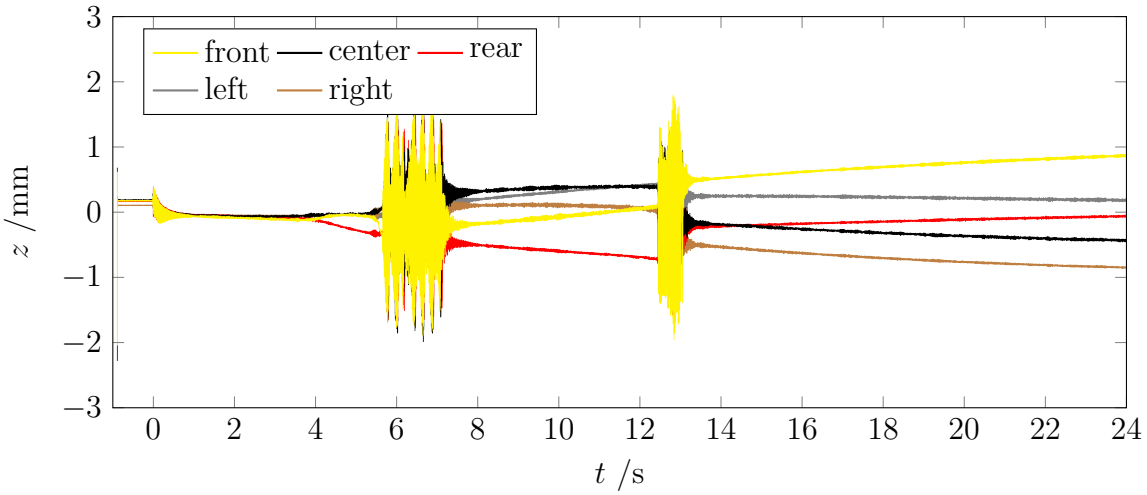


**Figure 4.18:** Panel displacement for 0.3 mm panel no. 1 without shock generator, modified leading edge (run 24)

changes in panel dynamics. Flow conditions from the wind tunnel are the same as in the other runs with this panel (Figs. 4.16 and 4.17). The panel briefly exhibits oscillations of significant amplitude at about $t = 6\,\mathrm{s}$ and $t = 13\,\mathrm{s}$. Starting at $t = 4\,\mathrm{s}$, the panel shows thermal buckling and snaps through between different shapes around $t = 13\,\mathrm{s}$, which may be connected to the occurring dynamics. This impressively demonstrates the sensitivity of such FSI-problems to very small aerodynamic disturbances, and may be an interesting starting point for further studies.

### Variation of Total Temperature for a 0.3 mm Panel

The observed connection between buckling and panel dynamics in the preceding experiments was very small (in the nominal cases). Since this is an effect of particular interest, it was investigated further using another 0.3 mm panel. To increase panel buckling, $T_0$ was increased in small steps. Increased panel buckling is also expected to lead to a distinct change in panel dynamics. The results of these experiments are shown in Figs. 4.19 to 4.22. $T_0$ was increased in steps of 20 K, starting at the nominal 390 K. The first run with this panel shows similar behavior to the previous runs with flutter onset about 2 s later (Fig. 4.19). The average deformation remains near 0 mm throughout the wind tunnel run with the exception of small deviations near flutter onset at about $t = 6\,\mathrm{s}$ (Fig. 4.19b). The predominant frequency of the panel oscillations also slightly decreases during the run (Fig. 4.19c). Figure 4.20 shows the next run, for which $T_0$ was raised by about 20 K (see Appendix A for exact flow conditions). The behavior is very similar but, in line with the assumption that a certain heating-related reduction in stiffness is necessary, the flutter onset occurs about 2 s earlier than in the previous run. For the next two runs (Figs. 4.21 and 4.22), $T_0$ was again increased by another 20 K. For this configuration, the panel assumes a buckled state before oscillations set in (Fig. 4.21b). The first maximum in deformation is reached at about $t = 5\,\mathrm{s}$, after which a quick change to a different buckled state without large oscillations occurs. This is followed by the onset

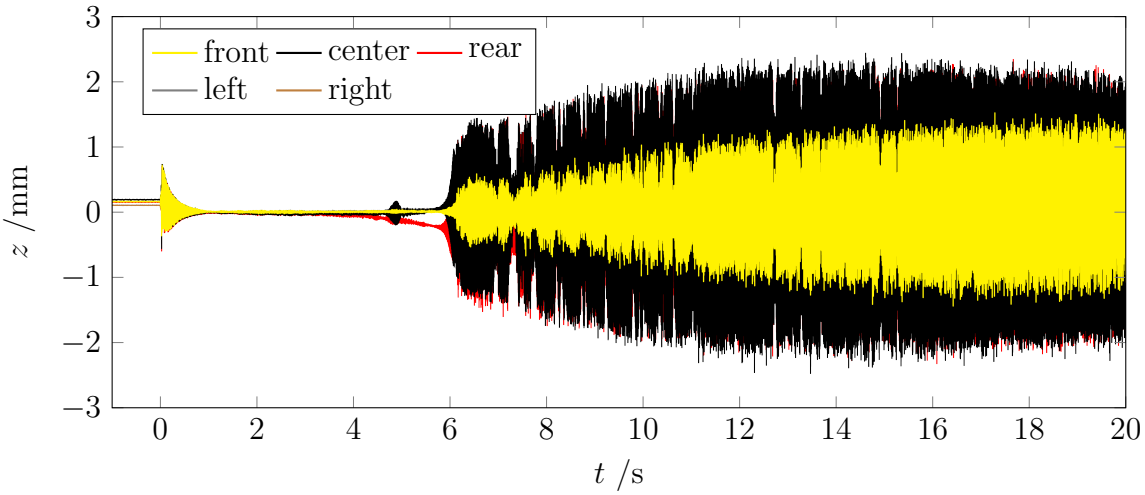


**(a)** Time series plot of the panel displacement

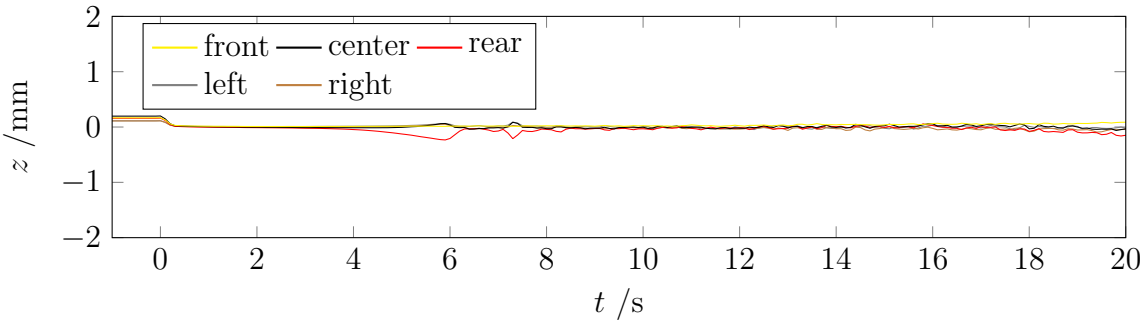


**(b)** Moving average of the panel displacement

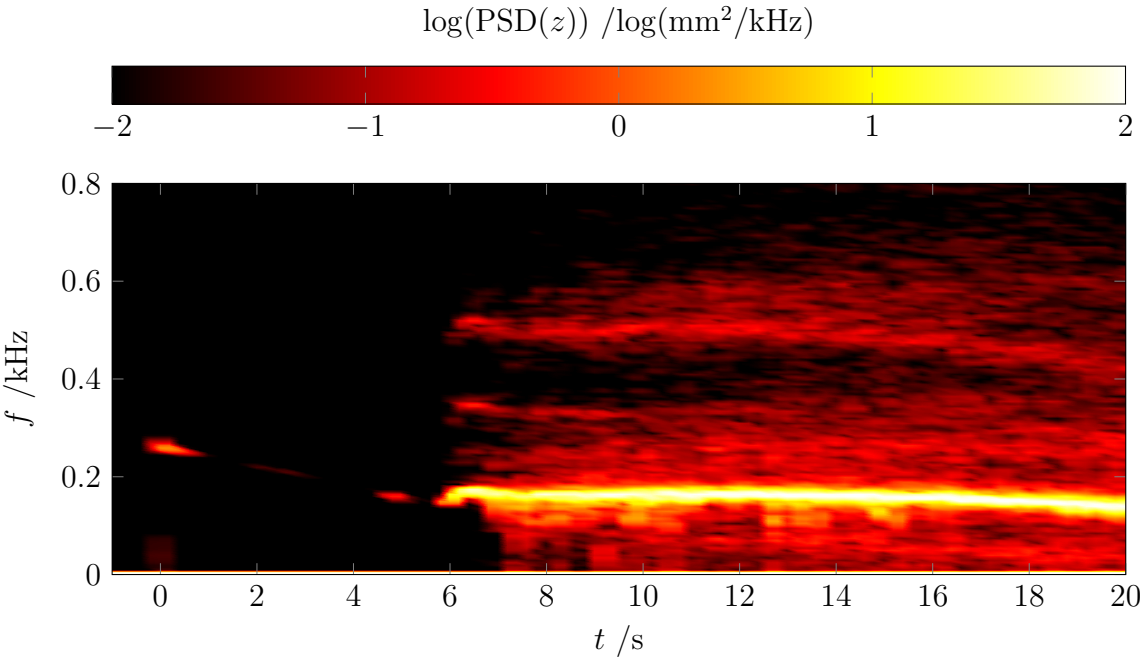


**(c)** PSD of the center displacement

**Figure 4.19:** Panel displacement for 0.3 mm panel no. 2 without shock generator – nominal flow conditions (run 105)

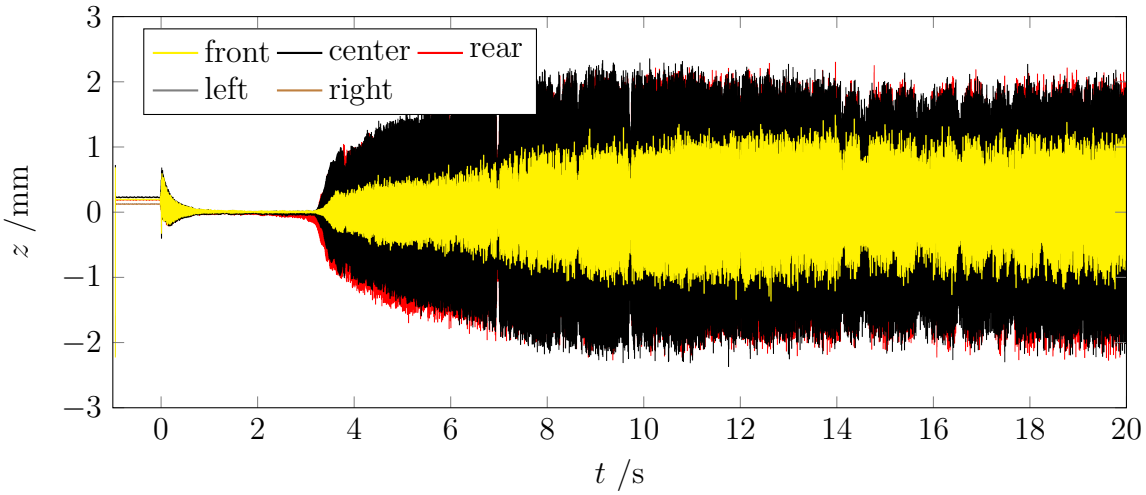


**(a)** Time series plot of the panel displacement

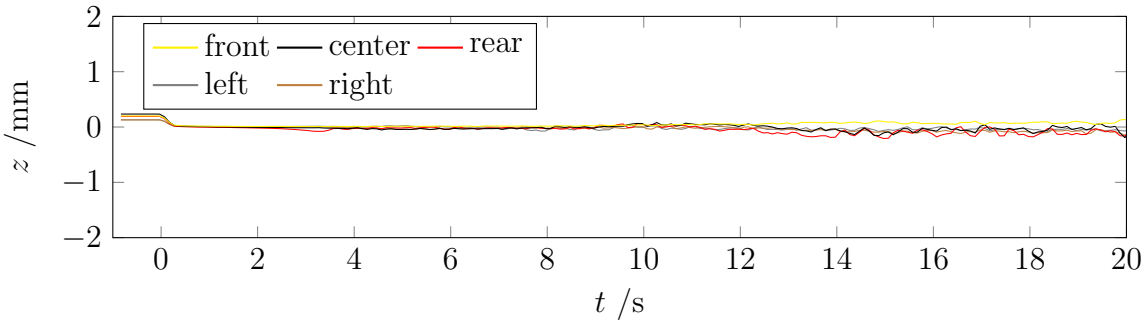


**(b)** Moving average of the panel displacement

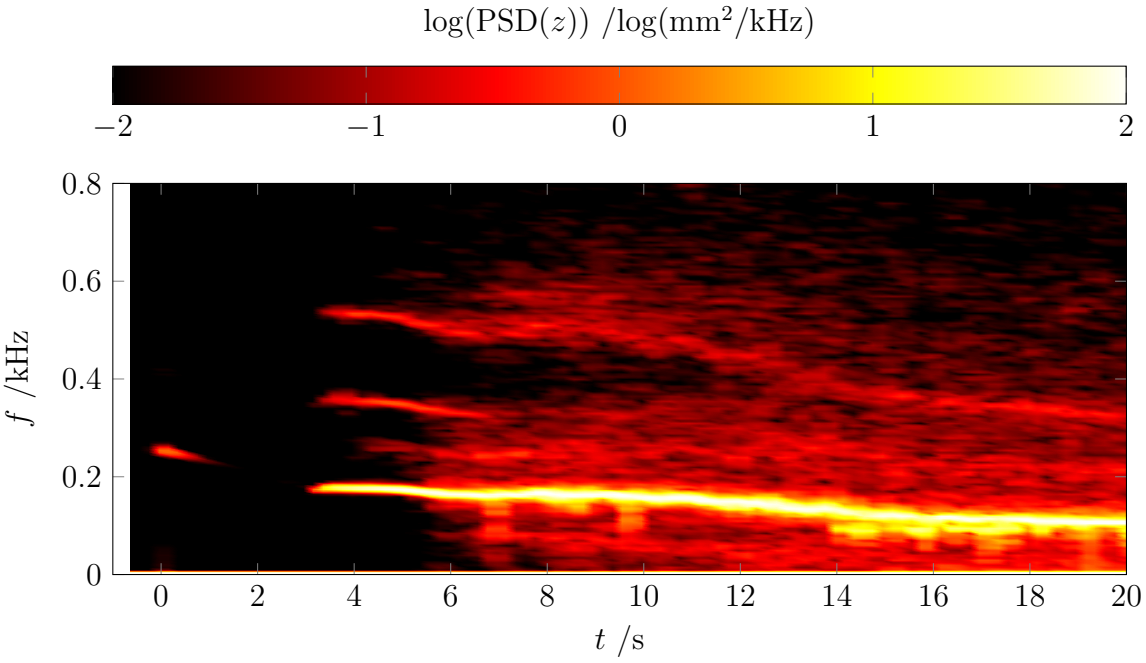


**(c)** PSD of the center displacement

**Figure 4.20:** Panel displacement for 0.3 mm panel no. 2 without shock generator – $T_0 + 20\,\mathrm{K}$ (run 106)

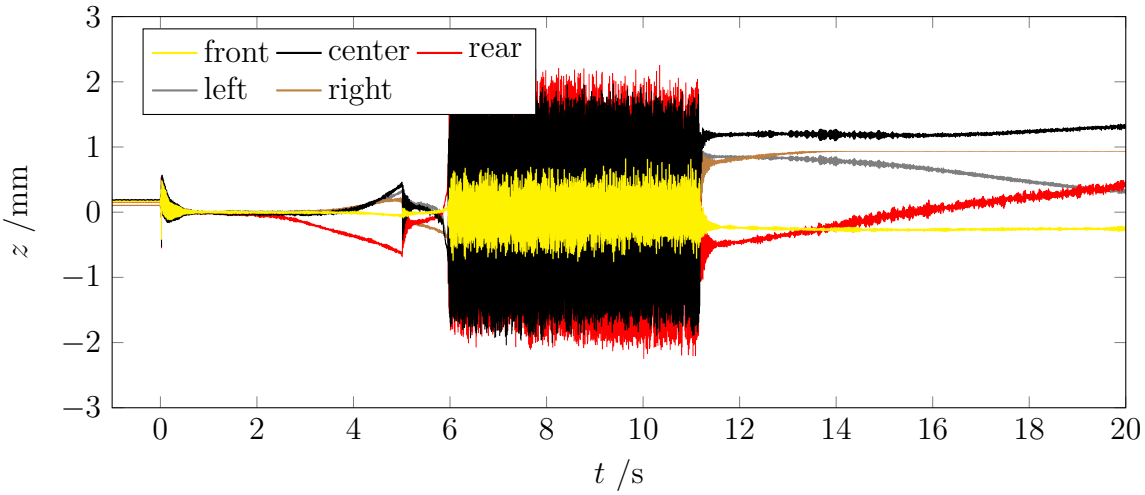


**(a)** Time series plot of the panel displacement

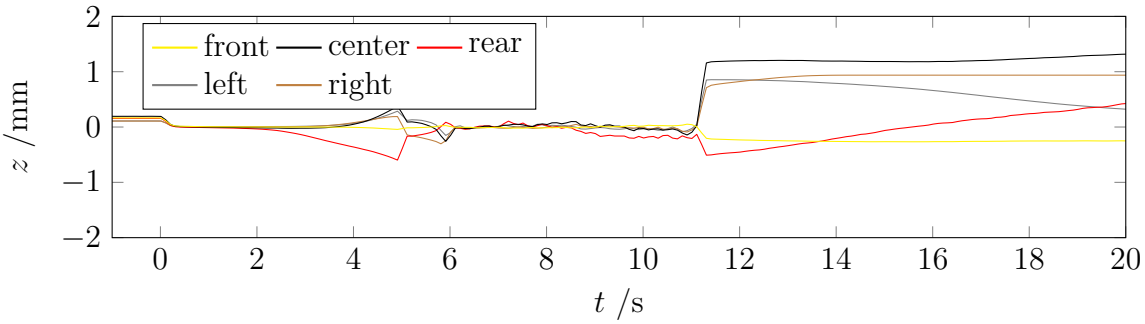


**(b)** Moving average of the panel displacement

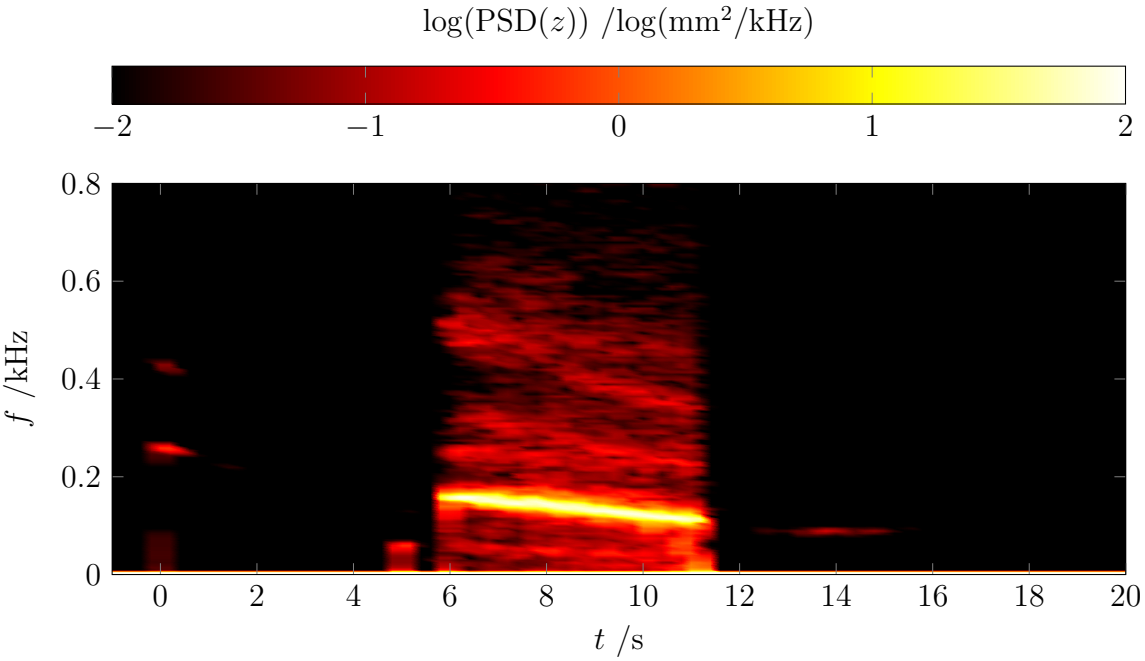


**(c)** PSD of the center displacement

**Figure 4.21:** Panel displacement for 0.3 mm panel no. 2 without shock generator – $T_0 + 40\,\mathrm{K}$ (run 107)

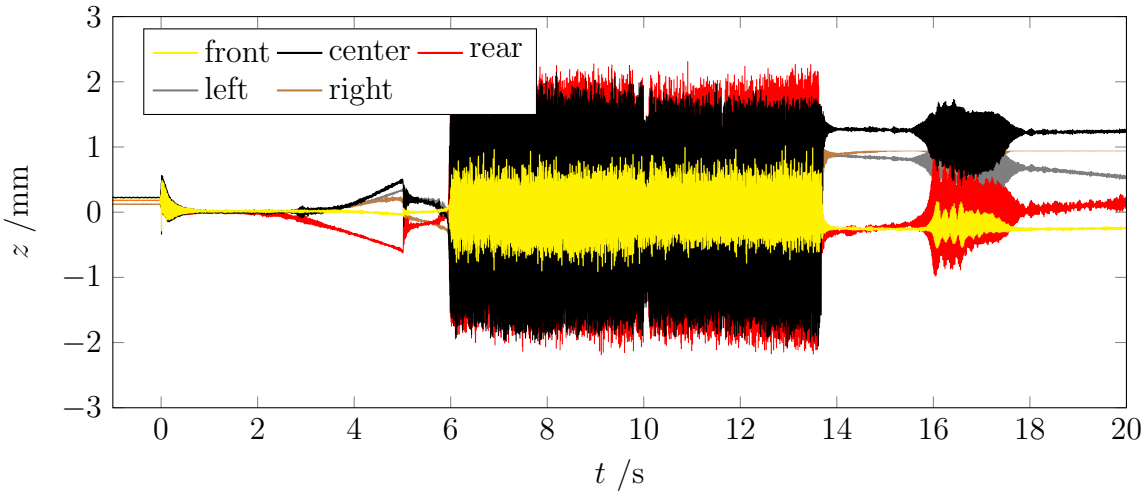


**(a)** Time series plot of the panel displacement

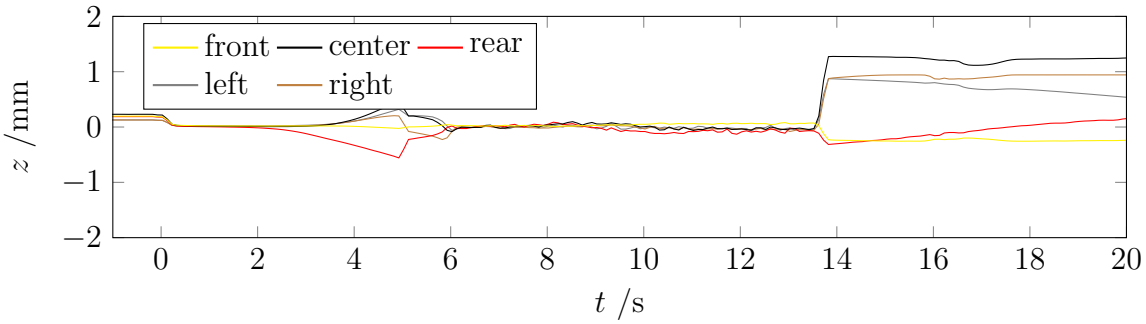


**(b)** Moving average of the panel displacement

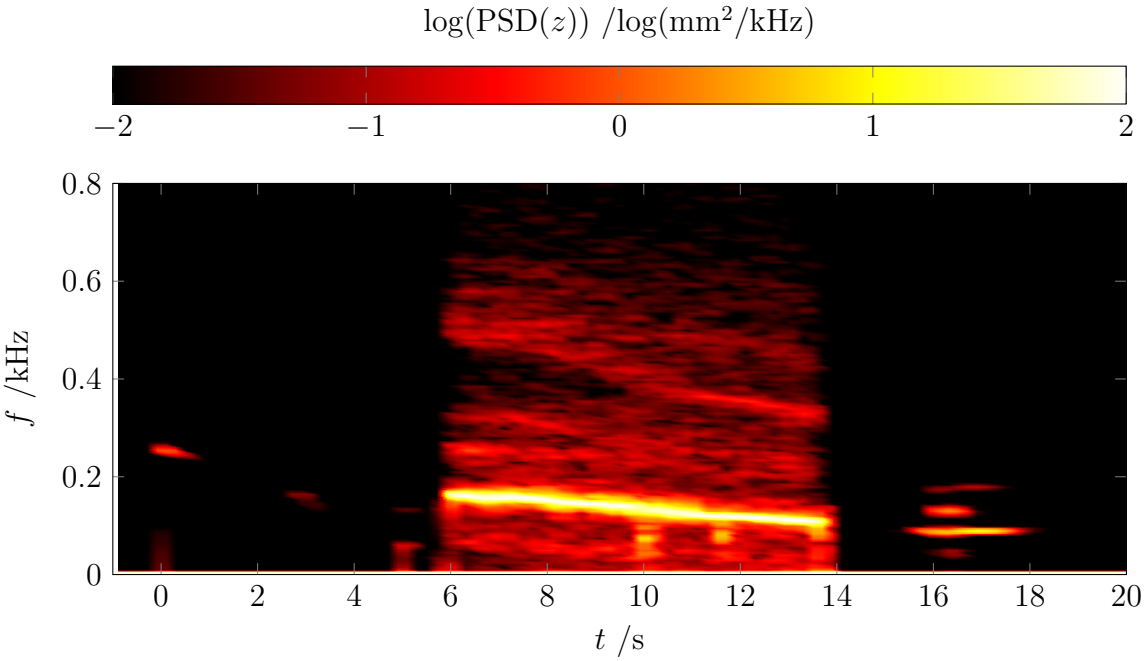


**(c)** PSD of the center displacement

**Figure 4.22:** Panel displacement for 0.3 mm panel no. 2 without shock generator – $T_0 + 40\,\mathrm{K}$ (run 108)

of large panel oscillations at $t = 6\,\mathrm{s}$, during which average deformation nearly disappears. Presumably, a buckled state remains, but is not detectable in the average deformation due to the oscillations. At about $t = 11\,\mathrm{s}$, oscillations cease and the panel assumes a buckled state that stiffens the panel sufficiently to end oscillations. This takes place while the wind tunnel is still running at constant conditions. This run was repeated at the same conditions and shows good agreement (Fig. 4.22). Interestingly, at about $t = 16\,\mathrm{s}$, a brief incident of oscillation takes place when the panel is already in a strongly buckled state.

### 4.2.3 FSI with Incident Shock

#### 0.5 mm Panel

In a next step, the panel thickness was changed and a variation of shock generator angles was investigated. Figures 4.23 and 4.24 show the deformation of the 0.5 mm panel during wind tunnel runs without shock generator and with various shock generator angles ($\alpha$). In a reference run without shock generator, moderate buckling occurred (Fig. 4.23a). In contrast to the previous runs with the 0.3 mm panel, no significant dynamics took place for the configuration without shock generator due to the increased stiffness of the thicker panel.

Figure 4.23b shows the results after addition of a shock generator at $\alpha = 15°$. The cavity pressure for all runs with shock generator is set to the average wall pressure on the rigid wall for the respective shock generator angle (Figs. 4.6 and 4.7). Thus, the deformation of the panels towards the test section before flow startup ($t < 0\,\mathrm{s}$) is greater for runs with shock generator. After the flow is started, the panels generally assume a deformed state where the front position moves up (positive $z$-direction) and the center and rear parts of the panel deform into the cavity. Initially, this is only due to the pressure distribution caused by the SWBLI (see Figs. 4.6 and 4.7 for the respective pressure distributions on the rigid wall). During the wind tunnel run, the occurring thermal buckling increases drastically compared to the first run without shock generator and adds to the initial pressure-induced panel deformation by thermal expansion of the panel. This corresponds to the significant change in $T_w$ caused by the incident shock and SWBLI (see Figs. 4.8a and 4.10a for the respective temperature distributions on the rigid wall). Also there is an increase in panel dynamics, but the amplitude is very low.

Figures 4.23c and 4.24a show runs with $\alpha = 17.5°$. In these runs, large panel oscillations with amplitudes of several millimeters set in directly after flow startup. Throughout the run, these oscillations decrease while the panel shows thermal buckling to an even greater extent than in the runs with $\alpha = 15°$, which is consistent with the increased wall temperatures reached with $\alpha = 17.5°$ (Fig. 4.10b). Repeatability between the two runs is very good. For the next run (Fig. 4.24b), the shock generator angle was increased further to $\alpha = 20°$. Interestingly, panel dynamics also start immediately when the wind tunnel flow starts, but amplitudes are considerably lower than in the previous case and again, dynamics decline as the panel buckles during the run.

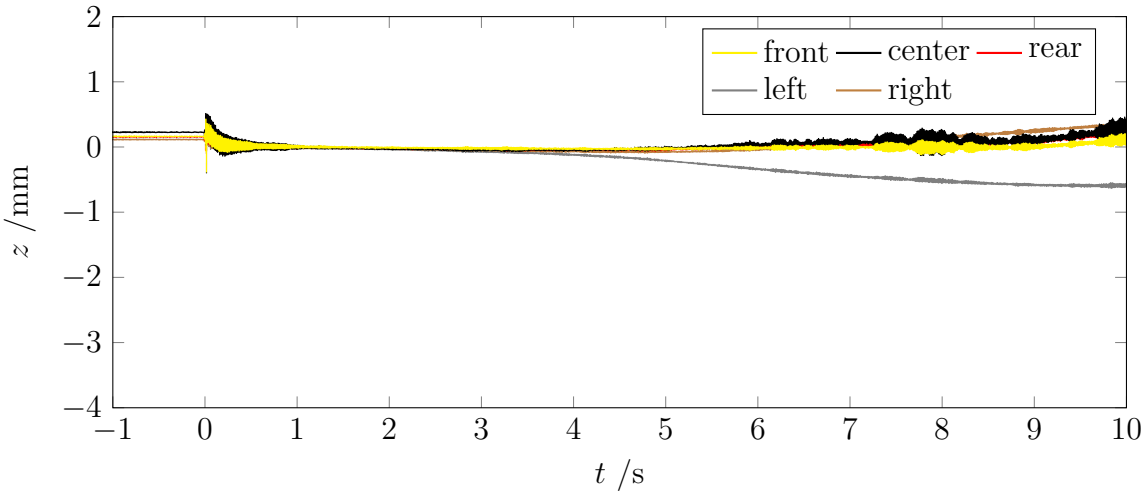


**(a)** Time series plot of the panel displacement without shock generator (run 85)

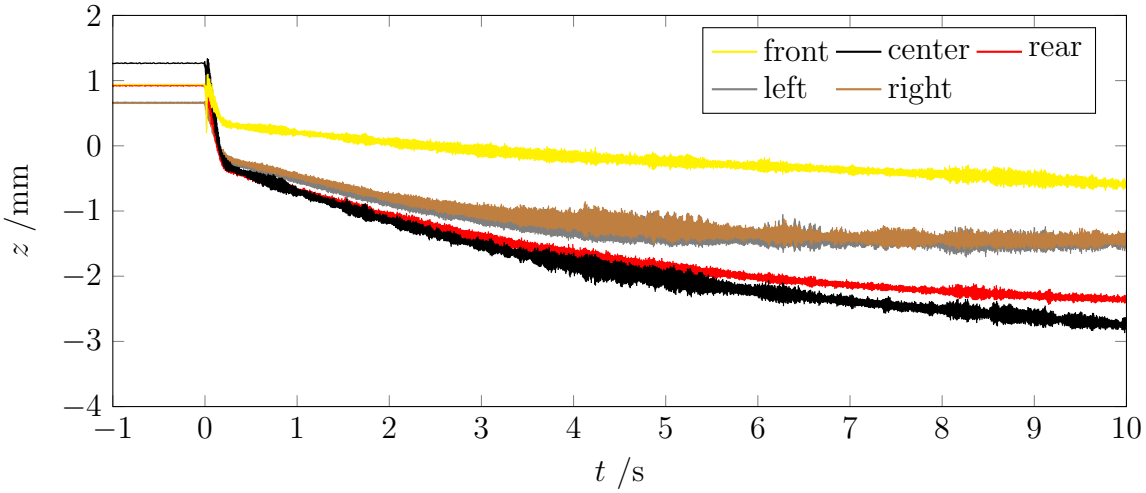


**(b)** Time series plot of the panel displacement at $\alpha = 15°$ (run 87)

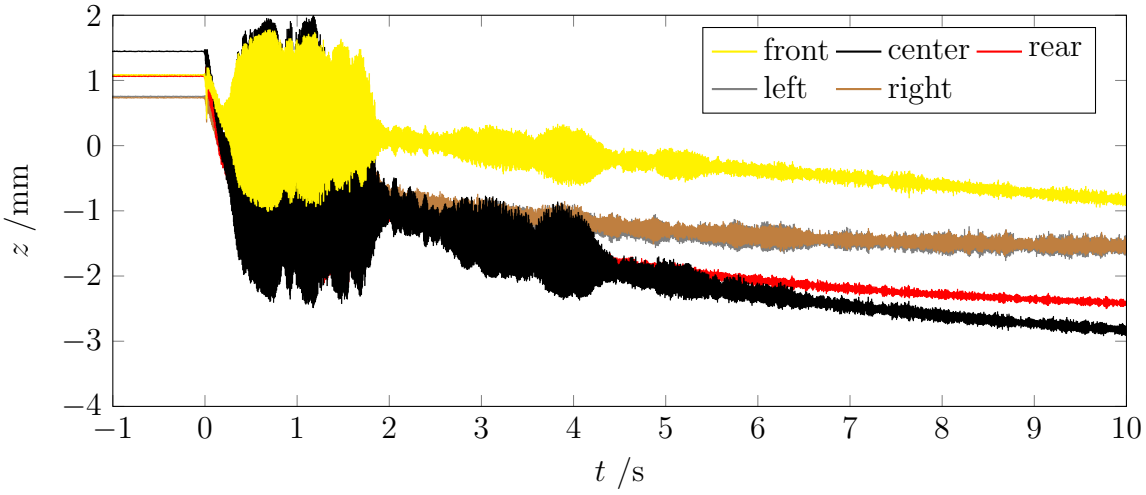


**(c)** Time series plot of the panel displacement at $\alpha = 17.5°$ (run 88)

**Figure 4.23:** Panel displacement for a 0.5 mm panel with and without shock generator

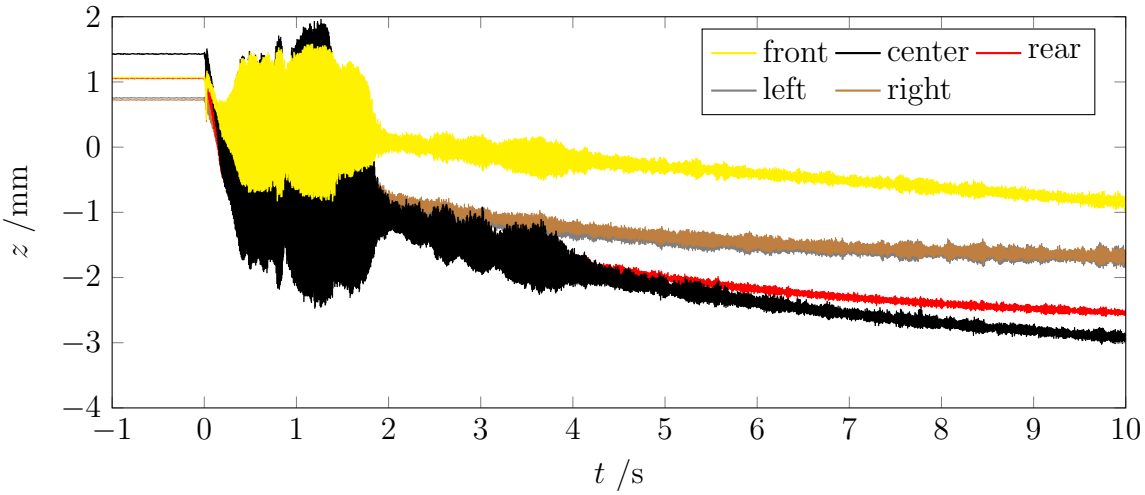


**(a)** Time series plot of the panel displacement at $\alpha = 17.5°$ (run 89)

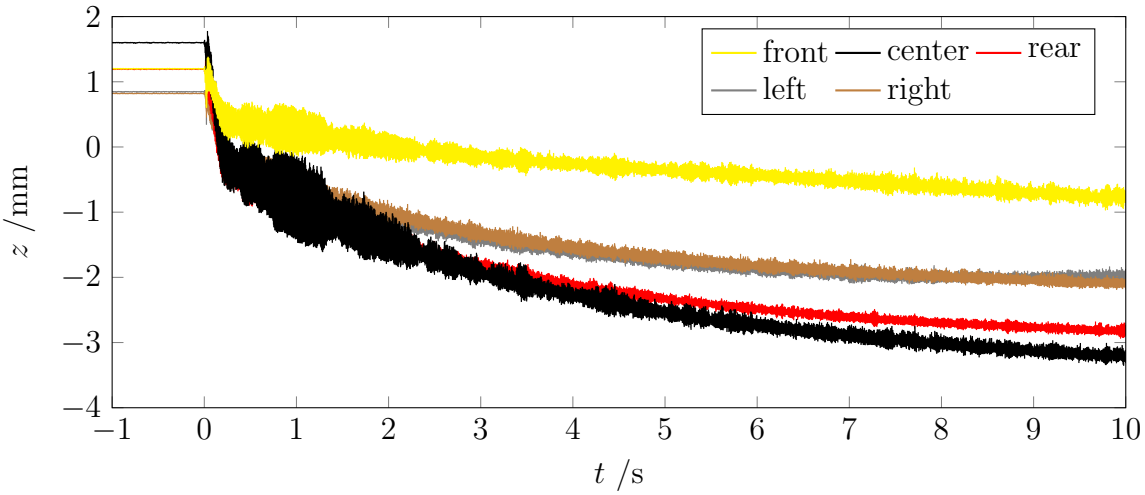


**(b)** Time series plot of the panel displacement at $\alpha = 20°$ (run 90)

**Figure 4.24:** Panel displacement for a 0.5 mm panel with shock generator

**Table 4.6:** Computed panel modes for the 0.7 mm panel (number of neutral lines in x;y-direction)

| | Panel modes | | | | | | | | |
|---|---|---|---|---|---|---|---|---|---|
| Mode (x;y) | 0;0 | 1;0 | 0;1 | 1;1 | 2;1 | 2;1 | 4;0 | 0;2 | 1;2 |
| $f$ /Hz | 231 | 337 | 439 | 478 | 520 | 642 | 650 | 715 | 787 |

These runs with the 0.5 mm panel demonstrate that the incident shock configuration leads to flutter in cases where is does not occur without incident shock, but also that an increase in incident shock angle can reduce or suppress flutter. Furthermore, the increase in thermal buckling of the panel with rising incident shock angle shows the effect of the heat flux augmentation caused by the SWBLI also increasing with rising incident shock angle.

### 0.7 mm Panel

After a wide variety of panel dynamics was observed for the 0.3 mm and 0.5 mm panels, panel thickness is further increased to 0.7 mm. Figures 4.25 to 4.35 show results from wind tunnel runs with a 0.7 mm panel with and without shock generator. Figures 4.25a to 4.25c show time series plots for runs with the 0.7 mm panel without shock generator. Again, the panel is slightly deformed towards the test section before flow startup and then assumes an undeformed position. Towards the end of the run, well visible from about $t = 12$ s, the panel starts to buckle due to the thermal expansion of the panel. Interestingly, the timing of the onset of panel buckling is similar in all three cases whereas the direction and amplitude vary. This is seen as positive regarding the quality of the manufactured panel, e. g. a panel that shows initial deformation after manufacturing is likely to clearly show a preferred direction of buckling. Also, this is once a again a good example of the difficulty of predicting the behavior of a real structure. Similar to the 0.5 mm panel, no significant panel dynamics occur.

Figures 4.25d and 4.26 show the PSD of the displacement measurements directly after flow startup to characterize panel dynamics of the mounted panel in cold condition without pressure difference across the panel. In Fig. 4.25d, this is compared to an ANSYS solution (Tab. 4.6) as described in Section 4.1.4. Good agreement was achieved regarding the predicted frequencies of the lower modes. Furthermore, the modes can clearly be attributed to the PSD of the panel displacment. For example, the 0;0 mode at 231 Hz leads to large amplitudes at all locations, while the 0;1 mode at 439 Hz mostly shows up at the left and right positions consistent with its neutral line in $y$-direction.

Figure 4.26 shows spectra from the runs before and after the runs with high amplitude dynamics (Figs. 4.27 to 4.35). The good agreement in the spectra before and after these runs suggests that the panel has not been substantially damaged in the course of these runs. Some differences occur around 0.7 kHz, but orders of magnitude lower than the dynamics at lower panel modes (note the logarithmic scale). The complete disappearance

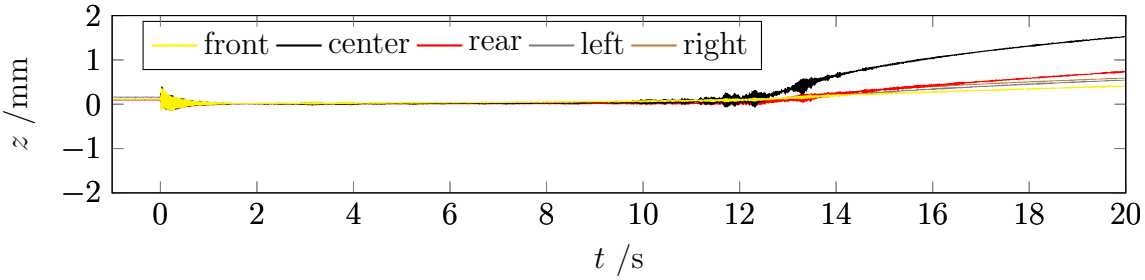


**(a)** Time series plot of the panel displacement without shock generator (run 91)

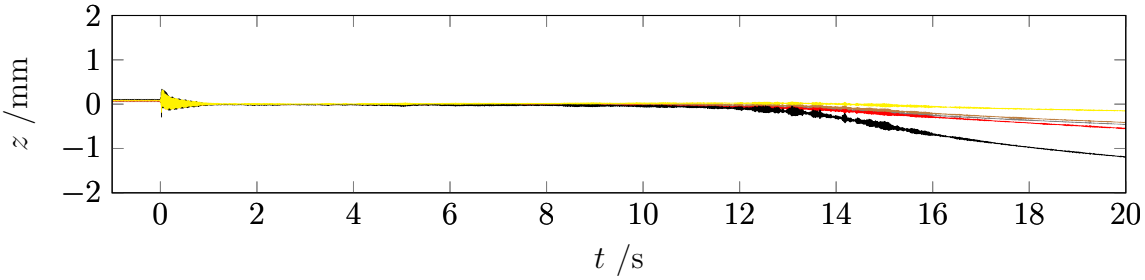


**(b)** Time series plot of the panel displacement without shock generator (run 92)

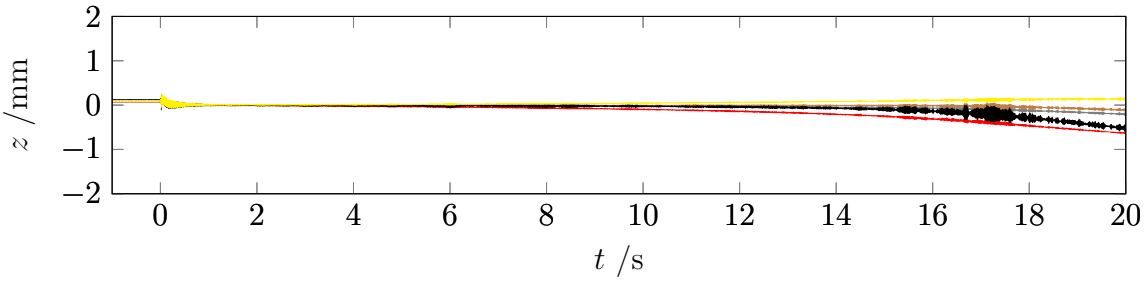


**(c)** Time series plot of the panel displacement without shock generator (run 101)

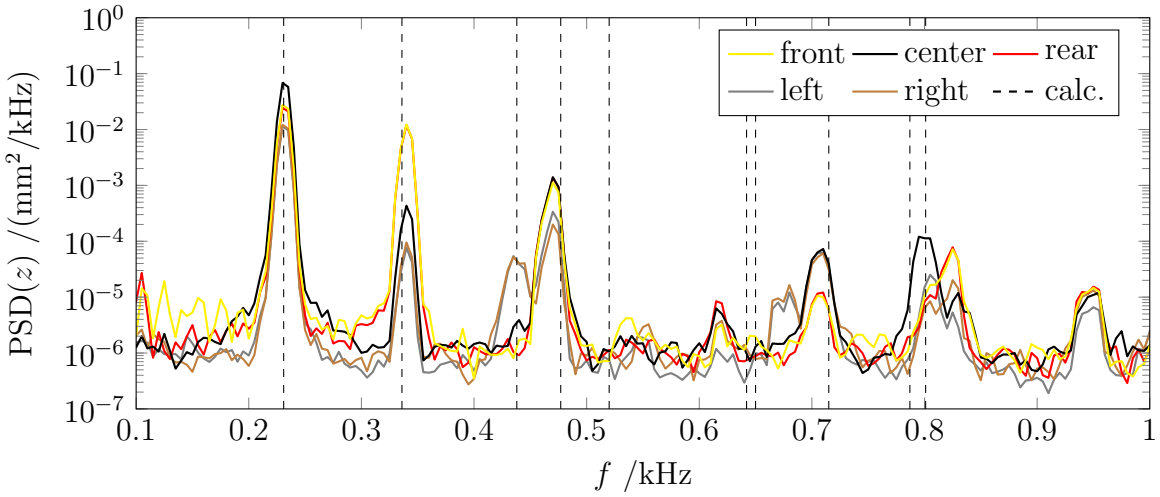


**(d)** PSD of the panel displacement (run 91)

**Figure 4.25:** Panel displacement for a 0.7 mm panel without shock generator

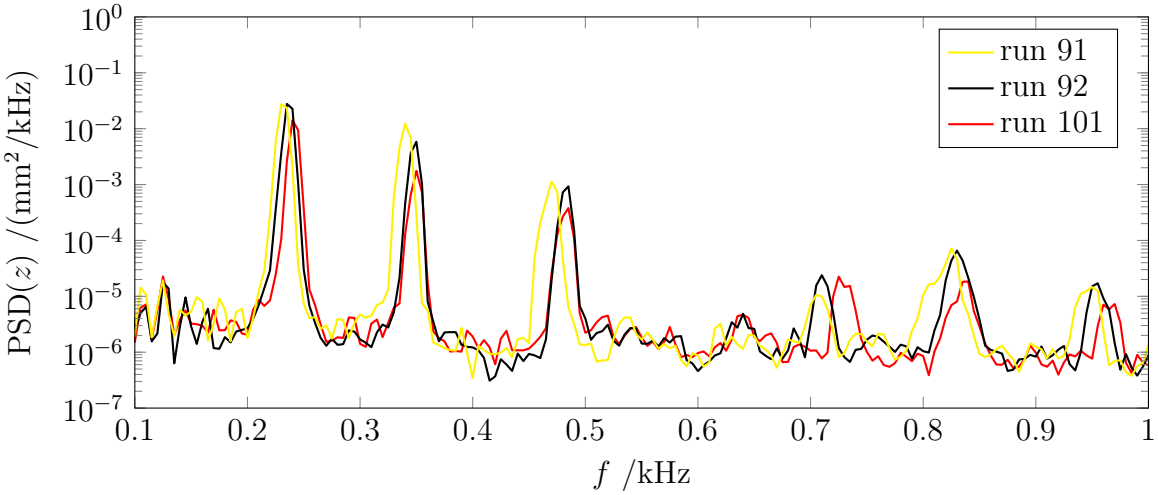


**(a)** PSD of the panel displacement at the front position

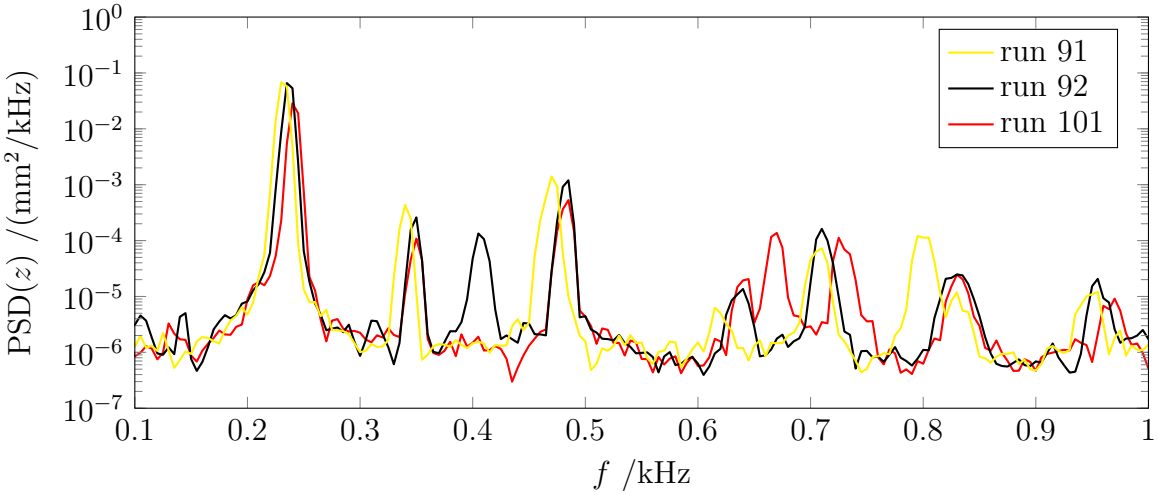


**(b)** PSD of the panel displacement at the center position

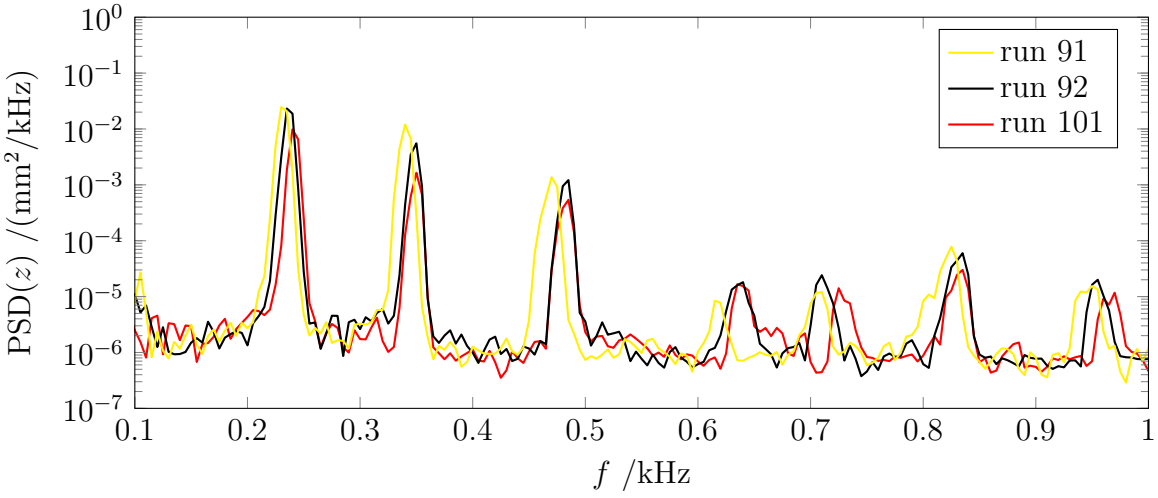


**(c)** PSD of the panel displacement at the rear position

**Figure 4.26:** PSD of panel displacement for a 0.7 mm panel without shock generator (run 91, 92, 101)

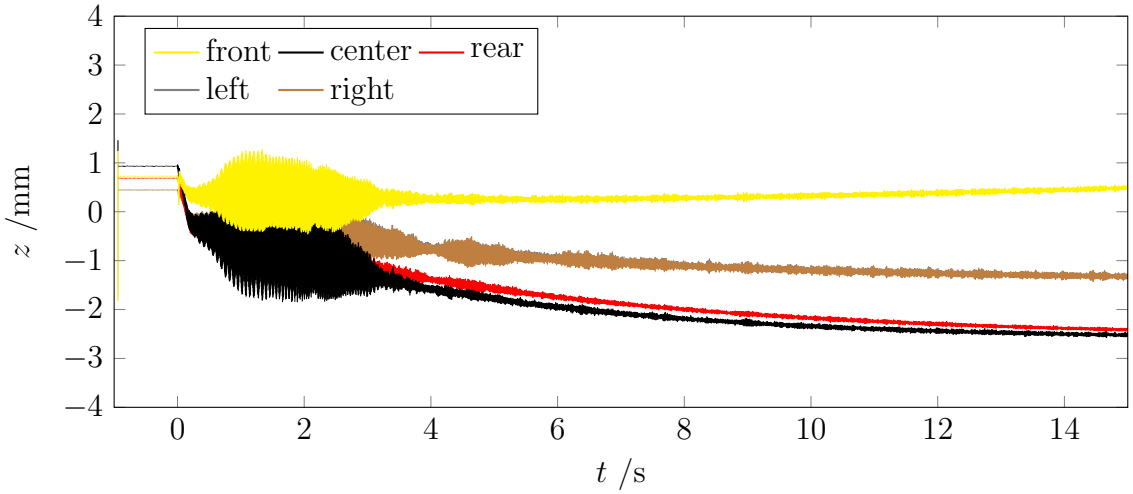


**(a)** Time series plot of the panel displacement

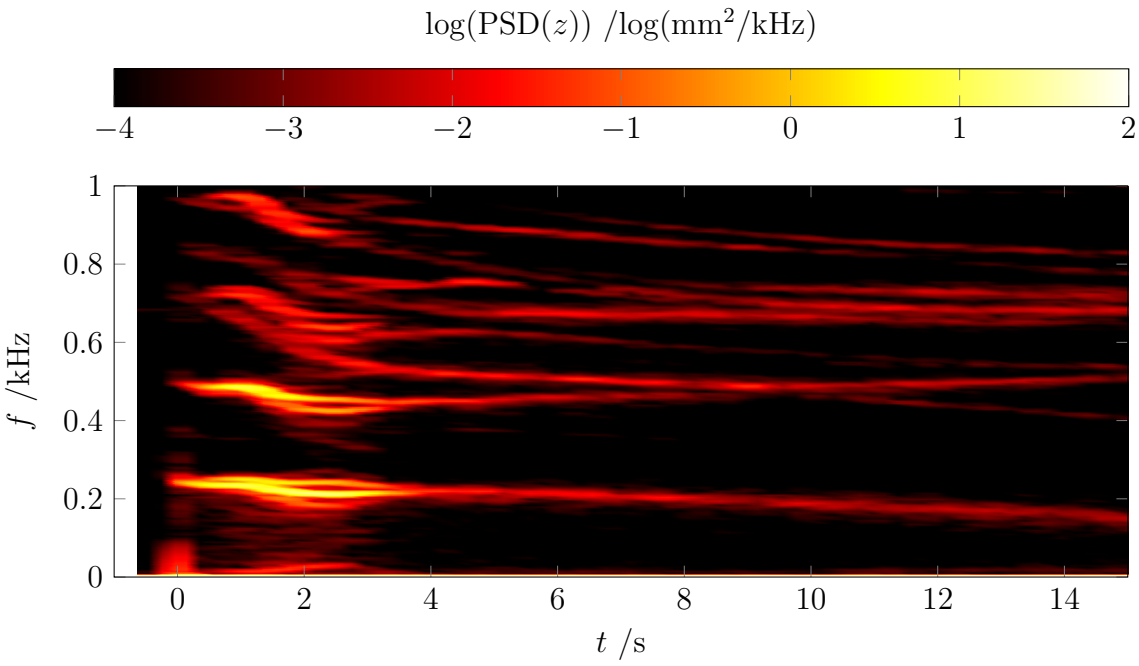


**(b)** PSD of the center displacement

**Figure 4.27:** Panel displacement for a 0.7 mm panel with shock generator at $\alpha = 17.5°$, $\Delta x = 0$ mm (run 93)

of panel deformation after cool-down after each wind tunnel run is monitored as additional health check.

Figure 4.27 shows a time series plot and spectrogram of a wind tunnel run with the 0.7 mm panel with shock generator at $\alpha = 17.5°$. After flow startup, the panel assumes a deformed state with the upstream part of the panel (front sensor) bending into the flow and the rest of the panel deformed into the cavity caused by the pressure distribution in the SWBLI. This deformation continues to increase throughout the run, but at a declining rate of change. This is due to the heating of the panel structure. Dynamics with a maximum amplitude of about 2 mm set in shortly after flow startup, reaching a maximum between about $t = 1\,\mathrm{s}$ and $t = 2\,\mathrm{s}$ and mostly subsiding around $t = 4\,\mathrm{s}$ due to the increased stiffness of the structure caused by the deformation. This again demonstrates that the incident shock facilitates structural dynamics where they would not occur otherwise. The amplitude of the panel dynamics, as expected, is lower than for the same configuration with 0.5 mm panel (Figs. 4.23c and 4.24a).

### Variation of the Shockgenerator Position for the 0.7 mm Panel

Figures 4.28 to 4.35 show the results from various wind tunnel runs with an increased shock generator angle of $\alpha = 20°$. Generally, unlike for the 0.5 mm panel, the increase in incident shock angle from $\alpha = 17.5°$ to $\alpha = 20°$ leads to an increase in panel dynamics. This shows that, depending on the configuration, an increase in incident shock angle can both inhibit and facilitate structural dynamics.

In the runs shown in Figs. 4.28 to 4.35, the shock generator at $\alpha = 20°$ is placed at several $x$-positions starting with the nominal position ($\Delta x = 0\,\mathrm{mm}$) with impingement in the panel center. From there it is moved downstream by $\Delta x$ relative to the nominal position to investigate the effect of the resulting change in static (Figs. 4.6 and 4.7) and dynamic (Figs. 4.14 and 4.15) pressure loads as well as structural heating (Figs. 4.11 and 4.12).

Figure 4.28 shows a wind tunnel run with shock generator at nominal position (shock impingement at $x = 150\,\mathrm{mm}$). As in the previously discussed runs, the panel is deformed towards the test section before flow startup because of the pre-set pressure in the cavity. As the flow is started, the panel assumes a deformed position with the upstream part of the panel (front sensor) deforming into the flow and all other positions deforming away from the flow caused by the wall pressure distribution in the SWBLI. As expected, the deformation in the center is greater than at the sides. With the shock generator moved downstream (Figs. 4.30a, 4.31a, 4.33a and 4.34a) the maximum of the deformation into the cavity moves downstream as well. It reaches a maximum amplitude at the center position for a shock generator position of $\Delta x = 25\,\mathrm{mm}$ shown in Fig. 4.30a. When the shock generator is moved further downstream, the absolute deformation is reduced (Figs. 4.31a, 4.33a and 4.34a) as the wall pressure rise caused by the SWBLI is shifted downstream and partly off the elastic area. For the rearmost position of the shock generator ($\Delta x = 100\,\mathrm{mm}$), the panel is only deformed into the cavity at the rear sensor position, but into the flow on all other positions.

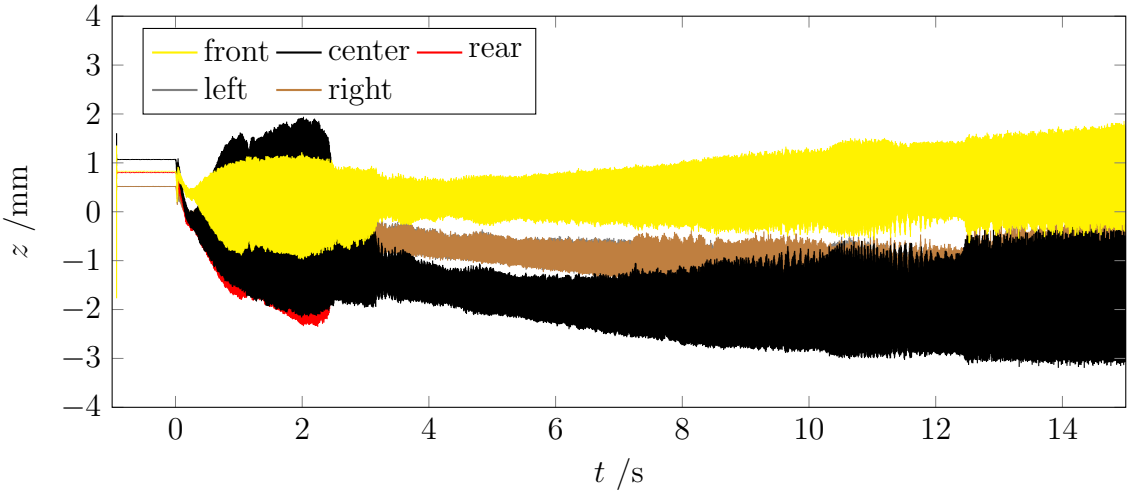


**(a)** Time series plot of the panel displacement

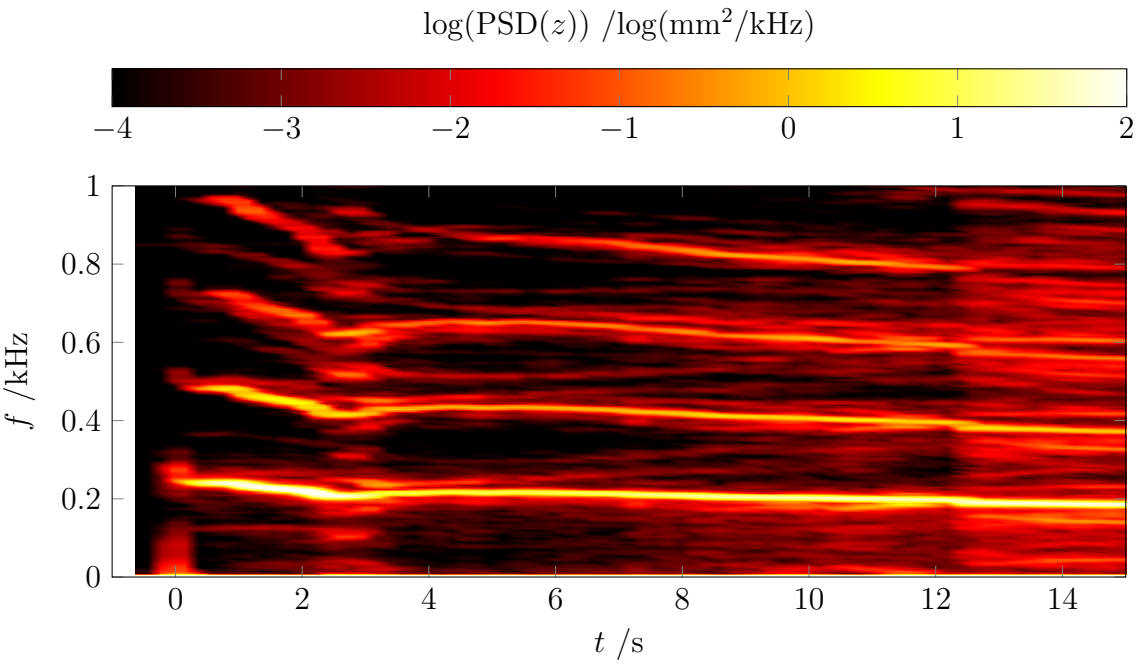


**(b)** PSD of the center displacement

**Figure 4.28:** Panel displacement for a 0.7 mm panel with shock generator at $\alpha = 20°$, $\Delta x = 0$ mm (run 95)

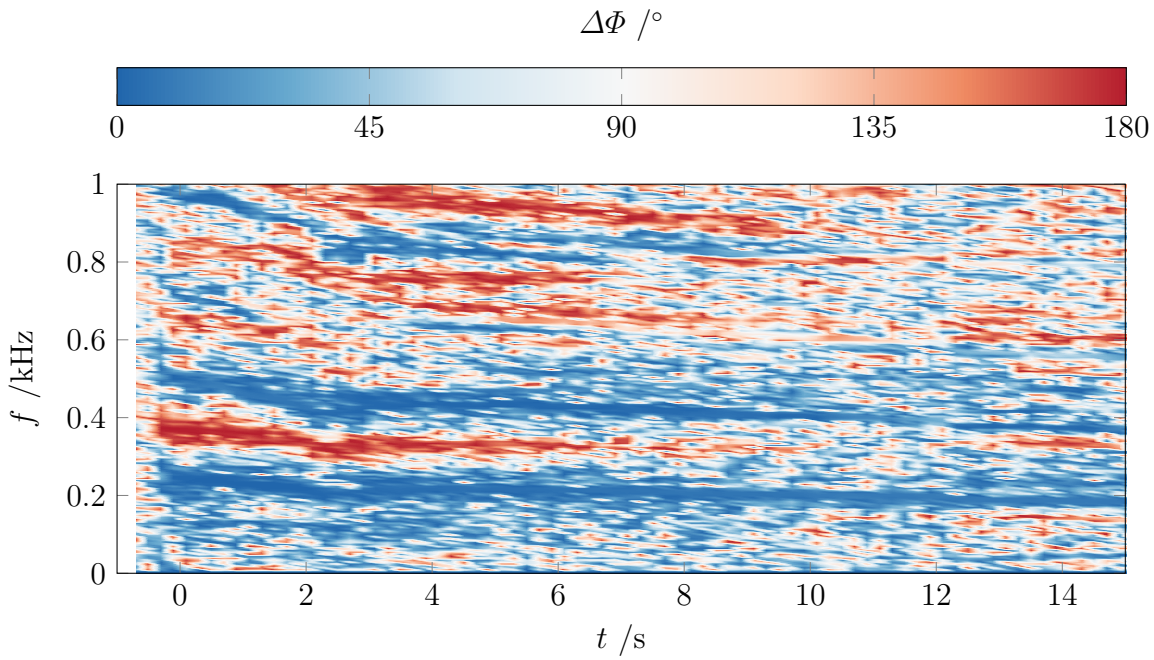


**(a)** Phase difference between front and rear displacement signals

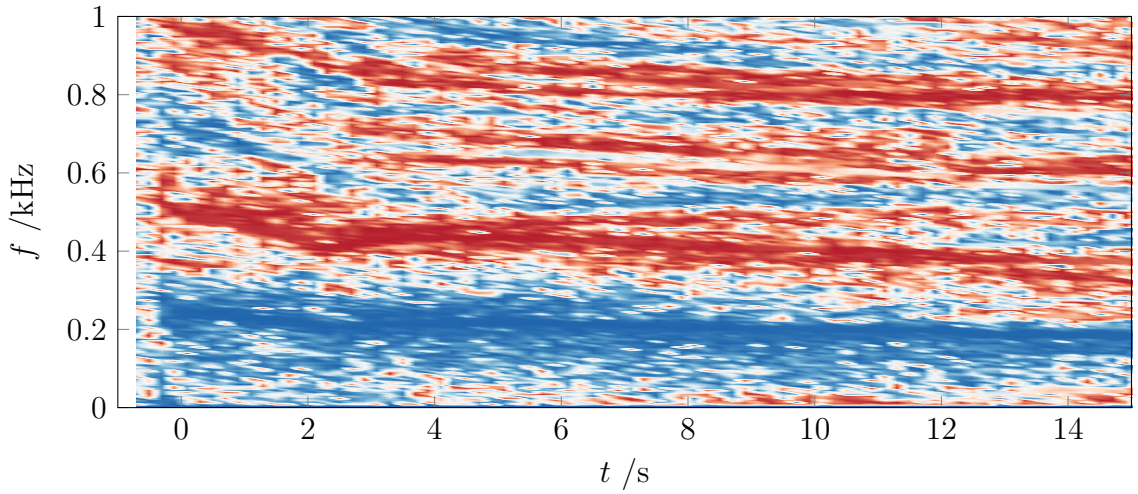


**(b)** Phase difference between front and center displacement signals

**Figure 4.29:** Panel displacement for a 0.7 mm panel with shock generator at $\alpha = 20°$, $\Delta x = 0$ mm (run 95)

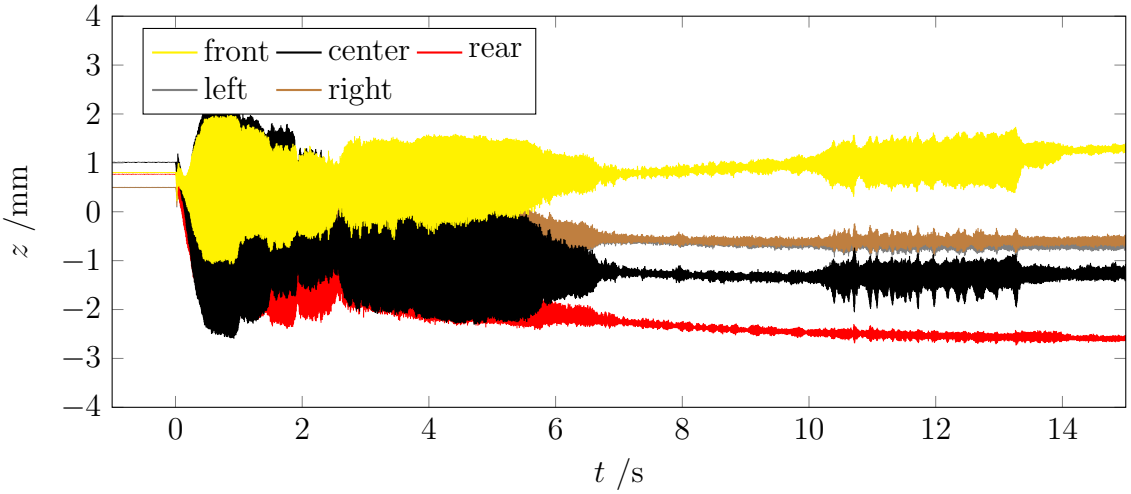


**(a)** Time series plot of the panel displacement

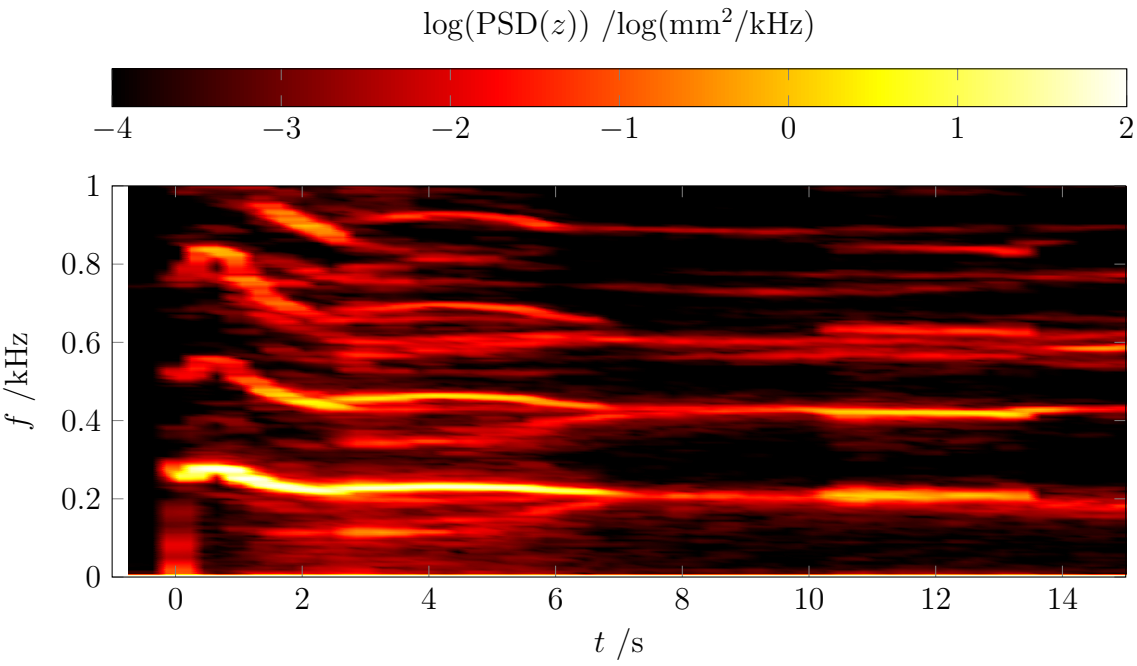


**(b)** PSD of the center displacement

**Figure 4.30:** Panel displacement for a 0.7 mm panel with shock generator at $\alpha = 20°$, $\Delta x = 25\,\text{mm}$ (run 96)

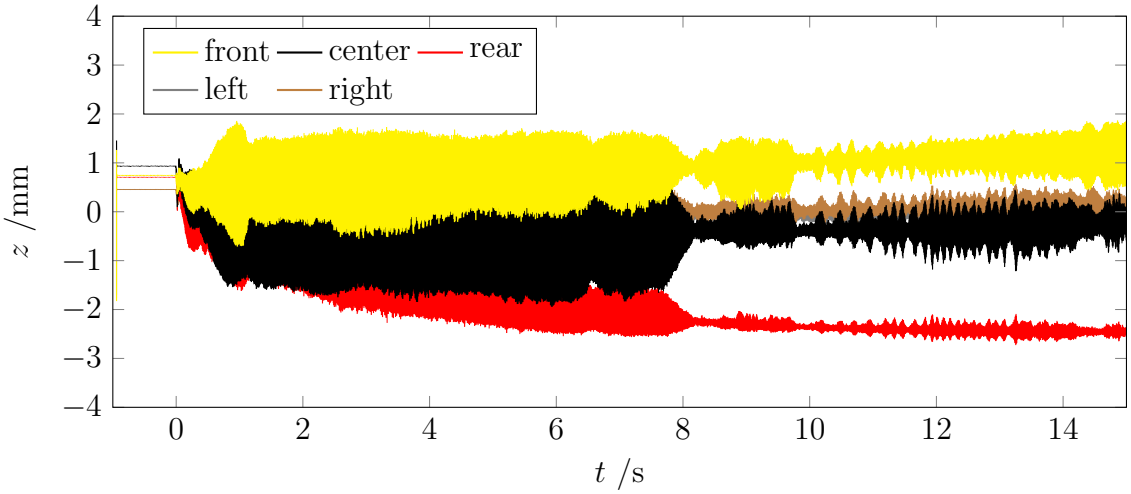


**(a)** Time series plot of the panel displacement

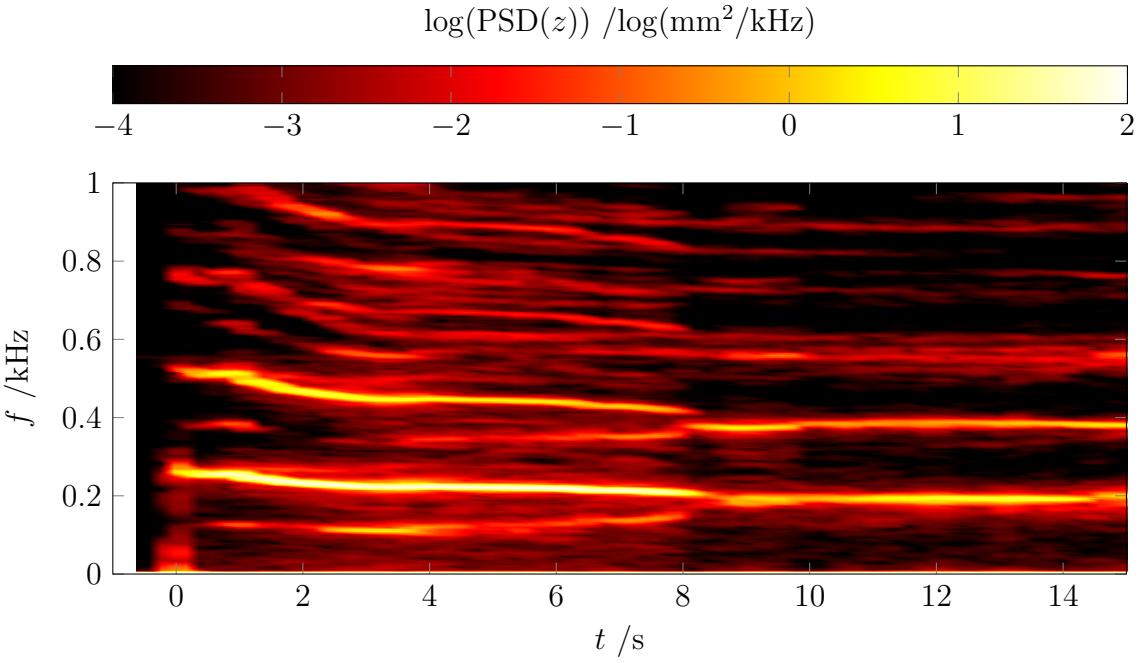


**(b)** PSD of the center displacement

**Figure 4.31:** Panel displacement for a 0.7 mm panel with shock generator at $\alpha = 20°$, $\Delta x = 50\,\text{mm}$ (run 100)

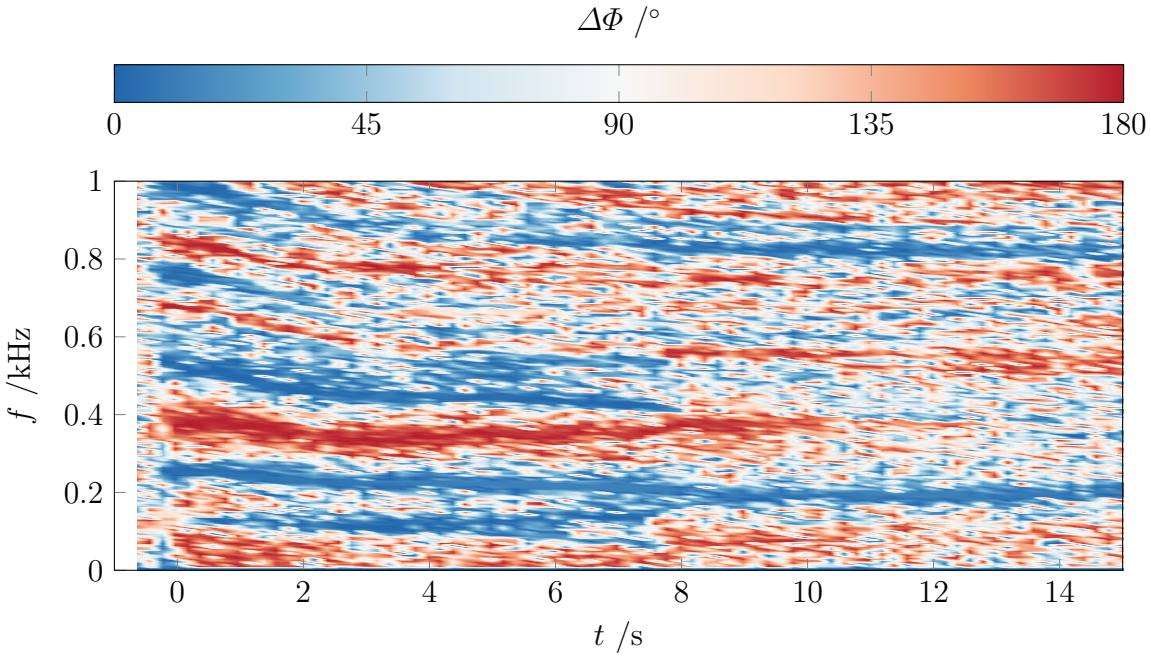


**(a)** Phase difference between front and rear displacement signals

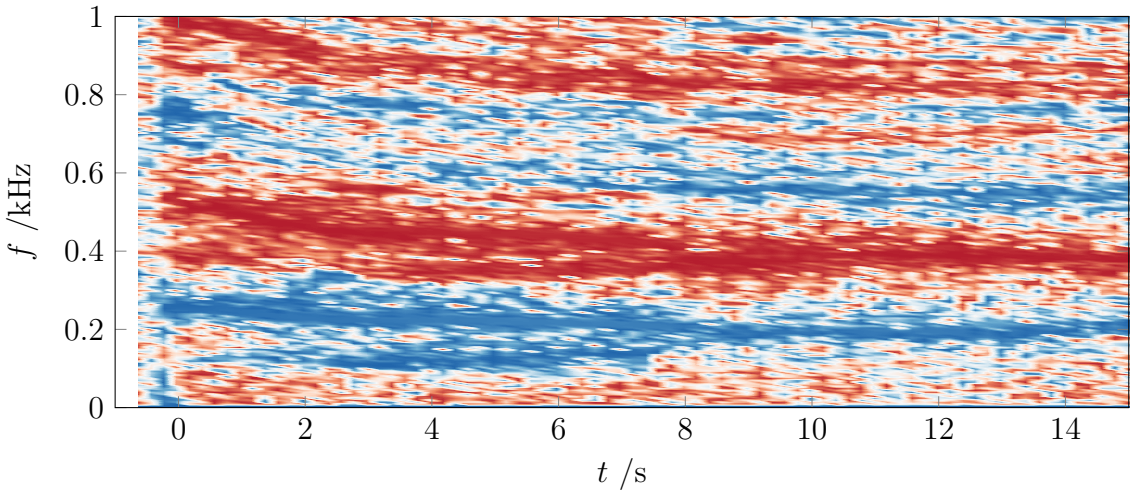


**(b)** Phase difference between front and center displacement signals

**Figure 4.32:** Panel displacement for a 0.7 mm panel with shock generator at $\alpha = 20°$, $\Delta x = 50\,\text{mm}$ (run 100)

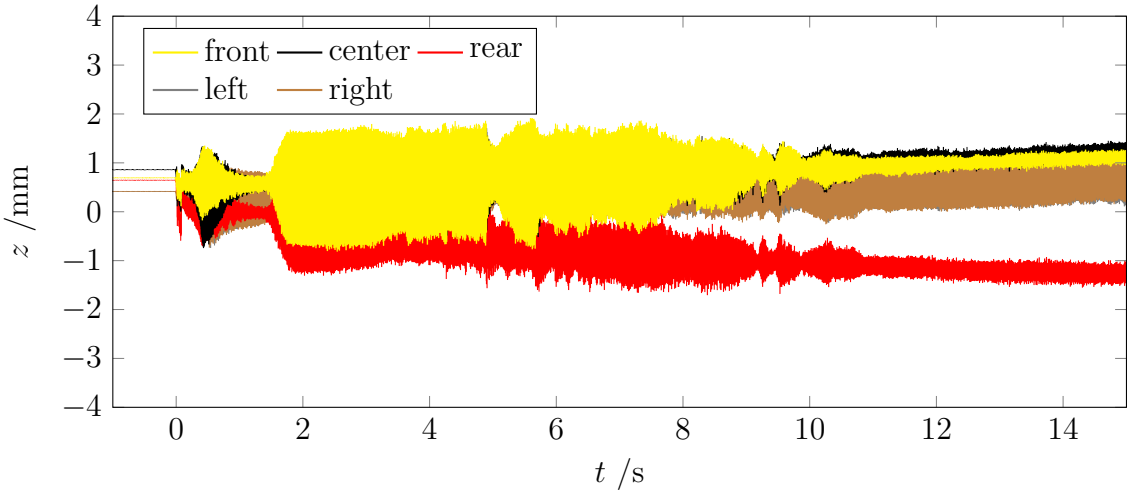


**(a)** Time series plot of the panel displacement

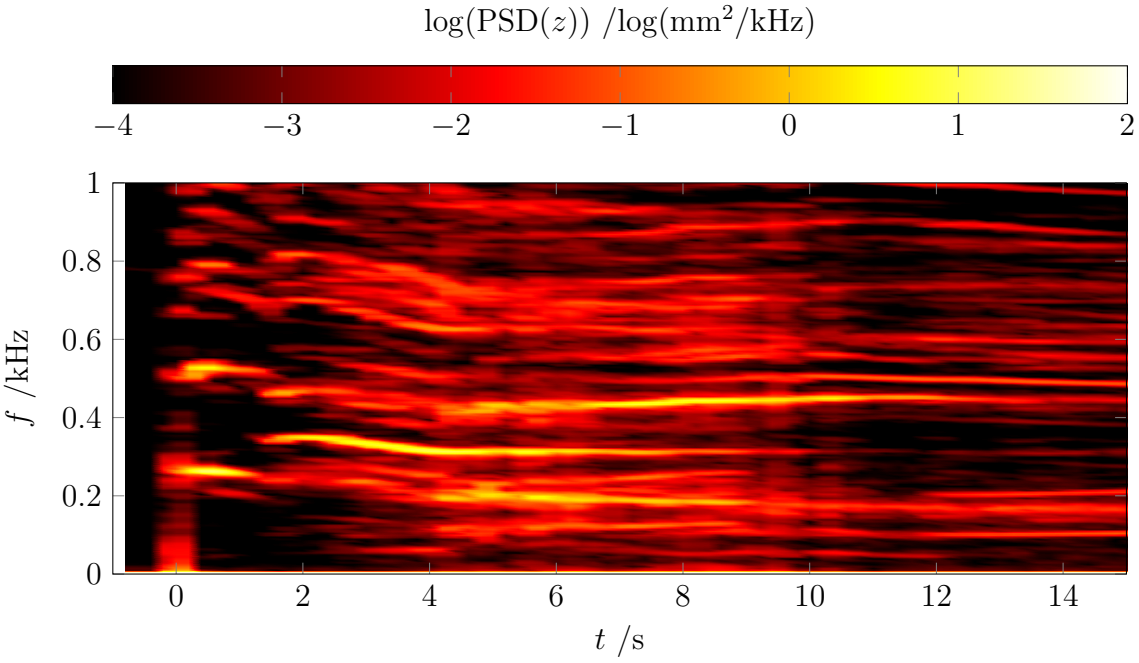


**(b)** PSD of the center displacement

**Figure 4.33:** Panel displacement for a 0.7 mm panel with shock generator at $\alpha = 20°$, $\Delta x = 100\,\text{mm}$ (run 98)

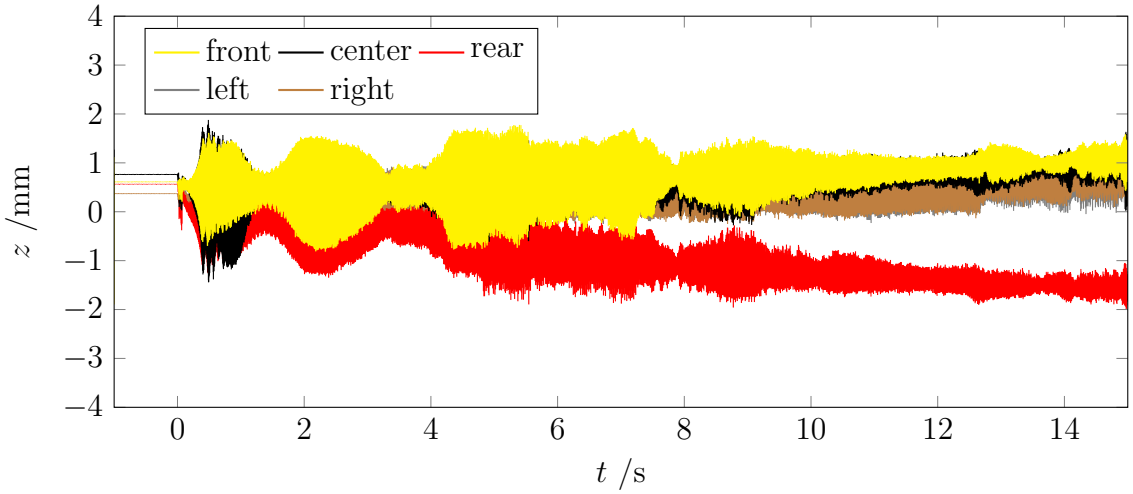


**(a)** Time series plot of the panel displacement

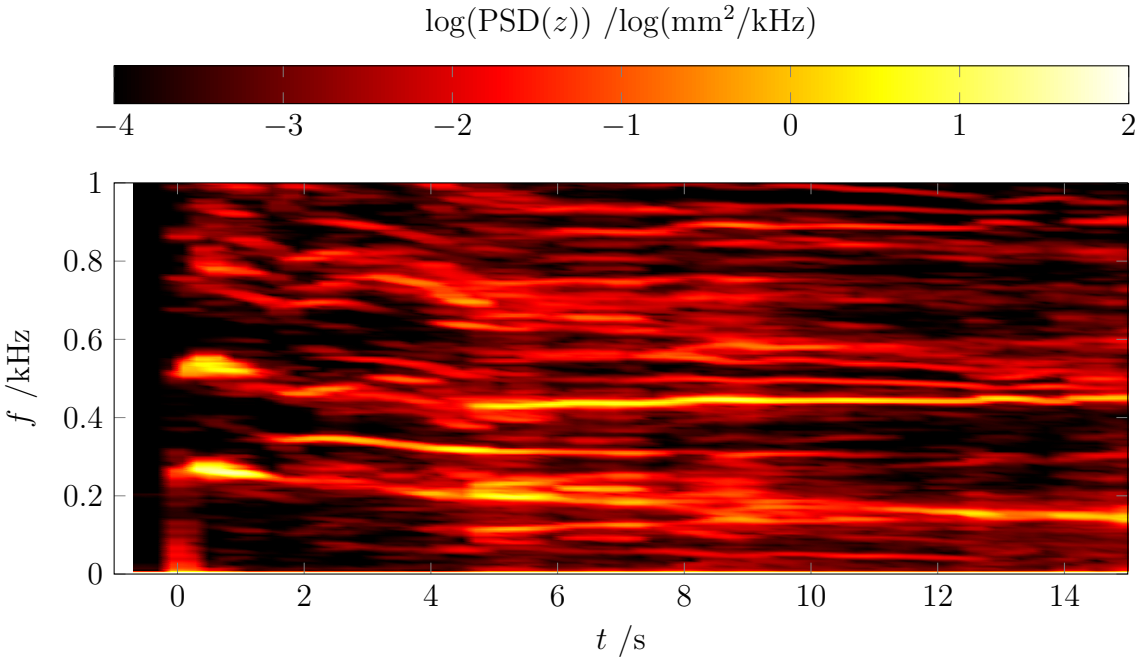


**(b)** PSD of the center displacement

**Figure 4.34:** Panel displacement for a 0.7 mm panel with shock generator at $\alpha = 20°$, $\Delta x = 100\,\text{mm}$ (run 99)

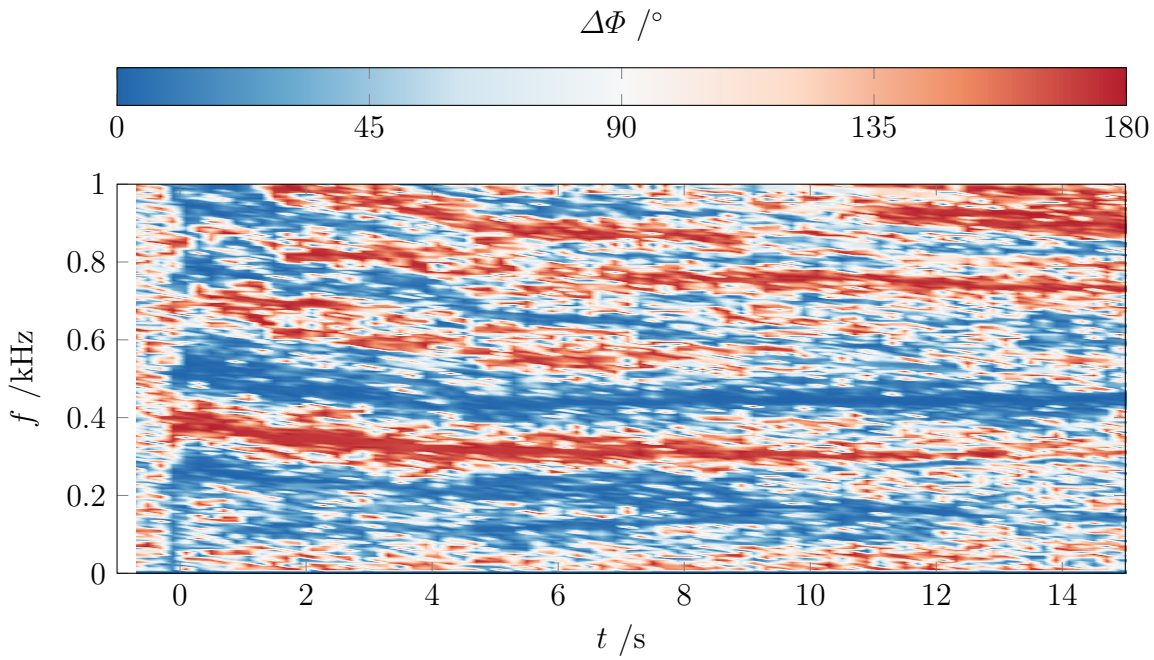


**(a)** Phase difference between front and rear displacement signals

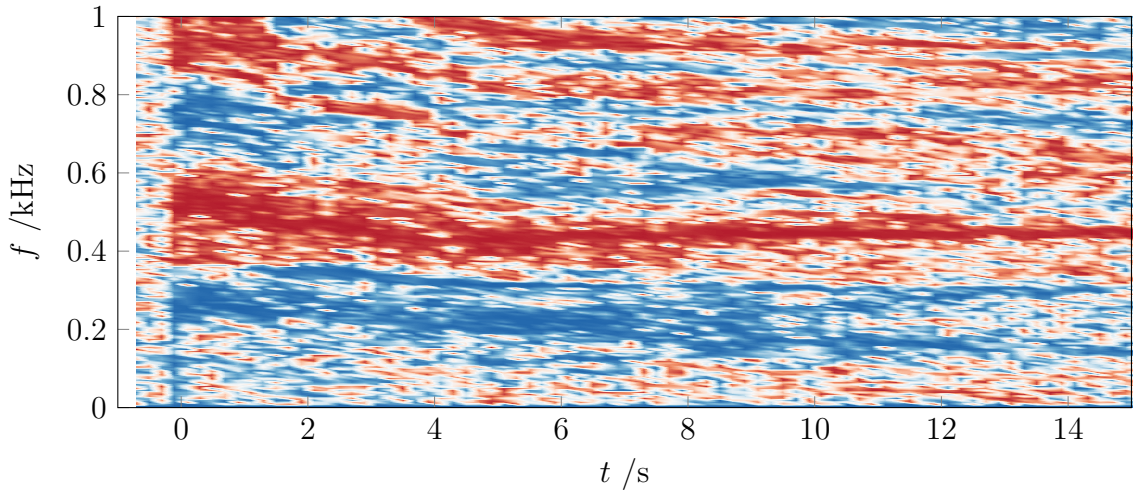


**(b)** Phase difference between front and center displacement signals

**Figure 4.35:** Panel displacement for a 0.7 mm panel with shock generator at $\alpha = 20°$, $\Delta x = 100\,\text{mm}$ (run 99)

The presence of the SWBLI at various positions leads to different dynamic behavior of the structure. Throughout the wind tunnel runs, the properties of the panel are further changed by the heating of the structure which also strongly depends on the SWBLI. As shown in some of the previous cases, this can facilitate an increase in structural dynamics but can also lead to a stiffening of the elastic structure and consequently to a reduction of structural dynamics. Such a reduction of structural dynamics in the course of the wind tunnel run can be observed for all of the runs with the 0.7 mm panel and $\alpha = 20°$ except for $\Delta x = 0\,\mathrm{mm}$ (Fig. 4.28a), where dynamics increase throughout most of the wind tunnel run. With the shock generator moved downstream by just $\Delta x = 25\,\mathrm{mm}$ (Fig. 4.30a), dynamics almost ceased completely towards the end of the run, whereas large amplitude dynamics occurred for about $t = 6\,\mathrm{s}$ in the beginning of the run. For the runs with the shock generator at $\Delta x = 50\,\mathrm{mm}$ (Fig. 4.31a) and $\Delta x = 100\,\mathrm{mm}$ (Figs. 4.33a and 4.34a), amplitudes at the beginning of the wind tunnel run are lower than in the previous cases and mostly declining throughout the wind tunnel run but they do not subside entirely.

Further insight into the occurring structural dynamics is provided by the spectrograms for the respective cases. A general trend at many of the excited frequencies is the decrease of these frequencies as the panel heats up during the wind tunnel run (e. g. Fig. 4.28b). However, this is not always the case for all frequencies. In particular in run 96 (Fig. 4.30b) and run 100 (Fig. 4.31b), there appears to be a convergence of several pairs of two modes of which one declines in frequency while the other one rises till they converge at $t = 7\,\mathrm{s}$ and $t = 8\,\mathrm{s}$ respectively. It appears that this convergence coincides with a distinct decrease in oscillation amplitude (Figs. 4.30a and 4.31a). An interesting feature that becomes evident in the spectrograms is that for some configurations and conditions, large amplitude dynamics take place with relatively sharp peaks in PSD of the displacement (e. g. run 95, Fig. 4.28b) while similarly large dynamics occur with a significantly more broadband excitation of the structure for other configurations or even just thermal conditions of the panel (e. g. run 99, Fig. 4.34b). In the latter cases, distinct maxima at various frequencies are still visible, but the PSD in other areas is about an order of magnitude greater.

The phase plots shown were computed for the phase difference between the front and rear sensor as well as the front and center sensor. For example, a phase difference of 0° indicates that the signals are in phase, while a phase difference of 180° would indicate that they are opposite in phase. The result is considered relevant in areas where the respective spectrogram shows a significant result. Thus, the suggested way to read the diagrams is to identify the feature of interest in the PSD spectrogram and then consult the respective position in the phase diagram. In this way, the phase plots indicate that the maxima in the PSD spectrograms are linked to various panel modes. First, the lowest local maximum in the PSD plots (Figs. 4.28, 4.31 and 4.34) is considered. At the same frequency in the phase plots (Figs. 4.29, 4.32 and 4.35), it can be seen that the respective measurements are all in phase regarding the measurements at front, center, and rear positions. This indicates that no neutral lines in $x$-direction exist and that the 0;0-mode of the panel is observed. The frequency of course differs from the value for the cold panel without pressure load that was shown in Fig. 4.25d, as the panel changes its deformation and thermal state throughout the wind tunnel run. The PSD and phase

plots for run 95 (Figs. 4.28 and 4.29) for the mode starting at about 500 Hz show that the front and rear signals are in phase, but the center signal is opposite in phase, indicating a mode with two neutral lines in $x$-direction. In areas where significant dynamics occur at a broader frequency range, distinct maxima in the spectrograms at 0° or 180° phase are still present. For the dynamics outside the frequency with maximum PSD where there are still significant levels of excitation, the phase output is constantly changing over time (see Fig. 4.35 throughout the run as well as Fig. 4.32 until about $t = 8\,\mathrm{s}$ at frequencies above 500 Hz). Another interesting feature can be found in run 100, where the spectrogram (Fig. 4.31) shows converging branches of maxima of the PSD between the beginning of the run and approximately $t = 8\,\mathrm{s}$. The respective spectrograms indicate that the branches converging around 200 Hz are all in phase while for the branches around 400 Hz the branches are of opposite phase regarding the front and rear signal (Fig. 4.32).

### Shadowgraph Images

In the case with a rigid wall, it was shown that a small change in shock generator position leads to a drastic change in the size of the separation (Fig. 4.13). Similar changes also occurred during wind tunnel runs with elastic insert, but within the wind tunnel run without change of the shock generator position. It appears that this was caused by the panel dynamics. Some frames from the high-speed shadowgraph recordings have been selected to illustrate this (Figs. 4.36 and 4.37). The frames are instantaneous examples of the flow structure chosen to demonstrate the range of the occurring behavior.

Figure 4.36 shows frames from run 95 (Fig. 4.28) with the shock generator at nominal position. At the beginning of the run at $t = 1\,\mathrm{s}$ (Fig. 4.36a), only a large separation occurs similar to what was observed for the rigid wall at the same shock generator position. Later during that run, at $t = 12\,\mathrm{s}$ (Fig. 4.36b) and $t = 12.003\,\mathrm{s}$ (Fig. 4.36c), the situation is drastically different. It appears that towards the end of the wind tunnel run, a large difference in separation size occurs in the course of the panel oscillation.

Interestingly, during run 100 (Fig. 4.31) with the shock generator moved downstream by $\Delta x = 50\,\mathrm{mm}$, the situation is changed such that a similar large change in separation size is again observed (Figs. 4.37a and 4.37b), but in this case during the beginning of the run when the largest panel oscillations occur. At a later time, the flow separation remained small (Fig. 4.37c), coinciding with smaller panel dynamics.

These large changes in separation size correspond to the occurrence of structural dynamics with the largest observed amplitude, which allows the conclusion that the structural dynamics are facilitating this large change in separation size by acting on the SWBLI, but also that the large change in wall pressure connected to this change in the SWBLI (Fig. 4.7) significantly contributes to the occurring structural dynamics. In conjunction with the analysis of the SWBLI on the rigid wall, it appears that the change in separation size is so large that the separation location moves back and forth between the laminar and turbulent part of the boundary layer. The observation of this behavior for the cold panel after wind tunnel startup and for the warm panel towards the end of the wind tunnel run shows that this effect is not primarily driven by the temperature or static deformation of the structure.

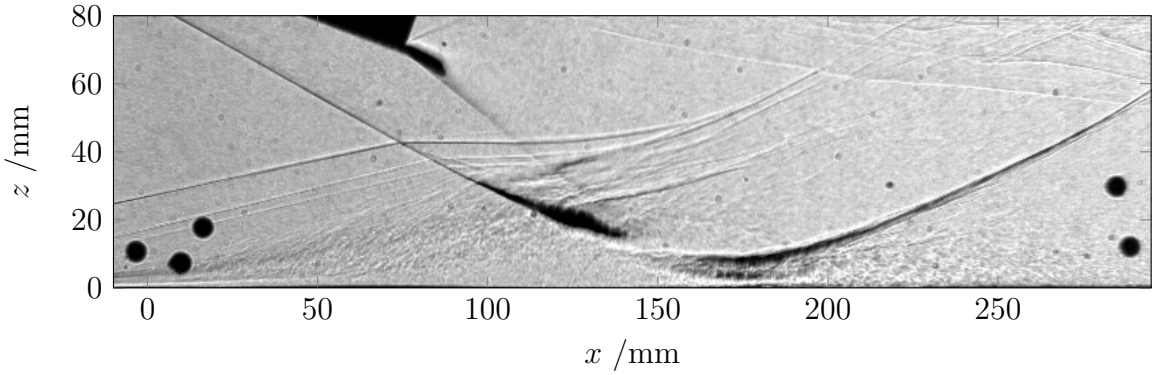


**(a)** $t = 1\,\mathrm{s}$

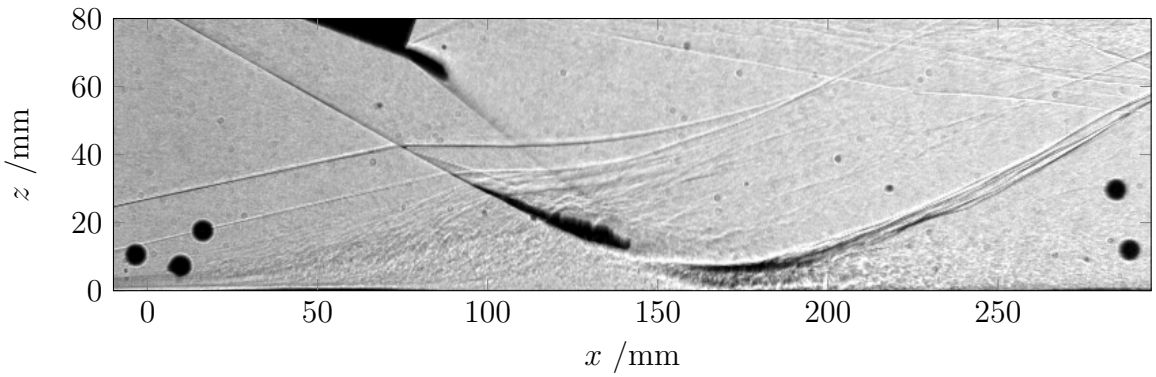


**(b)** $t = 12\,\mathrm{s}$

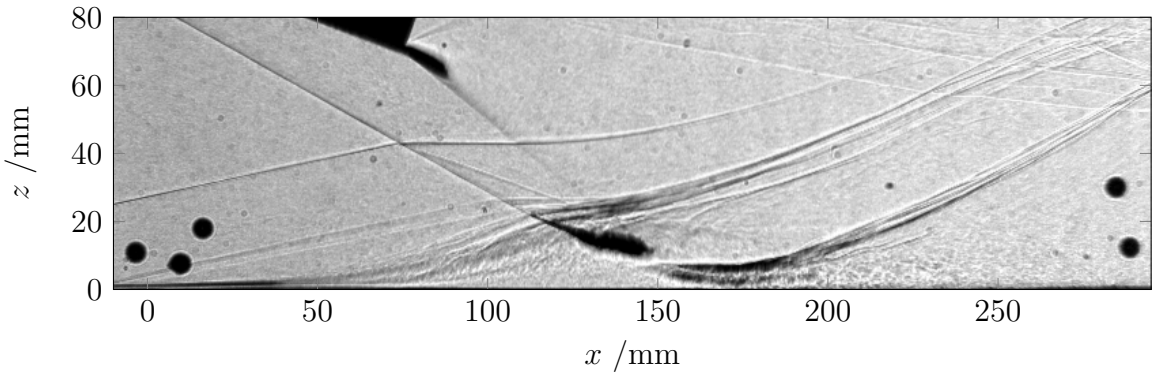


**(c)** $t = 12.003\,\mathrm{s}$

**Figure 4.36:** Frames from high-speed shadowgraph videos for 0.7 mm panel with shock generator at $\alpha = 20°$, $\Delta x = 0\,\mathrm{mm}$ (run 95)

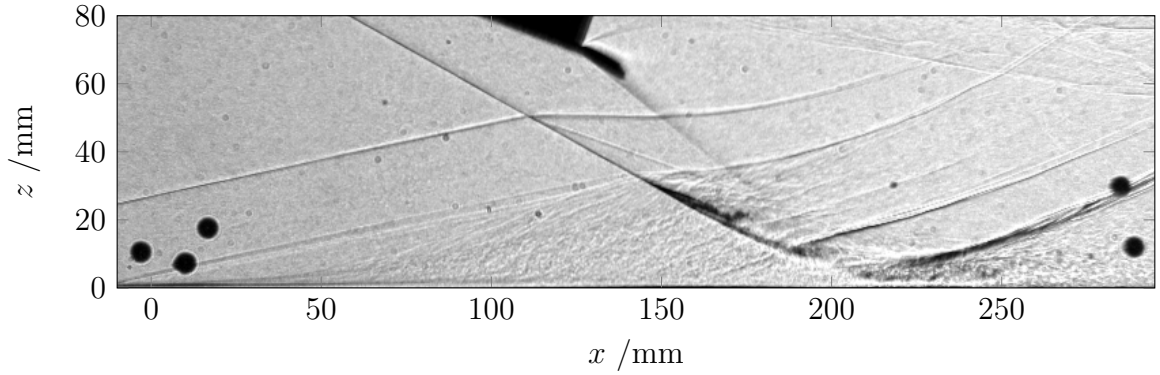


**(a)** $t = 1\,\mathrm{s}$

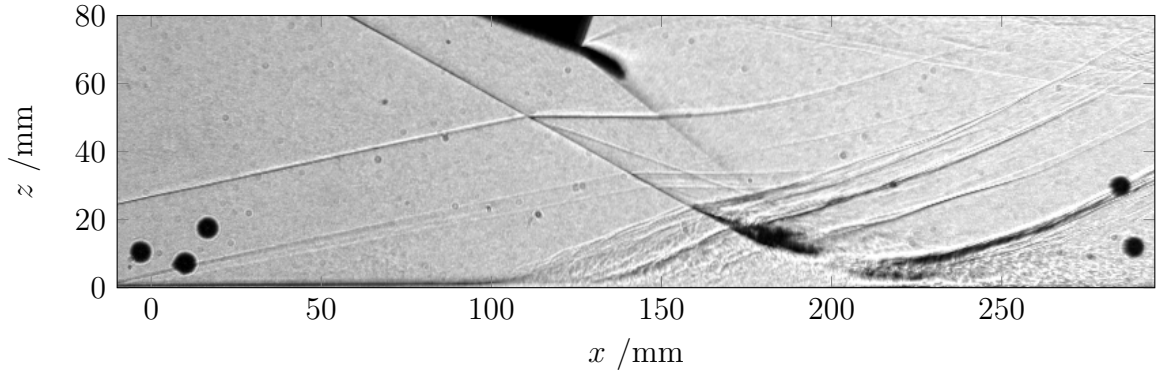


**(b)** $t = 1.002\,\mathrm{s}$

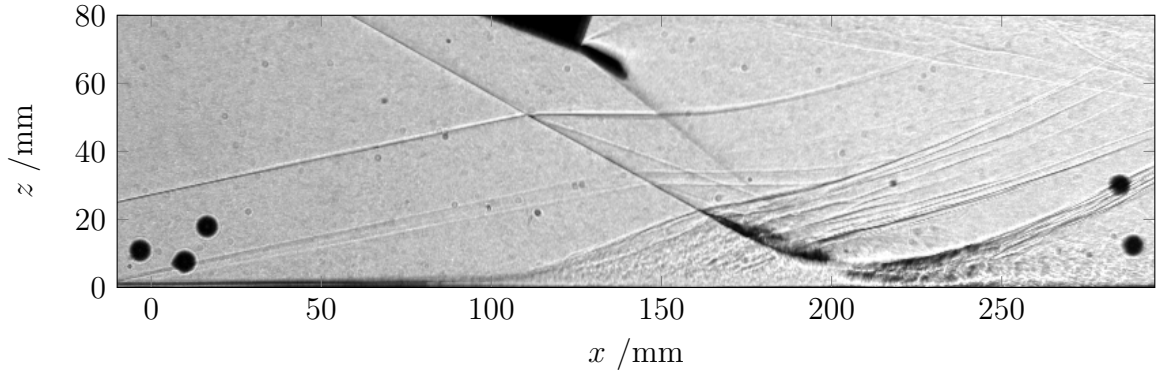


**(c)** $t = 12\,\mathrm{s}$

**Figure 4.37:** Frames from high-speed shadowgraph videos for 0.7 mm panel with shock generator at $\alpha = 20°$, $\Delta x = 50\,\mathrm{mm}$ (run 100)

### Dynamics of the Shadowgraph Video

To gain further insight into the flow field dynamics, the PSD of the grey scale values of the high-speed shadowgraph recordings is inspected again. Figures 4.38 to 4.40 show the mean PSD of these recordings. The PSD was computed for intervals of 1 s from $t = 1\,\mathrm{s}$ and $t = 12\,\mathrm{s}$ in order to allow for observation of changes during the wind tunnel run.

Besides the structures directly related to the SWBLI, local maxima can be observed near the wall around $z = 0\,\mathrm{mm}$ that are related to the direct observation of the elastic panel and boundary layer oscillations visible in the images. In all cases, there are increased dynamics in the vicinity of the reattachment area. However, in most cases with elastic panel, no distinct local maximum appears at the location of the separation shock, differing from observations with the rigid insert (Figs. 4.14a and 4.14c). This is probably due to the continuous change in separation shock location caused by the panel movement. The only exception appears for the rearmost shock generator position at $\Delta x = 100\,\mathrm{mm}$ for the later time interval (Fig. 4.40b), which is a case with relatively low panel dynamics (Fig. 4.34). Earlier during the same wind tunnel run, when higher amplitude panel dynamics are still taking place, no distinct maximum at the separation shock is present, but the PSD of the grey scale values is increased within the separation area, showing the strong dependency of the SWBLI dynamics on the panel dynamics. Throughout all runs (Figs. 4.38 to 4.40), higher levels of structural dynamics correspond to higher levels of dynamics in the shadowgraph images and vice versa.

Additionally, as also computed for the rigid cases, Figs. 4.41 to 4.43 show spectra for PSD of grey scale values along $z = 10\,\mathrm{mm}$. Generally, the frequencies of the lower panel modes are strongly visible as horizontal lines, highlighting the drastic influence of the panel dynamics on the flow field. In contrast to this, broadband excitation near the reattachment appears as a vertical band. This is different from the observations made in the rigid case where only vertical structures stemming from broadband SWBLI dynamics were found (Fig. 4.15). Again, no distinct maximum at the separation shock appears in the elastic cases. However, for the case with the rearmost shock generator position of $\Delta x = 100\,\mathrm{mm}$ (Fig. 4.43b), several additional local maxima appear at various frequencies in the displayed range near the separation shock at about $x = 160\,\mathrm{mm}$. It is also interesting to note how large the change in the observed distribution is even within the same run. Initially, mostly two distinct panel frequencies show up but not the additional maxima near the separation shock (Fig. 4.43a).

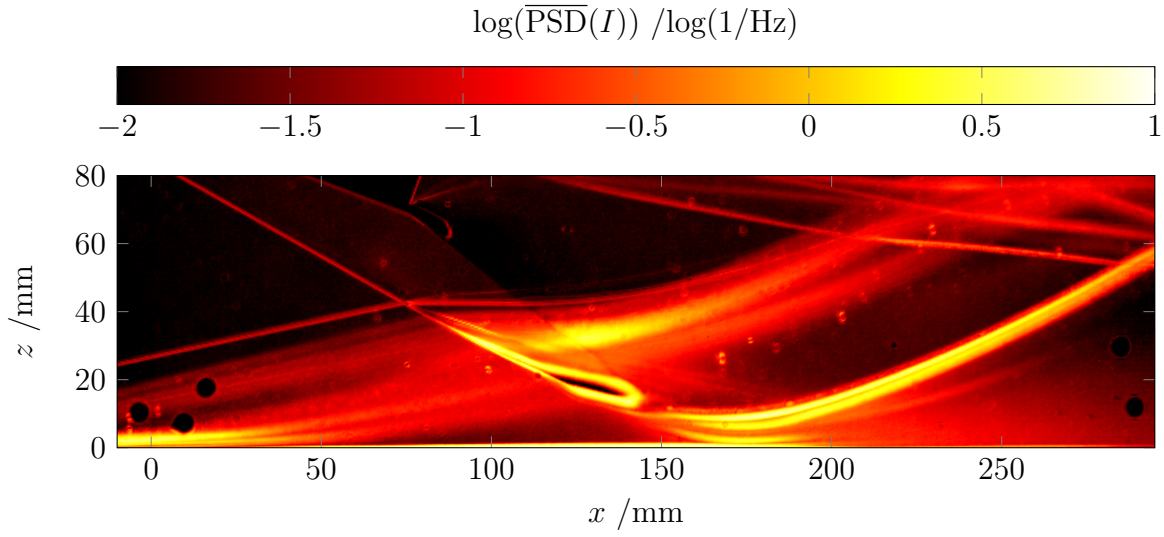


**(a)** $\Delta x = 0\,\mathrm{mm}$ (run 95), $t = 1\,\mathrm{s}$ to $t = 2\,\mathrm{s}$

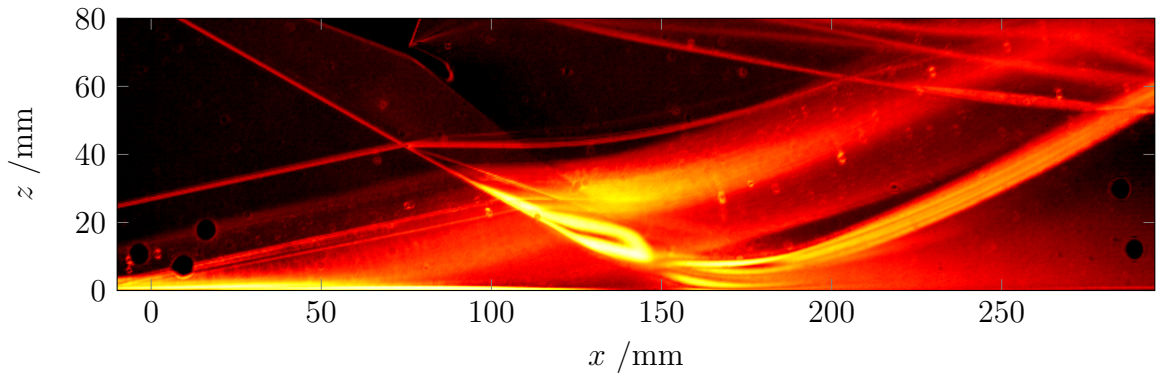


**(b)** $\Delta x = 0\,\mathrm{mm}$ (run 95), $t = 12\,\mathrm{s}$ to $t = 13\,\mathrm{s}$

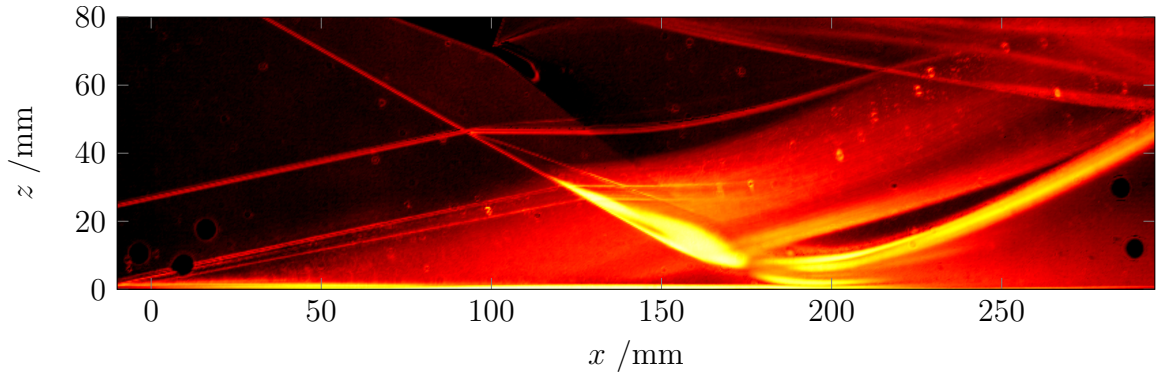


**(c)** $\Delta x = 25\,\mathrm{mm}$ (run 96), $t = 1\,\mathrm{s}$ to $t = 2\,\mathrm{s}$

**Figure 4.38:** Mean PSD of grey scale values ($I$) from high-speed shadowgraph videos for 0.7 mm panel at $\alpha = 20°$

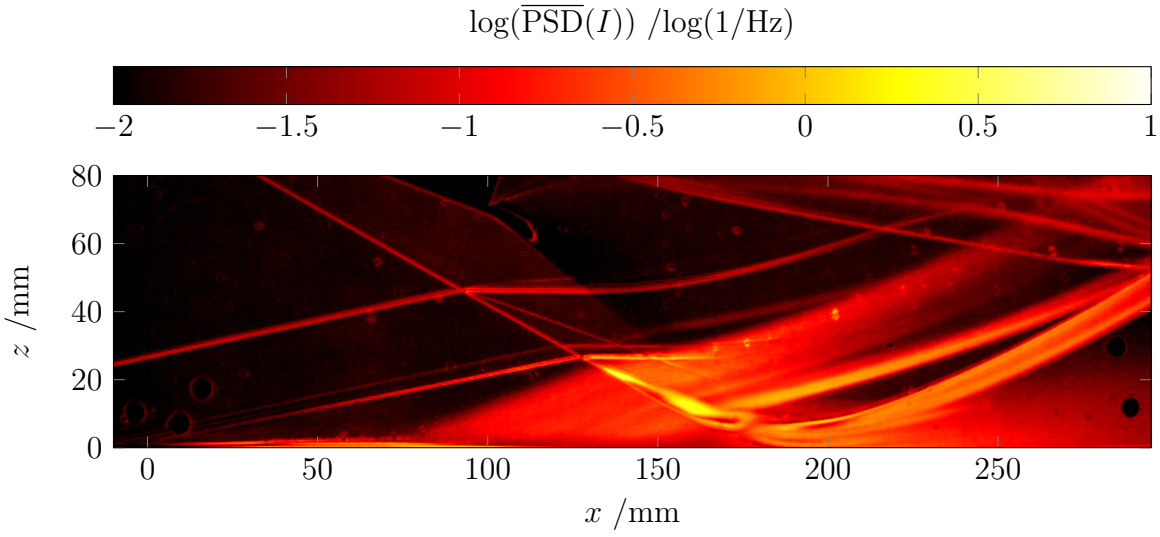


**(a)** $\Delta x = 25\,\mathrm{mm}$ (run 96), $t = 12\,\mathrm{s}$ to $t = 13\,\mathrm{s}$

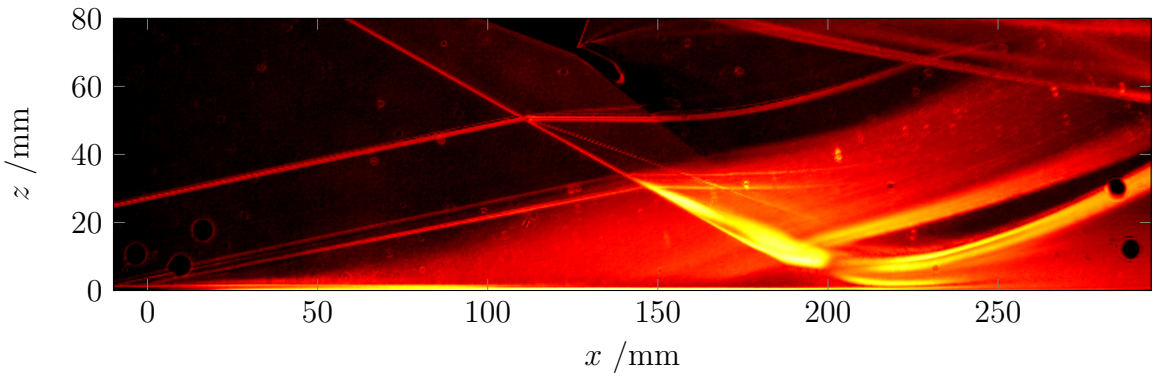


**(b)** $\Delta x = 50\,\mathrm{mm}$ (run 100), $t = 1\,\mathrm{s}$ to $t = 2\,\mathrm{s}$

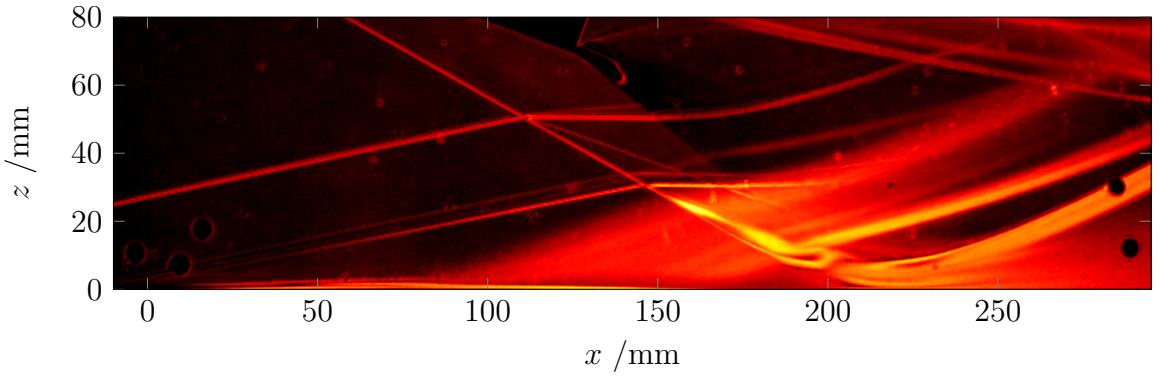


**(c)** $\Delta x = 50\,\mathrm{mm}$ (run 100), $t = 12\,\mathrm{s}$ to $t = 13\,\mathrm{s}$

**Figure 4.39:** Mean PSD of grey scale values ($I$) from high-speed shadowgraph videos for 0.7 mm panel at $\alpha = 20°$

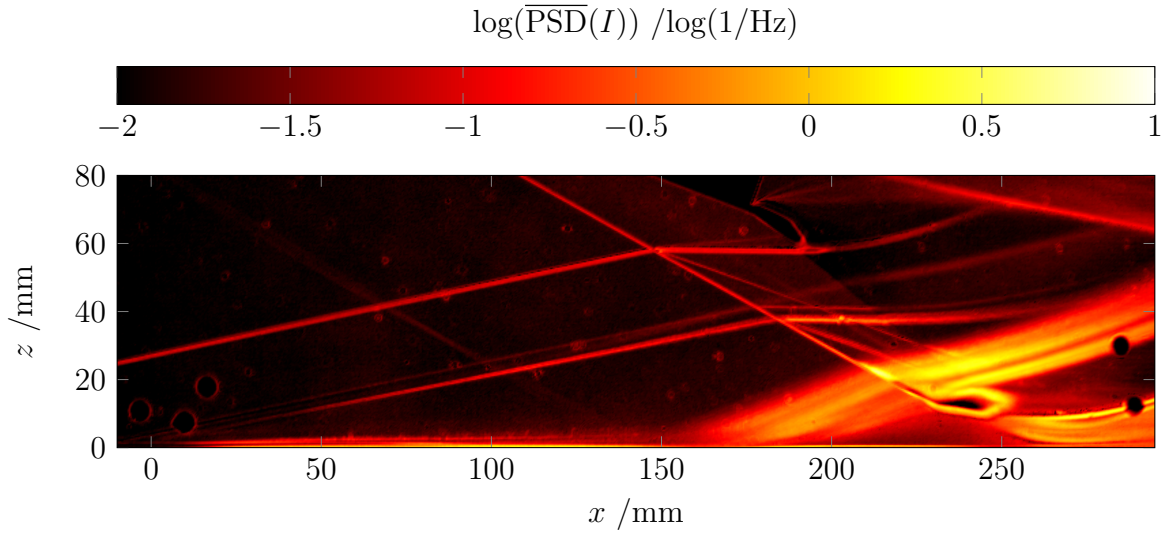


**(a)** $\Delta x = 100\,\mathrm{mm}$ (run 99), $t = 1\,\mathrm{s}$ to $t = 2\,\mathrm{s}$

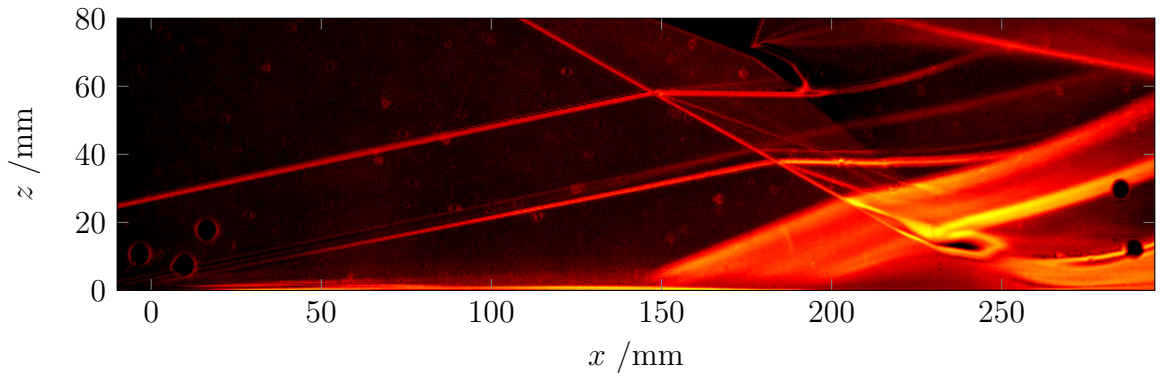


**(b)** $\Delta x = 100\,\mathrm{mm}$ (run 99), $t = 12\,\mathrm{s}$ to $t = 13\,\mathrm{s}$

**Figure 4.40:** Mean PSD of grey scale values ($I$) from high-speed shadowgraph videos for 0.7 mm panel at $\alpha = 20°$

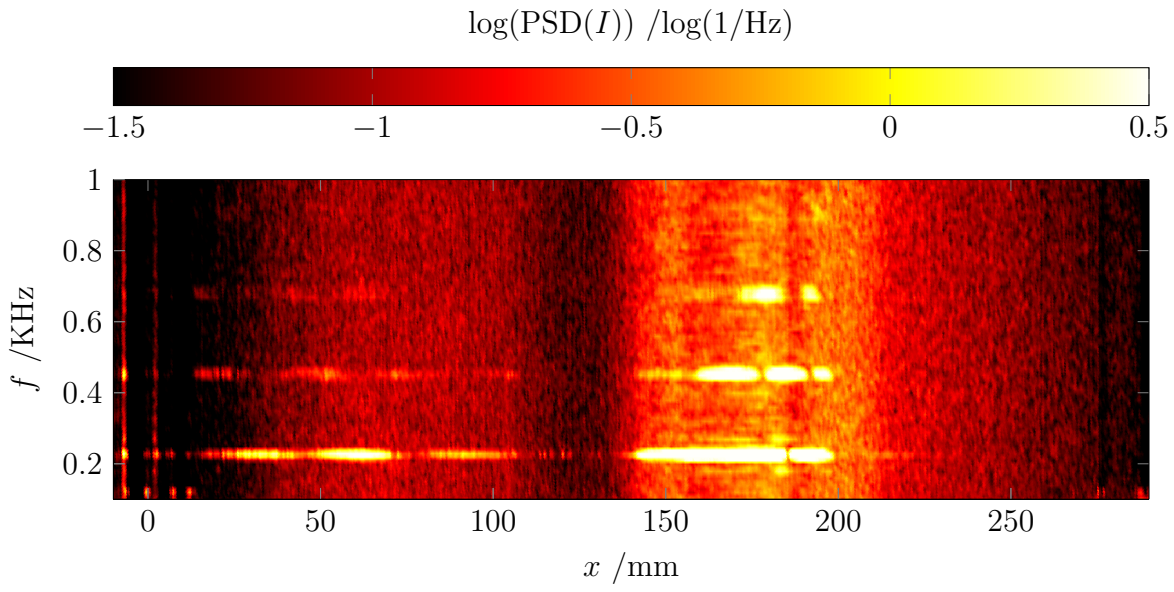


**(a)** $\Delta x = 0\,\mathrm{mm}$ (run 95), $t = 1\,\mathrm{s}$ to $t = 2\,\mathrm{s}$

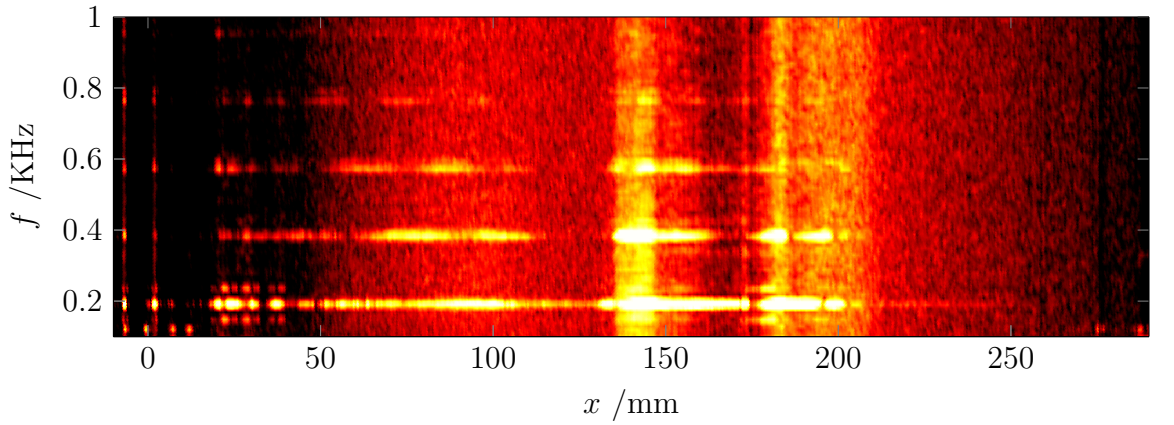


**(b)** $\Delta x = 0\,\mathrm{mm}$ (run 95), $t = 12\,\mathrm{s}$ to $t = 13\,\mathrm{s}$

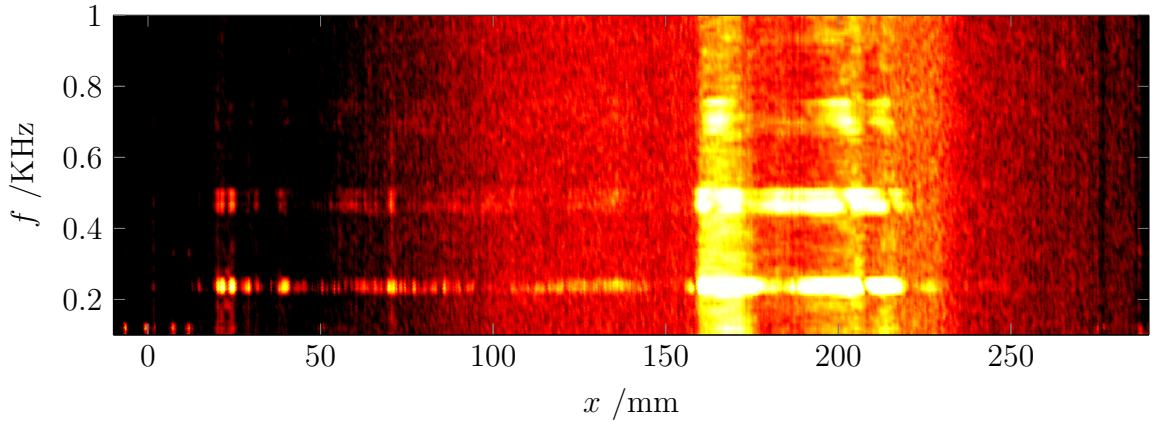


**(c)** $\Delta x = 25\,\mathrm{mm}$ (run 96), $t = 1\,\mathrm{s}$ to $t = 2\,\mathrm{s}$

**Figure 4.41:** PSD of grey scale values ($I$) from high-speed shadowgraph videos for 0.7 mm panel at $\alpha = 2\,0°$ at $z = 10\,\mathrm{mm}$

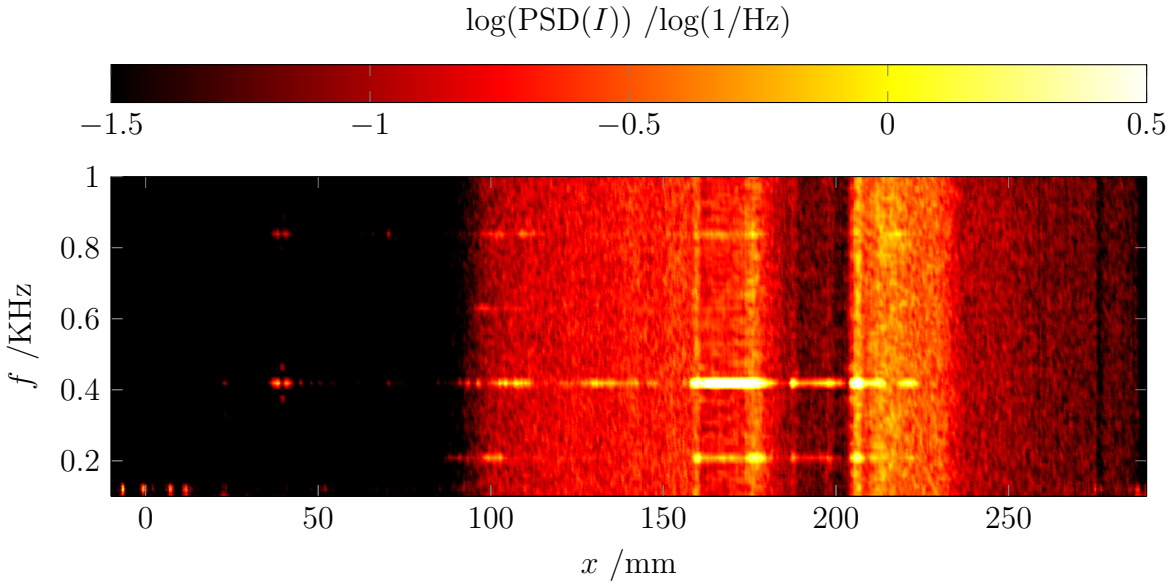


**(a)** $\Delta x = 25\,\mathrm{mm}$ (run 96), $t = 12\,\mathrm{s}$ to $t = 13\,\mathrm{s}$

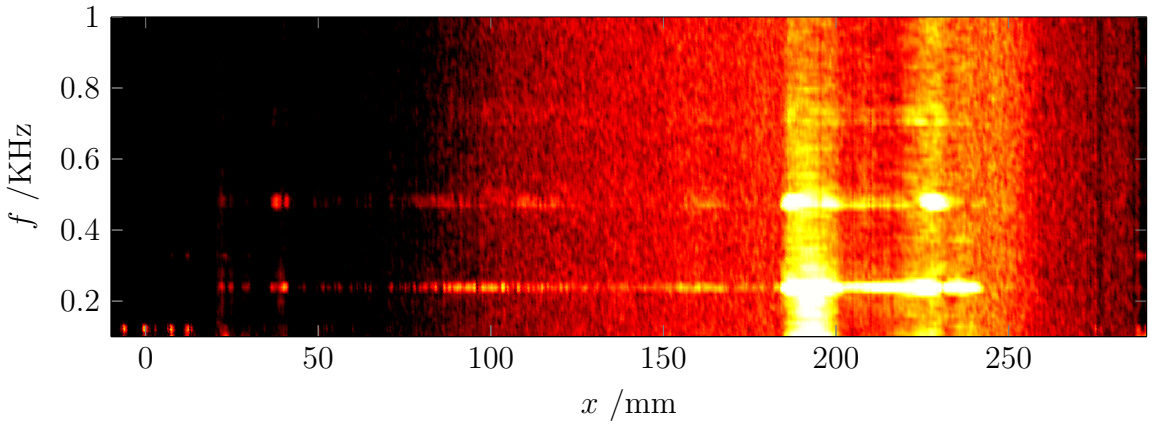


**(b)** $\Delta x = 100\,\mathrm{mm}$ (run 100), $t = 1\,\mathrm{s}$ to $t = 2\,\mathrm{s}$

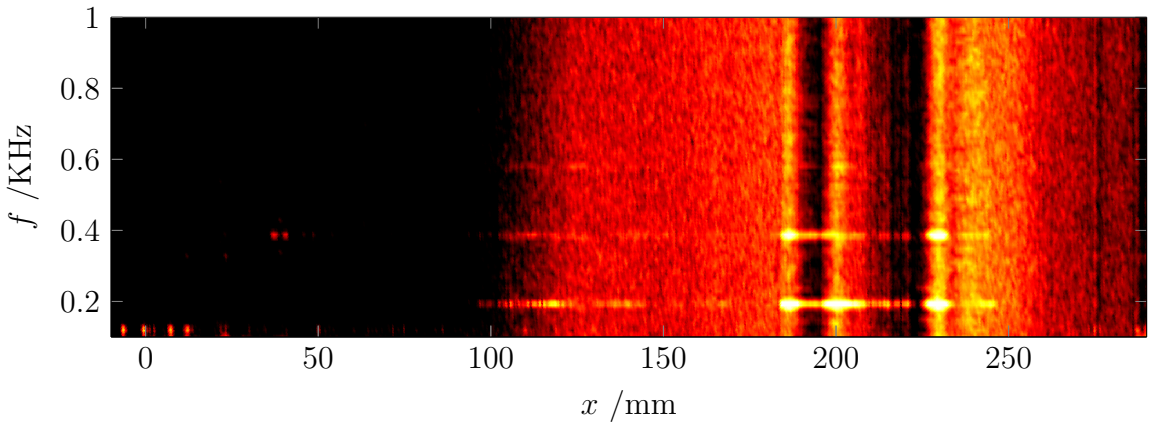


**(c)** $\Delta x = 100\,\mathrm{mm}$ (run 100), $t = 12\,\mathrm{s}$ to $t = 13\,\mathrm{s}$

**Figure 4.42:** PSD of grey scale values ($I$) from high-speed shadowgraph videos for 0.7 mm panel at $\alpha = 20°$ at $z = 10\,\mathrm{mm}$

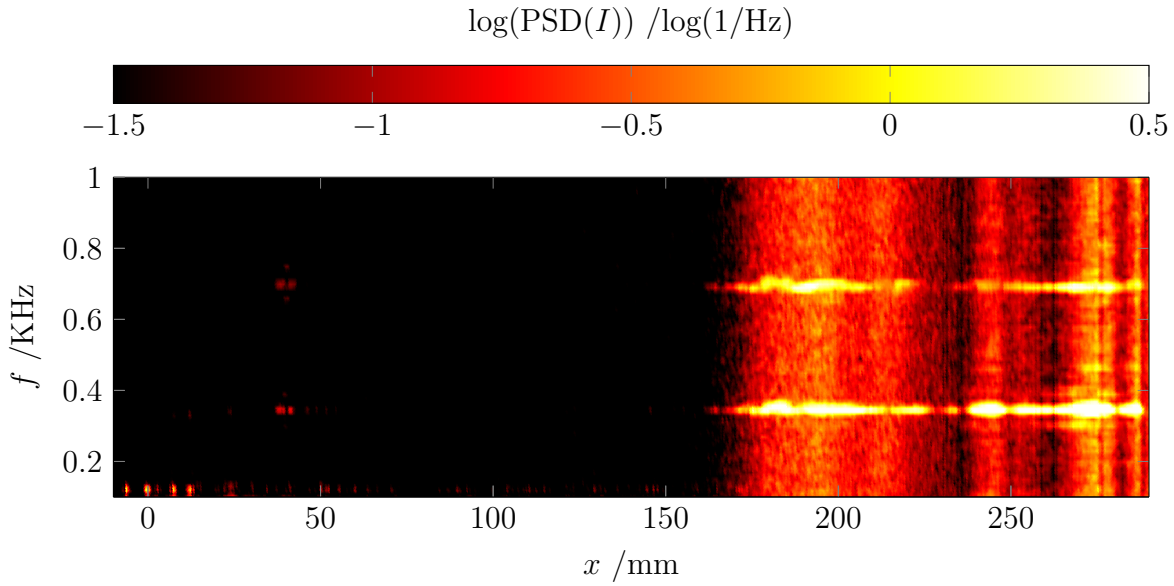


**(a)** $\Delta x = 100\,\mathrm{mm}$ (run 99), $t = 1\,\mathrm{s}$ to $t = 2\,\mathrm{s}$

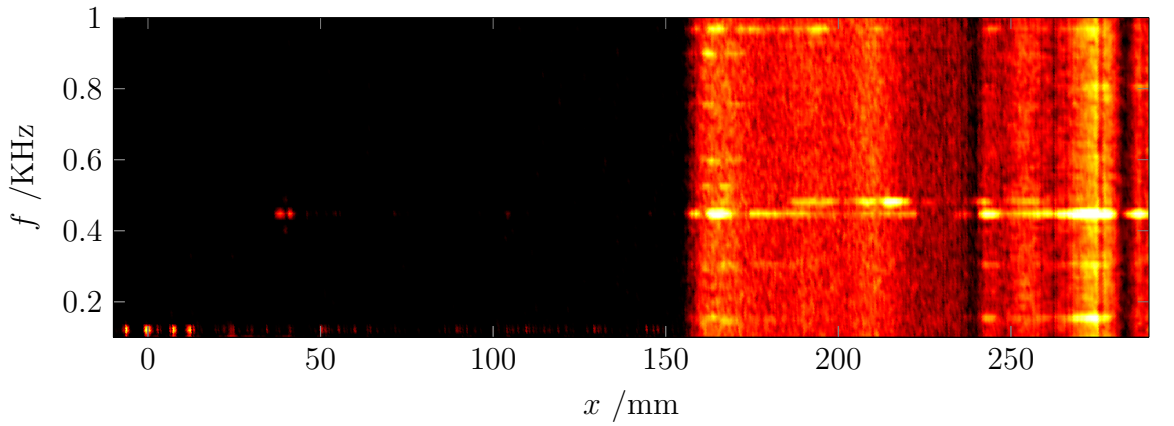


**(b)** $\Delta x = 100\,\mathrm{mm}$ (run 99), $t = 12\,\mathrm{s}$ to $t = 13\,\mathrm{s}$

**Figure 4.43:** PSD of grey scale values ($I$) from high-speed shadowgraph videos for 0.7 mm panel at $\alpha = 20°$ at $z = 10\,\mathrm{mm}$

### Phase Portraits

The spectra of the measured panel displacement show substantial differences in panel response between various runs. For example, narrow maxima were observed during run 95 (Fig. 4.28) and more broadband excitation in run 99 (Fig. 4.34). Excerpts of the time series of the displacement measurements from these runs are shown in Figs. 4.44a and 4.44b. The same interval is used to plot the phase portraits shown in Figs. 4.44c and 4.44d. In the case of run 95, both the time series and phase plots indicate harmonic oscillation predominately at about 215 Hz with additional oscillation at higher frequency of drastically lower amplitude. Run 99 shows a considerably more complicated behavior with varying amplitudes at various frequencies, which is also reflected in the phase portrait in Fig. 4.44d. Such a behavior of the phase portrait can be indicative of chaotic dynamics (in this context see also [10], where similar plots have been computed for a supersonic FSI case without incident shock). Figures 4.44e and 4.44f show the corresponding spectra. The plot for the displacement dynamics is essentially a "slice" from the spectrograms (Figs. 4.28b and 4.34b). They clearly show the higher level in broadband dynamics in the latter case. A plot of the dynamics extracted from the shadowgraph recordings is added to show that the respective peaks are also present there.

### 0-1 Test for Chaos

Based on the previous results (e. g. Fig. 4.44), the question arises whether additional analysis can contribute to understanding potential distinctions between these behaviors. Gottwald and Melbourne [61] propose a procedure called "0-1 Test for Chaos" intended to distinguish cases with regular dynamics from cases with deterministic chaotic dynamics. In the present case, the test cannot distinguish deterministic chaotic FSI behavior appearing independently of flow turbulence (e. g. [10, 43]) from turbulence-driven dynamics, which can also be considered deterministic chaos but are typically treated stochastically [2, 88, 156]. However, the difference between such cases and cases with regular dynamics independent of turbulent fluctuations is detectable.

The implementation follows [62, 63] and is briefly summarized. First, translation variables are computed for a number of $N$ samples of a measured value $\Phi(j)$ for 100 random values of $c \in (\pi/5, 4\pi/5)$ as suggested in [62]:

$$P_c(n) = \sum_{j=1}^{n} \Phi(j) \cos(jc) \tag{4.1}$$

$$Q_c(n) = \sum_{j=1}^{n} \Phi(j) \sin(jc) \tag{4.2}$$

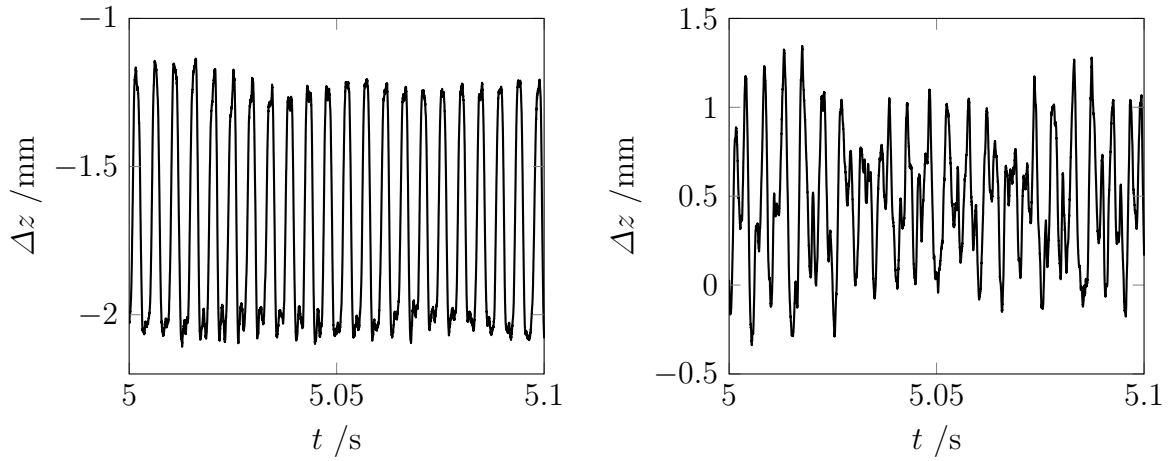


**(a)** Run 95: Times series

**(b)** Run 99: Times series

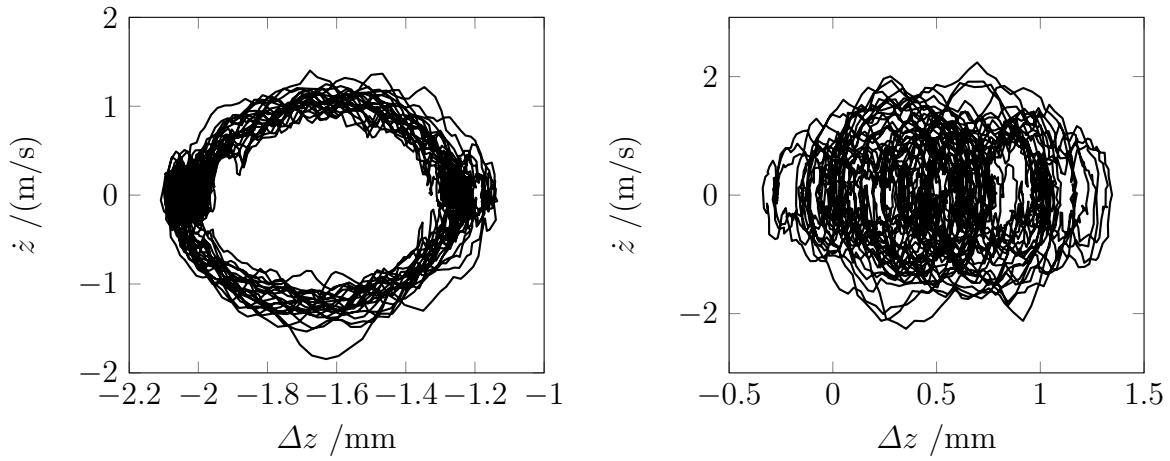


**(c)** Run 95: Phase portrait (5 s – 5.1 s)

**(d)** Run 99: Phase portrait (5 s – 5.1 s)

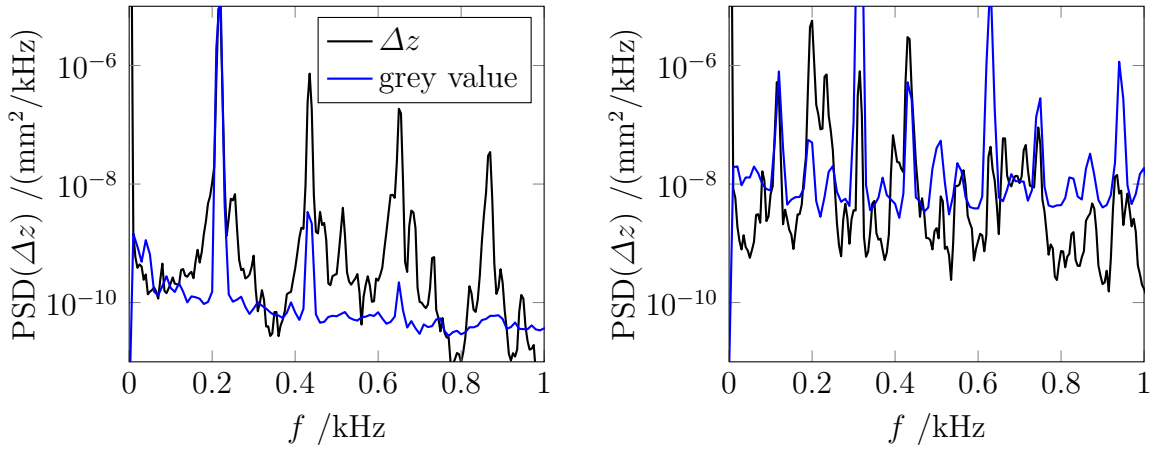


**(e)** Run 95: PSD (5 s – 6 s)

**(f)** Run 99: PSD (5 s – 6 s)

**Figure 4.44:** Dynamics of the center displacement sensor measurements, plots e and f include the PSD spectrum of grey scale values from the respective high-speed shadowgraph recording

Plots of $P$ and $Q$ yield an indication whether chaotic behavior is present. Computed examples for generic test cases are given in [63]. Experimental results for a supersonic FSI case are given in [10].

Next, the behavior of the translation variables is analysed by computing the mean square displacement $M_c(n)$ for $n \leq N/10$:

$$M_c\,(n) = \frac{1}{N} \sum_{j=1}^{N} \left( [P_c\,(j+n) - P_c\,(j)]^2 + [Q_c\,(j+n) - Q_c\,(j)]^2 \right) \tag{4.3}$$

A correction removing oscillations of $M_c(n)$ as shown in [60] is applied. This only changes convergence but not the mean growth rate. The growth rate $K_c$ is determined by fitting a straight line through $\log(M_c(n))$ versus $\log(n)$, minimizing absolute deviation. If $K_c$ converges near 0, the observed dynamics are regular. In a chaotic case, $K_c$ converges to 1, but convergence may not be reached for a given sample size. Even if full convergence is not reached, this still gives a reliable indication (see [62] for a detailed discussion and examples).

Intervals taken from displacement measurements and shadowgraph videos were low-pass filtered and downsampled to 2 kHz to cover most relevant modes of structural dynamics and low-frequency content in SWBLI (see [62] for comments regarding the sampling rate on the 0-1 Test). The investigated intervals start at $t = 5\,\mathrm{s}$ to exclude the larger changes in deformation and temperature at the beginning of the wind tunnel run. However, it should be noted that small temperature and deformation changes with an effect on structural dynamics still take place during the later part of the wind tunnel runs.

Figure 4.45 shows the results based on the measurements of the center displacement sensor from runs 95 and 99 (Figs. 4.28a and 4.34a). The plots of the translation variables $P$ and $Q$ for an arbitrary value of $c$ (Figs. 4.45a and 4.45b) yield a first indication that there is a detectable difference in the dynamics between the analysed runs. This is confirmed by the trend observed for the median $K$ in Fig. 4.45c, where a clear distinction between regular dynamics in run 95 and chaotic behavior for run 99 is found. In contrast to this, the computations based on shadowgraph recordings of the same time interval (Fig. 4.46) do not show such a difference for the translation variables (Figs. 4.46a and 4.46b) or median $K$ (Fig. 4.46c). The results indicate chaotic behavior in both cases.

This analysis does not allow a conclusion as to what extent the observed difference between run 95 and 99 is caused by intrinsic SWBLI-dynamics. Nevertheless, it provides a useful addition to analysing such data as chaotic behavior of the coupled system may be an indication of unsteady aerodynamic effects from the flow field in some cases. In this context, it is interesting to note that Brouwer et al. [12] were able to reproduce experimentally observed chaotic dynamics for a panel exposed to supersonic flow without shock generator by using numerical methods without considering turbulence, thus supporting the validity of this approach.

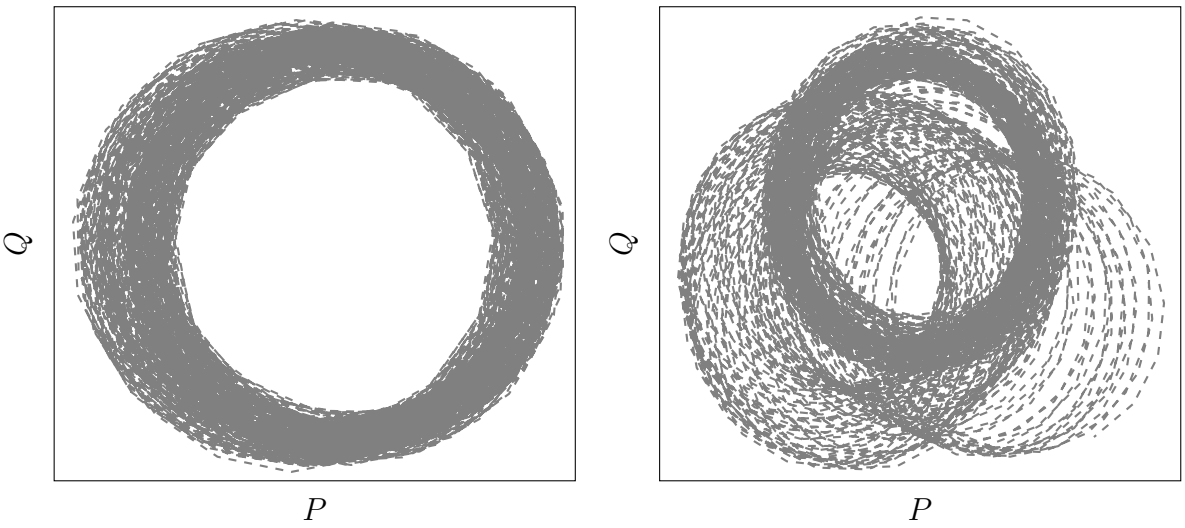


**(a)** Translation variables $P$, $Q$ for run 95 ($c = 0.4$, $N = 4000$)

**(b)** Translation variables $P$, $Q$ for run 99 ($c = 0.4$, $N = 4000$)

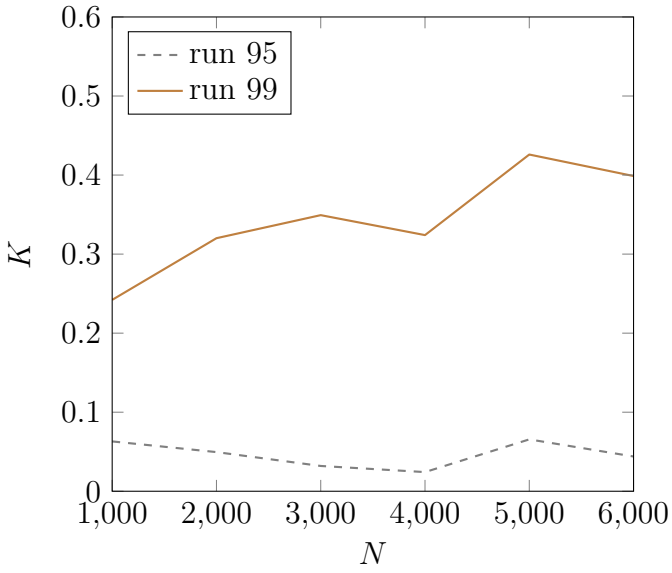


**(c)** Median $K$ versus sample number $N$

**Figure 4.45:** Results of the 0-1 Test for Chaos for panel displacement measurements

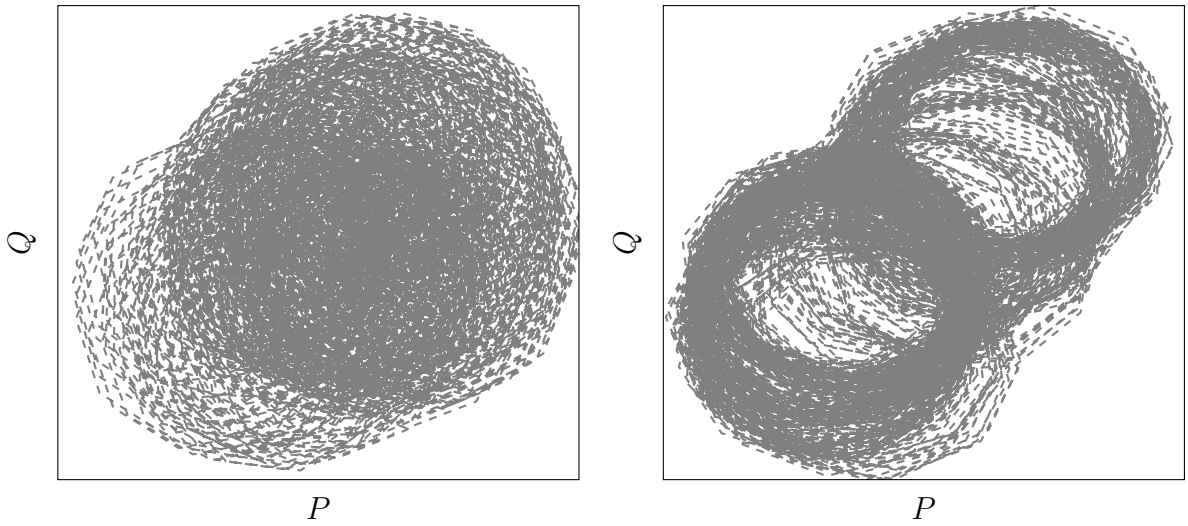


**(a)** Translation variables $P$, $Q$ for run 95 shadowgraph video ($c = 0.7$, $N = 4000$)

**(b)** Translation variables $P$, $Q$ for run 99 shadowgraph video ($c = 0.7$, $N = 4000$)

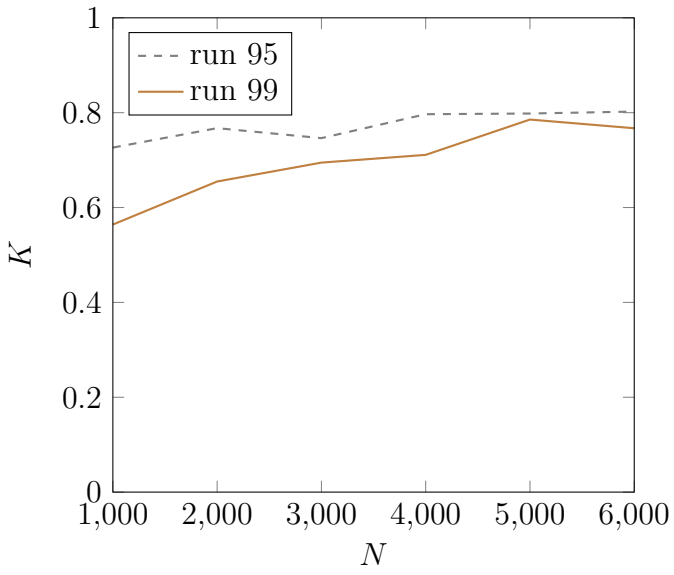


**(c)** Median $K$ versus sample number $N$

**Figure 4.46:** Results of the 0-1 Test for Chaos for grey scale value from high-speed shadowgraph videos

## 4.3 Discussion

As shown numerically for inviscid and laminar flows at lower supersonic Mach numbers in [161, 162], the presence of an incident shock can either facilitate or prevent flutter. With the present setup, this has been experimentally demonstrated for the first time in hypersonic flow by a large variation of the incident shock angle. Large amplitude dynamics were obtained for a configuration in which it would not occur for lower incident shock angles or in the absence of an incident shock. Vice versa a drastic reduction of structural dynamics was obtained by increasing the incident shock angle in another case. In a recent study [11], such behavior, again at lower supersonic Mach numbers, could be well predicted using simplified piston theory-based models that were modified to include an incident shock. However, the results start to deviate for cases where the coupled behavior depends on detailed knowledge of heat transfer and the mean and unsteady wall pressure distribution, e. g. SWBLI cases with flow separation.

In [162], the influence of the SWBLI was found to lead to complex non-periodic dynamics for simulations of a configuration with laminar flow. For a similar configuration with turbulent SWBLI in [147], it was observed using a fluid-structure coupled LES that panel dynamics were only present in this turbulent configuration but not in an inviscid reference case. In [9], large increases in flutter amplitude were found in comparison of an inviscid reference case to a case with laminar incoming boundary-layer. In the present study, a large variation of flutter dynamics was obtained by shifting the incident shock in flow direction. The configurations obtained in this way included cases where the initial flow separation took place in the laminar or turbulent part of the boundary layer. The experiments showed a broad variety of resulting structural dynamics. In most cases, lower modes of the panels were excited. However, substantial broadband dynamics were also observed in some cases. These panel dynamics were distinctly detectable in the flow field, and in some cases caused the separation shock to move back and forth between the laminar and turbulent part of the boundary layer. This raises the question which part of the influence of the SWBLI on the coupled system is dependent on the changed mean pressure distribution or the intrinsic dynamics of the flow field.

Experiments and supporting simplified modelling suggest that for a case similar to the present at lower Mach number, SWBLI dynamics have an influence on the resulting panel dynamics [11, 58, 59, 150]. In other studies in [169, 174] as well as in Chapter 2 and [31], setups were created that made it possible to look at the effect of SWBLI on a structure without flutter, showing structural excitation by intrinsic SWBLI dynamics. This is an important contribution in this area, but does not resolve the problem of untangling these effects in cases such as the ones presented here, where both SWBLI dynamics and flutter play a role in the resulting dynamics of the coupled system. Similar to a recent study on a FSI case without SWBLI in [10], the present study showed that chaotic behavior is likely to be present in the measured structural dynamics in some cases, but it was not possible to distinguish effects stemming from the structure from the effects of the SWBLI dynamics. This problem should ideally be addressed by joint experimental and numerical studies with improved full-field instrumentation in the experiment and various levels of fidelity in the simulations. Such studies would improve understanding of which mechanisms drive the various aspects of the observed behavior. Regarding the study

in [10], it was shown in [12] that chaotic behavior can also be found in an inviscid model because it is not or not mainly driven by turbulence in such cases. This could also point to a path forward regarding further analyses of the present experiments. However, given the results, it appears likely the outcome will be more complicated and will also require a complementary study resolving SWBLI dynamics.

It is remarkable how very small changes in temperature can completely alter the dynamics of a structure in hypersonic flow. This has previously been shown for supersonic flows at lower Mach number, e. g. experimentally in [95, 150] and theoretically in [39], and also numerically for hypersonic configurations (e. g. [126]). In most cases in the literature, only the flutter boundaries were obtained and the post-flutter behavior was not investigated. The thermal state of the structure is directly related to the appearance of chaotic panel motion in cases where the thermal expansion leads to in-plane compressive loads [12, 43]. The present experiments add full time records of flutter of panels in hypersonic flow with and without SWBLI undergoing transient heating. This leads to heating-induced starting and stopping of panel dynamics for which very small temperature changes were sufficient. From an aerodynamics point of view, this sensitivity to small temperature changes means that reliable knowledge of the heat transfer to the structure is crucial, especially for flow fields that may include laminar-turbulent boundary-layer transition or SWBLI. In the case of boundary-layer transition, it may not be certain whether the flow is turbulent or laminar at a particular location which can even depend on structural dynamics, leading to substantial uncertainty regarding the resulting structural heating. As the present experiments show, using the highest expected temperature as worst case estimate may very well be quite far from the worst case in terms of structural dynamics. Heating prediction for SWBLI cases can be even more prone to error as it relies on the properties of the incoming boundary layer as was drastically shown in the present experiments. This adds to the complication of flow separation and in some cases resulting Görtler-like vortices [17, 101]. Furthermore, changes in surface geometry drastically alter heat transfer (e. g. Chapter 3 or [25]) and surface pressure, making coupled treatment of such problems necessary.

Related to these considerations, the snap-through behavior of buckled structures is an area that poses a significant challenge. This has been observed in the present study in some cases, including a demonstration of its sensitivity to small upstream disturbances. It can quickly and drastically alter mean panel deformation but also dynamic properties resulting in changed heating and dynamics. Such snap-through behavior for a similar setup at lower Mach number was also observed by [150]. It would merit focused studies such as have been begun in [46, 90, 118], where experiments on detailed dynamic characterization of structures under thermal loads without flow were conducted. In [55], it was shown for a simplified model with artificially applied pressure fluctuations that such pressure fluctuations can lead to repeated snap-through events of the panel. Ideally, such studies should be continued using a combination of the aforementioned techniques with wind tunnel experiments, detailed thermomechanical calibration of the test structures, and supporting simulations.

While it is in principle not surprising that the dynamics described above can cause damage to a structure, only very few such instances are documented. Given the described

complexity and uncertainty it becomes clear how much of a challenge reliable life-time prediction or SHM of a structure poses in such a highly non-linear system. E. g. detecting the difference between a change in dynamics driven by structural failure or a temperature change can be quite difficult. By obtaining FSI-driven damage on a panel in hypersonic flow, an initial data set of such a failure was obtained, which demonstrates that further studies on this subject are a feasible and promising extension of the present work.

# 5 Conclusion

Efficient and reliable orbital launch vehicles need to be designed for minimum weight and to withstand severe aerothermodynamic loads. Understanding the interdependency of the thermal and deformation state of the structure with the surrounding flow field (FSI) is crucial for the reliable prediction of loads and thus design of such weight-optimized super- and hypersonic vehicle structures. The recent push towards reusable vehicles leads to drastic increases in desired vehicle life time and a substantial extension of the relevant flight envelops which considerably adds to this challenge.

Many supersonic and hypersonic FSI configurations exhibit non-linear or path-dependent behavior even without detailed consideration of aerodynamic problems (e. g. [55, 162]). In addition, a broad range of FSI problems show an interdependency with complex aerodynamic features such as flow separation, turbulence or even non-equilibrium chemistry. All of these can influence heat transfer as well as static and dynamic pressure distribution, fundamentally altering the resulting behavior of the structure (e. g. [150, 151, 169, 174]). The experimental database and modelling capabilities are quite limited regarding both aspects.

## 5.1 Wind Tunnel Experiments

Three configurations were used to investigate a broad range of supersonic and hypersonic FSI cases previously not available in the literature:

- A significant improvement to the supersonic incident SWBLI FSI setup by Willems [174] was made by adding a novel high-speed rotatable shock generator that made it possible to study nearly two-dimensional configurations. This included both experiments with stationary incident shock for the study of the effect of intrinsic SWBLI dynamics on FSI as well as fast-changing incident shock angles to study the resulting high-amplitude structural oscillations.
- The first study of FSI with large panel deformation caused by thermal buckling in hypersonic high-enthalpy flow with both spatially and temporally resolved deformation and temperature field measurements was conducted to investigate the interdependency between local heat transfer and deformation state in such conditions. This setup is based on previous work by Niesner [124].
- The first investigation of an incident SWBLI FSI configuration in hypersonic flow was conducted. This novel setup enabled the study of thermal buckling, flutter, and snap-through effects for configurations with and without incident shock. Previously, experimental results from such configurations were only available at considerably

lower Mach numbers and only few cases included thermal effects (e. g. [111, 150, 174]).

## 5.2 Results

These experiments yielded results on the following aspects of FSI:

It was shown experimentally that the onset of flutter for an incident shock configuration can be either inhibited or facilitated by the presence of an incident shock depending on its strength. This is the only such experimental study in hypersonic flow. Similar observations were made in fluid–structure coupled numerical simulations in [161, 162] for simplified cases and recently also experimentally at lower Mach numbers [10].

Cases with high-speed moving incident SWBLI were observed to incite large panel dynamics at different modes of the structure far greater than the structural dynamics caused by the intrinsic SWBLI dynamics from a steady incident shock for the same setup. On a rigid reference panel, it was also shown that the instantaneous wall pressure depends on the movement of the shock generator similar to recent results in [17] where a continuously rotating shock generator was used. Results of this FSI case have already been used for comparison to three coupled simulations using LES to resolve the flow field [81, 130, 185].

The preceeding study by Willems [174] showed a detectable influence of intrinsic SWBLI dynamics on incident shock FSI. The present results using the new quasi two-dimensional setup show that the effect of the intrinsic SWBLI dynamics increases panel dynamics with increasing incident shock angle even despite the effective stiffening of the panel that also increases with incident shock angle. In a configuration with adjusted cavity pressure, this effect would be even more drastic. This observation corresponds to recent results in [169] for a ramp configuration. The study also included reference experiments on a rigid wall that were used to validate a LES by Pasquariello et al. [131], showing good agreement of the pressure dynamics in the SWBLI.

FSI configurations with combinations of SWBLI dynamics and panel flutter were also investigated. The results show a distinct change in SWBLI dynamics in comparison to rigid reference cases that are clearly linked to the observed panel dynamics. Variations in the occurring panel dynamics suggest that the SWBLI dynamics have a significant influence on the structure. In some particularly interesting configurations, it appears that the SWBLI initial separation shock changes between the laminar and turbulent part of the boundary layer during the oscillation cycles of the panel. In all cases with combinations of flutter and SWBLI dynamics, further work will be required to untangle the respective contributions to the resulting dynamics.

Adding to previous hypersonic wind tunnel experiments on aerothermal heat flux augmentation caused by rigid spherical protuberances [57] and deformable structures in [73, 124], the present work presents the first spatially and temporally resolved surface deformation and temperature data of an FSI experiment in an high-enthalpy flow field. Deformations up to 12 times the panel thickness including plastic deformation were

observed. The resulting temperature and deformation distribution clearly demonstrate the interdependency of structural deformation and aerothermal heating, in particular the locally increased heat transfer caused by deformations of the structure. The results were used for validation of a coupled numerical simulation by Martin et al. [113, 114].

The drastic effect even of small temperature changes on the onset or stop of flutter as well as buckling and snap-through behavior of a structure was demonstrated both for configurations with and without incident shock that exhibited significant structural dynamics. In cases without large oscillations of the structure, the heat flux augmentation caused by the SWBLI increased structural deformation with rising incident shock strength. This strong temperature dependency of the structural behavior is particularly critical as reliable prediction of heat transfer remains a major challenge because of its strong dependency on the state of the boundary layer and SWBLI as well as its coupling with the local deformation state of the structure.

In one of the wind tunnel runs without SWBLI and large panel dynamics, a failure of a panel occurred at the interface of the mounting frame and the panel, similar to an incident described in [150] during experiments at lower Mach number. This demonstrates that structural failure can be obtained with such a setup and could serve as a starting point for future systematic studies.

## 5.3 Outlook

### 5.3.1 Experiments and Modelling

Given the broad range of FSI problems discussed, it is crucial to have reliable modelling on various levels of fidelity as well as to have a good understanding of where the specific limitations of the various approaches lie. Progress in modelling goes hand in hand with suitable experiments that can be used for validation and to improve fundamental understanding of the underlying mechanisms.

FSI-cases that have an interdependency with SWBLI-dynamics or a strong sensitivity to aerothermal heat transfer are particularly important subjects for further study since they pose the greatest challenge for modelling. Regarding cases with SWBLI, the interaction between the dynamics inherent to the SWBLI and structural dynamics needs to be analysed in more detail. Aerothermal heat transfer in itself remains a critical area of research. Its prediction is further complicated in cases with quasi-static deformations of the structure, singular dynamic changes in deformation, or sustained oscillations. Furthermore, all this can, as demonstrated, lead to damage of panel structures, making the observation and reliable prediction of the limits of structural capabilities in such environments an important objective.

An extension of the experimental data base is crucial for further development in this area. This should include advances in full-field methods, e. g. DIC, Particle image velocimetry (PIV), and Schlieren-based analysis. Such FSI experiments have to be combined with an extensive thermal and structural dynamics characterization structures, providing detailed

data for modelling and analysis of FSI experiments. This should be complemented by further advances in high-fidelity modelling, for example FSI simulations including LES, to allow the detailed study of the influence of turbulence-dependent effects on the coupled configuration regarding heat transfer and wall pressure. At the same time, it is crucial to show how central features of these FSI problems can be captured with simplified models to make such simulations available for engineering. These approaches have to be validated or perhaps also calibrated against high-fidelity simulations and experiments.

### 5.3.2 Application-Oriented Considerations

A central question arising from the present and related works is how to assure a reliable design if the worst case load is not a combination of maximum thermal and mechanical loads but a specific combination of intermediate loads along some part of the trajectory that yields the worst outcome. This is further complicated by the problem of designing for large uncertainties in heat transfer that, as has been demonstrated, can have implications far beyond changing the temperature of the vehicle structure.

Considering the sensitivity of the structural behavior to the mechanical boundary conditions and the thermal environment, it would be important to conduct detailed studies on the influence of realistic mounting and a realistic thermal environment, e. g. for TPS panels on a launch vehicle. This might also include insulation materials and thermal boundary conditions related to a cryogenic tank in different conditions throughout a vehicle trajectory [172, 173]. Such considerations are also directly linked to the life-time prediction for actual vehicle structures as well as SHM, which both pose significant challenges when facing such a broad range of aerothermodynamic load conditions.

# 6 Bibliography


[1] Alder, M., "Development and Validation of a Fluid–Structure Solver for Transonic Panel Flutter", *AIAA Journal*, vol. 53, no. 12, pp. 3509–3521, 2015. DOI: 10.2514/1.J054013.

[2] Argyris, J., G. Faust, and M. Haase, *Die Erforschung des Chaos*. Braunschweig/Wiesbaden, Germany: Vieweg, 1994, ISBN: 3528089415.

[3] Baehr, H. D. and K. Schwier, *Die thermodynamischen Eigenschaften der Luft*, Thermodynamische Eigenschaften der Gase und Flüssigkeiten. Berlin/Göttingen/Heidelberg: Springer-Verlag, 1961.

[4] Barfusz, O., F. Hötte, S. Reese, and M. Haupt, "Pseudo-transient 3D Conjugate Heat Transfer Simulation and Lifetime Prediction of a Rocket Combustion Chamber", in *Future Space-Transport-System Components under High Thermal and Mechanical Loads*, Adams, N., W. Schröder, R. Radespiel, O. Haidn, T. Sattelmayer, C. Stemmer, and B. Weigand, Eds., Notes on Numerical Fluid Mechanics and Multidisciplinary Design, vol. 146, Springer, 2021, pp. 265–278. DOI: 10.1007/978-3-030-53847-7_17.

[5] Bathel, B. F., C. R. Litzner, S. B. Jones, S. A. Berry, N. T. Smith, and T. J. Garbeff, "High-Speed Schlieren Analysis of Retropropulsion Jet in Mach 10 Flow", *Journal of Spacecraft and Rockets*, vol. 57, no. 1, pp. 33–48, 2020. DOI: 10.2514/1.a34522.

[6] "Bestimmung des Emissionsgrades von drei PEEK-Proben bei unterschiedlichen Temperaturen", Bayerisches Zentrum für Angewandte Energieforschung e. V., Tech. Rep., 2014.

[7] *Betriebsanleitung optoNCDT 1420 (received 10.2.2022)*, Micro-Epsilon Messtechnik, Ortenburg, Germany.

[8] Bisplinghoff, R., "Some Structural and Aeroelastic Considerations of High-Speed Flight - The Nineteenth Wright Brothers Lecture", *Journal of the Aeronautical Sciences*, vol. 23, no. 4, pp. 289–329, 1956.

[9] Boyer, N. R., J. McNamara, D. Gaitonde, C. J. Barnes, and M. R. Visbal, "Features of panel flutter response to shock boundary layer interactions", *Journal of Fluids and Structures*, vol. 101, p. 103 207, 2021. DOI: 10.1016/j.jfluidstructs.2020.103207.

[10] Brouwer, K. R., R. A. Perez, T. J. Beberniss, S. M. Spottswood, and D. A. Ehrhardt, "Experiments on a Thin Panel Excited by Turbulent Flow and Shock/Boundary-Layer Interactions", *AIAA Journal*, pp. 2737–2752, 2021. DOI: 10.2514/1.j060114.

[11] Brouwer, K. R., R. A. Perez, T. J. Beberniss, S. M. Spottswood, and D. A. Ehrhardt, "Evaluation of reduced-order aeroelastic simulations for shock-dominated flows", *Journal of Fluids and Structures*, vol. 108, p. 103 429, 2022. DOI: 10.1016/j.jfluidstructs.2021.103429.

[12] Brouwer, K. R., R. A. Perez, T. J. Beberniss, S. M. Spottswood, D. A. Ehrhardt, and R. Wiebe, "Investigation of aeroelastic instabilities for a thin panel in turbulent flow", *Nonlinear Dynamics*, 2021. DOI: 10.1007/s11071-021-06571-4.

[13] Casper, K. M., S. J. Beresh, J. F. Henfling, R. W. Spillers, P. Hunter, and S. Spitzer, "Hypersonic Fluid-Structure Interactions Due to Intermittent Turbulent Spots on a Slender Cone", *AIAA Journal*, vol. 57, no. 2, pp. 749–759, 2019. DOI: 10.2514/1.j057374.

[14] Clemens, N. T. and V. Narayanaswamy, "Low-Frequency Unsteadiness of Shock Wave/Turbulent Boundary Layer Interactions", *Annual Review of Fluid Mechanics*, vol. 46, no. 1, pp. 469–492, 2014. DOI: 10.1146/annurev-fluid-010313-141346.

[15] "CODATA Recommended Values of the Fundamental Physical Constants: 2018", National Institute of Standards and Technoloy, Tech. Rep. NIST SP 961, 2019. URL: https://physics.nist.gov/cuu/pdf/wall_2018.pdf.

[16] Coe, C. F. and W. J. Chyu, "Pressure-Fluctuation Inputs and Response of Panels Underlying Attached and Separated Supersonic Turbulent Boundary Layers", NASA, Ames Research Center, Moffett Field, Ca., Tech. Rep. TM X-62,189, 1972.

[17] Currao, G. M. D., R. Choudhury, S. L. Gai, A. J. Neely, and D. R. Buttsworth, "Hypersonic Transitional Shock-Wave–Boundary-Layer Interaction on a Flat Plate", *AIAA Journal*, vol. 58, no. 2, pp. 814–829, 2020. DOI: 10.2514/1.j058718.

[18] Curry, D. M., "Space Shuttle Orbiter Thermal Protection System Design and Flight Experience", NASA, Tech. Rep. TM 104773, 1993.

[19] *Datasheet: Ensinger – TECAPEEK natural (received 28.6.2021).*

[20] Daub, D., B. Esser, S. Willems, and A. Gülhan, "Experiments on Thermomechanical Fluid-Structure Interaction in Supersonic Flows", in *SFB/TRR40 Annual Report*, Stemmer, C., N. A. Adams, O. J. Haidn, R. Radespiel, T. Sattelmayer, W. Schröder, and B. Weigand, Eds., Garching bei München: Lehrstuhl für Aerodynamik und Strömungsmechanik, Technische Universität München, 2017, pp. 243–254.

[21] Daub, D., B. Esser, S. Willems, and A. Gülhan, "Experimental Studies on Aerothermal Fluid-Structure Interaction with Plastic Deformation", in *SFB/TRR40 Annual Report*, Stemmer, C., N. A. Adams, O. J. Haidn, R. Radespiel, T. Sattelmayer, W. Schröder, and B. Weigand, Eds., Garching bei München: Lehrstuhl für Aerodynamik und Strömungsmechanik, Technische Universität München, 2018, pp. 269–279.

[22] Daub, D., S. Willems, B. Esser, and A. Gülhan, "Experiments on Elastic Aerothermal Fluid/Structure Interaction in Supersonic Flows", in *SFB/TRR40 Annual Report*, Stemmer, C., N. A. Adams, O. J. Haidn, R. Radespiel, T. Sattelmayer, W. Schröder, and B. Weigand, Eds., Garching bei München: Lehrstuhl für Aerodynamik und Strömungsmechanik, Technische Universität München, 2019, pp. 277–290.

[23] Daub, D., S. Willems, A. Gülhan, and B. Esser, "Experimental Setup for Excitation of Fluid-Structure Interaction", in *SFB/TRR40 Annual Report*, Stemmer, C., N. A. Adams, O. J. Haidn, R. Radespiel, T. Sattelmayer, W. Schröder, and B. Weigand, Eds., Garching bei München: Lehrstuhl für Aerodynamik und Strömungsmechanik, Technische Universität München, 2014, pp. 305–314.

[24] Daub, D., S. Willems, A. Gülhan, and B. Esser, "Experimental Results on Fluid-Structure Interaction excited by an Incident Shockwave on an Elastic Panel", in *SFB/TRR40 Annual Report*, Stemmer, C., N. A. Adams, O. J. Haidn, R. Radespiel, T. Sattelmayer, W. Schröder, and B. Weigand, Eds., Garching bei München: Lehrstuhl für Aerodynamik und Strömungsmechanik, Technische Universität München, 2015, pp. 281–292.

[25] Daub, D., B. Esser, and A. Gülhan, "Experiments on High-Temperature Hypersonic Fluid-Structure Interaction with Plastic Deformation", *AIAA Journal*, vol. 58, no. 4, pp. 1423–1431, 2020. DOI: 10.2514/1.j059150.

[26] Daub, D., B. Esser, S. Willems, and A. Gülhan, "Experimental Studies on Aerothermal Fluid-Structure Interaction with Plastic Deformation", in *69th International Astronautical Congress*, Bremen, 2018.

[27] Daub, D., S. Willems, B. Esser, and A. Gülhan, "Experimental Studies on Supersonic Aerothermal Fluid-Structure Interaction.", in *68th International Astronautical Congress*, Adelaide, Australia, 2017.

[28] Daub, D., S. Willems, B. Esser, and A. Gülhan, "Experiments on Aerothermal Supersonic Fluid-Structure Interaction", in *Future Space-Transport-System Components under High Thermal and Mechanical Loads*, Adams, N., W. Schröder, R. Radespiel, O. Haidn, T. Sattelmayer, C. Stemmer, and B. Weigand, Eds., Notes on Numerical Fluid Mechanics and Multidisciplinary Design, vol. 146, Springer, 2021, pp. 323–339. DOI: 10.1007/978-3-030-53847-7_21.

[29] Daub, D., S. Willems, and A. Gülhan, "Experimental Results on Shock-Wave/Boundary-Layer Interaction induced by a Movable Wedge", in *8th European Symposium on Aerothermodynamics*, Lisbon, 2015.

[30] Daub, D., S. Willems, and A. Gülhan, "Experimental results on unsteady shock-wave/boundary-layer interaction induced by an impinging shock", *CEAS Space Journal*, vol. 8, no. 1, pp. 3–12, 2016. DOI: 10.1007/s12567-015-0102-4.

[31] Daub, D., S. Willems, and A. Gülhan, "Experiments on the Interaction of a Fast-Moving Shock with an Elastic Panel", *AIAA Journal*, vol. 54, no. 2, pp. 670–678, 2016. DOI: 10.2514/1.J054233.

[32] Daub, D., S. Willems, and A. Gülhan, "Experiments on Shock Induced Instationary Fluid-Structure Interaction", in *1st International Aerospace Symposium on Acoustic Fatigue*, Glasgow, UK, 2017.

[33] Daub, D., S. Willems, and A. Gülhan, "Experiments on aerothermoelastic fluid-structure interaction in hypersonic flow", *Journal of Sound and Vibration*, 2022. DOI: 10.1016/j.jsv.2021.116714.

[34] Diamanti, K. and C. Soutis, "Structural health monitoring techniques for aircraft composite structures", *Progress in Aerospace Sciences*, vol. 46, no. 8, pp. 342–352, 2010. DOI: 10.1016/j.paerosci.2010.05.001.

[35] *DIN 1319-3 Grundlagen der Meßtechnik - Teil 3: Auswertung von Messungen einer einzelnen Meßgrösse und Meßunsicherheiten*, Deutsches Institut für Normung e.V. (DIN), 1996.

[36] *DIN 1319-4 Grundlagen der Meßtechnik - Teil 4: Auswertung von Messungen und Meßunsicherheit*, Deutsches Institut für Normung e.V. (DIN), 1999.

[37] Doebling, S. W., C. R. Farrar, and M. B. Prime, "A Summary Review of Vibration-Based Damage Identification Methods", *The Shock and Vibration Digest*, vol. 30, no. 2, pp. 91–105, 1998. DOI: 10.1177/058310249803000201.

[38] Dolling, D. S., "Fifty Years of Shock-Wave/Boundary-Layer Interaction Research: What Next?", *AIAA Journal*, vol. 39, no. 8, pp. 1517–1531, 2001. DOI: 10.2514/2.1476.

[39] Dowell, E. H., "Panel Flutter – A review of the Aeroelastic Stability of Plates and Shells", *AIAA Journal*, vol. 8, no. 3, pp. 385–399, 1970. DOI: 10.2514/3.5680.

[40] Dowell, E. H., "Aerodynamic Boundary Layer Effects on Flutter and Damping of Plates", *Journal of Aircraft*, vol. 10, no. 12, pp. 734–738, 1973. DOI: 10.2514/3.60298.

[41] Dowell, E. H., *Aeroelasticity of Plates and Shells*, Meirovitch, L., Ed. Leyden, Netherlands: Noordhoff International Publishing, 1975.

[42] Dowell, E. H. and H. M. Voss, "The Effect of a Cavity on Panel Vibration", *AIAA Journal*, vol. 1, no. 2, pp. 476–477, 1963. DOI: 10.2514/3.1568.

[43] Dowell, E., "Flutter of a buckled plate as an example of chaotic motion of a deterministic autonomous system", *Journal of Sound and Vibration*, vol. 85, no. 3, pp. 333–344, 1982. DOI: 10.1016/0022-460x(82)90259-0.

[44] Drogoul, S., "From the Failure to the Success - The Return to Flight of the Ariane 5 ECA Launcher", in *56th International Astronautical Congress*, Fuduoka, Japan, 2005. DOI: 10.2514/6.iac-05-d2.2.08.

[45] Edberg, D. and W. Costa, *Design of Rockets and Space Launch Vehicles*. Reston, Va.: American Institute of Aeronautics and Astronautics, 2020, ISBN: 9781624105937.

[46] Ehrhardt, D. A. and L. N. Virgin, "Experiments on the thermal post-buckling of panels, including localized heating", *Journal of Sound and Vibration*, vol. 439, pp. 300–309, 2019. DOI: 10.1016/j.jsv.2018.08.043.

[47] "Equations, Tables, and Charts for Compressible Flow", National Advisory Committee for Aeronautics, Tech. Rep. 1135, 1953.

[48] Esch, H., "Inauguration of the Arc Heated Facility L3K", Deutsches Zentrum für Luft- und Raumfahrt e.V. (DLR), Köln, Tech. Rep., 1996.

[49] Esch, H., "Die 0,6-m x 0,6-m-Trisonische Meßstrecke (TMK) der DFVLR in Köln-Porz (Stand 1986)", DLR, Köln, Tech. Rep. 86-21, 1986.

[50] Fedorov, A. and A. Khokhlov, "Receptivity of Hypersonic Boundary Layer to Wall Disturbances", *Theoretical and Computational Fluid Dynamics*, vol. 15, no. 4, pp. 231–254, 2002. DOI: 10.1007/s001620100052.

[51] Fedorov, A., "Transition and Stability of High-Speed Boundary Layers", *Annual Review of Fluid Mechanics*, vol. 43, no. 1, pp. 79–95, 2011. DOI: 10.1146/annurev-fluid-122109-160750.

[52] Fedorova, N. N. and I. A. Fedorchenko, "Computations of Interaction of an Incident Oblique Shock Wave with a Turbulent Boundary Layer on a Flat Plate", *Journal of Applied Mechanics and Technical Physics*, vol. 45, no. 3, pp. 358–366, 2004. DOI: 10.1023/B:JAMT.0000025017.49191.14.

[53] Fiedler, T., J. Rösler, M. Bäker, F. Hötte, C. v. Sethe, D. Daub, M. Haupt, O. Haidn, B. Esser, and A. Gülhan, "Mechanical Integrity of Thermal Barrier Coatings - Coating Development and Micromechanics", in *Future Space-Transport-System Components under High Thermal and Mechanical Loads*, Adams, N., W. Schröder, R. Radespiel, O. Haidn, T. Sattelmayer, C. Stemmer, and B. Weigand, Eds., Notes on Numerical Fluid Mechanics and Multidisciplinary Design, vol. 146, Springer, 2021, pp. 295–307. DOI: 10.1007/978-3-030-53847-7_19.

[54] Fish, R. and K. Parnham, "Focussing Schlieren Systems", Aeronautical Research Council, London, Tech. Rep., 1950.

[55] Freydin, M., E. H. Dowell, S. M. Spottswood, and R. A. Perez, "Nonlinear dynamics and flutter of plate and cavity in response to supersonic wind tunnel start", *Nonlinear Dynamics*, 2020. DOI: 10.1007/s11071-020-05817-x.

[56] Garbos, R., L. Melvin, B. Childers, and B. Jambor, "System health management/vehicle health management for future manned space systems", in *16th DASC. AIAA/IEEE Digital Avionics Systems Conference. Reflections to the Future. Proceedings*, IEEE, 1997. DOI: 10.1109/dasc.1997.637284.

[57] Glass, C. E. and L. R. Hunt, "Aerothermal Tests of Spherical Dome Protuberances on a Flat Plate at a Mach Number of 6.5", National Aeronautics and Space Administration, Tech. Rep. TP-2631, 1986.

[58] Gogulapati, A., R. Deshmukh, J. J. Crowell A. R. McNamara, V. Vyas, X. Q. Wang, M. Mignolet, T. Beberniss, S. M. Spottswood, and T. G. Eason, "Response of a Panel to Shock Impingement: Modeling and Comparison with Experiments", in *55th AIAA/ASME/ASCE/AHS/ASC Structures, Structural Dynamics, and Materials Conference*, National Harbor, Md.: American Institute of Aeronautics and Astronautics, 2014. DOI: 10.2514/6.2014-0148.

[59] Gogulapati, A., R. Deshmukh, J. J. McNamara, V. Vyas, X. Wang, M. P. Mignolet, T. Beberniss, S. M. Spottswood, and T. G. Eason, "Response of a Panel to Shock Impingement: Modeling and Comparison with Experiments - Part 2", in *56th AIAA/ASCE/AHS/ASC Structures, Structural Dynamics, and Materials Conference*, Kissimmee, Fl.: American Institute of Aeronautics and Astronautics, 2015. DOI: 10.2514/6.2015-0685.

[60] Gottwald, G. A. and I. Melbourne, "On the validity of the 0–1 test for chaos", *Nonlinearity*, vol. 22, no. 6, pp. 1367–1382, 2009. DOI: 10.1088/0951-7715/22/6/006.

[61] Gottwald, G. A. and I. Melbourne, "A new test for chaos in deterministic systems", *Proceedings of the Royal Society of London. Series A: Mathematical, Physical and Engineering Sciences*, vol. 460, no. 2042, pp. 603–611, 2004. DOI: 10.1098/rspa.2003.1183.

[62] Gottwald, G. A. and I. Melbourne, "On the Implementation of the 0–1 Test for Chaos", *SIAM Journal on Applied Dynamical Systems*, vol. 8, no. 1, pp. 129–145, 2009. DOI: 10.1137/080718851.

[63] Gottwald, G. A. and I. Melbourne, "The 0-1 Test for Chaos: A Review", in *Chaos Detection and Predictability*, Berlin, Heidelberg: Springer, 2016, pp. 221–247. DOI: 10.1007/978-3-662-48410-4_7.

[64] Gramola, M., P. J. K. Bruce, and M. Santer, "Photogrammetry for accurate model deformation measurement in a supersonic wind tunnel", *Experiments in Fluids*, vol. 60, no. 1, 2019. DOI: 10.1007/s00348-018-2652-7.

[65] Gülhan, A. and B. Esser, "Arc-Heated Facilities as a Tool to Study Aerothermodynamic Problems of Reentry Vehicles", in, Lu, F. and D. Marren, Eds., Progress in Astronautics and Aeronautics. Reston, Va.: American Institute of Aeronautics and Astronautics, 2002, vol. 198, ch. 13, pp. 375–403. DOI: 10.2514/5.9781600866678.0375.0403.

[66] Gülhan, A., B. Esser, U. Koch, M. Fischer, E. Magens, and V. Hannemann, "Characterization of High-Enthalpy-Flow Environment for Ablation Material Tests Using Advanced Diagnostics", *AIAA Journal*, vol. 56, no. 3, pp. 1072–1084, 2018. DOI: 10.2514/1.j056312.

[67] Gülhan, A., S. Willems, and D. Neeb, "Shock interaction induced heat flux augmentation in hypersonic flows", *Experiments in Fluids*, vol. 62, no. 12, 2021. DOI: 10.1007/s00348-021-03336-y.

[68] Haidn, O. J., N. A. Adams, R. Radespiel, T. Sattelmayer, W. Schröder, C. Stemmer, and B. Weigand, "Collaborative Research for Future Space Transportation Systems", in *Future Space-Transport-System Components under High Thermal and Mechanical Loads*, Adams, N., W. Schröder, R. Radespiel, O. Haidn, T. Sattelmayer, C. Stemmer, and B. Weigand, Eds., Notes on Numerical Fluid Mechanics and Multidisciplinary Design, Springer, 2021, pp. 1–30. DOI: 10.1007/978-3-030-53847-7_1.

[69] Haidn, O. J., N. A. Adams, T. Sattelmayer, C. Stemmer, R. Radespiel, W. Schröder, and B. Weigand, "Fundamental Technologies for the Development of Future Space Transportsystem Components under High Thermal and Mechanical Loads", in *2018 Joint Propulsion Conference*, Cincinnati, Oh.: American Institute of Aeronautics and Astronautics, 2018. DOI: 10.2514/6.2018-4466.

[70] Hammerl, G., A. Seitz, F. Verdugo, W. Wall, D. Daub, S. Willems, and Gülhan, "FSI of rocket nozzles - On the influence of simplified modeling of structural boundary conditions for an FSI experiment & scalable solvers for strongly coupled problems", in *SFB/TRR40 Annual Report*, Stemmer, C., N. A. Adams, O. J. Haidn, R. Radespiel, T. Sattelmayer, W. Schröder, and B. Weigand, Eds., Garching bei München: Lehrstuhl für Aerodynamik und Strömungsmechanik, Technische Universität München, 2016, pp. 253–262.

[71] Hashimoto, A., T. Aoyama, and Y. Nakamura, "Effects of Turbulent Boundary Layer on Panel Flutter", *AIAA Journal*, vol. 47, no. 12, pp. 2785–2791, 2009. DOI: 10.2514/1.35786.

[72] Haupt, M., "Ein Beitrag zur thermischen und mechanischen Analyse von heißen Flugzeugstrukturen", PhD thesis, Technische Universität Braunschweig, Aachen, 1997, ISBN: 3-8265-3124-8.

[73] Haupt, M., R. Niesner, B. Esser, and A. Gülhan, "Model Configuration for the Validation of Aerothermodynamic Thermal-Mechnical Fluid-Structure-Interactions", in *Proceedings of the ASME 2012 11th Biennial Conference on Engineering Systems Design and Analysis*, Nantes, France, 2012.

[74] Henckels, A., A. Kreins, and F. Maurer, "Experimental investigations of hypersonic shock-boundary layer interaction", *Zeitschrift für Flugwissenschaften und Weltraumforschung*, vol. 17, pp. 116–124, 1993.

[75] Henckels, A. and P. Gruhn, "Study on Aerothermal Effects of Viscous Shock Interaction in Hypersonic Inlets", in *Proceedings of the Fifth European Symposium on Aerothermodynamics for Space Vehicles*, Cologne, Germany: European Space Agency, 2005.

[76] Herron, A. J., W. A. Crosby, and D. K. Reed, "Overview of the Space Launch System Ascent Aeroacoustic Environment Test Program", in *54th AIAA Aerospace Sciences Meeting*, California, Ca.: American Institute of Aeronautics and Astronautics, 2016. DOI: 10.2514/6.2016-0543.

[77] Heyser, A., H. Pfeiffer, and H.-J. Schepers, "Der Hyperschallwindkanal H 2 der DFVLR in Porz-Wahn", Deutsche Forschungs- und Versuchsanstalt für Luft- und Raumfahrt e.V. (DFVLR), Tech. Rep., 1969.

[78] Hirsch, C., "WP-4 RANS/URANS Simulations", in *Unsteady Effects of Shock Wave Induced Separation*, Doerffer, P., C. Hirsch, J.-P. Dussauge, H. Babinsky, and G. N. Barakos, Eds., Notes on Numerical Fluid Mechanics and Multidisciplinary Desig, vol. 114, Springer, 2010, pp. 327–338, ISBN: 978-3-642-03003-1. DOI: 10.1007/978-3-642-03004-8.

[79] Hirschel, E. H., *Basics of Aerothermodynamics*. Berlin, Heidelberg, New York: Springer-Verlag, 2005, ISBN: 3-540-22132-8.

[80] Hötte, F., O. Günther, C. von Sethe, M. Haupt, P. Scholz, and M. Rohdenburg, "Lifetime Experiments of Regeneratively Cooled Rocket Combustion Chambers and PIV Measurements in a High Aspect Ratio Cooling Duct", in *Future Space-Transport-System Components under High Thermal and Mechanical Loads*, Adams, N., W. Schröder, R. Radespiel, O. Haidn, T. Sattelmayer, C. Stemmer, and B. Weigand, Eds., Notes on Numerical Fluid Mechanics and Multidisciplinary Design, vol. 146, Springer, 2021, pp. 265–278. DOI: 10.1007/978-3-030-53847-7_18.

[81] Hoy, J. F. and I. Bermejo-Moreno, "Numerical study of STBLI on flexible panels with wall-modeled LES", in *AIAA Scitech 2021 Forum*, American Institute of Aeronautics and Astronautics, 2021. DOI: 10.2514/6.2021-0250.

[82] Huang, R., Z. Li, and J. Yang, "Engineering Prediction of Fluctuating Pressure over Incident Shock/Turbulent Boundary-Layer Interactions", *AIAA Journal*, vol. 57, no. 5, pp. 2209–2213, 2019. DOI: 10.2514/1.j057903.

[83] Hurst, A. M., T. R. Olsen, S. Goodman, J. VanDeWeert, and T. Shang, "An Experimental Frequency Response Characterization of MEMS Piezoresistive Pressure Transducers", in *Proceedings of ASME Turbo Expo 2014: Turbine Technical Conference and Exposition*, Düsseldorf, 2014.

[84] Jaunet, V., J.-F. Debiève, and P. Dupont, "Length Scales and Time Scales of a Heated Shock-Wave/Boundary-Layer Interaction", *AIAA Journal*, vol. 52, no. 11, pp. 2524–2532, 2014. DOI: 10.2514/1.J052869.

[85] Jenkins, J. M. and R. D. Quinn, "A Historical Perspective of the YF-12A Thermal Loads and Structures Program", NASA, Dryden Flight Research Center, Edwards, Ca., Tech. Rep. TM-104317, 1996.

[86] Jordan, G. H., N. J. McLeod, and L. D. Guy, "Structural Dynamic Experiences of the X-15 Airplane", NASA, Flight Research Center, Edwards, Ca., Tech. Rep. TN D-1158, 1962.

[87] Joyce, B., J. Dodson, S. Laflamme, and J. Hong, "An Experimental Test Bed for Developing High-Rate Structural Health Monitoring Methods", *Shock and Vibration*, vol. 2018, pp. 1–10, 2018. DOI: 10.1155/2018/3827463.

[88] Kachanov, Y. S., "Physical Mechanisms of Laminar-Boundary-Layer Transition", *Annual Review of Fluid Mechanics*, vol. 26, no. 1, pp. 411–482, 1994. DOI: 10.1146/annurev.fl.26.010194.002211.

[89] Kappus, H. P., C. E. Lemley, and N. H. Zimmermann, "An Experimental Investigation of High Amplitude Panel Flutter", NASA, McDonnell Douglas Corporation, St. Louis, Mo. for George C. Marshall Space Flight Center, Al., Tech. Rep. CR-1837, 1971, p. 129.

[90] Kim, H.-G. and R. Wiebe, "Experimental and numerical investigation of nonlinear dynamics and snap-through boundaries of post-buckled laminated composite plates", *Journal of Sound and Vibration*, vol. 439, pp. 362–387, 2019. DOI: 10.1016/j.jsv.2018.09.056.

[91] Kirchheck, D., A. Marwege, J. Klevankski, and A. Gülhan, "Hypersonic Retrograde Propulsion Experiments – A Basis for Validation of CFD within RETPRO", in *Proceedings of the 9th European Conference for Aeronautics and Space Sciences*, Lille, France, 2022.

[92] Kirchheck, D., D. Saile, and A. Gülhan, "Spectral Analysis of Rocket Wake Flow-Jet Interaction by Means of High-speed Schlieren Imaging", in *Proceedings of the 8th European Conference for Aeronautics and Space Sciences*, Madrid, 2019. DOI: 10.13009/EUCASS2019-1057.

[93] Kontinos, D., "Coupled Thermal Analysis Method with Application to Metallic Thermal Protection Panels", *Journal of Thermophysics and Heat Transfer*, vol. 11, no. 2, pp. 173–181, 1997. DOI: 10.2514/2.6249.

[94] Kontinos, D. A. and G. Palmer, "Numerical Simulation of Metallic Thermal Protection System Panel Bowing", *Journal of Spacecraft and Rockets*, vol. 36, no. 6, pp. 842–849, 1999. DOI: 10.2514/2.3523.

[95] Kordes, E. E., W. J. Tuovila, and L. D. Guy, "Flutter Research on Skin Panels", NASA, Langley Research Center, Langley Field, Va., Tech. Rep. TN D-451, 1960.

[96] Korkegi, R. H., *Hypersonic Aerodynamics*. Rhode-Saint-Genese, Belgium: Von Karman Institute for Fluids Dynamics, 1962.

[97] Koschel, W., "Arianespace Flight 157 - Report of the Inquiry Board", European Space Agency, Tech. Rep., 2003.

[98] Krause, F., "Ueber die Einzelteile einer Toepler'schen Schlierenoptik mit parallelem Licht", Aerodynamische Versuchsanstalt (AVA), Göttingen, Tech. Rep. 62 A 30, 1962.

[99] Krausse, S. C., "Saturn V Aerothermodynamics Flight Evaluation Summary AS-501 through AS-503", The Boeing Company, Tech. Rep. D5-15796-1, 1969.

[100] Kreins, A. F., "Wärmestromverteilung und Strömungsfelduntersuchung in gestörten Hyperschall-Plattengrenzschichten", PhD thesis, DLR/RWTH Aachen University, 1994.

[101] Kreins, A. F., A. Henckels, and F. Maurer, "Experimental studies of hypersonic shock induced boundary layer separation", *Zeitschrift für Flugwissenschaften und Weltraumforschung*, vol. 2, no. 20, pp. 80–88, 1996.

[102] Kröplin, B.-H., R. Kochendörfer, T. Reimer, T. Ullmann, R. Kornmann, R. Schäfer, and T. Wallmersperger, "Design and Evaluation of Fibre Ceramic Structure", in *Basic Research and Technologies for Two-Stage-to-Orbit Vehicles: Final Report of the Collaborative Research Centres 253, 255 and 259*, Jacob, D., G. Sachs, and S. Wagner, Eds., Deutsche Forschungsgemeinschaft, WILEY-VCH Verlag, 2005, pp. 549–580, ISBN: 3527277358.

[103] LaFontaine, J. H., A. Gogulapati, and J. J. McNamara, "Effects of Strain Hardening on Response of Skin Panels in Hypersonic Flow", *AIAA Journal*, vol. 54, no. 6, pp. 1974–1986, 2016. DOI: 10.2514/1.j054582.

[104] Lall, T. R., "Interstage Adapter Panel Flutter on Atlas-Centaur AC-2, AC-3, and AC-4 Vehicles", NASA, Lewis Reserach Center, Cleveland, Oh., Tech. Rep. TM X-1179, 1965.

[105] Launius, R. D., J. Krige, and J. I. Craig, *Space Shuttle Legacy: How We Did It and What We Learned*. American Institute of Aeronautics and Astronautics, Inc., 2013, ISBN: 978-1-62410-216-5. DOI: 10.2514/4.102172.

[106] Lemmon, E. W., R. T. Jacobsen, S. G. Penoncello, and D. G. Friend, "Thermodynamic Properties of Air and Mixtures of Nitrogen, Argon, and Oxygen From 60 to 2000 K at Pressures to 2000 MPa", *Journal of Physical and Chemical Reference Data*, vol. 29, no. 3, pp. 331–385, 2000. DOI: 10.1063/1.1285884.

[107] Lewis, T. L. and N. J. McLeod, "Flight Measurements of Boundary-Layer Noise on the X-15", NASA, Flight Research Center, Edwards, Ca., Tech. Rep. TN D-3364, 1966.

[108] Lynch, K. P., E. Jones, and J. L. Wagner, "Simultaneous PSP and surface deformation measurements for fluid-structure interactions in a shock tube", in *2018 Fluid Dynamics Conference*, Atlanta, Ga.: American Institute of Aeronautics and Astronautics, 2018. DOI: 10.2514/6.2018-3870.

[109] Mack, A. and V. Hannemann, "Validation of the Unstructured DLR-TAU-Code for Hypersonic Flows", in *32nd AIAA Fluid Dynamics Conference and Exhibit*, St. Louis, Mo.: American Institute of Aeronautics and Astronautics, 2002. DOI: 10.2514/6.2002-3111.

[110] Maestrello, L., "Radiation from and Panel Response to a Supersonic Turbulent Boundary Layer", *Journal of Sound and Vibration*, vol. 10, no. 2, pp. 261–295, 1969. DOI: 10.1016/0022-460X(69)90200-4.

[111] Maestrello, L. and T. L. J. Linden, "Measurements of the Response of a Panel Excited by Shock Boundary-Layer Interaction", *Journal of Sound and Vibration*, vol. 16, no. 3, pp. 385–391, 1971. DOI: 10.1016/0022-460X(71)90594-3.

[112] Mancini, S., G. Tumino, and P. Gaudenzi, "Structural Health Monitoring for Future Space Vehicles", *Journal of Intelligent Material Systems and Structures*, vol. 17, no. 7, pp. 577–585, 2006. DOI: 10.1177/1045389x06059077.

[113] Martin, K., D. Daub, B. Esser, A. Gülhan, and S. Reese, "Numerical Modelling of Fluid-Structure Interaction for Thermal Buckling in Hypersonic Flow", in *Future Space-Transport-System Components under High Thermal and Mechanical Loads*, Adams, N., W. Schröder, R. Radespiel, O. Haidn, T. Sattelmayer, C. Stemmer, and B. Weigand, Eds., Notes on Numerical Fluid Mechanics and Multidisciplinary Design, vol. 146, Springer, 2021, pp. 341–355. DOI: 10.1007/978-3-030-53847-7_22.

[114] Martin, K., D. Daub, B. Esser, A. Gülhan, and S. Reese, "Coupled Simulation of Hypersonic Fluid–Structure Interaction with Plastic Deformation", *AIAA Journal*, vol. 60, no. 6, pp. 3424–3437, 2022. DOI: 10.2514/1.j060561.

[115] Martin, K., S. Reese, D. Daub, B. Esser, A. Gülhan, F. Hötte, and M. Haupt, "Simulationsmethoden und experimentelle Validierung für thermisches Beulen dünnwandiger Strukturen unter aerothermodynamischen Lasten", in *66. Deutscher Luft- und Raumfahrtkongress*, München, 2017.

[116] Mei, C., K. Abdel-Motagaly, and R. Chen, "Review of Nonlinear Panel Flutter at Supersonic and Hypersonic Speeds", *Applied Mechanics Reviews*, vol. 52, no. 10, pp. 321–332, 1999. DOI: 10.1115/1.3098919.

[117] Merlin, P. W., "Design and Development of the Blackbird: Challenges and Lessons Learned", in *47th AIAA Aerospace Sciences Meeting Including The New Horizons Forum and Aerospace Exposition*, Orlando, Fl.: American Institute of Aeronautics and Astronautics, 2009.

[118] Miller, B., J. McNamara, S. Spottswood, and A. Culler, "The impact of flow induced loads on snap-through behavior of acoustically excited, thermally buckled panels", *Journal of Sound and Vibration*, vol. 330, no. 23, pp. 5736–5752, 2011. DOI: 10.1016/j.jsv.2011.06.028.

[119] Moix-Bonet, M., B. Eckstein, and P. Wierach, "Temperature Compensation for Damage Detection in Composite Structures using Guided Waves", in *9th European Workshop on Structural Health Monitoring*, Manchester, United Kingdom, 2018.

[120] Musk, E., "Making Life Multi-Planetary", *New Space*, vol. 6, no. 1, pp. 2–11, 2018. DOI: 10.1089/space.2018.29013.emu.

[121] Nacht, M. L. and R. L. Greene, "Panel Flutter Studies of Boost-Vehicle Full-Scale Flight Insulation Panels", NASA, Lewis Research Center, Cleveland, Oh., Tech. Rep. TM X-1417, 1967.

[122] Natke, H. G., *Einführung in Theorie und Praxis der Zeitreihen- und Modalanalyse*. Braunschweig; Wiesbaden: Vieweg, 1983, 564 pp., ISBN: 3528081457.

[123] Nichols, J., "Final Report: Saturn V, S-IVB Panel Flutter Qualification Test", NASA, George C. Marshall Space Flight Center, Marshall, Al., Tech. Rep. TN D-5439, 1969.

[124] Niesner, R., "Gekoppelte Simulation thermisch-mechanischer Fluid-Struktur-Interaktionen für Hyperschall-Anwendungen (Coupled Simulation of Thermomechanical Fluid-Structure Interaction for Hypersonic Applications)", PhD thesis, Technische Universität Braunschweig, 2009, ISBN: 9783832279578.

[125] Niezgodka, F.-J., "Der Hyperschallwindkanal H2K des DLR in Köln-Porz (The Hypersonic Wind Tunnel H2K of DLR in Köln-Porz)", Köln, Tech. Rep. 2001-01, 2001.

[126] Nydick, I. H., "Studies in Hypersonic Aeroelasticity", PhD thesis, University of California, Los Angeles, Ca., 2000.

[127] Palmer, G., D. Kontinos, and B. Sherman, "Surface heating effects of X-33 vehicle TPS panel bowing, steps, and gaps", in *36th AIAA Aerospace Sciences Meeting and Exhibit*, Reno, Nv.: American Institute of Aeronautics and Astronautics, 1998. DOI: 10.2514/6.1998-865.

[128] Pasquariello, V., "Analysis and Control of Shock-Wave/Turbulent Boundary-Layer Interactions on Rigid and Flexible Walls", PhD thesis, Technische Universität München, 2018.

[129] Pasquariello, V., G. Hammerl, D. Daub, S. Willems, S. Hickel, W. A. Wall, A. Gülhan, and N. Adams, "Coupled simulation of shock-wave/turbulent boundary-layer interaction over a flexible panel", in *SFB/TRR40 Annual Report*, Stemmer, C., N. A. Adams, O. J. Haidn, R. Radespiel, T. Sattelmayer, W. Schröder, and B. Weigand, Eds., Garching bei München: Lehrstuhl für Aerodynamik und Strömungsmechanik, Technische Universität München, 2015, pp. 261–280.

[130] Pasquariello, V., S. Hickel, N. Adams, G. Hammerl, W. A. Wall, D. Daub, S. Willems, and A. Gülhan, "Coupled simulation of shock-wave/turbulent boundary-layer interaction over a flexible panel", in *6th European Conference for Aerospace Sciences*, Krakow, Poland: EUCASS, 2015.

[131] Pasquariello, V., S. Hickel, and N. A. Adams, "Unsteady effects of strong shock-wave/boundary-layer interaction at high Reynolds number", *Journal of Fluid Mechanics*, vol. 823, pp. 617–657, 2017. DOI: 10.1017/jfm.2017.308.

[132] Perkins, T. M., "Aeroelastic Stability of an Array of Full-Scale Panels from the Saturn S-IVB Stage at Transonic Mach Numbers", Arnold Engineering Development Center, Arnold Air Force Station, Tn., Tech. Rep. AEDC-TR-67-9, 1967.

[133] Pham, H. T., Z. N. Gianikos, and V. Narayanaswamy, "Compression Ramp Induced Shock-Wave/Turbulent Boundary-Layer Interactions on a Compliant Material", *AIAA Journal*, pp. 1–5, 2018. DOI: 10.2514/1.j056652.

[134] Physikalisch-Technische Bundesanstalt, B., "Praxisgerechte Ermittlung der Messunsicherheit: Leitfaden DKD-L 13-1", de, 2019. DOI: 10.7795/550.20191105.

[135] Polivanov, P. A., A. A. Sidorenko, and A. A. Maslov, "Experimental Study of Unsteady Effects in Shock Wave / Turbulent Boundary Layer Interaction", in *47th AIAA Aerospace Sciences Meeting Including The New Horizons Forum and Aerospace Exposition*, Orlando, Fl.: American Institute of Aeronautics and Astronautics, 2009, ISBN: 978-1-60086-973-0. DOI: 10.2514/6.2009-409.

[136] Quentmeyer, R., "Rocket combustion chamber life-enhancing design concepts", in *26th Joint Propulsion Conference*, Reston, Virigina: American Institute of Aeronautics and Astronautics, 1990. DOI: 10.2514/6.1990-2116.

[137] Riley, Z. B., R. A. Perez, G. W. Bartram, S. M. Spottswood, B. P. Smarslok, and T. J. Beberniss, "Aerothermoelastic experimental design for the AEDC/VKF Tunnel C: Challenges associated with measuring the response of flexible panels in high-temperature, high-speed wind tunnels", *Journal of Sound and Vibration*, vol. 441, pp. 96–105, 2019. DOI: 10.1016/j.jsv.2018.10.022.

[138] Schäfer, R., "Thermisch-mechanisches Verhalten heißer Strukturen in der Wechselwirkung mit einem umströmenden Fluid", PhD thesis, DLR/Universität Kassel, 2005.

[139] Schlichting, H. and K. Gersten, *Boundary-Layer Theory*. Berlin, Heidelberg: Springer, 2017. DOI: 10.1007/978-3-662-52919-5.

[140] Schülein, E., "Skin Friction and Heat Flux Measurements in Shock/Boundary Layer Interaction Flows", *AIAA Journal*, vol. 44, no. 8, pp. 1732–1741, 2006. DOI: 10.2514/1.15110.

[141] Schülein, E., P. Krogmann, and E. Stanewsky, "Documentation of two-dimensional impinging shock/turbulent boundary layer interaction flow", DLR Institut für Aerodynamik und Strömungstechnik, Göttingen, Tech. Rep. DLR-IB 223 - 96 A 49, 1996.

[142] Schweikhard, K. A., W. L. Richards, J. Theisen, W. Mouyos, and R. Garbos, "Flight Demonstration of X-33 Vehicle Health Management System Components on the F/A-18 Systems Research Aircraft", National Aeronautics and Space Administration, Tech. Rep. TM-2001-209037, 2001.

[143] Seltner, P. M., S. Willems, and A. Gülhan, "Aerodynamic Coefficients of Free-Flying Cubes in Hypersonic Flowfield", *Journal of Spacecraft and Rockets*, vol. 56, no. 6, pp. 1725–1734, 2019. DOI: 10.2514/1.a34345.

[144] Settles, G. S., *Schlieren and Shadowgraph Techniques*. Berlin, Heidelberg: Springer, 2006, ISBN: 3540661557.

[145] Shideler, J. L., S. C. Dixon, and C. P. Shore, "Flutter at Mach 3 of Thermally Stressed Panels and Comparison with Theory for Panels with Edge Rotational Restraint", NASA, Langley Research Center, Langley Station, Hampton, Va., Tech. Rep. TN D-3498, 1966.

[146] Shinde, V., J. McNamara, D. Gaitonde, C. Barnes, and M. Visbal, "Transitional shock wave boundary layer interaction over a flexible panel", *Journal of Fluids and Structures*, vol. 90, pp. 263–285, 2019. DOI: 10.1016/j.jfluidstructs.2019.07.007.

[147] Shinde, V. J., J. J. McNamara, and D. V. Gaitonde, "Shock Wave Turbulent Boundary Layer Interaction Over a Flexible Panel", in *AIAA Scitech 2021 Forum*, American Institute of Aeronautics and Astronautics, 2021. DOI: 10.2514/6.2021-0488.

[148] SpaceX, *Starship High-Altitude Flight Test (CC BY-NC 2.0: https://www.creativecommons.org/licenses/by-sa/2.0/, received 24.3.2022)*, 2021. URL: https://www.flickr.com/photos/spacex/50906488116/.

[149] Spottswood, S. M., T. J. Beberniss, and T. G. Eason, "Full-field, dynamic pressure and displacement measurements of a panel excited by shock boundary-layer interaction", in *19th AIAA/CEAS Aeroacoustics Conference*, Berlin: American Institute of Aeronautics and Astronautics, 2013, ISBN: 9781624102134. DOI: 10.2514/6.2013-2016.

[150] Spottswood, S. M., T. J. Beberniss, T. G. Eason, R. A. Perez, J. M. Donbar, D. A. Ehrhardt, and Z. B. Riley, "Exploring the response of a thin, flexible panel to shock-turbulent boundary-layer interactions", *Journal of Sound and Vibration*, vol. 443, pp. 74–89, 2019. DOI: 10.1016/j.jsv.2018.11.035.

[151] Spottswood, S. M., B. P. Smarslok, R. A. Perez, T. J. Beberniss, B. J. Hagen, Z. B. Riley, K. R. Brouwer, and D. A. Ehrhardt, "Supersonic Aerothermoelastic Experiments of Aerospace Structures", *AIAA Journal*, vol. 59, no. 12, pp. 5029–5048, 2021. DOI: 10.2514/1.j060403.

[152] Spottswood, S. M., T. G. Eason, and T. J. Beberniss, "Influence of shock-boundary layer interactions on the dynamic response of a flexible panel", in *Proceedings of the 25th International Conference on Noise and Vibration Engineering (ISMA 2012)*, Leuven, Belgium, 2012, pp. 603–616, ISBN: 9781622768257.

[153] Steva, T. B., V. J. Pollard, A. Herron, and W. A. Crosby, "Space Launch System Aeroacoustic Wind Tunnel Test Results", in *AIAA Aviation 2019 Forum*, Dallas, Tx.: American Institute of Aeronautics and Astronautics, 2019. DOI: 10.2514/6.2019-3303.

[154] Stillwell, W. H., "X-15 Research Results - With a Selected Bibliography", NASA, Washington, D.C., Tech. Rep. SP-60, 1965.

[155] Sun, Z., T. Gan, and Y. Wu, "Shock-Wave/Boundary-Layer Interactions at Compression Ramps Studied by High-Speed Schlieren", *AIAA Journal*, vol. 58, no. 4, pp. 1681–1688, 2020. DOI: 10.2514/1.j058257.

[156] Tennekes, H. and J. L. Lumley, *A First Course in Turbulence*. Cambridge, Massachusetts: The MIT Press, 1972, ISBN: 9780262200196.

[157] Thornton, E. A. and P. Dechaumphai, "Coupled Flow, Thermal, and Structural Analysis of Aerodynamically Heated Panels", *Journal of Aircraft*, vol. 25, no. 11, pp. 1052–1059, 1988. DOI: 10.2514/3.45702.

[158] Touré, P. S. R. and E. Schülein, "Scaling for steady and traveling shock wave/turbulent boundary layer interactions", *Experiments in Fluids*, vol. 61, no. 7, 2020. DOI: 10.1007/s00348-020-02989-5.

[159] Tripathi, A., L. Mears, K. Shoele, and R. Kumar, "Oblique Shockwave Boundary Layer Interactions on a Flexible Panel at Mach 2", in *AIAA Scitech 2020 Forum*, Orlando, Fl.: American Institute of Aeronautics and Astronautics, 2020. DOI: 10.2514/6.2020-0568.

[160] Ventres, C. S. and E. H. Dowell, "Comparison of Theory and Experiment for Nonlinear Flutter of Loaded Plates", *AIAA Journal*, vol. 8, no. 11, pp. 2022–2030, 1970. DOI: 10.2514/3.6041.

[161] Visbal, M., "On the interaction of an oblique shock with a flexible panel", *Journal of Fluids and Structures*, vol. 30, pp. 219–225, 2012. DOI: 10.1016/j.jfluidstructs.2012.02.002.

[162] Visbal, M., "Viscous and inviscid interactions of an oblique shock with a flexible panel", *Journal of Fluids and Structures*, vol. 48, pp. 27–45, 2014. DOI: 10.1016/j.jfluidstructs.2014.02.003.

[163] Volpiani, P. S., M. Bernardini, and J. Larsson, "Effects of a nonadiabatic wall on supersonic shock/boundary-layer interactions", *Physical Review Fluids*, vol. 3, no. 8, 2018. DOI: 10.1103/physrevfluids.3.083401.

[164] Volpiani, P. S., M. Bernardini, and J. Larsson, "Effects of a nonadiabatic wall on hypersonic shock/boundary-layer interactions", *Physical Review Fluids*, vol. 5, no. 1, 2020. DOI: 10.1103/physrevfluids.5.014602.

[165] Wang, B., N. D. Sandham, Z. Hu, and W. Liu, "Numerical study of oblique shock-wave/boundary-layer interaction considering sidewall effects", *Journal of Fluid Mechanics*, vol. 767, pp. 526–561, 2015. DOI: 10.1017/jfm.2015.58.

[166] Watts, J. D., "Flight Experience with Shock Impingement and Interference Heating on the X-15-2 Research Airplane", NASA, Flight Research Center, Edwards, Ca., Tech. Rep. TM X-1669, 1968.

[167] Weinstein, L. M., "Large-field high-brightness focusing schlieren system", *AIAA Journal*, vol. 31, no. 7, pp. 1250–1255, 1993. DOI: 10.2514/3.11760.

[168] Welch, P., "The Use of Fast Fourier Transform for the Estimation of Power Spectra: A Method Based on Time Averaging Over Short, Modified Periodograms", *IEEE Transactions on Audio and Electroacoustics*, vol. 15, no. 2, pp. 70–73, 1967. DOI: 10.1109/TAU.1967.1161901.

[169] Whalen, T. J., A. G. Schöneich, S. J. Laurence, B. T. Sullivan, D. J. Bodony, M. Freydin, E. H. Dowell, and G. M. Buck, "Hypersonic Fluid–Structure Interactions in Compression Corner Shock-Wave/Boundary-Layer Interaction", *AIAA Journal*, vol. 58, no. 9, pp. 4090–4105, 2020. DOI: 10.2514/1.j059152.

[170] Wheaton, B. M., D. C. Berridge, T. D. Wolf, R. T. Stevens, and B. E. McGrath, "Boundary Layer Transition (BOLT) Flight Experiment Overview", in *2018 Fluid Dynamics Conference*, Atlanta, Ga.: American Institute of Aeronautics and Astronautics, 2018. DOI: 10.2514/6.2018-2892.

[171] Wiebe, R. and S. Spottswood, "On the dimension of complex responses in nonlinear structural vibrations", *Journal of Sound and Vibration*, vol. 373, pp. 192–204, 2016. DOI: 10.1016/j.jsv.2016.03.009.

[172] Wilken, J., S. Callsen, D. Daub, A. Fischer, M. Liebisch, C. Rauh, T. Reimer, H. Scheufler, and M. Sippel, "Testing combined cryogenic insulation and thermal protection systems for reusable stages", in *72nd International Astronautical Congress*, Dubai, United Arab Emirates, 2021.

[173] Wilken, J., S. Callsen, D. Daub, A. Fischer, M. Liebisch, C. Rauh, T. Reimer, H. Scheufler, and M. Sippel, "Combined cryogenic insulation and thermal protectionsystems for reusable stages", in *Proceedings of the 9th European Conference for Aeronautics and Space Sciences*, Lille, France, 2022.

[174] Willems, S., "Strömungs-Struktur-Wechselwirkung in Überschallströmungen (Fluid/Structure Interaction in Supersonic Flows)", PhD thesis, DLR/RWTH Aachen University, 2017. URL: https://elib.dlr.de/116735/.

[175] Willems, S., *User Guide: ROBOT 8.8 - Render Object Based Orientation Tracking*, DLR, Cologne, Germany, 2019.

[176] Willems, S., B. Esser, and A. Gülhan, "Experimental and numerical investigation on thermal fluid-structure interaction on ceramic plates in high enthalpy flow", *CEAS Space Journal*, vol. 7, no. 4, pp. 483–497, 2015. DOI: 10.1007/s12567-015-0101-5.

[177] Willems, S., A. Gülhan, and B. Esser, "Shock Induced Fluid-Structure Interaction on a Flexible Wall in Supersonic Turbulent Flow", *Progress in Flight Physics*, vol. 5, pp. 285–308, 2013. DOI: 10.1051/eucass/201305.

[178] Willems, S., A. Gülhan, and J. Steelant, "Experiments on the Effect of Laminar-Turbulent Transition on the SWBLI in H2K at Mach 6", *Experiments in Fluids*, pp. 1–19, 2015. DOI: 10.1007/s00348-015-1904-z.

[179] Wisspeinter, C., "Measurement deviation depending on tilt at differenc distances for Sensor CS5", Micro-Epsilon, Ortenburg, Germany, Tech. Rep., 2015.

[180] Worden, K., C. R. Farrar, G. Manson, and G. Park, "The Fundamental Axioms of Structural Health Monitoring", *Proceedings of the Royal Society A: Mathematical, Physical and Engineering Sciences*, vol. 463, no. 2082, pp. 1639–1664, 2007. DOI: 10.1098/rspa.2007.1834.

[181] "X-33 Operations Center – Annual Performance Report", Lookheed Martin Skunk Works, Tech. Rep., 1999.

[182] Xie, W.-Z., Z.-M. Wu, A.-Y. Yu, and S. Guo, "Control of Severe Shock-Wave/ Boundary-Layer Interactions in Hypersonic Inlets", *Journal of Propulsion and Power*, vol. 34, no. 3, pp. 614–623, 2018. DOI: 10.2514/1.b36614.

[183] Xie, W.-Z., S.-Z. Yang, C. Zeng, K. Liao, R.-H. Ding, L. Zhang, and S. Guo, "Improvement of the free-interaction theory for shock wave/turbulent boundary layer interactions", *Physics of Fluids*, vol. 33, no. 7, p. 075 104, 2021. DOI: 10.1063/5.0050113.

[184] Young, R. W., "Inharmonicity of Plain Wire Piano Strings", *The Journal of the Acoustical Society of America*, vol. 24, no. 3, pp. 267–273, 1952. DOI: 10.1121/1.1906888.

[185] Zope, A., C. Horner, E. M. Collins, S. Bhushan, and M. Bhatia, "Investigation of Flexible Panel Dynamic Response Induced by Coherent Turbulent Vortical Structures", in *AIAA Scitech 2021 Forum*, American Institute of Aeronautics and Astronautics, 2021. DOI: 10.2514/6.2021-0251.

# A H2K Flow Conditions

## A.1 Rigid Insert

**Table A.1:** H2K flow conditions – rigid wall

| $Ma$ | $\alpha$ | $\Delta x$ | $p_0$ | $T_0$ | $p_\infty$ | $T_\infty$ | $Re_\infty$ |
|---|---|---|---|---|---|---|---|
| 5.33 | — | — | 1258 kPa | 392.9 K | 1638 Pa | 58.9 K | $19.2 \cdot 10^6$ /m |
| 5.33 | 5° | — | 1236 kPa | 391.0 K | 1610 Pa | 58.6 K | $19.0 \cdot 10^6$ /m |
| 5.33 | 10° | — | 1261 kPa | 391.7 K | 1642 Pa | 58.7 K | $19.3 \cdot 10^6$ /m |
| 5.33 | 15° | — | 1257 kPa | 393.0 K | 1637 Pa | 58.9 K | $19.2 \cdot 10^6$ /m |
| 5.33 | 17.5° | — | 1249 kPa | 390.0 K | 1626 Pa | 58.4 K | $19.3 \cdot 10^6$ /m |
| 5.33 | 20° | — | 1266 kPa | 393.7 K | 1649 Pa | 59.0 K | $19.3 \cdot 10^6$ /m |
| 5.33 | 20° | 50 mm | 1251 kPa | 395.1 K | 1631 Pa | 59.2 K | $19.0 \cdot 10^6$ /m |

## A.2 Elastic Panel

**Table A.2:** H2K flow conditions – elastic panels

| Run | $Ma$ | $\alpha$ | $\Delta x$ | $p_0$ | $T_0$ | $p_\infty$ | $T_\infty$ | $Re_\infty$ |
|---|---|---|---|---|---|---|---|---|
| 24 | 5.33 | — | — | 1240 kPa | 389.8 K | 1616 Pa | 58.4 K | $19.2 \cdot 10^6$ /m |
| 25 | 5.33 | — | — | 1237 kPa | 389.7 K | 1611 Pa | 58.4 K | $19.1 \cdot 10^6$ /m |
| 26 | 5.33 | — | — | 1231 kPa | 390.8 K | 1604 Pa | 58.6 K | $19.0 \cdot 10^6$ /m |
| 85 | 5.33 | — | — | 1257 kPa | 393.7 K | 1637 Pa | 59.0 K | $19.1 \cdot 10^6$ /m |
| 87 | 5.33 | 15° | — | 1251 kPa | 390.5 K | 1630 Pa | 58.5 K | $19.3 \cdot 10^6$ /m |
| 88 | 5.33 | 17.5° | — | 1251 kPa | 391.1 K | 1630 Pa | 58.6 K | $19.2 \cdot 10^6$ /m |
| 89 | 5.33 | 17.5° | — | 1255 kPa | 394.5 K | 1635 Pa | 59.1 K | $19.1 \cdot 10^6$ /m |
| 90 | 5.33 | 20° | — | 1266 kPa | 401.4 K | 1651 Pa | 60.2 K | $18.7 \cdot 10^6$ /m |
| 91 | 5.33 | — | — | 1262 kPa | 403.3 K | 1646 Pa | 60.5 K | $18.5 \cdot 10^6$ /m |
| 92 | 5.33 | — | — | 1255 kPa | 392.7 K | 1635 Pa | 58.8 K | $19.2 \cdot 10^6$ /m |
| 93 | 5.33 | 17.5° | — | 1254 kPa | 390.9 K | 1633 Pa | 58.6 K | $19.3 \cdot 10^6$ /m |
| 95 | 5.33 | 20° | — | 1250 kPa | 392.4 K | 1628 Pa | 58.8 K | $19.1 \cdot 10^6$ /m |
| 96 | 5.33 | 20° | 25 mm | 1264 kPa | 396.1 K | 1646 Pa | 59.4 K | $19.1 \cdot 10^6$ /m |
| 98 | 5.33 | 20° | 100 mm | 1263 kPa | 400.6 K | 1647 Pa | 60.0 K | $18.8 \cdot 10^6$ /m |
| 99 | 5.33 | 20° | 100 mm | 1259 kPa | 393.2 K | 1640 Pa | 58.9 K | $19.2 \cdot 10^6$ /m |
| 100 | 5.33 | 20° | 50 mm | 1258 kPa | 391.9 K | 1639 Pa | 58.7 K | $19.3 \cdot 10^6$ /m |
| 101 | 5.33 | — | — | 1261 kPa | 395.2 K | 1643 Pa | 59.2 K | $19.1 \cdot 10^6$ /m |
| 105 | 5.33 | — | — | 1253 kPa | 391.6 K | 1631 Pa | 58.7 K | $19.2 \cdot 10^6$ /m |
| 106 | 5.33 | — | — | 1250 kPa | 409.8 K | 1632 Pa | 61.4 K | $17.9 \cdot 10^6$ /m |
| 107 | 5.33 | — | — | 1263 kPa | 437.3 K | 1651 Pa | 65.6 K | $16.5 \cdot 10^6$ /m |
| 108 | 5.33 | — | — | 1234 kPa | 428.5 K | 1614 Pa | 64.3 K | $16.6 \cdot 10^6$ /m |

# B H2K Schlieren Setup

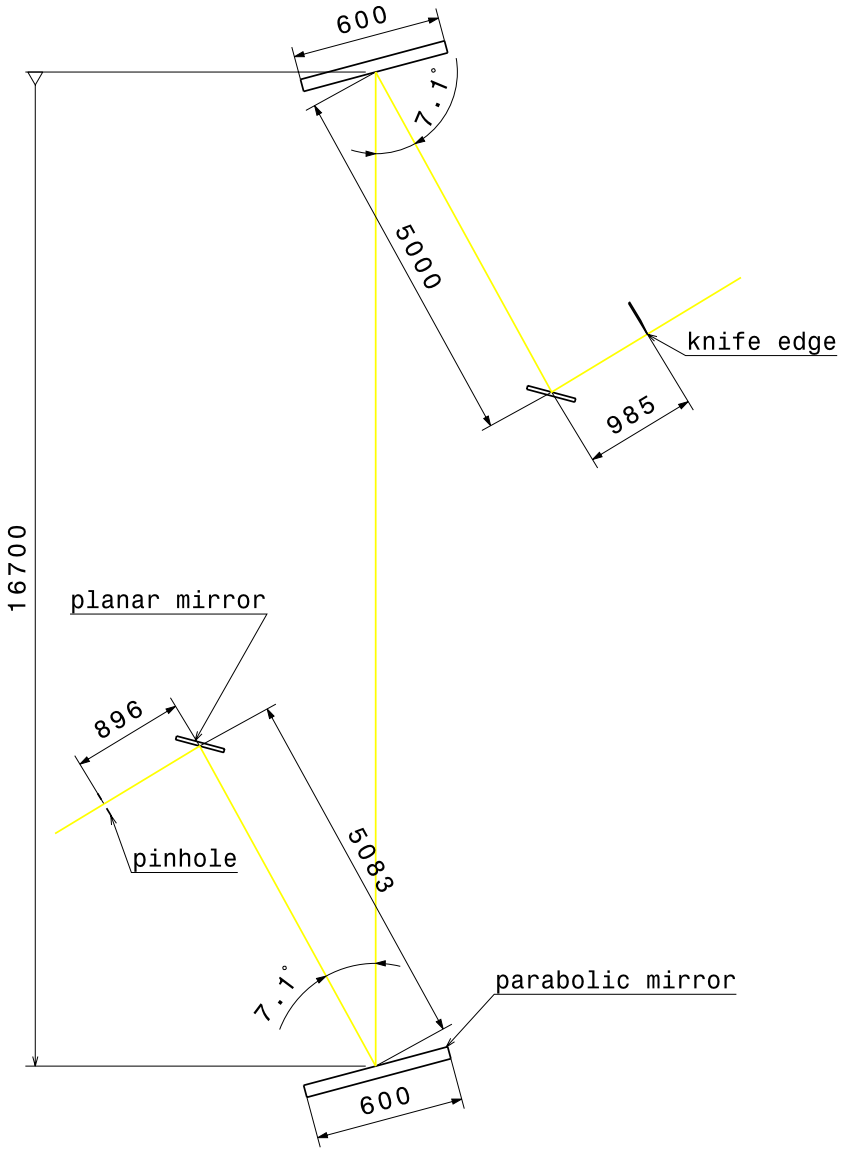


**Figure B.1:** Schlieren setup at Hypersonic Wind Tunnel H2K (H2K) (drawing not to scale, measures in mm)

The H2K Schlieren system uses two mirrors of 600 mm diameter and a nominal focal length of 6 m. The angle of these mirrors is minimized to reduce optical errors. The minimum angle is limited by the space required for opening the test section door. A constant light source was used for the present work. Test runs with a short duration

light source to obtain improved images of turbulent structures are shown in [20]. For a general discussion of such systems refer to [98, 144].